A Single-photon Source Based on a Lateral n-i-p Junction Driven by a Surface Acoustic Wave

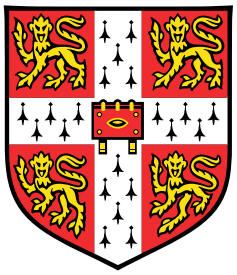

Tzu-Kan Hsiao

Department of Physics
University of Cambridge

This dissertation is submitted for the degree of
Doctor of Philosophy

Robinson College October 2018

Abstract

A Single-photon Source Based on a Lateral n-i-p Junction
Driven by a Surface Acoustic Wave

Tzu-Kan Hsiao

Single-photon sources are essential building blocks in quantum photonic networks, where quantum-mechanical properties of photons are utilised to achieve quantum technologies such as quantum cryptography and quantum computing. In this thesis, a single-photon source driven by a surface acoustic wave (SAW) is developed and characterised. This single-photon source is based on a SAW-driven lateral n-i-p junction in a GaAs quantum-well structure. On this device, the lateral n-i-p junction is formed by gate-induced electrons and holes in two adjacent regions. The SAW potential minima create dynamic quantum dots in a 1D channel between these two regions, and are able to transport single electrons to the region of holes along the channel. Single-photon emission can therefore be generated as these electrons consecutively recombine with holes.

After characterisation and optimisation in four batches of devices, clear SAW-driven charge transport and the corresponding electroluminescence (EL) can be observed on an optimised SAW-driven n-i-p junction. Time-resolved measurements have been carried out to study the dynamics of SAW-driven electrons. Time-resolved EL signals indicate that a packet of electrons is transported to the region of holes in each SAW minimum. In addition, the carrier lifetime of SAW-driven electrons in the region of holes is shown to be $\sim 100\,\mathrm{ps}$, which is much shorter than the SAW period of 860 ps. Hence, it is promising to observe single-photon emission in the optimised device.

In order to test single-photon emission, a Hanbury Brown-Twiss experimental setup has been employed to record an autocorrelation histogram of the SAW-driven EL signal at the single-electron regime. Suppression of autocorrelation coincidences at time delay $\Delta t = 0$ is evidence of photon antibunching. By fitting theoretical functions describing the SAW-driven EL signal, it is found that the second-order correlation function shows $g^{(2)}(0) = 0.39 \pm 0.05$, which is lower than the common criterion for a single-photon source $g^{(2)}(0) < 0.5$. Moreover,

theoretical calculation and simulation suggest that, if a constant background signal can be filtered out, $\sim 80\%$ of the SAW-driven EL is single-photon emission.

Declaration

This dissertation is the result of my own work and includes nothing which is the outcome of work done in collaboration except as declared in the Declaration and specified in the text.

It is not substantially the same as any that I have submitted, or, is being concurrently submitted for a degree or diploma or other qualification at the University of Cambridge or any other University or similar institution except as declared in the Declaration and specified in the text. I further state that no substantial part of my dissertation has already been submitted, or, is being concurrently submitted for any such degree, diploma or other qualification at the University of Cambridge or any other University or similar institution except as declared in the Declaration and specified in the text

It does not exceed the prescribed word limit of 60,000 words including abstract, tables, footnotes and appendices.

Tzu-Kan Hsiao
October 2018

Acknowledgements

This thesis summarises most of the works in my PhD. They simply cannot be one man's job. I need to thank a lot of people for their support. First of all, I would like to thank my supervisor, Professor Chris Ford, for always inspiring me and being patient. One can really learn a lot when his/her supervisor is willing to spend time working with him/her in the lab. For this reason, I think I am really lucky to have him as my supervisor.

I also want to express my gratitude to Dr Ateeq Nasir, and Dr Youson Chung for their initial training when I started my PhD. Thanks to Dr Jorge Pedrós, Dr Youson Chung, and Dr Seok-Kyun Son for their hard work in the early stage of this project. Thanks also to Hangtian Hou and Antonio Rubino who worked close to me and shared their helpful ideas for this project. The other members of the Friday-morning SAW meeting — Stuart, Bruno, Hugo, and Shak — have all given me useful advice and opinions.

I would like to thank Dr Ian Farrer and Professor Dave Ritchie for growing the GaAs/AlGaAs heterostructures; Jon Griffiths and Thomas Mitchell for performing the E-beam lithography; Dr Girish Rughoobur and Kham Niang for sputtering the ZnO film; Dr Ateeq Nasir, Professor Richard Phillips, Dr Gabriel Éthier-Majcher, Dr Megan Stanley, and Dr Peter Spencer for the optical setups; Dan Cross and Mariusz Naguszewski for the liquid Helium supply; and Melanie Tribble for keeping cleanroom running. I would also like to acknowledge financial support from the Semiconductor Physics Group, Robinson College, Taiwanese Government, and Cambridge Overseas Trust.

I would like to thank my family and many friends for their encouragement and support. Finally, I want to thank my wife, Yu-Chieh, for her endless support over the last five years.

Table of contents

Chapter 1

Introduction and Motivation

Quantum photonics can be used in many quantum technologies such as quantum cryptography [1–3], quantum communication [4–6], quantum metrology [7, 8], and quantum computing [9, 10]. In quantum photonics, photons, the quanta of electromagnetic radiation, are used as fundamental quantum states to utilise their quantum mechanical properties. Quantum mechanics allows these quantum states to be individually manipulated and also mutually entangled to exhibit nonclassical behaviour such as quantum teleportation and the no-cloning theorem [4, 5, 11, 12]. These photons can thus be exploited to achieve applications that are impossible in a classical system. In order to benefit from quantum photonics, well-controlled photonic quantum states must be produced by a nonclassical light source. The development of single-photon sources is thus important for these purposes [13–15].

1.1 Single-photon Source

An ideal single-photon source is a nonclassical light source that can generate temporally and spatially separated indistinguishable quantum states with photon number = 1 on demand [13]. These quantum states are single photons that are emitted one after another by the single-photon source when they are periodically triggered by a user, as shown in figure 1.1. In order to realise practical quantum-technology applications, single-photon sources need to meet a few requirements [13]: (1) high single-photon purity, (2) good indistinguishability, (3) high repetition rate and high photon collection efficiency. These requirements are described in the following sections.

Fig. 1.1 Schematic of a single-photon source, where a stream of single-photons is emitted using a periodic trigger.

1.1.1 Single-photon Purity

An ideal single-photon source should always generate no more than one photon at any arbitrary moment. Multi-photon states will allow eavesdropping, which compromises security. In quantum cryptography, they can also contribute to error mechanisms in other applications. A single-photon source with high single-photon purity has a high probability of producing exactly one photon when the source is triggered. The single-photon purity of a single-photon source can be characterised by the second-order intensity correlation function $g^{(2)}(\Delta t)$ in a Hanbury Brown-Twiss experimental setup, where Δt is the time delay of two photon detection events [16, 17]. Perfect single-photon states with a photon number of no more than 1 in each state give rise to $g^{(2)}(0) = 0$. On the other hand, in a coherent light source, like lasers, the emitted quantum states have no well-defined photon number and give $g^{(2)}(0) = 1$.

1.1.2 Indistinguishability

In long-distance quantum communication and quantum metrology, photons need to be entangled by photon-photon interaction [4]. If photons are not identical, they cannot be engineered into entangled states. Therefore, in addition to a high single-photon purity, an ideal single-photon source for applications requiring quantum entanglement should also produce indistinguishable photons. In a quantum network in which multiple single-photon sources are involved, not only should each source produce identical photons itself, but photons from different sources should also be identical. The indistinguishability of photons can be measured by the interference visibility V_{HOM} in a Hong-Ou-Mandel experiment [18–20]. A stream of perfectly indistinguishable photons leads to $V_{\mathrm{HOM}} = 1$ while a stream of distinguishable photons results in $V_{\mathrm{HOM}} < 1$.

1.1.3 Repetition Rate and Photon Collection Efficiency

A high single-photon repetition rate is desirable in most quantum photonics applications since it can increase communication speed and make quantum technologies more time-efficient [21, 22]. Photon collection efficiency, which is the ratio of collected single photons to the total actually produced, is also important in quantum technologies for the same reasons. Moreover, photon collection efficiency directly affects the scalability of quantum photonics applications. This is because in a system with n identical single-photon sources with collection efficiency C, the overall collection efficiency becomes C^n [13]. The repetition rate of a single-photon source is limited by the radiative decay lifetime of excitons. If the triggering rate is so high that a previous exciton still has a significant probability of decaying into a photon when the next exciton is triggered, more than one photon may be generated at a time. Hence, the highest single-photon repetition rate is inversely proportional to the radiative decay lifetime. On the other hand, the photon collection efficiency is related to the internal quantum efficiency and optical coupling of a single-photon-emission site, which can both be improved by proper device design [17, 23].

1.2 Applications of Single-photon Sources

1.2.1 Quantum Key Distribution

Quantum Key Distribution (QKD) is one of the most direct applications of single-photon sources. QKD is a cryptographic protocol employing quantum mechanics to generate a shared secret key between two parties [24, 25]. These two parties can then use this secret key to encrypt and decrypt information in their communications. The no-cloning theorem of quantum mechanics allows the two parties to detect attempts at eavesdropping in the process of secret-key generation. Therefore, security of communication can be guaranteed provided that there is successful secret-key generation. In QKD, a string of bits (0 or 1) is sent by the sender (Alice, in this case) to the receiver (Bob) in the form of single-photons. With the common QKD protocol BB84 (figure 1.2), for example, single-photons with information in bits are randomly engineered into two orthogonal bases where a bit (either 0 or 1) in one basis can be equally projected into 0 and 1 in the other basis. Bob then randomly chooses one of these two bases to detect the photons sent by Alice and records the results of his measurement. A shared secret key can be generated after Alice and Bob have compared their choices of bases in public [26]. Most importantly, they can tell if a third party (Eve) was trying to obtain information about the bits because attempted eavesdropping leads to an increased error when they compare their recorded strings of bits. However, if multiple

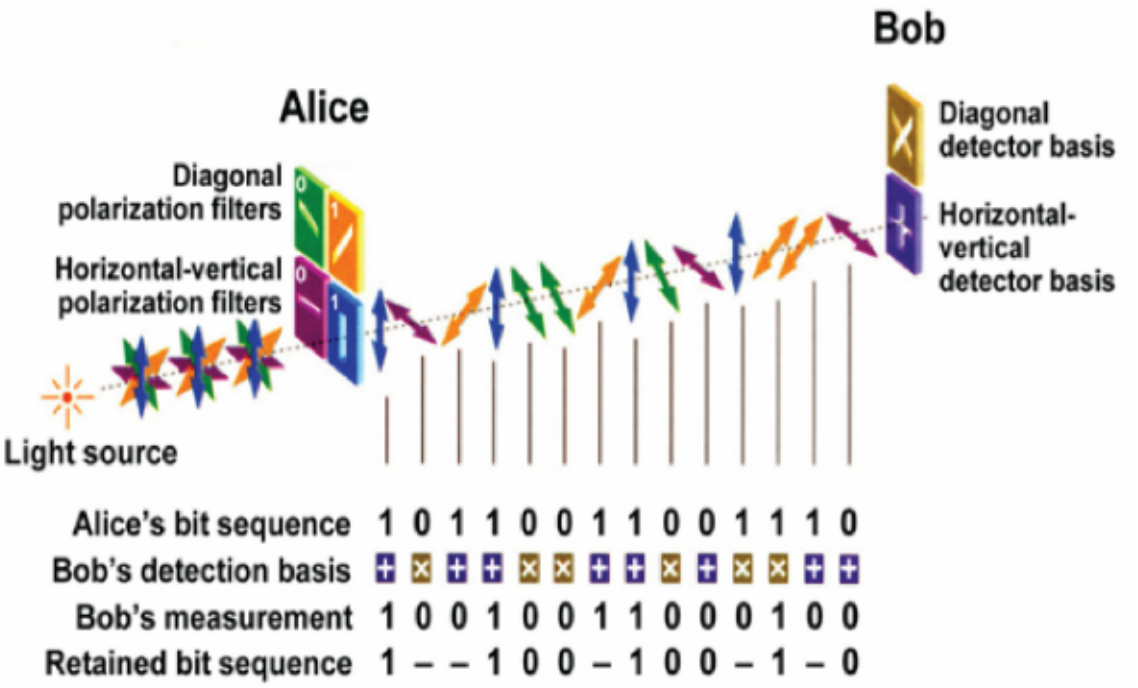

Fig. 1.2 Schematic diagram describing the BB84 QKD protocol. Alice sends Bob a stream of bits that are encoded randomly in one of two bases. Bob also randomly chooses one basis to perform measurements. A shared secret key can be generated after they compare their choices of bases. Diagram from [27].

photons are sent with information on the same bit, Eve can theoretically intercept one of the photons and eventually obtain the same secret key or part of it without being detected by Alice and Bob. Therefore, a single-photon source with high single-photon purity is crucial in QKD. Moreover, a high repetition rate is desirable since it can speed up the process of shared-key generation. Indistinguishability is not necessary as long as single-photons can be projected into the bases required for the protocol, and provided that no repeaters is required.

1.2.2 Quantum Repeater

In order to cope with photon losses over a long distance, intermediate quantum repeaters are essential to link distant nodes to achieve quantum communication between two distant points [28, 29]. Quantum repeaters exploit the property of quantum teleportation in a pair of entangled photons. When two entangled photons are separately sent to two parties (Alice and Bob), the measurement (i.e. polarisation) of the photon at Alice's end will affect the measurement of the other photon at Bob's end in a correlated manner described by quantum mechanics. In this way, quantum teleportation of a quantum state is realised using these

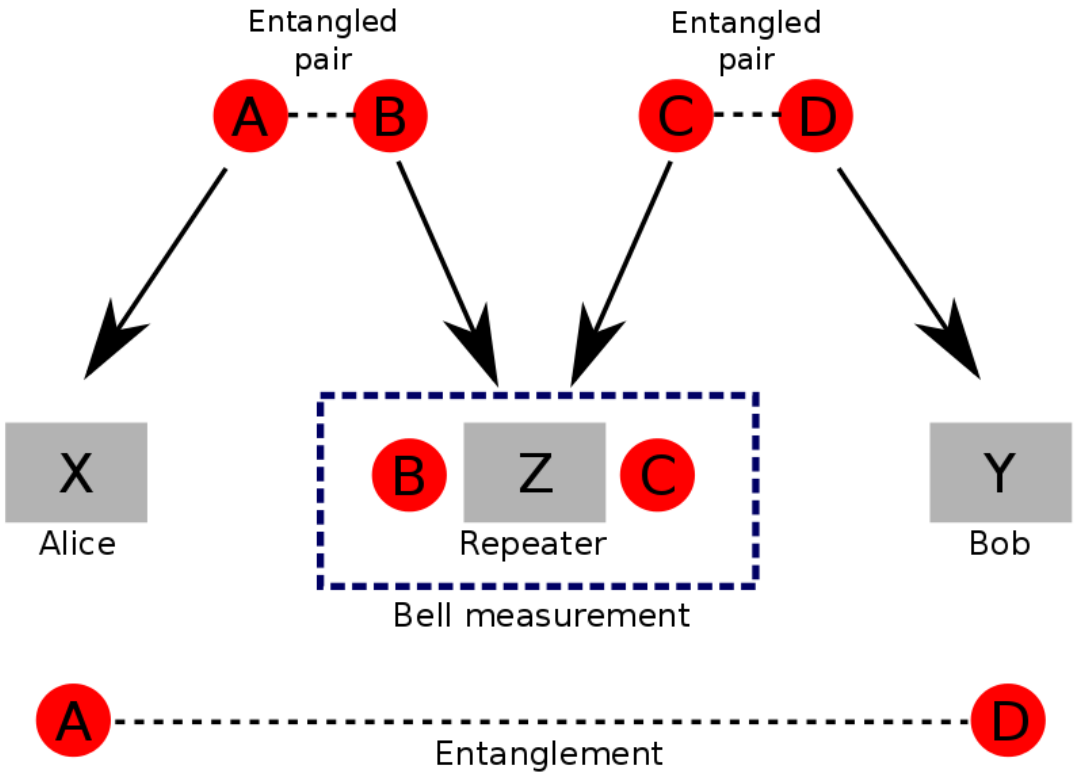

Fig. 1.3 Schematic diagram of a quantum repeater. Two entangled photon pairs (A–B and C–D) are sent to three nodes X, Y, and Z. The repeater at Z performs a Bell measurement to entangle B and C, which results in the entanglement between A and D.

two entangled photons. A quantum repeater shown in figure 1.3 can extend the quantum teleportation in a network. This can be explained as follows: two pairs of entangled photons (photons A and B, and C and D) are first prepared and sent to three nodes including two communication points X and Y, and the quantum repeater Z located between X and Y. A is sent to point X, and D is sent to point Y. B and C are both sent to repeater Z. Before X and Y measure their photon states, Z performs a Bell measurement to entangle B and C [30]. Because A–B and C–D are originally entangled pairs, the entanglement of B and C will also lead to entanglement of A and D. Therefore, the distance of entanglement will double (X–Z and Z–Y $\rightarrow$ X–Y) after Z performs the Bell measurement. The distance can be further extended by adding more quantum-repeater nodes between X and Y. Therefore, quantum teleportation can in principle be carried out over a long distance in order to transmit quantum states for applications like QKD.

Since quantum repeaters have to perform operations of entanglement, the photons in the network need to be indistinguishable. Hence, single-photon sources with good indistinguisha-

bility are necessary for a quantum communication network using quantum repeaters [19, 31]. A high single-photon repetition rate and a high photon collection efficiency are also important for a high-speed and scalable communication network.

1.2.3 Quantum Metrology

Quantum metrology employs many entangled quantum states to perform a quantum-enhanced measurement in which the statistical error of the result can be reduced compared with the error in a classical method [8, 32–34]. In a classical measurement approach, if a measurement is repeated n times, the statistical error will scale as $1/\sqrt{n}$ as a consequence of the central-limit theorem [35]. However, it has been pointed out that probing a system using n entangled quantum states as depicted in figure 1.4 can give rise to a statistical error scaling as $1/n$, meaning the accuracy of the measurement can be enhanced [7]. Therefore, the reduced statistical error using quantum metrology may be utilised in experiments requiring high accuracy such as gravitational-wave detection [36, 37]. Furthermore, a recent experiment has demonstrated the violation of the shot-noise limit in an interferometric phase measurement [38]. This shows that entangled photons can be employed in quantum metrology.

To use single-photon sources in quantum metrology, multiple single-photons have to be entangled together. As mentioned earlier, the single-photon sources need to produce indistinguishable single photons. Also, as multiple single-photon sources must be employed, high photon collection efficiency is an important factor in this application [39].

1.3 Single-photon Source Using Single Emitter

The simplest form of single-photon source can be constructed using a single quantum system with discrete energy levels. For example, a single electron in a two-level system can produce single photons when excited by a laser. The electron excited from the ground state will decay and generate a photon within its radiative decay lifetime, and this system cannot emit another photon before the excited electron decays back to the ground state. Therefore, single-photon generation is guaranteed from this single-electron two-level system. This kind of single quantum system, which can produce single-photons, is called a single emitter [14]. Single-photon sources based on the idea of a single emitter have been widely studied because they allow deterministic and indistinguishable single-photon generation. A few types of single-emitter single-photon source are described with their respective advantages and disadvantages in the following sections.

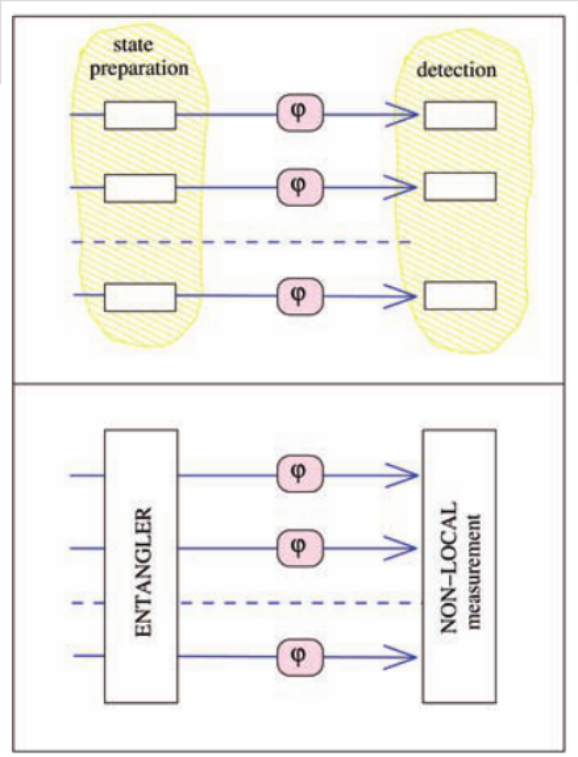

Fig. 1.4 Comparison between classical and quantum measurement approaches. In classical measurements (top panel), N independent measurements are performed and the outcomes are detected independently as well. In quantum enhanced measurement, N correlated (entangled) probing states are used for a non-local measurement. Diagram from [7].

1.3.1 Single-atom and Single-molecule

Natural atoms and molecules are quantum systems with discrete energy levels. They can therefore become single-photon sources if photon emission from a single atom or a single molecule can be collected exclusively. Since they are single-emitters by nature, early studies of single-photon sources were based on single atoms and single molecules [40]. Also, atoms and molecules are identical quantum systems themselves, so single photons from two single atoms (of the same chemical species) are indistinguishable, which is desirable for applications requiring entanglement [41]. Nevertheless, a single atom in the air has to be trapped in a cavity in order to produce stable single-photons [42]. The complexity of trapping makes this kind of single-photon source difficult to integrate into practical quantum devices.

1.3.2 Colour centre in a Diamond

A single quantum system can also be found in a solid-state system. One such case is a nitrogen-vacancy (NV) or a silicon-vacancy (SiV) centre in diamond [43, 44]. Because the ground state and excited states of this defect are decoupled from the band structure of the diamond crystal, this defect optically resembles a single atom embedded in a solid-state host. This single emitter thus does not require any trapping technique since it is fixed in the crystal. NV centres in diamond can occur naturally or be embedded by ion-implantation techniques. If the density of NV centres is low, single-photon emission can be collected from individual NV centres. Due to their stable structures, these single-photon sources can be operated even at room temperature, although the indistinguishability is sacrificed due to phonon scattering [44]. However, because the site of the NV centre in diamond is difficult to control and the emission wavelength is sensitive to inhomogeneous strain and electric field, NV-centre single-photon sources are not identical. This is a problem for the entanglement of single photons from two such emitters, although it has been shown that the emission wavelength can be tuned by applying an external electric field [45, 46].

1.3.3 Epitaxial Quantum Dot

Currently most high-performance single-photon sources are self-assembled InGaAs-based quantum dots (QD) [17, 47]. Quantum dots as artificial single atoms can be embedded in a semiconductor structure like GaAs using molecular beam epitaxy (MBE). The semiconductor structure allows a more sophisticated device design using advanced lithography technologies. For instance, optical cavities in various shapes can be formed around an embedded QD to improve photon collection efficiency due to the Purcell effect, which enhances the spontaneous emission rate [47–49]. In an optically-pumped QD single-photon source, single excitons are created by optical pumping using an external light source. These excitons then decay into photons. If QD density is low enough for photon emission from one QD to be collected exclusively, single photons can be obtained. Hence, photon collection has to be performed with careful focusing and spectral filtering in order to concentrate on one individual QD.

Because the properties of QDs are well-studied, high single-photon purity, high photon indistinguishability, and high repetition rate have all been demonstrated in many QD single-photon sources. However, one major issue is the randomness of the single-photon-emission site. In conventional growth of epitaxial QDs, the formation of self-assembled QDs is a totally random process. Therefore, it is necessary to rely on statistics to create structures like optical cavities and gates around a QD. This issue makes the fabrication of a deterministic QD device very difficult and hinders its integration into a quantum network [13]. There are

some studies that have focused on directed self-assembled QDs, although this involves a complicated regrowth process [50, 51]. Additionally, the emission wavelength of a QD is sensitive to its dimension, local strains, and electric fields, so different QDs are usually not identical single emitters. However, the emission wavelength can be tuned by applying an electric field or strain, and interference of single photons from two separate QD single-photon sources has been shown in experiments [52, 53].

1.3.4 Electrically-driven QD Single-photon Source

With careful material growth and device fabrication, QDs can be placed at an n-i-p junction. This junction enables electron–hole pairs to be injected into QDs by applying a source-drain bias across the junction. As a result, these QDs can emit single photons without optical pumping using an external light source [22, 49, 54, 55]. The fact that they do not require optical pumping makes electrically-driven QD single-photon sources more portable and scalable. However, they have the same issue as the optically-pumped QD single-photon sources. It is difficult to fabricate a deterministic device, and it is challenging to inject electron–hole pairs into just one QD due to their random distribution. Sophisticated device design and optical setup are essential to make it feasible to collect photon emission from a single QD [15].

1.4 SAW-driven Single-photon Source

In 2000, a scheme was proposed to produce single-photons using a surface-acoustic-wave (SAW) [56]. The scheme is shown in figure 1.5 and is described as follows. The basic device consists of a lateral n-i-p junction and an interdigitated transducer. The lateral n-i-p junction is formed by a two-dimensional electron gas (2DEG) and a two-dimensional hole gas (2DHG) in a GaAs quantum-well structure. The interdigitated transducer is employed to launch SAWs by applying RF signals at its resonance frequency. Unlike all of the previously mentioned single-photon sources, in which excitons (electrons) are optically-excited or electrically-injected in an atom-like quantum system, in this scheme single electrons are carried in dynamic potential minima of the SAW [57–59]. Single electrons are dragged from the 2DEG region by the SAW. Because a SAW has the capability of transporting charge carriers across a barrier, these single electrons can overcome the potential difference across the n-i-p junction and arrive at the 2DHG region [60, 61]. If the recombination lifetime of a single electron is shorter than the period of the SAW, an electron will recombine with a hole

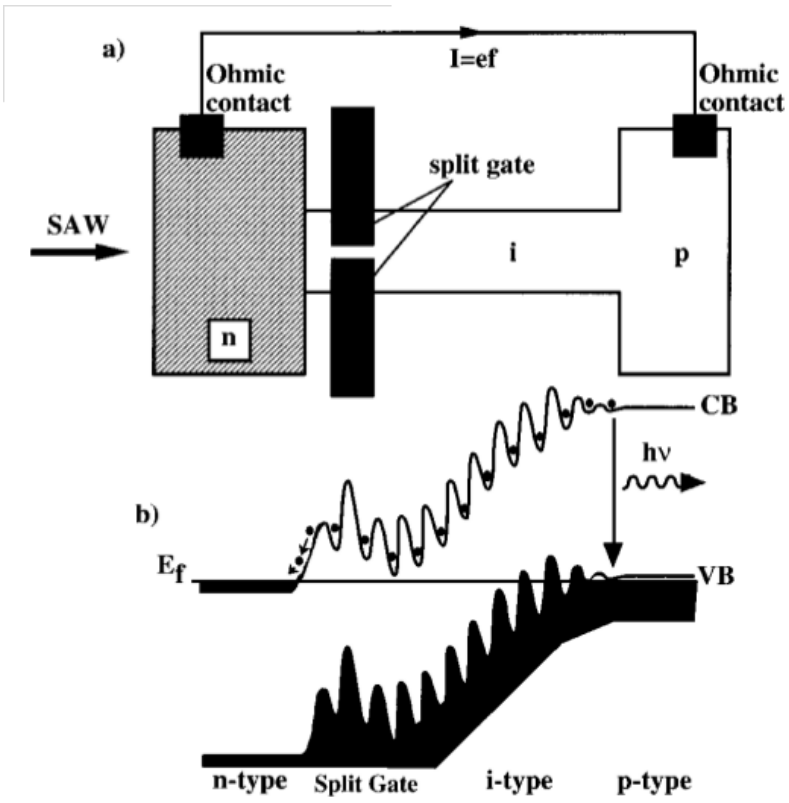

Fig. 1.5 Schematic diagram of a SAW-driven single-photon device. (a) A surface-acoustic-wave carries single electrons from a 2DEG region to a 2DHG region. (b) These single electrons can each recombine with a hole. Single photons are thus produced. Diagram from [56].

in the 2DHG region and create a photon before the next electron arrives. As a consequence, single photons are created one after another.

There are several advantages to this SAW-driven single-photon source compared with other systems. First of all, the single photons are purely electrically driven without the need for an external light source. Next, a high single-photon repetition rate can be obtained since a GHz SAW can be easily launched from a transducer. The high repetition rate can benefit applications like QKD and quantum repeaters. In terms of fabrication difficulty, this scheme is better than QD-based single-photon sources. The quantisation of electrons, which leads to the quantisation of electromagnetic fields (single photons), is caused by the confinement in the dynamic SAW potential. Hence, a static QD is not required in this scheme. Without the issue of QD randomness, the single-photon-emission site (the n-i-p junction) can be made deterministically by mesa etching or gating. This makes device fabrication less complicated and more reproducible, both of which are desirable for further integration. In

addition, this device can potentially be used as an entangled twin-photon source or even a multi-photon source since quantised charge transport with a well-defined electron number has been realised by SAW [61–63]. This ability can therefore be utilised in a quantum repeater and quantum metrology. Finally, this device may be integrated with a proposed SAW-driven quantum computation scheme, which allows quantum state manipulation and entanglement in SAW-driven channels [64]. Quantum states after computation can be projected into the polarisation of single photons. Hence, a SAW-driven single-photon source can serve as the interface between on-chip SAW-driven quantum computation and an external quantum photonic network.

1.5 Thesis Outline

This thesis mainly presents the development and characterisation of a single-photon source based on a SAW-driven lateral n-i-p junction. Chapter 1 introduces basic properties of single-photon sources, their applications in quantum technologies, as well as common types of single-photon source. In addition, as a motivation for this thesis, a scheme to make a SAW-driven single-photon source is described. Next, in order to understand the experimental work in this thesis, Chapter 2 discusses essential theoretical background about low-dimensional systems and photon quantum states. A literature review for SAW-driven charge transport and SAW-driven luminescence is also presented. In Chapter 3, experimental methods including device fabrication, low-temperature systems, and basic measurement techniques are explained. Chapter 4 presents the characterisation and optimisation in four batches of devices. Issues and improvement in each batch are described so that the development process leading to an optimised SAW-driven n-i-p junction is shown. To gain information about the dynamics of SAW-driven electrons, in Chapter 5, results from time-resolved measurements of SAW-driven electroluminescence are shown and analysed. Chapter 6 presents the results from autocorrelation measurements of SAW-driven electroluminescence. Those measurements confirm that photon antibunching or even single-photon emission is produced by the SAW-driven n-i-p junction. Further theoretical analyses are carried out to estimate the probability distribution of photon numbers in SAW-driven electroluminescence. Finally, Chapter 7 concludes the experiments and main results in this thesis, along with a short discussion about future work.

Chapter 2

Background and Theories

This chapter introduces background theories and a literature review that are essential to understanding the working principle of the SAW-driven n-i-p junctions characterised in this thesis. First, low-dimensional systems including quantum-well structures, one-dimensional channels and quantum dots are presented. Next, in order to understand the difference between single-photon sources and classical light sources, the Fock states and the coherent states are explained as well as their photon coherence. Finally, basic properties of surface acoustic waves are introduced, along with a review of previous studies about SAW-driven charge transport and SAW-driven luminescence.

2.1 Low-Dimensional Systems in Semiconductors

When nanostructures in semiconductors are created with at least one dimension comparable to or smaller than the Fermi wavelength λ_F of charge carriers, the motion of these charge carriers is confined in these reduced dimensions. As a consequence, interesting quantum phenomena will arise in these nanostructures.

2.1.1 Two-dimensional Systems

Charge carriers can be confined to a two-dimensional system if a layer of charge is created at the interface of two semiconductors. In a GaAs-AlGaAs system, this is commonly achieved by growing a high-electron-mobility-transistor (HEMT) structure using molecular beam epitaxy (MBE) [65]. Electrons from a doped AlGaAs layer are trapped in the triangular potential well at the GaAs-AlGaAs interface. These electrons are thus confined in the direction of growth (the z axis) and only allowed to move freely in the other two directions (the x and y axes), forming a two-dimensional electron gas (2DEG). Using the same MBE

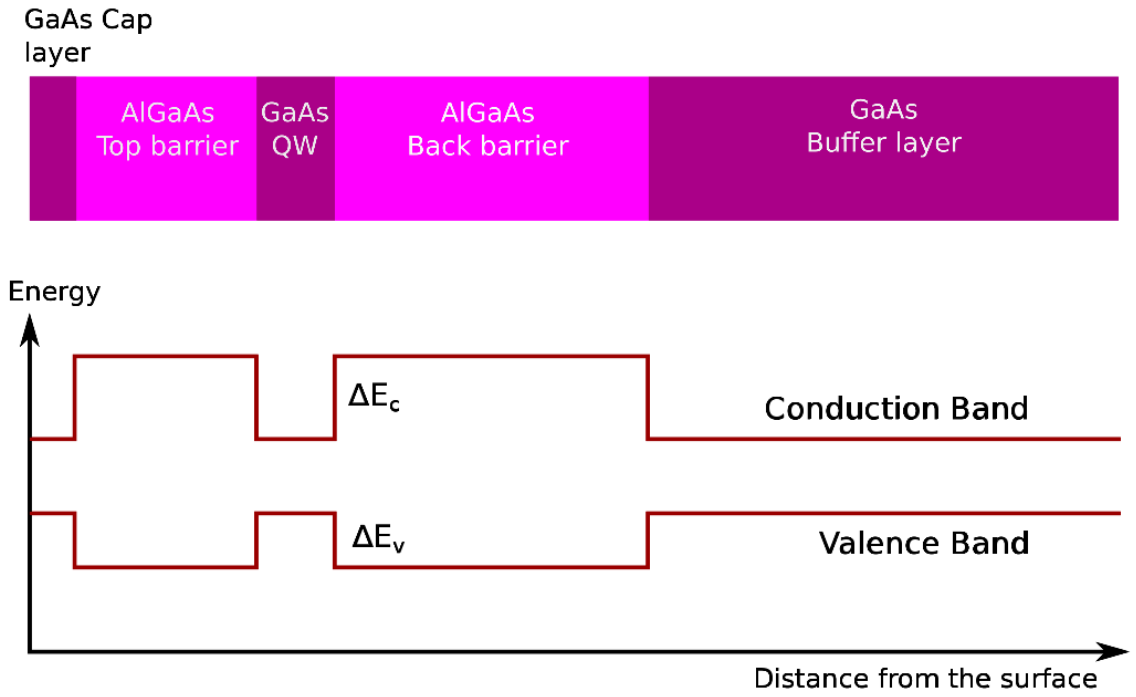

Fig. 2.1 Schematic of the layer structure and the band diagram of a GaAs quantum well sandwiched between two AlGaAs layers. Electrons (holes) are confined in a well with a barrier height ΔE_c (ΔE_v).

growth method but different doping, a two-dimensional hole gas (2DHG) can also be created in a HEMT structure.

Another similar method to create a 2DEG or 2DHG in a GaAs-AlGaAs system is to grow a quantum-well structure, in which a thin GaAs layer is sandwiched between two AlGaAs layers (see Figure 2.1). Charge carriers will be confined in the rectangular potential well. A benefit of using a quantum well in a device is that it allows a 2DEG and a 2DHG to be created simultaneously in the same narrow potential well. As a result, electron-hole recombination can happen and produce photons if the 2DEG and the 2DHG overlap in the x-y plane. Moreover, the discrete quantum levels in the quantum well give rise to 2D subbands that can be observed in the quantised photon energies.

Because electrons and holes are both confined in the rectangular potential well, they exhibit quantised subband energies $E_{n(\text{charge})}$, which can be solved using the Schrödinger equation for a finite quantum well. In a common $Al_{0.3}Ga_{0.7}As$-GaAs-$Al_{0.3}Ga_{0.7}As$ quantum-well structure, the potential height for electrons is $\Delta E_c = 0.24\,\text{eV}$ and the potential height

for holes is $\Delta E_v = 0.14$ eV. For lower subbands, the equation can be simplified to an infinite-quantum-well case, in which

$$E_{n(\text{charge})} = \frac{\pi^2 \hbar^2 n^2}{2m^* W^2}, \tag{2.1}$$

where n is the quantum number of the subband, m^* is the effective mass of the charge carrier, and W is the width of the quantum well (the thickness of the GaAs layer). For instance, in a quantum-well structure with $W = 15$ nm, a photon caused by the transition from the first electron subband to the first heavy-hole subband, and another photon caused by the transition from the first electron subband to the second heavy-hole subband will have a difference in photon energy equal to the difference between the first and the second heavy-hole subbands. Given that the effective mass of heavy holes in GaAs is $\sim 0.45m_0$ ($m_0 =$ electron rest mass), this photon energy difference is thus about 10 meV, which will cause multiple peaks in a photoluminescence spectrum. In such a 15 nm quantum well, PL peaks corresponding to other transitions are more difficult to observed because they require larger excitation energy (the energy difference between the first and second electron subbands is 66 meV, and the energy difference between the first heavy-hole and first light-hole subbands is 17 meV). At 4 K, photon emission is dominated by decay of exciton. The exciton binding energy in a 15 nm GaAs quantum is about 8 meV [66]. Hence, the decay of the lowest exciton state will create a photon with energy $= 1.536$ meV.

2.1.2 One-dimensional Channels

One-dimensional systems can be created from either a 2DEG or 2DHG. A quasi-1D channel can be formed by depleting charge carriers beneath a pair of gates, leaving only a narrow region of charge carriers. Also, the electrostatic potential inside the channel will lead to a lower carrier density, which leads to a larger λ_F according to

$$K_F = \frac{2\pi}{\lambda_F} = \sqrt{2\pi n_{2D}}, \tag{2.2}$$

where K_F is the Fermi wavevector and n_{2D} is the carrier density. If the channel length is shorter than the mean free path of the electrons, the electrons will move ballistically along the channel. If the channel width is comparable to λ_F of the electrons, then 1D subbands will be discrete. Ballistic transport of electrons in a set of 1D subbands gives rise to a quantised conductance in units of $2e^2/h$ [67]. On the other hand, a 1D constriction can also be achieved with the help of 1D etched channels, where the 1D system is formed primarily due to the physical discontinuity beside the channel, though gates are still needed to tune the channel

width. Quantised conductance has also been observed in devices that combine this kind of 1D etched channel and gates [68–70].

2.1.3 Quantum Dots

Electrons can be further confined to a zero-dimensional quantum dot (QD) [71]. This can be achieved by growing self-assembled quantum dots, or by patterning enclosing gates on a 2D system to deplete electrons underneath, leaving only a small isolated region of 2DEG. Quantum dots can be seen as artificial atoms, which have discrete energy levels E_n. Moreover, owing to the Coulomb interaction between electrons in the dot, as well as the interaction between electrons and conductors nearby, the additon energy E_{add} required to add an extra electron into a quantum dot is larger than the difference ΔE_n between consecutive single-particle energy levels. This effect known as Coulomb blockade can be observed in QD-based devices such as single-electron transistors.

2.2 Photon Quantum States

In quantum optics, light signals emitted by a single-photon source can be described as a quantised photon-number state (Fock state). In order to understand the difference between a single-photon source and a classical light source, it is essential to compare a quantised electromagnetic field with its classical counterpart.

2.2.1 Fock States

In quantum mechanics, the Hamiltonian of an electromagnetic field in vacuum can be expressed as [72]

$$H_{\text{EM}} = \sum_{kj} \hbar\omega_k (\hat{a}^{\dagger}_{kj}\hat{a}_{kj} + \frac{1}{2}), \tag{2.3}$$

where k is the wavevector of a field component (or a mode) in k space, ω_k is frequency of the mode, j $(= 1,2)$ specifies the two mutually orthogonal directions transverse to k, and $\hat{a}^{\dagger}_{kj}$ $(\hat{a}_{kj})$ represents the creation (annihilation) operators for the mode k, j. Equation 2.3 represents the electromagnetic field as a set of harmonic oscillators. For a single mode with a

frequency ω, the eigenstates $|n\rangle$ and the corresponding energies E_n are

$$\begin{aligned} |n\rangle &= \frac{(\hat{a}^\dagger)^n}{\sqrt{n!}}|0\rangle \\ E_n &= \hbar\omega(n+\frac{1}{2}), \end{aligned} \tag{2.4}$$

where $|0\rangle$ is the ground state (vacuum state) of the harmonic oscillator, and the operators $\hat{a}^\dagger$ and $\hat{a}$ satisfy

$$\begin{aligned} \hat{a}|n\rangle &= \sqrt{n}|n-1\rangle \\ \hat{a}^\dagger|n\rangle &= \sqrt{n+1}|n+1\rangle . \end{aligned} \tag{2.5}$$

A quantised state $|n\rangle$ of the single-mode field represents a state with n photons in this mode, so $|n\rangle$ is called a photon-number state, also known as a Fock state. In addition, the set of state $\{|n\rangle\}$ forms the Fock basis $\{|n\rangle, n = 0,1,2\ldots\}$, in which any arbitrary state of this single-mode field can be expressed.

Each photon-number state $|n\rangle$ has a well-defined photon number n. This can be seen by computing the average photon number

$$N = \langle n|N|n\rangle = \langle n|\hat{a}^\dagger\hat{a}|n\rangle = n \tag{2.6}$$

and the fluctuation in photon number

$$(\Delta N)^2 = \langle n|(N-\langle N\rangle)^2|n\rangle = 0 . \tag{2.7}$$

Hence, a state $|n\rangle$ has a well-defined photon number n with no uncertainty in the photon number. Furthermore, the probability of measuring m photons in a state $|n\rangle$ is

$$|\langle m|n\rangle|^2 = \delta_{mn} \tag{2.8}$$

as expected.

A photon-number state exhibits non-classical coherence of light, which cannot be explained by classical theories. The second-order correlation function $g^{(2)}(\Delta t)$, which measures the correlation of the field intensities at two different moments t and $t+\Delta t$, can be expressed quantum mechanically as

$$g^{(2)}(\Delta t) = \frac{\langle\psi|\hat{a}^\dagger(t)\hat{a}^\dagger(t+\Delta t)\hat{a}(t+\Delta t)\hat{a}(t)|\psi\rangle}{\langle\psi|\hat{a}^\dagger(t)\hat{a}(t)|\psi\rangle^2}, \tag{2.9}$$

where $|\psi\rangle$ is the field to be measured. If the field is a pure photon-number state ($|\psi\rangle = |n\rangle$), Equation 2.9 gives the second-order correlation function at $\Delta t = 0$

$$g^{(2)}(0) = \frac{n(n-1)}{n^2} = \frac{n-1}{n}. \tag{2.10}$$

So, for a photon-number state $|n\rangle$ with $n \geq 1$, $g^{(2)}(0)$ is always less than 1. This non-classical effect of $g^{(2)}(0) < 1$ is called "photon antibunching", meaning photons are more equally-spaced in space-time. A light source can be called a quantum light emitter if it can produce a light signal showing $g^{(2)}(0) < 1$. Moreover, since $g^{(2)}(0) = 0$ for a single-photon state $|1\rangle$, an ideal single-photon source will give $g^{(2)}(0) = 0$.

2.2.2 Coherent States

A coherent state is a quasiclassical state that approximates an electromagnetic wave produced by a coherent source such as a laser [73]. Such a quasiclassical state $|\alpha\rangle$ should satisfy the correspondence principle, which states that classical quantities can be reproduced by quantum mechanics in the limit of large quantum numbers [74]. It is shown in reference [73] that $|\alpha\rangle$ is an eigenstate of the annihilation operator $\hat{a}$

$$\hat{a}|\alpha\rangle = \alpha|\alpha\rangle \tag{2.11}$$

and it can be expressed in the Fock basis as

$$|\alpha\rangle = \exp\frac{-|\alpha|^2}{2} \sum_{n=0}^{\infty} \frac{\alpha^n}{\sqrt{n!}}|n\rangle. \tag{2.12}$$

Unlike in the case of a pure photon-number state, a coherent state does not have a well-defined photon number. This is shown by the facts that the average photon number and the fluctuation in the photon number of this state are

$$N = \langle\alpha|\hat{a}^\dagger\hat{a}|\alpha\rangle = |\alpha|^2 \tag{2.13}$$

and

$$(\Delta N)^2 = \langle\alpha|(N - \langle N\rangle)^2|\alpha\rangle = |\alpha|^2. \tag{2.14}$$

Therefore, $|\alpha\rangle$ exhibits an uncertainty of $\Delta N = |\alpha|$ in the photon number. Furthermore, the probability P_n of measuring n photons from the coherent state is

$$P_n = |\langle n|\alpha\rangle|^2 = \frac{\alpha^{2n}}{n!}\exp\left(-|\alpha|^2\right) = \frac{N^n}{n!}\exp\left(-N\right), \tag{2.15}$$

which is the Poisson distribution with an average of N.

Finally, a coherent state has $g^{(2)}(0) = 1$, meaning photons are randomly distributed in space-time.

2.3 Surface Acoustic Waves

Surface acoustic waves (SAWs) are sound waves that propagate along the surface of an elastic material [75]. The amplitude of a SAW decays exponentially into the bulk over a distance of one SAW wavelength. On a piezoelectric material, a SAW can be generated by applying a AC voltage to an inter-digitated transducer (IDT) at its resonant frequency. If a SAW propagates on a piezoelectric material, the mechanical strain caused by the SAW will lead to an electric field. Hence, a periodic electric potential will move along with the SAW. This electric potential can affect charge carriers near the surface (within about one SAW wavelength from the surface). Many previous studies have therefore utilised SAWs' capability of charge manipulation in semiconductors and demonstrated interesting results, which will be discussed in the following paragraphs.

2.3.1 SAW-driven Charge Transport

The periodic electric potential moving with SAWs can transport electrons (holes) by trapping them in the potential minima (maxima). When a SAW propagates along a 1D channel, these potential minima and maxima become dynamic quasi-0D dots, which can transport a certain number of charge carriers in each dot. As shown in Figure 2.2(a), SAW minima carry a few electrons from the left region. Some electrons fall back to the Fermi sea to the left as the SAW minima climb up the potential barrier. Eventually, only one electron can remain in each SAW minimum when it reaches the top of the potential barrier, resulting in a SAW-driven current $I_{\mathrm{SD}} = e f_{\mathrm{SAW}}$, where e is the unit charge and f_{SAW} is the frequency of the SAW [57, 60]. An example of this quantised SAW-driven current can be seen in Figure 2.2(b), where the number of electrons n in each SAW minimum decreases as the barrier becomes steeper by applying a more negative gate voltage. Clear steps in I_{SD} at nef_{SAW} can be observed [61]. In addition, it has been shown that a single electron in a

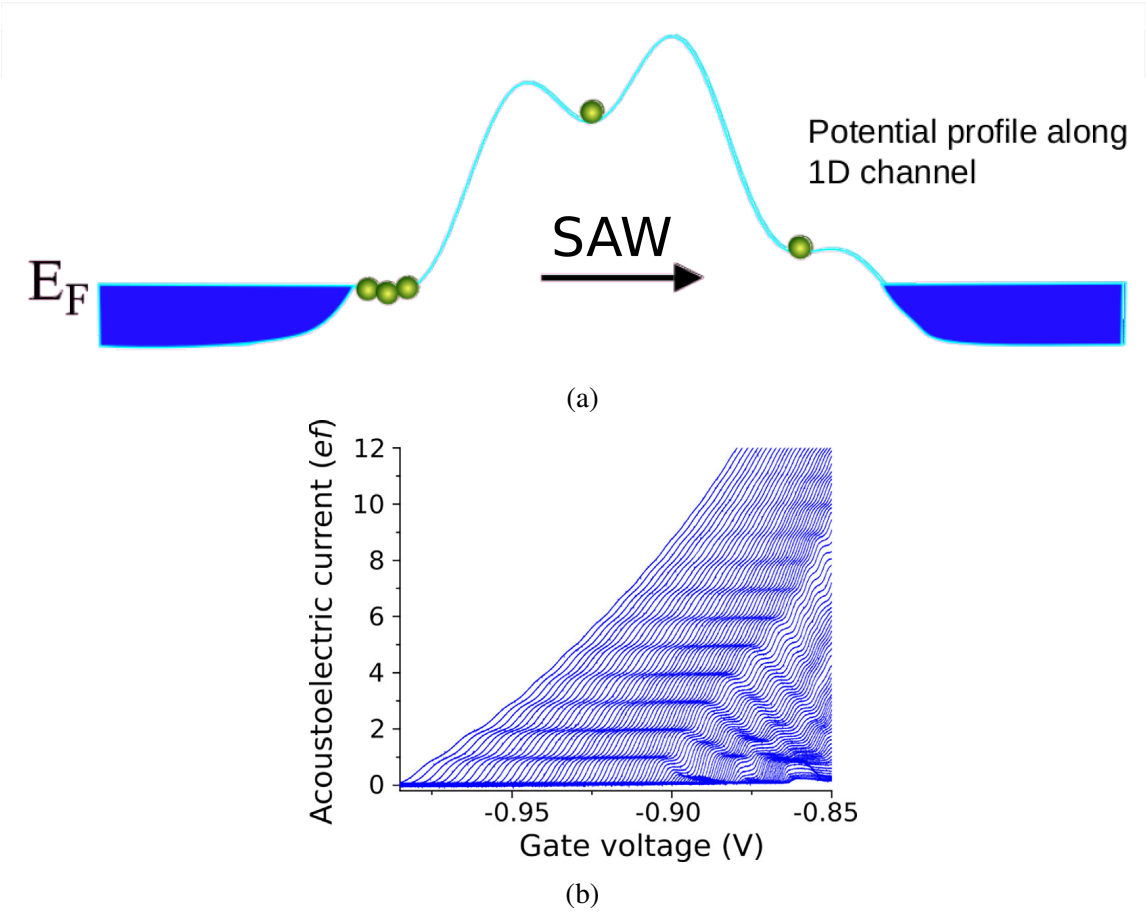

Fig. 2.2 (a) Schematic diagram showing SAW potential minima carry single electrons across a barrier. Diagram from [57]. (b) An example of quantised SAW-driven current. Quantised plateaus corresponding to nef_{SAW} can be seen. Figure from [61].

dynamic quantum dot, formed by a SAW minimum travelling in a 1D channel, exhibits coherent quantum oscillations, which give rise to a periodic feature in the SAW-driven current as a function of the 1D-channel tunnelling barrier [61, 76]. It suggests that electrons in these SAW-created quantum dots manifest quantum dynamics, which can be exploited in quantum information technologies [64]. It has also been demonstrated that a SAW can transfer a single electron between distant static quantum dots on demand with a high reliability [58, 59, 77]. Recently, using the same SAW-driven transport technique, spin-coherent single-electron transport between two quantum dots has also been realised [78]. The results above show that it may be be useful to integrate SAWs into quantum computation networks.

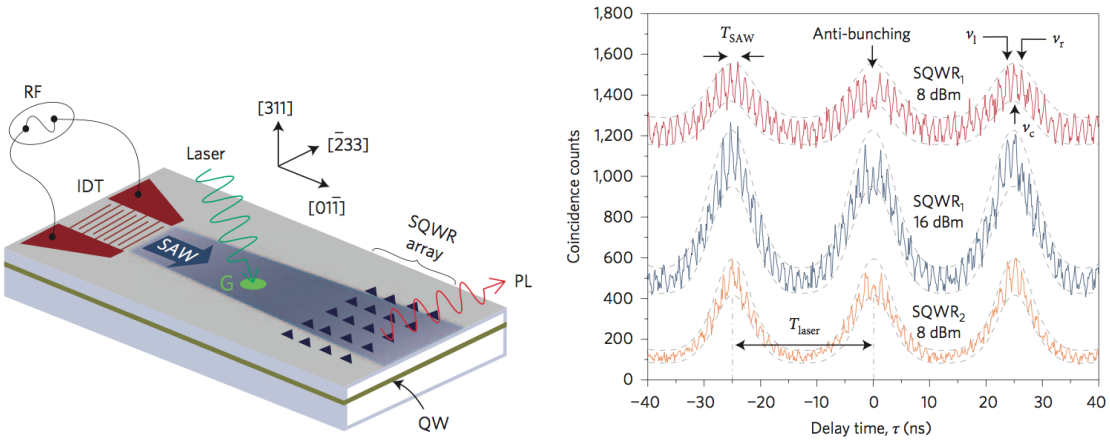

(a) (b)

Fig. 2.3 (a) Illustration showing a SAW transporting optically-excited carriers at G. These carriers move along with the SAW until they are captured by an array of quantum dots in short quantum wires (SQWRs) and recombine. (b) Autocorrelation histograms for two different SAW-pumped SQWRs. Suppression of signal at time delay $\tau = 0$ indicates photon antibunching in the PL signals. Illustration and figure from [80].

2.3.2 SAW-driven Luminescence

A SAW can cause a spatial separation of electrons and holes by trapping them in its minima and maxima respectively, so these electrons and holes will be carried by the SAW without recombining, until the SAW potential is weakened or they are stopped by other mechanisms. Using this idea, it has been demonstrated that a SAW can carry optically-excited electrons and holes, delaying the recombination, and eventually causing photoluminescence (PL) to occur at a region away from the site of the optical excitation [79]. In addition, it has been shown that a SAW can periodically inject optically-excited electron-hole pairs into a static quantum dot (Figure 2.3(a)) [80]. The PL from this SAW-pumped quantum dot shows suppression of $g^{(2)}(0)$, indicating photon antibunching in the PL signal (Figure 2.3(b)).

Alternatively, the mechanical strain caused by a SAW can modulate cavity modes and quantum-dot emission. Hence, a quantum dot can be dynamically coupled to a cavity by passing a SAW through this QD-cavity system. As a consequence, the PL of an optically-pumped quantum dot will be periodically enhanced by the SAW. It has been shown in a few QD-cavity systems that single-photon emission can be achieved using this technique [81, 82].

As for the scheme for a single-photon source based on a SAW-driven lateral n-i-p junction (see Section 1.4), many attempts have been made to try to realise this idea. By using a MBE system integrated with a focused ion beam, in a quantum-well structure, selected regions were doped with n-type or p-type dopants, which form a lateral n-i-p junction [83]. A

SAW-driven current and corresponding electroluminescence (EL) were observed when a SAW was launched by an IDT. On the other hand, a lateral n-i-p junction was fabricated in an InSb/$Al_xIn_{1-x}Sb$ heterostructure [84]. Level of n and p dopings in two separate layers were chosen so that the quantum well was initially p-type everywhere. A bevel etching was then performed to etch away the p dopants at one end to make it n-type. EL signal was observed in this device when a forward bias was applied. In addition, utilising the amphoteric nature of silicon dopants on (100) and (311)A GaAs planes, another SAW-driven lateral n-i-p junction was fabricated by MBE regrowth on a wet-etched step on GaAs [85, 86]. A SAW could drive electrons across the junction to reombine with holes, giving SAW-driven current and EL. Moreover, time-resolved measurements with a pulsed SAW showed that the EL signals were indeed modulated by the SAW. Nonetheless, all devices mentioned above required sophisticated material-growth processes, and their channels between n-type and p-type regions were both wider than 20μm such that SAW-created dynamic quantum dots would not form in these devices. To address these issues, a more recent device based on gate-induced carriers was fabricated [87]. On this device, electrons and holes were induced in adjacent regions by top gates, so the device only required a normal quantum-well structure. Also, a pair of lateral gates were patterned near the n-i-p junction to adjust the 1D-channel width. SAW-driven current and EL were both observed on this device, but no further experiments were performed to prove that the EL was caused by a SAW or to test photon antibunching. Later, a similar device utilising the same idea of a gate-induced lateral n-i-p junction was fabricated [88]. The design of surface gates, which extend carriers induced by top gates, provides a better control of the carrier densities near the junction. However, SAW-driven charge transport or SAW-driven EL were not tested in this device. To the author's knowledge, a SAW-driven lateral n-i-p junction that can produce single photons has not been achieved yet.

Chapter 3

Experimental Methods

This chapter focuses on the fabrication of SAW-driven n-i-p junction devices, experimental setups, and the basic measurement techniques. Details of the GaAs-quantum-well wafer, the fabrication process, difficulties encountered and solutions to those difficulties are described in the first part. After that, the design of a new sample holder, that incorporates RF input, electrical wiring, optical access, and cryostat compatibility in a single sample holder, is presented, as well as the old sample holder for comparison. In the next part, low-temperature measurement systems including a dipping system using a helium dewar (4 K), a helium-3 cryostat (below 1.5 K), and a continuous-flow helium cryostat (4-20 K) are introduced along with their respective advantages in terms of measurements. Finally, the basic electrical measurement techniques that apply to all measurements in the thesis are discussed in the last part.

3.1 Device Fabrication

In order to form a lateral n-i-p junction in a micrometre-scale region, the SAW-driven n-i-p junction devices are based on an induced two-dimensional electron gas (2DEG) and an induced two-dimensional hole gas (2DHG) in an undoped GaAs-quantum-well structure. Fabrication requires many more processing steps as well as more careful consideration and optimisation compared with the fabrication of normal HEMT-based devices. This section describes the process in each fabrication step together with difficulties encountered and the solutions found in each step respectively.

3.1.1 Wafer Selection

The wafer used for the SAW-driven single-photon devices is wafer W1002 grown using molecular beam epitaxy (MBE) in the Semiconductor Physics group at the Cavendish Laboratory by Dr Ian Farrer. The wafer is an undoped AlGaAs/GaAs/AlGaAs quantum-well wafer. A schematic diagram depicting the layer structure and the band structure is given in figure 3.1. From the wafer surface to the bottom, the layer structure consists of a 10nm GaAs capping layer, a 100 nm $Al_{0.33}Ga_{0.67}As$ top barrier, a 15 nm GaAs quantum well, a 285 nm $Al_{0.33}Ga_{0.67}As$ back barrier, and finally a 1 μm GaAs buffer layer. The cap layer is intended to protect the AlGaAs beneath from oxidation. The shallow quantum well is located 110 nm below the wafer surface. This is to allow the SAW to have enough electric potential to affect charge carriers in the quantum well since the electric potential of a SAW decays exponentially from the surface. There was no intentional doping introduced during the wafer growth. However, there was slight p-type background doping due to carbon, which is the majority of contamination in the MBE chamber. The background doping concentration is expected to be about $10^{13}cm^{-3}$.

The size of one SAW-driven n-i-p junction device is 5mm$\times$3mm. Ideally, it would be good to fabricate a grid of many devices on one big piece of wafer as this would maximise the yield and allow the testing of different parameters at once. However, because of the high cost of the MBE wafer and ease of handling in the cleanroom, a 2$\times$2 grid of devices is usually chosen for fabrication. Therefore, the wafer is cleaved into 11mm$\times$7mm chips to fit a 2$\times$2 grid of devices and also leave space at the edges to avoid scratching by tweezers. Since GaAs is piezoelectric along direction [110], which is the major flat of a (100) wafer, it is crucial to cleave the chips so that [110] is aligned with the SAW propagation direction on the devices.

After cleaving, the chips have to be cleaned thoroughly before any further processing, as the SAW propagation is very sensitive to surface roughness, and minute particles of dust would cause defects in the device. Cleaning is carried out by dipping and stirring the chips in acetone for 30 seconds, putting them in an ultrasonic bath for a few minutes if there are no e-beam features on the chips, then rinsing the chips in IPA for 30 seconds, drying with N_2 gas, and finally checking them under a microscope. The same cleaning procedure has to be carried out between any processing steps to make sure the chips are as clean as possible throughout fabrication.

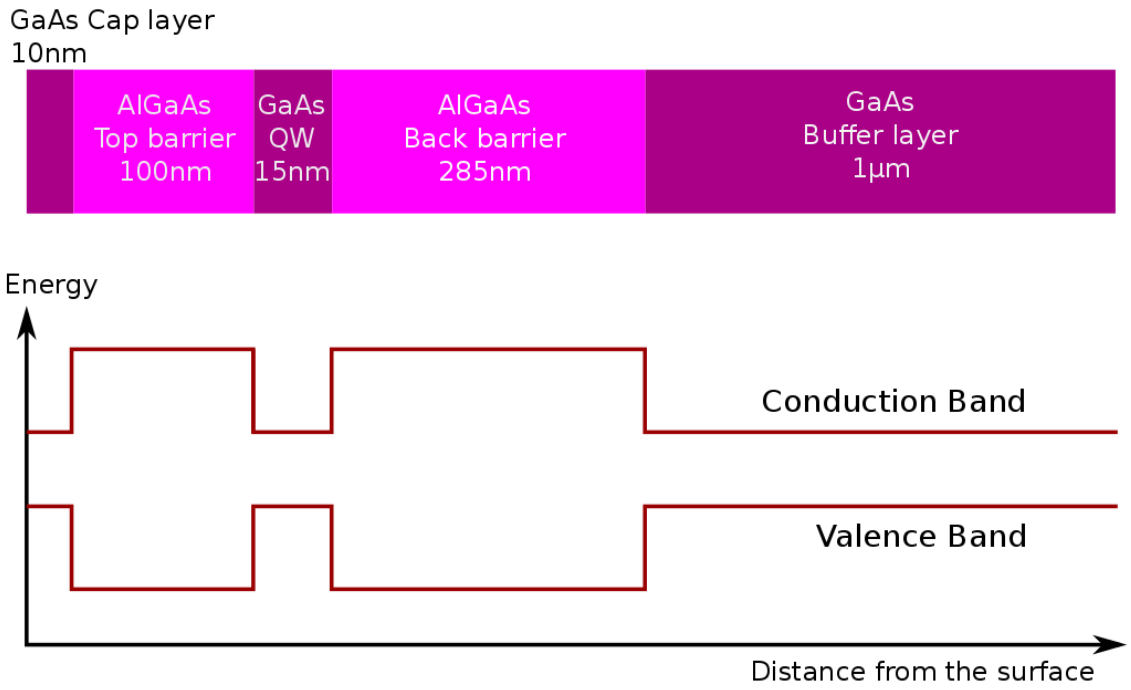

Fig. 3.1 Schematic of the layer structure (top panel) and the band diagram of the W1002 undoped quantum-well wafer. The GaAs quantum well is located at 110 nm to 125 nm from the surface.

3.1.2 Overview of a SAW-driven n-i-p Junction Device

Before details of each processing step are described, an overview of the SAW-driven n-i-p junction device is presented here. Top-view and cross-section diagrams of the device from the latest design are shown in figure 3.2. To allow both electrons and holes to exist in the same device, both n-type and p-type ohmic contacts, shown as blue and red areas in figure 3.2(a), are in direct contact with the quantum well, as depicted in figure 3.2(d). To induce charge carriers by applying an electric field, bridging gates are patterned above the ohmic contacts with a layer of insulator in between, as shown in figure 3.2(d). The ohmic contacts are separated into 6 groups by an etched region without a quantum well (the shaded area in figure 3.2(a)-(c)). Each group has either 2 or 4 ohmic contacts and one bridging gate, which controls the type of induced charge in the quantum well. In order to form a lateral micrometre-scale n-i-p junction, each group also has a surface gate, which can extend the regions of induced charges (Figure 3.2(d)). These surface gates are patterned either directly on the GaAs surface or with a thin insulator in between. Side gates are also deposited above

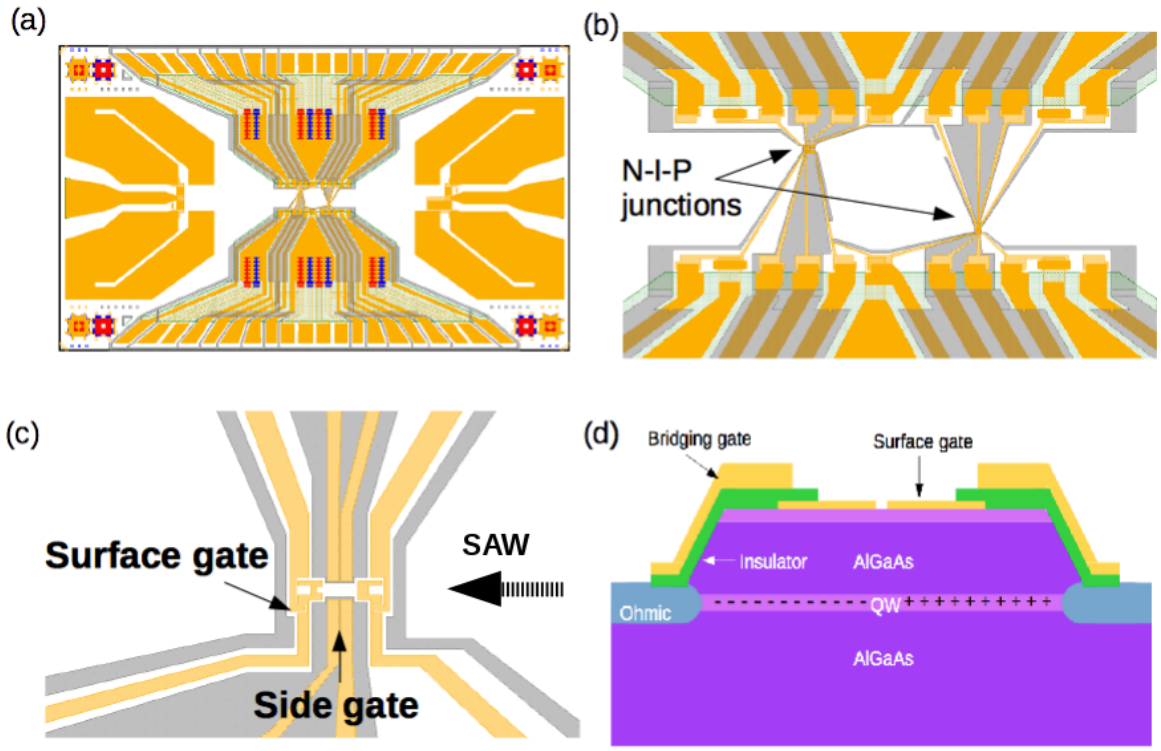

Fig. 3.2 Overview of a SAW-driven n-i-p junction device. (a) Top view of the full device design for the more recent batch. Yellow area is evaporated Ti/Au for gates and bonding pads. Red (blue) area is where the p-type (n-type) ohmic contacts are made. (b) Top view of the central area, where two n-i-p junctions are placed. The shaded area is wet-etched to confine charge carriers. (c) Top view of a lateral n-i-p junction. The area between the two surface gates is etched to form an 1-D channel. The side gates are patterned on top of the etched region. (d) Cross-section of the device. Electrons and holes are pulled from the ohmic contacts by the bridging gates, and then extended by the surface gates to form an n-i-p junction in the quantum well.

the etched area to adjust the potential barrier between the electron region and the hole region, as seen in Figure 3.2(c). With a proper combination of ohmic groups, two n-i-p junctions can be formed in a single chip, one at the bottom right and the other at the top left, as shown in Figure 3.2(b). In addition, to launch a SAW to transport charges across an n-i-p junction, two pairs of inter-digitated transducers (IDTs) are fabricated, on the left and right sides of the device. Each pair can launch two parallel SAW beams that run past the bottom-right and the top-left junctions respectively.

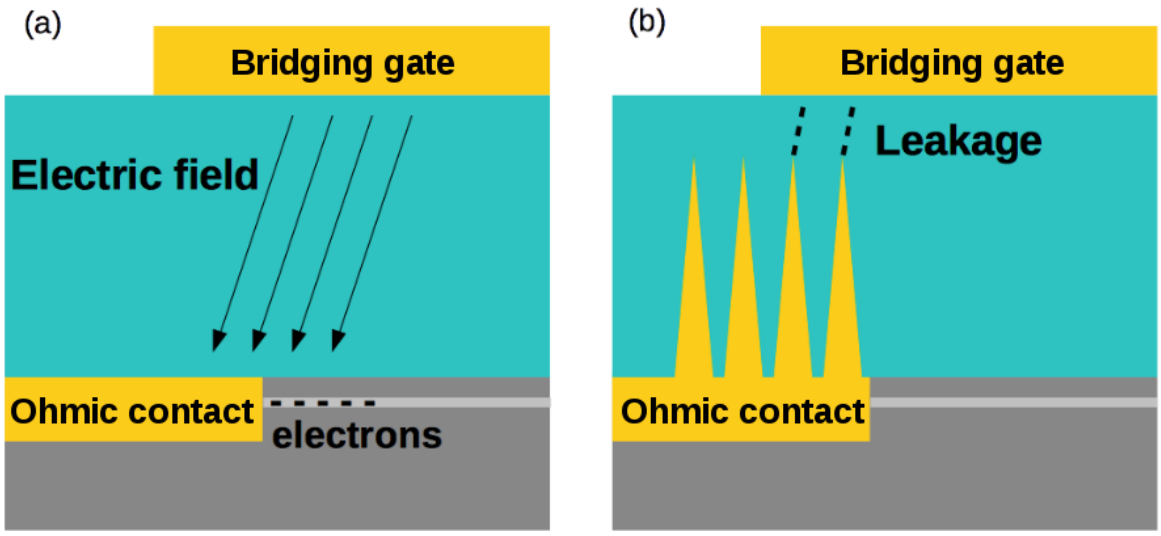

Fig. 3.3 Schematic of induced ohmic contacts, where (a) the electrons are successfully induced in the quantum well by the electric field from the bridging gate, and (b) leakage happens before electrons can be induced because of the spikes on the ohmic metal, which give rise to a locally high electric field across the insulator.

3.1.3 P-type Ohmic Contacts

The first processing step is to make p-type ohmic contacts that provide good conduction of holes between deposited ohmic metal and the quantum well. Good conductive ohmic contacts can usually be obtained by annealing the deposited ohmic metal to have a low resistance interface between the ohmic metal and a semiconductor. Nonetheless, the fabrication of ohmic contacts in an induced device requires more consideration than that in a device based on doped material. A typical induced ohmic contact works as depicted in Figure 3.3(a). Charges are pulled from an ohmic metal into the semiconductor (the quantum well) by an electric field. The electric field is provided by a top gate (the bridging gate) with an insulator between the ohmic metal and the gate to prevent a short. However, if the surface of the ohmic metal is too rough after annealing so that spikes are formed, there would be a high electric field on these spikes when a bias is applied to the gate. The high electric field could create electrical breakdown across the insulator and then cause a leakage current between the ohmic metal and the gate, as shown in Figure 3.3(b). An induced ohmic contact is considered to have failed if the leakage current appears before the charges can be induced in the quantum well. Therefore, the morphology of annealed ohmic metal, the choice of insulator, and the geometry of ohmic metal and gates must all be taken into account in the design and the fabrication of ohmic contacts.

For the development of the p-type ohmic contact recipe that was designed for SAW-driven n-i-p junction devices, please refer to Dr Yousun Chung's PhD thesis [89]. The final optimised recipe is described here as it is used in all the devices that will be discussed in later chapters. The process begins by recessing the ohmic contact area down to the quantum well (115 nm deep) by wet etching. The recessed ohmic contact area is designed to allow the ohmic metal to sit at a level very close to that of the quantum well when the metal is evaporated. In this case, the ohmic metal and the quantum well are in contact by lateral diffusion of ohmic metal into the quantum well during annealing. This is better for inducing charge carriers because the ohmic metal will not screen the electric field from the bridging gates. It has to be noted that the etch depth should be as close to the quantum-well level as possible, as an under-etched ohmic area would not cause sufficient metal diffusion and it was found that an over-etched ohmic area would cause charge carriers to be induced in the lower AlGaAs/GaAs interface rather than in the quantum well [89].

In order to wet-etch the ohmic contact area, the ohmic contact pattern in a layer of spin-coated photoresist is removed to expose the GaAs surface to be etched. The etching solution is H_2SO_4:H_2O_2:H_2O (1:8:1000). This is a dilute etching solution intended to etch the chip at a slow rate of 0.8 nm/s, which is desirable for obtaining a more precise etched depth. It is important to carry out a test etch on a dummy chip before the real chip is etched because the etch rate might vary to some extent due to a slight change in mixing ratio or solution temperature.

After the wet etching is done, the chip is de-scummed using an RF asher to clean off photoresist residue, and it is then dipped in a 20% HCl solution to remove oxide. The chip is then placed in an AuBe evaporator for metallisation. AuBe evaporation for devices in this thesis was performed by Dr Ateeq Nasir. After evaporation, the chip was placed in acetone for lift-off and then annealed at 520 °C for 120 seconds, which was found to produce a good yield, of 84% [89].

Regarding the ohmic pattern, there are two designs employed in the devices discussed in this thesis. The first p-type ohmic pattern was designed by Dr Yousun Chung. As shown in Figure 3.4(a), only two ohmic groups (top middle and bottom middle) have a p-type ohmic contact while the top-left, top-right, bottom-left, and bottom-right groups are reserved for n-type ohmic contacts only. This design has more p-type (or n-type) contacts in a single ohmic group so that the chance of having at least one working ohmic contact is higher. However, this design does not allow the induction of holes in four of the ohmic groups, and thus lacks the flexibility to swap the types of charge carriers across a junction, i.e. from an n-i-p junction to a p-i-n junction. Hence, once contact reliability is high enough, a new design was introduced for later batches of devices. As seen in Figure 3.4(b), the new design

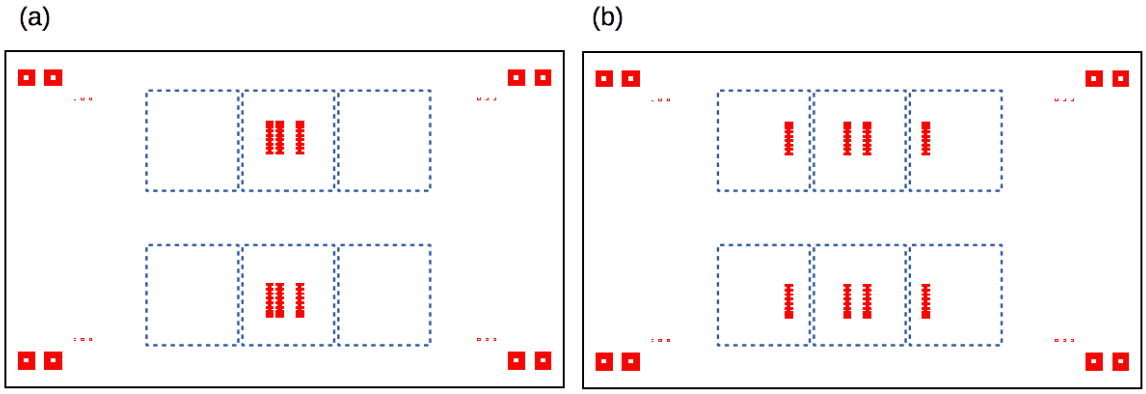

Fig. 3.4 Patterns for p-type ohmic contacts (red regions), where (a) p-type ohmic contacts are only in two of the six ohmic groups (enclosed by dashed line boxes) while (b) every ohmic group has at least one p-type ohmic contact.

ensures each ohmic group has at least one p-type and one n-type ohmic contact. In this case, every ohmic group can be used to induce electrons or holes, providing the yield of functional ohmic contacts is high.

3.1.4 N-type Ohmic Contacts

The fabrication of n-type ohmic contacts is very similar to that of p-type contacts mentioned above. The requirements and considerations for induced p-type ohmic contacts also apply to n-type ohmic contacts. Two different n-type ohmic recipes were used for these devices. The first one was developed by Dr Seok-Kyun Son [90]. Details of development can be found in his PhD thesis. This recipe uses layered ohmic metal Ni/Au/Ge/Ni/Au to enhance lateral metal diffusion and suppress the formation of spikes after annealing. However, this recipe requires many evaporation steps that complicate the processing, and also, micrometre-height spikes were observed during the fabrication of later batches, possibly due to contamination in the evaporator. Therefore, a simpler recipe was developed later by Mr Antonio Rubino and this showed a good yield, of 95% [91]. In this new recipe, AuGeNi alloy is used for evaporation instead of multiple evaporation of Ni, Au, and Ge. This simpler recipe makes the fabrication easier and more reproducible, and thus the two later batches of devices were made using this new recipe.

It should be noted that the fabrication of n-type ohmic contacts has to be carried out after that of p-type contacts. This is because the annealing temperature of both n-type recipes is 460 °C, which is lower than the p-type annealing temperature of 520 °C. If n-type ohmic contacts were made before p-type ones, these n-type ohmic contacts would eventually be annealed twice, above the diffusion temperature of ohmic metal, which would alter the

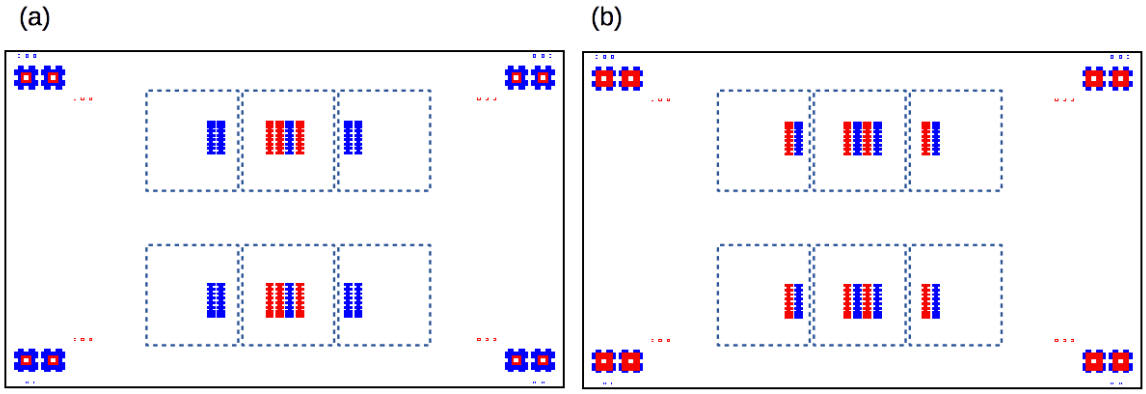

Fig. 3.5 Patterns for n-type ohmic contacts (blue regions), where (a) n-type ohmic contacts are only in four of the six ohmic groups (enclosed by dashed line boxes) while (b) every ohmic group has at least one n-type ohmic contact. P-type contacts are shown in red.

properties of these ohmic contacts. On the other hand, it was found that the behaviour of a p-type ohmic contact did not change at the n-type annealing temperature, allowing the n-type contacts to be made after the p-type contacts [89].

For the same reason as in the case of p-type ohmic contact fabrication, there are two different patterns for n-type ohmic contacts, as shown in Figures 3.5(a) and (b). The n-type patterns should be aligned with the corresponding p-type patterns as well as possible, since the bridging gates are designed to have an ideal overlap when the n-type and the p-type are well aligned.

3.1.5 E-beam Defined Wet Etching

In measurements of early batches of devices, which will be presented in Chapter 4, it was found that electron-hole recombination happened in unexpected regions rather than at the n-i-p junction. Therefore, it is necessary to confine charge carriers around the micrometre-scale n-i-p junction and eliminate unwanted current paths. Wet etching of regions defined by electron-beam (e-beam) lithography was thus introduced to remove the quantum well around the n-i-p junction for better charge confinement [89]. In addition, the etching pattern was further modified in later batches of devices to isolate each ohmic group so that the only recombination path was through the n-i-p junction. Figure 3.6 shows the latest design for e-beam-defined wet etching. This pattern separates the six ohmic groups using an enclosed etched area around each. The only path for current flow from an electron region to a hole region is via a micrometre-wide etched channel, in which the n-i-p junction is formed.

E-beam lithography (EBL) is performed by first spin-coating a layer of PMMA, then exposing the pattern using a focused electron-beam, and finally developing the pattern using

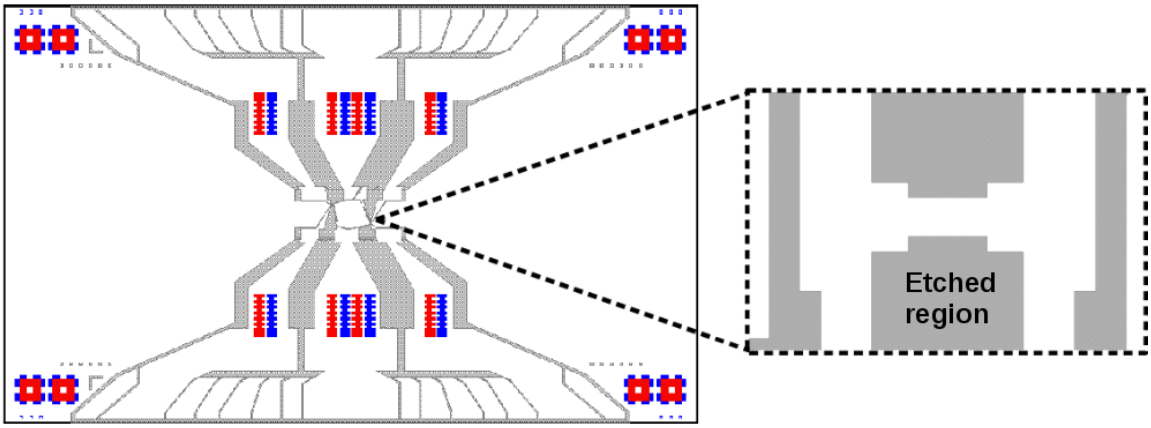

Fig. 3.6 Patterns for E-beam defined wet etching (shaded regions). The pattern separates the ohmic contacts into six groups. The magnified pattern near the n-i-p junction shows the etched 1D channel between two induced charge regions.

an MIBK:MEK:IPA mixture (1:5:15), which is an e-beam-feature developer. The focused electron-beam exposure was performed by Mr Jon Griffiths and Mr Thomas Mitchell. After E-beam feature development, the chip is ready for wet etching using the same etching solution as in the p-type and n-type ohmic contact fabrication. The etched depth should be more than 125 nm in order to remove the quantum well entirely from the etched region. To obtain a well-controlled etched depth, before the real etching, a test etch should be carried out on test chips prepared using the same EBL procedure. In addition, it is recommended that the developed chip be baked at 115 °C overnight in order to improve PMMA adhesion and cure tiny defects in the PMMA layer. Details of this baking are described in following paragraphs.

PMMA Adhesion Issue

One issue that can lead to failed etching is poor adhesion of PMMA to the surface of the chip. If adhesion is bad, etchant will flow into the gap between the PMMA and the chip surface. The area beneath the PMMA, which should remain intact after etching, will then be damaged by the etching solution. In the worst case, the PMMA may detach from the chip surface during wet etching so that the chip is etched everywhere. One example can be seen in Figure 3.7. Figure 3.7(a) shows developed PMMA on a test chip immediately after development. The developed etching pattern did not have any obvious defect in the PMMA-covered region at this stage. However, irregular stains appeared in the PMMA-covered region after the chip was dipped in a 20% HCl solution for 30 seconds, as shown in Figure 3.7(b). The test chip was then etched in the etching solution for 3 minutes. Surprisingly, a significant part of the PMMA layer peeled off the surface after the etching, as shown in Figure 3.7(c). The peeled

PMMA and the stains caused the test chip to be etched irregularly, which can be seen in Figure 3.7(d). This example of failed etching was clearly caused by poor adhesion. These stains after HCl dipping can be explained by the space under the PMMA being filled with HCl solution. The liquid under the PMMA caused a change in colour, and these spaces were later filled with etchant during wet etching, which caused the same irregular marks on the chip after the PMMA was removed. This poor adhesion could be due to moisture being trapped between the PMMA and the chip surface, or it could be related to stress in the PMMA. Therefore, baking the PMMA at 115 °C after development may improve adhesion, since it can drive the moisture away and maybe soften the PMMA to release the stress. It should be noted that the baking temperature should be lower than 125 °C as this is the glass transition temperature of PMMA. PMMA can flow again above this temperature and destroy a developed E-beam-defined pattern.

Pinhole Issue

A test chip that had the same poor adhesion issue was cut into several smaller chips to test whether baking could solve the problem. One of these chips was baked at 115 °C for 10 minutes and was then processed using the same etching procedure. The results are presented in Figure 3.8. After wet etching, there was no sign of PMMA peeling, as shown in Figure 3.8(a), indicating improved PMMA adhesion after the ten-minute bake. However, although there were almost no irregular stains, micrometre-size circular spots were observed instead (see Figure 3.8(c)). These spots also left etched pits on the chip surface, as seen in Figure 3.8(b) and (d), when PMMA was removed. This means that there were still tiny pinholes in the PMMA after 10 minutes of baking. In this case, the etching solution can damage the PMMA-covered region through these pin holes and therefore cause etched pits on the surface.

Overnight PMMA Baking

To solve the pinhole issue, another test chip was baked at 115 °C for 15 hours in the hope that an extended baking time might prevent these pinholes and any other defects in the PMMA. The result is shown in Figure 3.9. In Figure 3.9(a), the PMMA was intact after overnight baking and the entire etching procedure, indicating that both the adhesion and pin-hole issues were solved after overnight baking. After the PMMA was removed, as in Figure 3.9(b), the etched pattern was clear and there were no unexpected marks in the unetched area. Therefore, it is beneficial to perform overnight baking on developed chips to avoid the issues mentioned above.

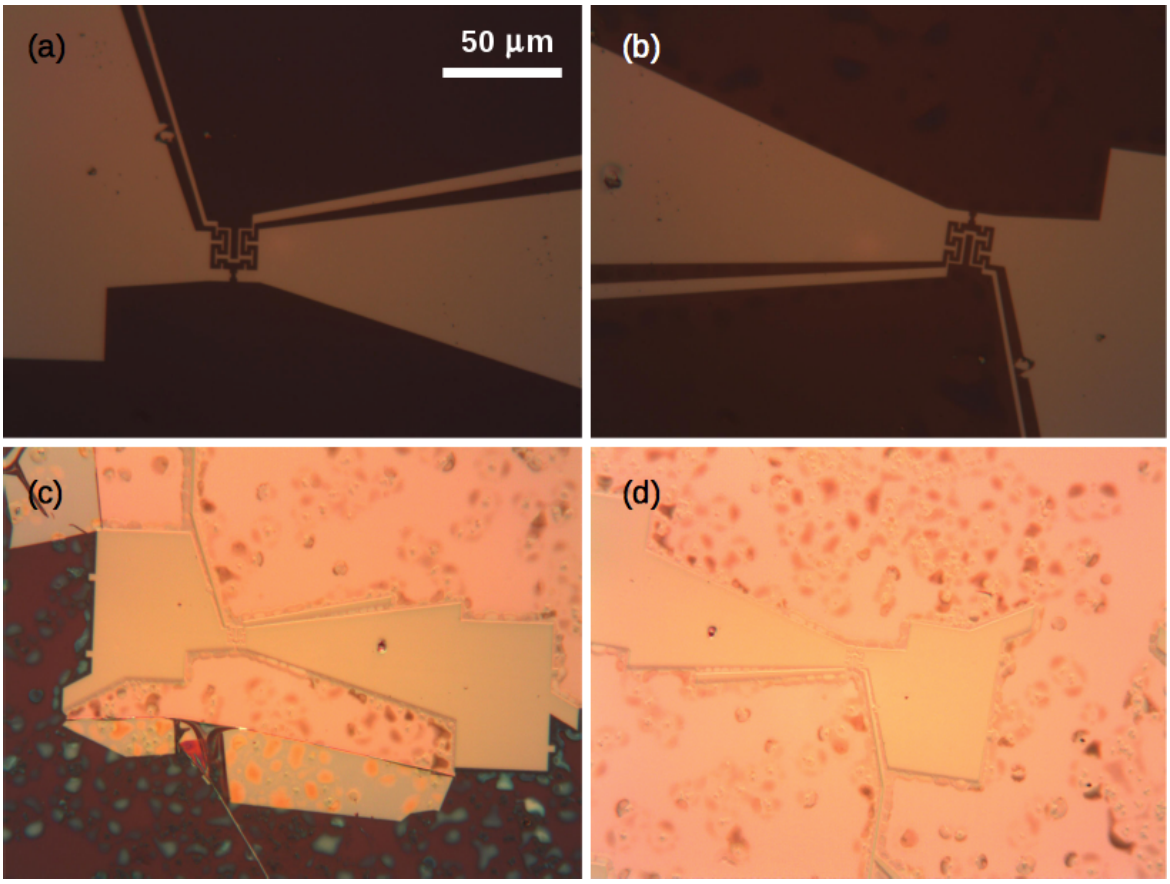

Fig. 3.7 Microscope images of poor-adhesion PMMA in a wet etching process. (a) The developed pattern in PMMA shows no obvious defects before the wet etching process. (b) Irregular stains appeared in PMMA-covered region after HCl dipping. (c) The PMMA layer was peeled off from the surface after wet etching. (d) The image after PMMA was removed. The stains and the peeled PMMA caused irregular etching on the surface.

3.1.6 Surface-Gate Insulator

As mentioned in the overview of the SAW-driven single-photon device, surface gates can induce electrons and holes to form a micrometre-scale lateral n-i-p junction. Ideally, there should be no charge flowing between the quantum well and the surface gates because of the Schottky barrier. However, leakage current can sometimes be observed between these two, presumably because of defects or metal-semiconductor inter-diffusion at the interface. Therefore, in the early batches of devices, a 20 nm thin layer of Al_2O_3 insulator was deposited using Atomic Layer Deposition (ALD) before fabricating the surface gates. ALD can provide well-controlled high-quality thin film, so it is an ideal technique to create a thin insulator to avoid leakage current. The 10nm GaAs cap layer in the surface-gate-insulator area (Figure 3.10) has to be removed by wet etching before ALD to prevent charge accumulation

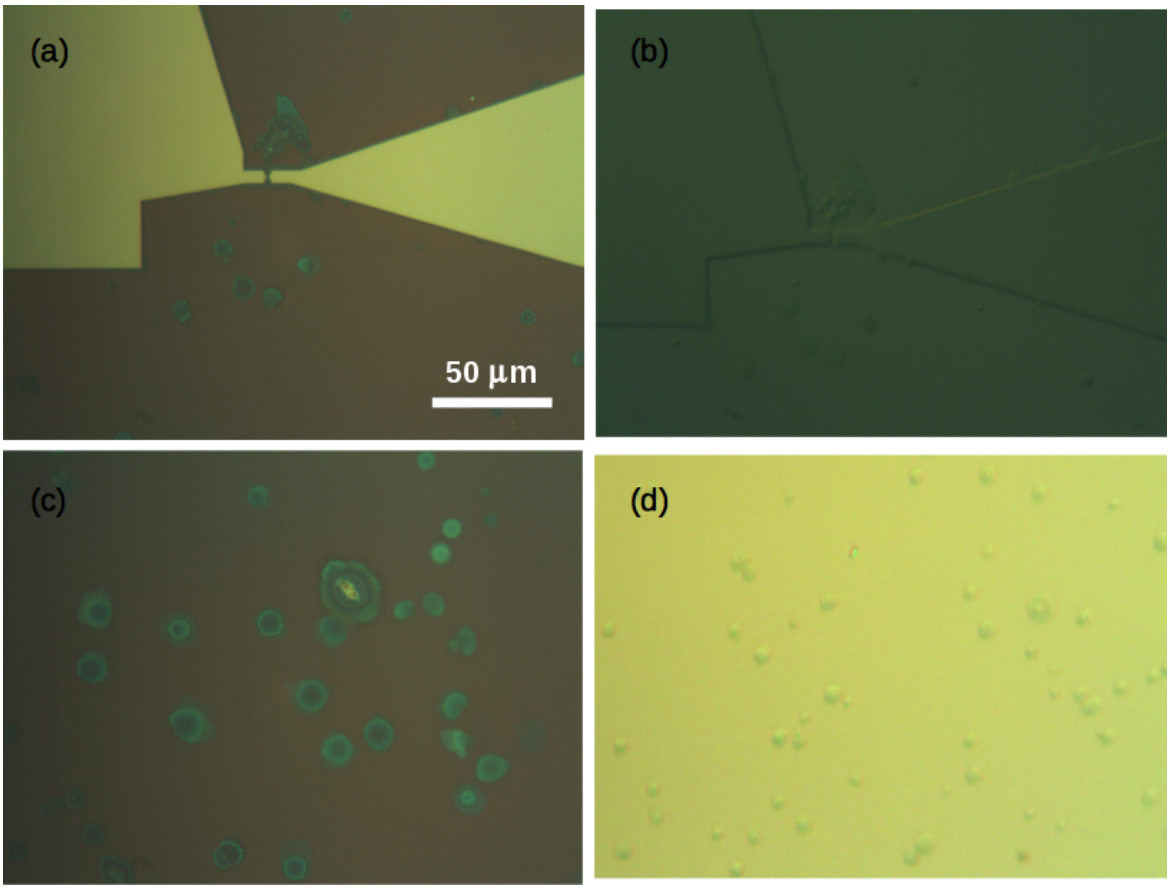

Fig. 3.8 Microscope images of a failed etch due to pin-hole issues. (a) Several circular spots appeared after a three-minute wet etch. They left marks with the same shapes in (b) after the PMMA was removed. (c) A magnified photograph shows circular spots in a different region. (d) Circular etched pits exhibited after PMMA was removed.

under the insulator. After ALD, the etch mask shown in Figure 3.10 is patterned using photolithography and then the Al_2O_3 film in the unwanted area is etched away using buffered HF (BHF). Nonetheless, depositing this thin Al_2O_3 layer makes the fabrication of a second thicker insulator for the bridging gates more complicated. Since the thicker insulator is more important and the device can still work with slight surface-gate leakage, the fabrication of this Al_2O_3 thin film was dropped in more recent batches.

3.1.7 Optical Surface Gates

Optical surface gates are patterned using photolithography before a thick insulator and optical top gates are fabricated. Figure 3.11 shows the latest design of the optical surface gates. There are three purposes for this stage. The first is to link the ohmic contacts, which are beneath the thick insulator, to bond pads so that these ohmic contacts can be addressed by a

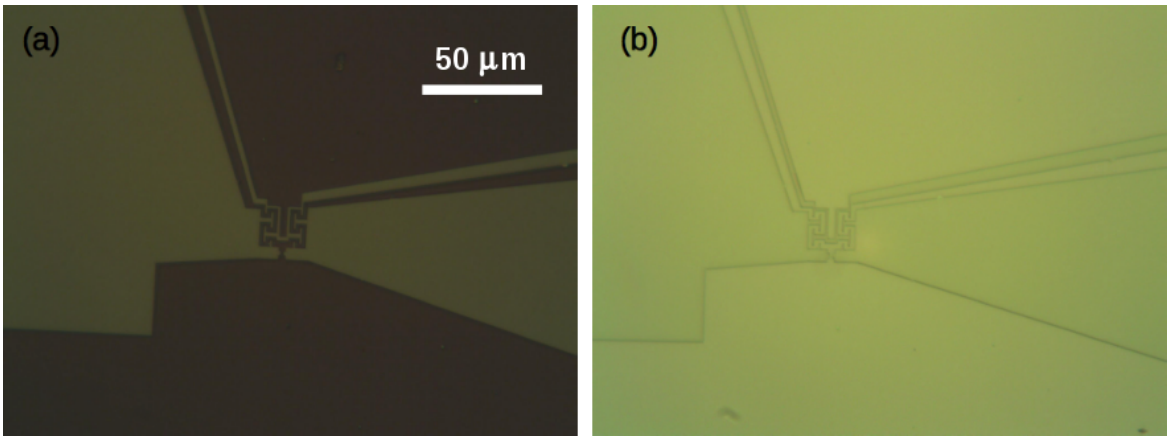

Fig. 3.9 Microscope images of a successful wet etching after overnight baking. (a) The PMMA pattern showed no irregular stains or circular spots after wet etching. (b) The etched surface was clear and had no unexpected etched marks after the PMMA was removed.

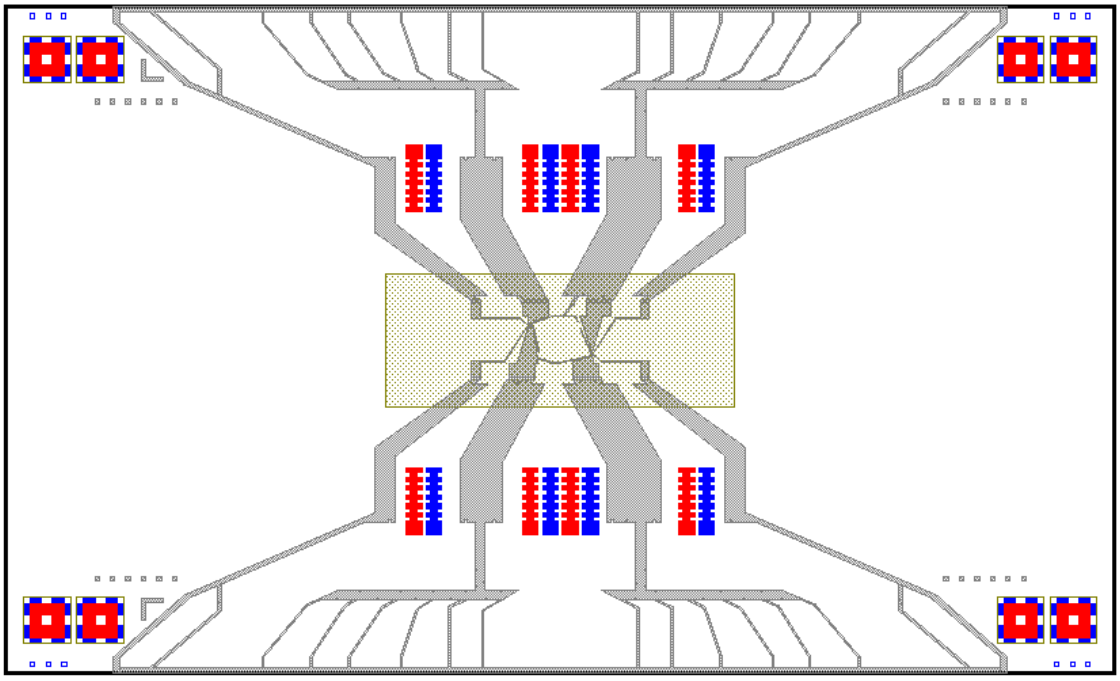

Fig. 3.10 Pattern for surface-gate insulator (green rectangle in the centre). The 10 nm GaAs cap layer is removed by wet etching in this area. Al_2O_3 is then deposited by ALD.

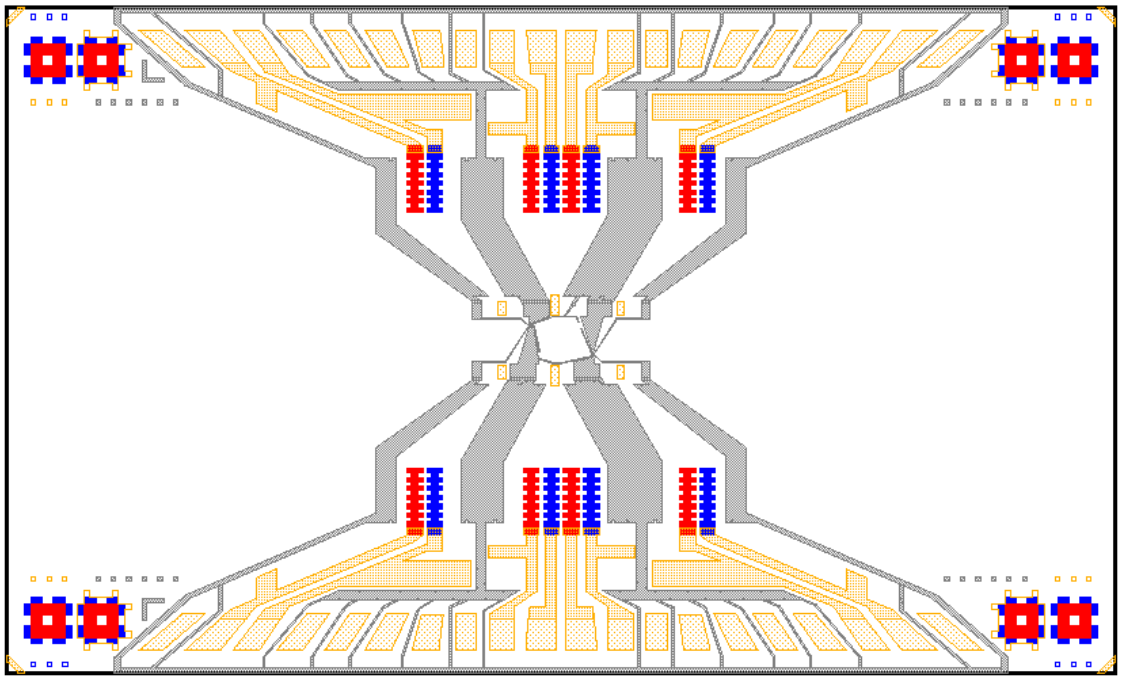

Fig. 3.11 Pattern for optical surface gates (yellow regions).

bonding machine. The second purpose is to create the bond pads for the bridging gates, the surface gates, and the side gates. The final purpose is to create the part of the surface gates that overlaps with the bridging gates, as shown in Figure 3.11(d), so that the surface gates can extend the induced charge carriers from the bridging-gate-covered area to form a lateral n-i-p junction. Regarding the fabrication, a double layer of photoresists LOR5B and S1805 is used to create an undercut profile for easier lift-off. The metallisation is performed using Ti/Au evaporation.

3.1.8 Ohmic-contact Insulator

Ohmic-contact insulator is an essential part in an induced ohmic contact that is necessary to prevent short-circuiting between the ohmic metal and the bridging gate. In previous devices made by Dr Seok-Kyun Son and Dr Yousun Chung, polyimide was chosen as the insulator [89, 90]. However, polyimide has a few disadvantages in terms of fabrication and device reliability. First of all, polyimide mixture (polyimide HD4014 : thinner T9039 = 3 :

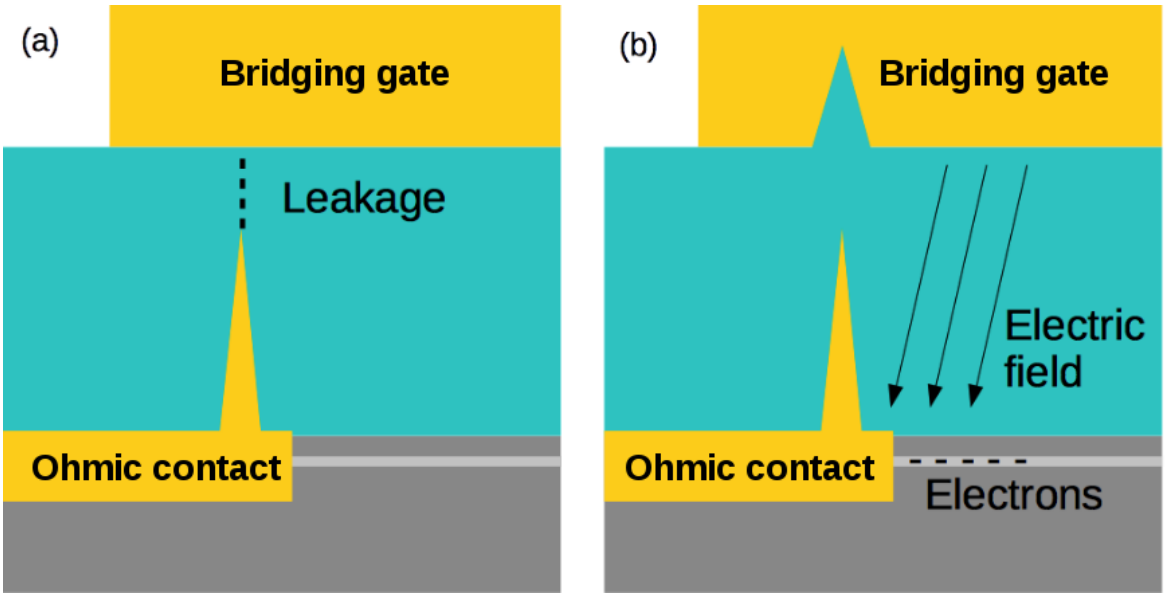

Fig. 3.12 Schematics of the effect of conformality of an insulator on an induced ohmic contact, where (a) the non-conformal insulator leads to a shorter distance between an ohmic metal spike and a top gate, which might cause a leakage current, and (b) a more conformal insulator with a better chance of inducing charge carriers before leakage occurs.

1), which covers the chip using spin-coating, is hard to prepare in a reproducible way, due to polyimide's high viscosity. The variation in mixture ratio will then cause variation in the polyimide thickness. Also, the mixed polyimide solution has a shelf-life of only one month. Additionally, the minimum curing temperature of 275 °C for polyimide is very close to the diffusion temperature of gold into GaAs [92]. This might cause surface gates to leak due to a lowered Schottky barrier. Most importantly, spin-coated polyimide tends to form a smooth top surface even if it is spin-coated on a rough surface. The lack of conformality means that the distance between the bridging gates and the ohmic spikes will be shorter, which makes the electrical breakdown of the insulator more likely to occur, as depicted in Figure 3.12(a). Therefore, it was suggested by Dr Ateeq Nasir that ALD Al_2O_3 could be a better choice for the insulator, since it is more reproducible and conformal (Figure 3.12(b)).

In order to create the insulator, the chip is cleaned and sent for ALD. A layer of 100nm-thick Al_2O_3 was deposited by Dr Ateeq Nasir using ALD. An etch mask, as shown in Figure 3.13, was then patterned by photolithography. S1813 photoresist was baked at 115 °C for 5 minutes in order to make it more resistant to HF. The ALD-covered chip was then etched using HF to remove insulator in the unwanted area.

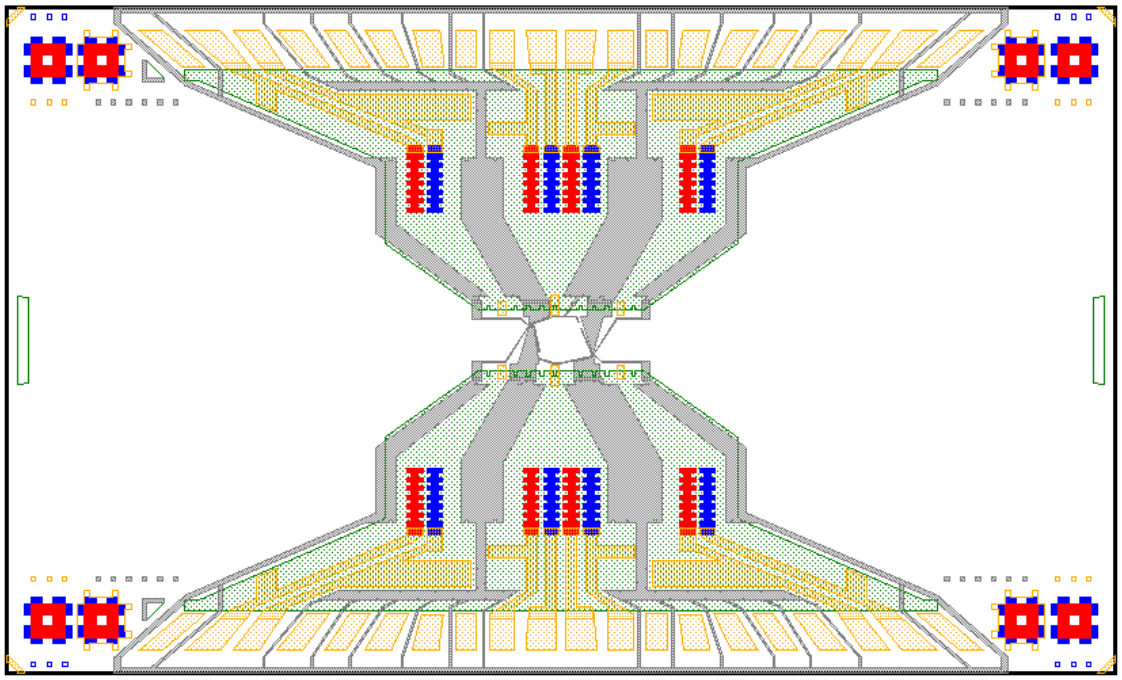

Fig. 3.13 Pattern for ohmic-contact insulator (green area). The insulator covers the ohmic contacts in order to prevent shorting when bridging gates are deposited.

3.1.9 E-beam Surface Gates

To create the micrometre-scale n-i-p junctions by inducing charge regions, sub-micrometre-resolution metals are metallised using e-beam lithography. These features include the surface gates, the side gates, and the IDT fingers. The design can be seen in Figure 3.14. In order to create an undercut profile for easier lift-off, a double layer of two types of PMMA was spin-coated onto the chip. A focused electron-beam was then used to exposed the desired pattern. E-beam exposure was performed by Mr Jon Griffiths and Mr Thomas Mitchell. The exposed pattern was then developed using the e-beam-feature developer. Next, the developed chip was de-scummed for 20 seconds in an RF asher and was dipped in HCl for 10 seconds. This step is intended to remove PMMA residue and oxide in order to allow better adhesion of the gates to the chip surface, which is discussed in the next paragraph. After the RF ashing and the HCl dip, the chip was placed in the evaporator to deposit Ti/Au. It is important to evaporate Ti quite quickly (with a deposition rate of 0.2 nm/s), as the PMMA might flow if it

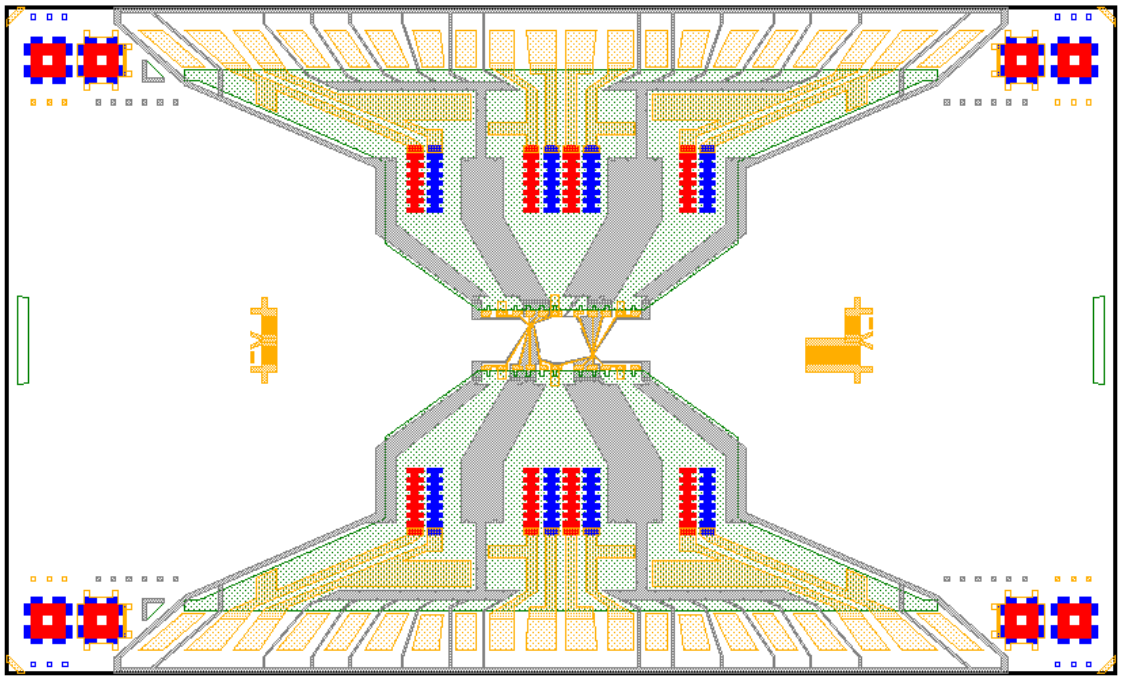

Fig. 3.14 Pattern for e-beam surface gates (yellow regions in the centre of the device). IDTs on the two sides are also patterned at this stage.

is exposed to a high temperature during Ti evaporation for too long, and a quicker formation of Ti layer on the chip can reflect thermal radiation to too much heating. The chip was then placed in acetone overnight for lift-off. It is recommended that lift-off be performed by the creation of strong liquid flow using a pipette. Lift-off using ultrasonic bath agitation should be avoided because it is very likely to damage the fine features.

Poor Metal Adhesion Issue

In the fabrication of early batches, Ti/Au evaporation was performed immediately after PMMA development without RF ashing or HCl dipping. However, in the case of one chip the deposited gates peeled off during lift-off due to poor adhesion. As can be seen in Figure 3.15(a), many surface gates were missing after lift-off. Therefore, it was suggested that a 25-second RF ashing and a 10-second HCl dip be performed to clean PMMA residue and oxide. The times for RF ashing and HCl dipping were kept short to minimise impact

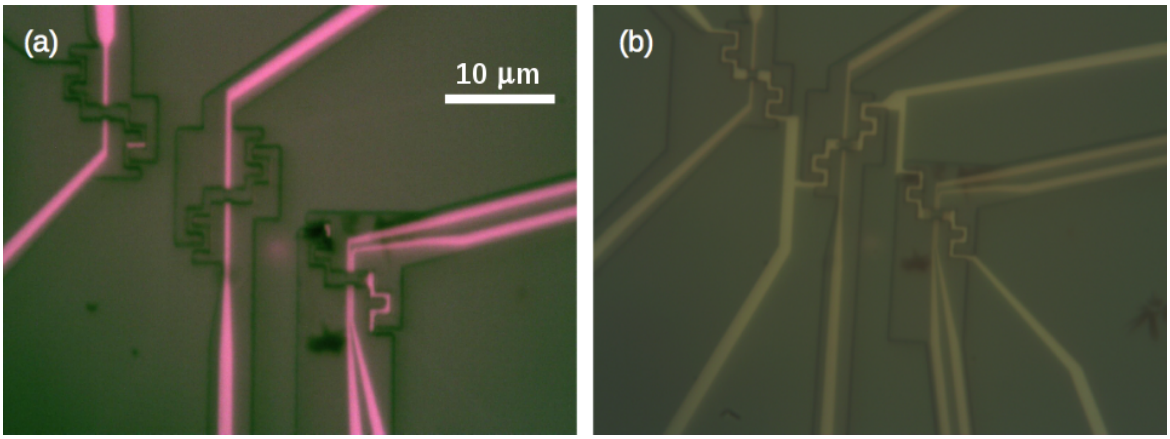

Fig. 3.15 Microscope images showing e-beam surface gates with different levels of adhesion to the chip surface, where (a) several e-beam gates were missing after lift-off due to poor adhesion, while (b) e-beam gates with good adhesion all remained on the chip after lift-off.

on fine features. After this cleaning step was introduced, a new layer of e-beam gates was deposited on the same chip, and it remained on the surface (Figure 3.15(b)), indicating that adhesion was improved by this cleaning.

3.1.10 Optical Top Gates

The last step for making a functional SAW-driven single-photon device is to pattern the bridging gates, the connections from the surface gates and the side gates to the bond pads, and also the IDT bond pads. The design is shown in Figure 3.16(a), which was patterned by photolithography. The alignment needed to be as precise as possible in order to provide a good overlap around the boundary of the ohmic contacts, as shown in Figure 3.16(b), in order to create a better chance of charge induction. In addition, a PMMA-S1805 double layer resist recipe was used to avoid etching by the MF319 developer of the Al_2O_3 insulator. In this recipe, the S1805 photoresist top layer was first exposed and developed while the bottom layer of PMMA (neat 495K A7) remained intact. Next, the chip was placed in a UV-O_3 chamber to expose the PMMA using deep-UV for 30 minutes. The exposed PMMA was then developed using a PMMA developer. During PMMA development, the previously-developed S1805 pattern acted as a development mask to protect the PMMA underneath. With this recipe, an undercut profile was formed while there was no direct contact between the Al_2O_3 insulator and the MF319 developer in the process. After development and surface cleaning, metallisation was performed using Ti/Au evaporation. It is recommended that this metallisation be made thicker (about 150 nm) because wire bonding will be easier on a thicker bond pad.

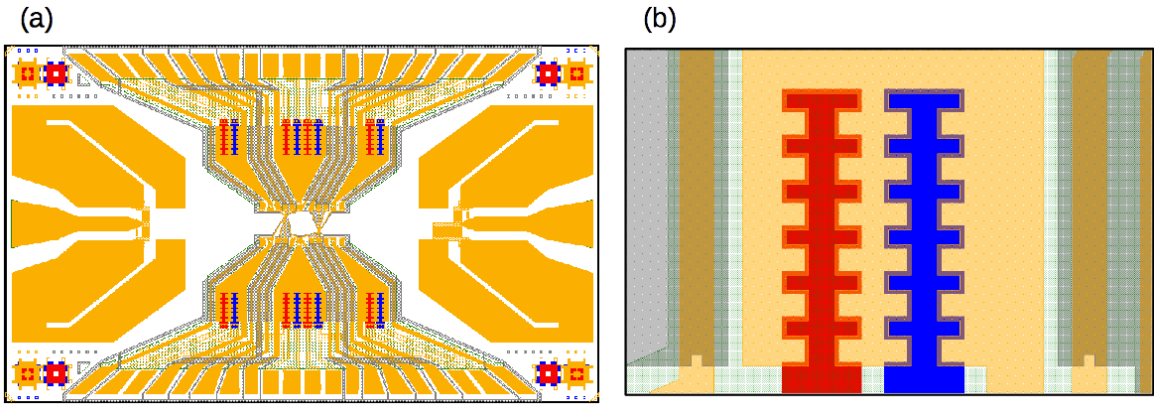

Fig. 3.16 (a) Pattern for optical surface gates (yellow regions). This metallisation stage includes the bridging gates, the connections for the surface gates and the side gates, and the bond pads for the IDTs. (b) Design of bridging gates at ohmic-contact regions has a crenellation-shaped overlap between the bridging gate and the ohmic contacts.

In an early batch of devices, the bridging gate was found to leak to the ohmic contacts not only via the insulator, but also through the bridging-gate bond pads, which is discussed in Chapter 4. This unexpected leakage path might be caused by the induced charge carriers that exist beneath the bridging gate bond pad, which can leak to the bridging gate if the quantum well is penetrated during the wire bonding, as depicted in Figure 3.17(a). There are two ways to solve this problem. The first, introduced by Dr Seok-Kyun Son, is to have the ohmic-contact-connection metal extending below the bridging gates to screen the electric field [90]. In this case, the induced charge carriers cannot reach the bond pad, as shown in Figure 3.17(b). The other way is to etch away the quantum well in a region so that the charge carriers are stopped at the etch, as shown in Figure 3.17(c). The designs for these two solutions were both introduced in the devices (Figure 3.17(d)). In addition, to improve the continuity of gate metal on wet-etched edges, notch-shaped features (Figure 3.17(e)) were made in the etch pattern so that the gate metal could climb from multiple etched facets [93]. This design can ensure that at least one facet has an overcut profile so that good continuity can be achieved in the gate metal.

3.1.11 ZnO Deposition

ZnO deposition was performed on one of the devices, which will be discussed in later chapters, to enhance the SAW signal. Details of the SAW enhancement using ZnO can be found in the literature [94]. The highly piezoelectric ZnO thin film deposited on the GaAs surface enhances the piezoelectric coupling. ZnO-enhanced SAW-driven charge transport

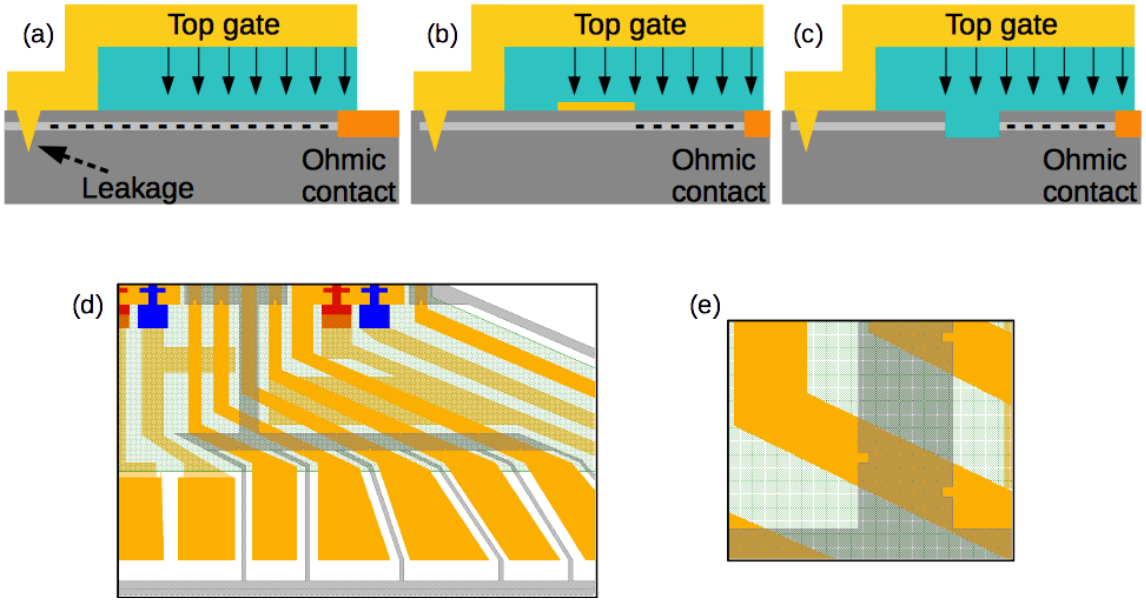

Fig. 3.17 Design consideration of the optical top gates. (a) Leakage between a bridging gate and an ohmic contact can happen if the metal at the bridging-gate bond pad penetrates into the quantum well. (b) This leakage path can be stopped if a metal layer is deposited on top of the leakage path to screen the electric field, or (c) this can also be done by etching away the quantum well in the leakage path. (d) The device design incorporating the methods in (b) and (c), where extended metal from the ohmic connections and the etched region both cut the leakage paths for all the gates. (e) The notch shape on etched edges was designed to help the optical top gates climb across these edges.

has been studied by Mr Hangtian Hou. The result shows that the required RF power for observing quantised SAW-driven current is reduced by 10 dB when an 800 nm-thick ZnO layer is deposited on a SAW split-gate device [95]. Therefore, ZnO deposition was attempted on one SAW-driven n-i-p junction device in the hope of improving the SAW signal. Before ZnO deposition, a 20 nm Al_2O_3 buffer layer was deposited using ALD because it was found by Dr Matthew Benesh that ZnO deposition damaged the 2DEG in HEMT-based devices, and it was confirmed by Mr Hangtian Hou that the 20nm-thick Al_2O_3 was able to protect the 2DEG [93, 95]. Processing of this ALD Al_2O_3 is carried out in the same way as discussed in the fabrication of surface-gate insulator. After the buffer layer had been created, an 800nm ZnO was then deposited using high-target-utilisation sputtering (HiTUS), performed by Miss Kham M. Niang. Next, photolithography was used to create an etch mask, as shown in Figure 3.18. Finally, ZnO in the unwanted area was etched away using HCl.

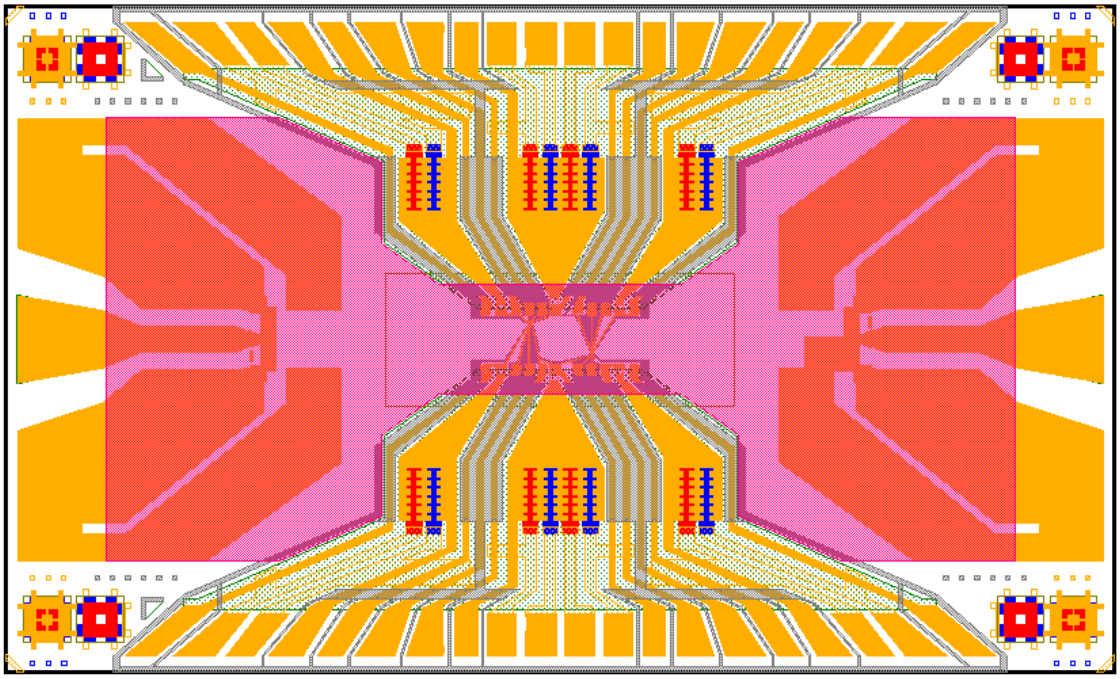

Fig. 3.18 Pattern for ZnO deposition (purple area).

3.1.12 Cleaving and Bonding

Generally, there was a 2×2 grid of devices on one chip, as mentioned in the section of wafer selection. When the fabrication was completed, the chip was cleaved into individual devices using a diamond-tipped scriber. The device to be bonded was first cleaned in acetone and IPA to remove any dust that might damp the SAW. GE varnish was then used to stick the device to one of the sample holders, which are described in the next section, and the device was pressed down by cocktail sticks to fix the device firmly to the sample holder. It is strongly recommended that GE varnish be applied at the left and right edges of the device rather than at the centre. This is because slight cracking might occur when a device is pushed down against a blob of the GE varnish acting as a central pivot, by pushing at the device edges with cocktail sticks. The slight cracking will expand and even break the whole device after a few thermal cycles to 4 K. One example of this can be seen in Figure 3.19. The cracks on the surface can be seen in Figure 3.19(a)-(c), and the cracking drawn in Figure 3.19(d) suggests

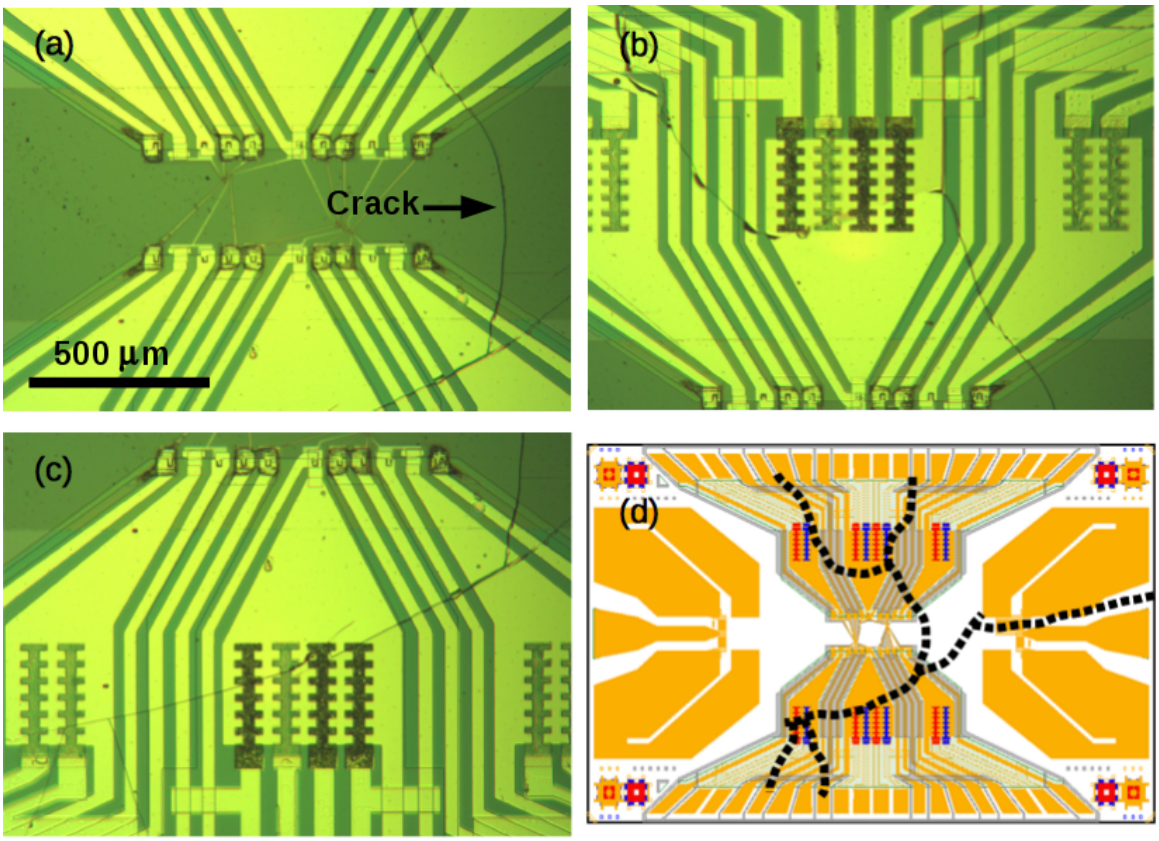

Fig. 3.19 Microscope images and diagram of a cracked device. (a)-(c) The cracking can be seen on the device after a few thermal cycles. (d) Diagram of the cracks drawn on the device design. The appearance of the cracking suggests that it was due to a blob of GE varnish at the centre.

that this was due to a blob of GE varnish at the centre. After the device was glued, a wedge bonder was used to connect the bond pads on the device to the sample holder.

3.2 Sample Holders

The characterisation of a SAW-driven single-photon device is possible only when an electrical transport measurement, an optical measurement, and the SAW-generation using RF can all be achieved at the same time. Therefore, customised sample holders need to have sufficient DC contacts for all the gates and the ohmic contacts, and they also have to be optically accessible, and finally they need to have RF input capability. Two sample holders were employed in the measurements that are discussed in this thesis. They are described in following paragraphs.

3.2.1 Black-helium-3 Sample Holder

The first sample holder was made specifically for a probe in the black helium-3 cryostat. It was first designed by Dr Seok-Kyun Son and Dr Yousun Chung, and later modified by Mr Hangtian Hou and the author [89, 90]. Photos of this sample holder are shown in Figure 3.20. This holder has 32 DC contacts patterned on two PCBs. These contacts were soldered to two Conan connectors. In addition, two coplanar wave guides (CPWs) with SMP connectors were made for RF access. In order to mitigate the crosstalk issue, an opaque lid, shown in Figure 3.20(c), can be used if a non-optical measurement is performed. If optical access is needed, there is another lid with a window, as seen in Figure 3.20(d).

3.2.2 μPL Sample Holder

The other sample holder used in this thesis is the μPL sample holder. This was designed for the μPL continuous-flow helium cryostat. A photo of a μPL sample holder can be seen in Figure 3.21. As with the black-helium-3 sample holder, the μPL sample holder has 32 DC contacts and two CPWs. Due to the limited space in the μPL cryostat, this sample holder is smaller than the black-helium-3 sample holder and miniaturised Hirose U.FL connectors with a smaller footprint were used for RF input. Although this sample holder was originally designed for the μPL cryostat, it is actually compatible with the black helium-3 cryostat. Therefore, once a device is bonded to the μPL sample holder, it can be characterised in both cryostat systems, using their respective advantages in measurements, which are described in the next section.

3.3 Low temperature systems

The SAW-driven n-i-p junction devices were all tested below 20K to minimise the effect of phonon scattering and thermally ionised defects. There were three low-temperature systems employed in measurements in later chapters. In this section, the characteristics of these low-temperature systems are described. In order to measure SAW-driven n-i-p junction devices, the wiring of these systems was rebuilt or modified. Hence, the rebuilding and the modification of these systems are explained in this section as well.

3.3.1 RF Dip Station

The simplest way to carry out low-temperature measurement is to place a sample holder in direct contact with liquid helium in a helium dewar. In this way, the device bonded

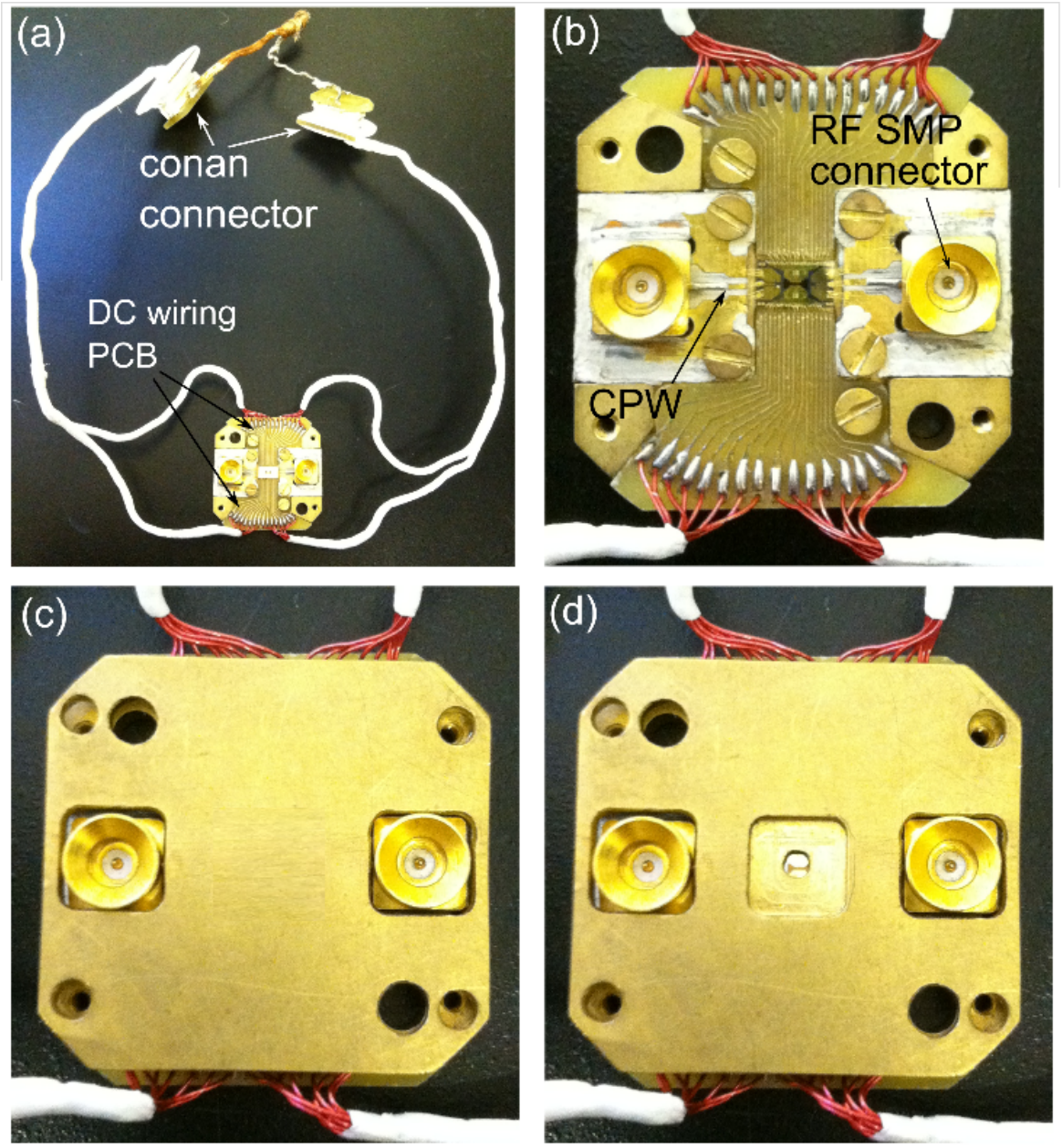

Fig. 3.20 Photographs of a black-helium-3 sample holder. (a) Overview of the sample holder shows two DC PCBs terminated to two Conan connectors. (b) Magnified photo shows the CPWs and SMP RF connectors. (c) The sample holder covered by an opaque lid. (d) The sample holder covered by a lid with a window. Photographs from [89].

on the sample holder can be cooled to the helium boiling temperature, 4K, by the liquid helium. The RF dip station consists of a liquid helium dewar and a dipping probe. A sample holder with a bonded device can be connected to the bottom end of the dipping probe. The dipping probe has 32 DC wires and two RF coaxial cables that can connect all DC contacts

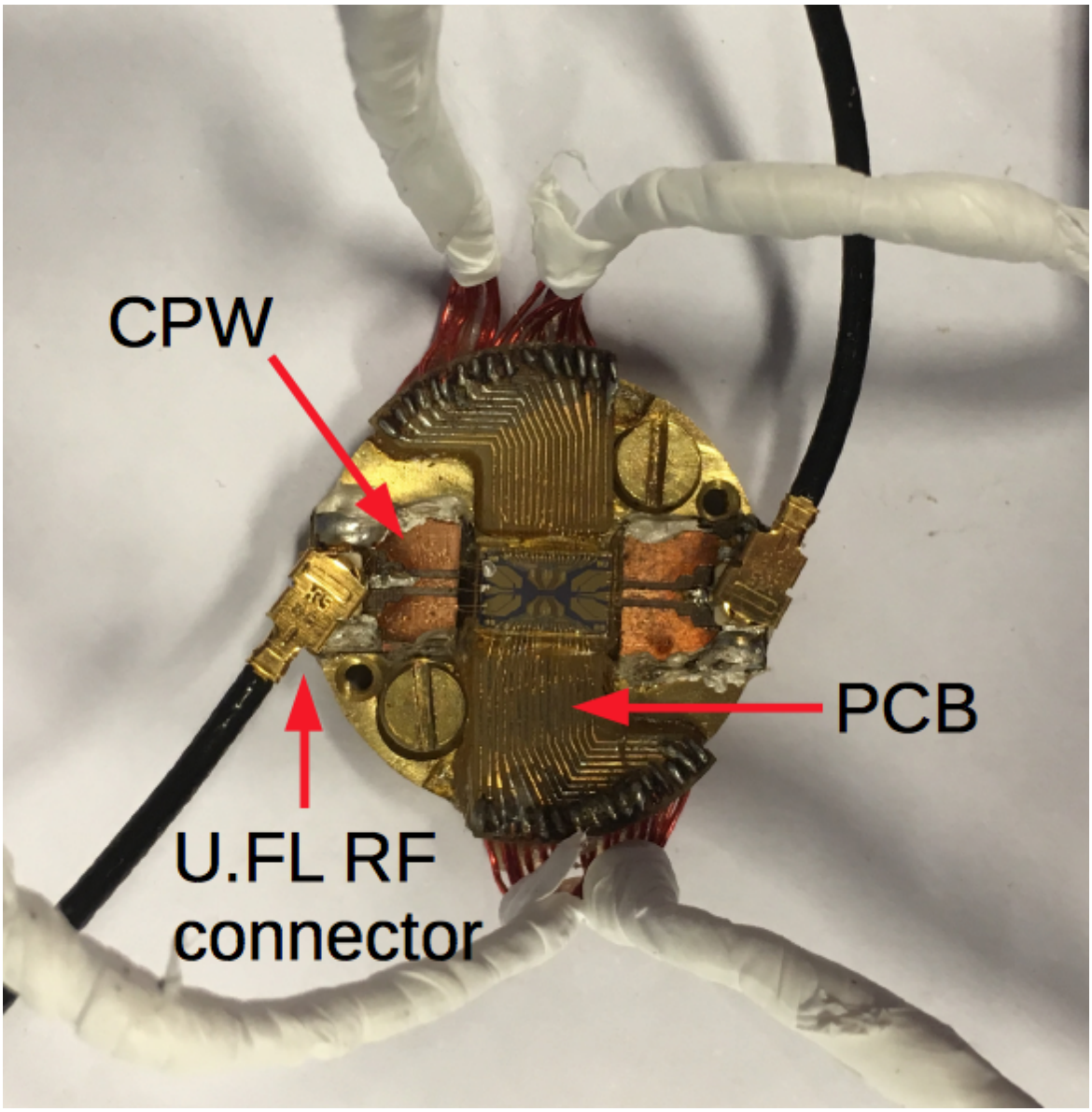

Fig. 3.21 Photographs of a μPL cryostat sample holder. Two PCBs terminated by Conan connectors provide 32 DC connections. The CPWs connected to U.FL RF connectors provide the access for RF signals.

and RF ports from the sample holder to external instruments. The operation of the RF dip station is performed simply by inserting the probe into the helium dewar so that it makes contact with the helium level. For SAW-related measurement, note that the sample holder cannot be dipped below the helium level as the increased mass load due to liquid helium on the IDTs would greatly reduce the SAW signal. The RF dip station provides an easy way to perform SAW-driven electrical transport measurements. However, this system has

no optical access for the SAW-driven electroluminescence (EL) measurements, which is essential for characterising a SAW-driven n-i-p junction device. To perform the SAW-driven EL measurement, one has to use the black helium-3 cryostat or the μPL continuous-flow cryostat.

3.3.2 Black Helium-3 Cryostat

The black helium-3 cryostat is a low-temperature system that is capable of SAW-driven electrical-transport measurement as well as SAW-driven EL measurement. As with the RF dip station, the sample holder is connected to the bottom of a customised measurement probe, which is inserted into the cryostat during measurement. To achieve optical measurement, a miniaturised lens assembly was made, together with electrical wiring, when the measurement probe was renewed [89, 90]. In this system, the lens assembly can be moved by a three-axis piezoelectric positioner to collect photon emission from a micrometre-size area on the device surface. The emission is then coupled into a single-mode fibre by the lens assembly. The photons are sent to optic components outside the cryostat for detection or manipulation. Regarding cooling, this system can be operated at 1.5 K continuously by reducing the helium-4 vapour pressure in the 1K pot, which is the main heat sink for the probe. It can also run at a temperature below 300 mK for a short time by utilising the reduced helium-3 boiling temperature in a condensation-pumping cycle. However, there was no SAW-driven n-i-p junction measurement tested at 300 mK in this thesis because the operation period at 300 mK was too short (a few minutes) when a high-power RF signal was applied.

The device is in a totally dark environment in the helium-3 cryostat during measurement if no external light source is fed into the single-mode fibre. This is beneficial because it can prevent the need for photon-excited charge carriers in the device, which might cause charging under the bridging gates. Therefore, the device is relatively more stable in this system compared with the μPL continuous-flow cryostat system, which is not completely light-tight. Besides, the black helium-3 cryostat can stay cool at 1.5 K for an indefinite period of time as long as it is regularly filled with liquid helium and liquid nitrogen. Because of the higher device stability and the long operational time of the cryostat, the black helium-3 cryostat is an ideal low-temperature system for measurements that require a long time for data accumulation. On the other hand, one major disadvantage of this system is the small field of view of the lens assembly. As mentioned earlier, the lens assembly can only collect photons in a 2 μm^2 area when it is focused. It has to be moved by the piezoelectric positioner for a bigger picture of the device to be seen. Hence, this takes time and is more difficult to find the photon emission from a micrometre-scale n-i-p junction on a 5mm$\times$3mm chip. Fortunately, once the emission spot is located, the lens assembly can remain fairly stable

and only needs to be adjusted occasionally by a few micrometres to maximise the photon collection efficiency.

Cooling of Black Helium-3 Cryostat

The basic structure of a helium-3 cryostat is shown in Figure 3.22. The outer vacuum chamber (OVC) and the inner vacuum chamber (IVC) are kept at high vacuum (1×10^{-6} mbar) to provide good thermal isolation between the room-temperature environment, the 77 K nitrogen jacket, and the 4 K helium bath. A charcoal adsorber (sorb) can either pump or release helium-3 gas in the sample space depending on its temperature, which can be tuned using the sorb heat exchanger. The 1K pot is in the cryostat at the point where the measurement probe makes direct contact when the probe is fully lowered. Therefore, the 1K pot serves as the heat sink for the measurement probe. Since the boiling temperature of helium-4 decreases to 1 K at 1 mbar, the 1K pot temperature can be reduced below 1.5 K by filling liquid helium from the main helium bath and lowering the vapour pressure using a pump. Therefore, the device on the measurement probe can be cooled to 1.5 K when it reaches thermal equilibrium with the 1K pot. Moreover, the 1K pot and the sorb can be used to lower the sample-space temperature further to 250 mK using a helium-3 condensation-pumping cycle, which was not employed in this thesis.

Rebuilding a Probe

The original measurement probe for the black helium-3 cryostat was designed only for electrical transport measurements. It is not capable of optical measurement. Hence, for the measurement of SAW-driven n-i-p junction devices, a probe was customised for this purpose. This new probe was designed by Dr Jorge Pedrós. Dr Seok-Kyun Son, Dr Yousun Chung, Mr Hangtian Hou and the author all contributed to the construction of the probe. A sketch of the new probe is shown in Figure 3.23. At the top end of the probe, a disc-shaped bulkhead provides all the electrical and optical connections, such as two Fischer connectors for DC wiring, five SMA connectors for RF signals, and the top end of a single-mode fibre terminated by an FC/PC connector. Inside the bulkhead, two DC looms with 48 available DC wires, which are used for electrical contacts to the device and to a thermometer, are soldered to the two Fischer connectors, along with three pairs of copper wires for driving the piezoelectric positioner. Three stainless-steel coaxial cables connected from three of the five SMA connectors are used to send RF signals to the device in order to generate SAWs or eventually to pulse gates. All these electrical wires, coaxial cables, and the single-mode fibre extend from the bulkhead to the bottom along the probe, which is an evacuated stainless-steel

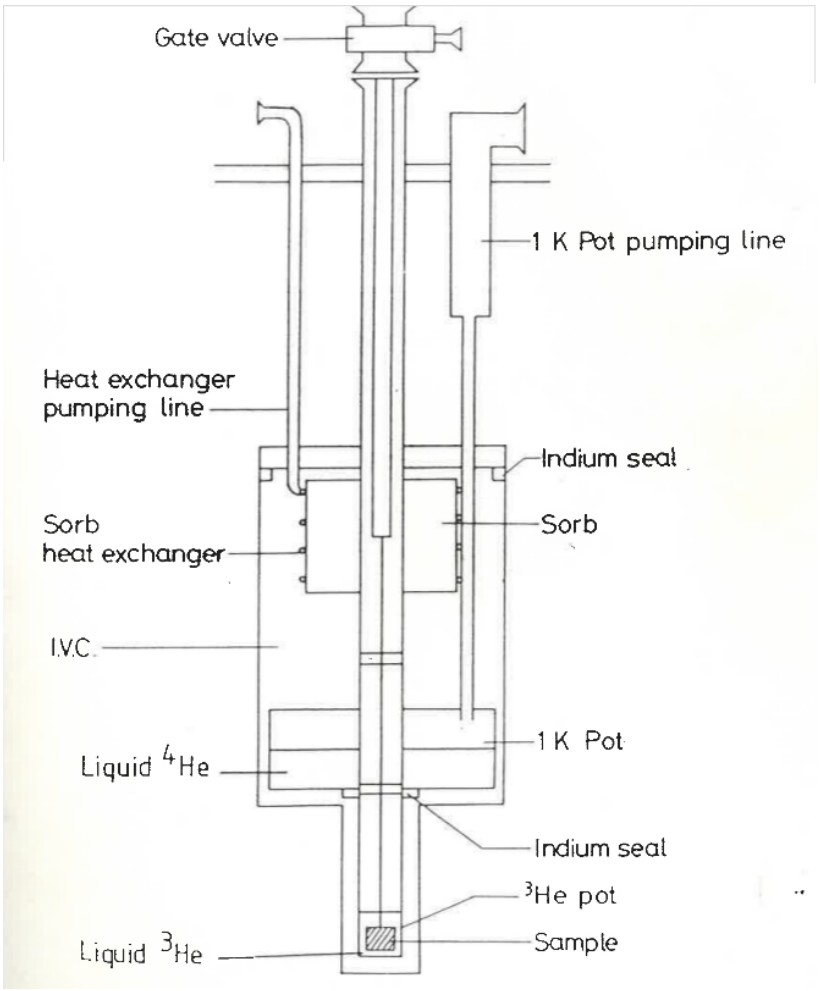

Fig. 3.22 Schematic of the structure of the black helium-3 cryostat. An evacuated outer vacuum chamber (OVC), a 77 K nitrogen jacket, and a helium main bath, which are not shown here, surround the system drawn in this schematic in order to isolate the system thermally from the room temperature environment. The inner vacuum chamber (IVC) is also evacuated to reduce convection in the system. The 1K pot filled with liquid helium provides a heat-sink at 1.5 K for the measurement probe. A charcoal adsorber (sorb) can either pump or release helium-3 gas in the sample space by utilising the sorb heat exchanger. Diagram from [96].

hollow tube. It can be slid into the cryostat sample space when the probe is mounted on the cryostat, making the device reach the bottom of the cryostat. A copper cone on the probe then makes direct contact with the 1K pot when the probe is fully slid down, so the probe can be cooled by the 1K pot. The piezoelectric stepper and the lens assembly, which are both mentioned above, are located below the copper cone in order to collect photon emission from the device fixed at the bottom end of the probe.

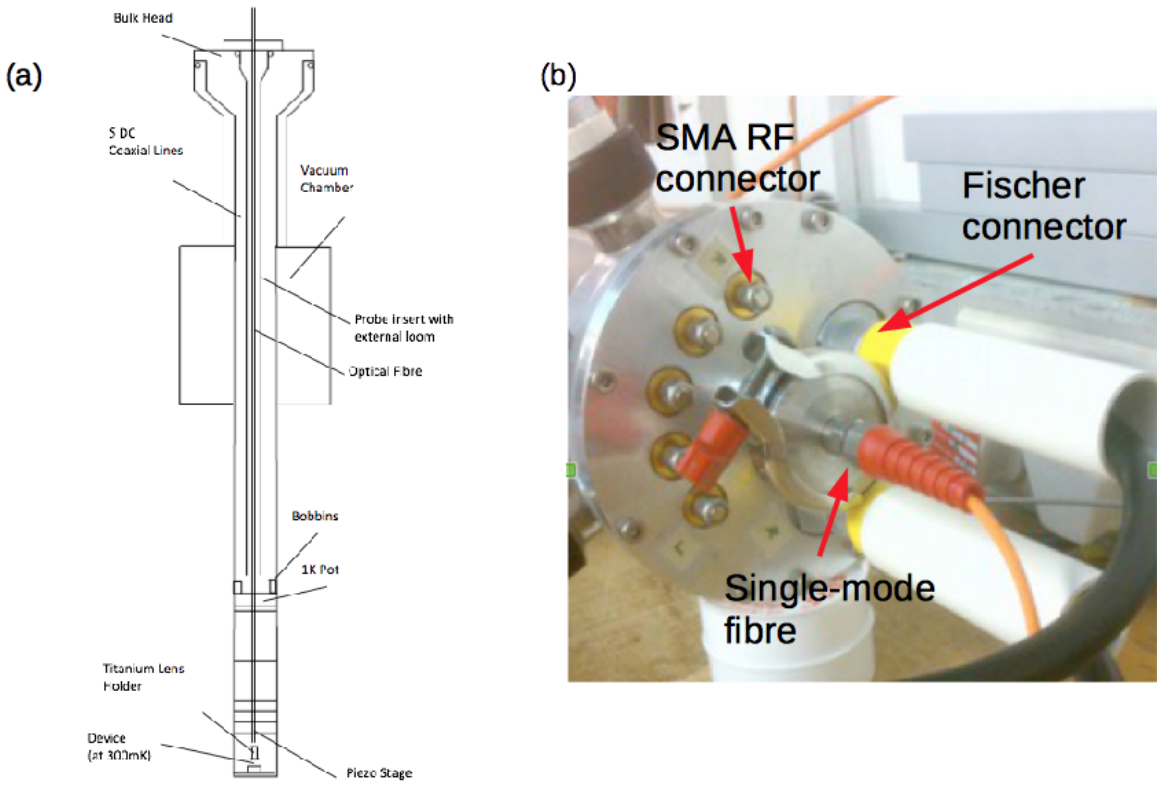

Fig. 3.23 Overview of the customised measurement probe for SAW-driven n-i-p junction measurements. (a) The schematic of the probe. The bulkhead provides all electrical and optical connections. Two looms with 48 DC connections, three coaxial cables, and one single-mode fibre extend from the top to the bottom. The copper cone is in contact with the 1K pot when the probe is fully inserted. A lens assembly anchored on a piezoelectric positioner is placed near the bottom to collect photon emissions from a device fixed at the bottom end. (b) Photograph of the top bulkhead. Two Fischer connectors, five SMA RF connectors, and one single-mode fibre are located on the bulkhead for electrical and optical connections. (a) from [97].

Wiring and Thermal Anchoring

As mentioned in the paragraph above, there are a pair of looms, and three pairs of twisted copper wires going down along the probe. The looms provide electrical connections for all the ohmic contacts and the gates on the device, and are also used to connect a thermometer to read the temperature of the sample holder. The wires in the looms were made of constantan (a copper-nickel alloy), which has moderate electrical conductivity and low thermal conductivity to minimise heat conduction. The low-resistance copper wires are used for control of the piezoelectric positioner since the voltage required to drive the piezoelectric positioner increases with the RC time constant of the wires. The copper wires were twisted into pairs so

as to cancel out noise induced by electromagnetic interference. The looms and copper wires were wrapped around the probe insert in a helical way. This wrapping was done loosely to avoid too much tension caused by differential thermal contraction when the probe is cooled down. GE varnish was applied to anchor the looms and the copper wires every two or three turns to fix the wiring and provide good thermal contact. When the probe is slid down, there will be some unavoidable touching between the probe insert and the wall of the sample space in the cryostat. To avoid damaging the wiring as a result of this touching, PTFE tape was wrapped on top of the anchored wires to reduce friction and provide protection.

Since the looms and the copper wires conduct heat from the room temperature bulkhead towards the bottom of the cryostat, the heat from the wiring must be transferred to a heat sink before the wiring reaches the bottom of the cryostat, otherwise the cryostat and the device will be warmed up. Therefore, the looms and copper wires were each wrapped tightly around a copper bobbin in good thermal contact with the copper cone mentioned above. The thermally anchored wiring on the bobbins can be seen in Figure 3.24. This was done by applying GE varnish while the wires were tightened on the bobbins. To improve the thermal contact between the wiring and the bobbins, the looms and copper wires were wrapped around the bobbins as many times as possible to maximise the contact area. In this way, most of the heat conducted in the wiring from the top of the probe can be dissipated into the 1K pot heat sink via the bobbins and the copper cone, instead of warming up the cryostat and the device. It should be noted that the looms and copper wires should be anchored to the bobbins from top to bottom, since heat resistance at the bottom of the cryostat is higher in this case, so less heat is transferred to the bottom. At the bottom end of the wiring, the looms were soldered to two Conan connectors to provide connections to the sample holder, and the copper wires were connected to the piezoelectric positioner.

Coaxial Cables

The coaxial cables are used to apply an RF signal to launch a SAW. They are semi-rigid coaxial cables consisting of a copper inner core, a stainless-steel sheath, and a dielectric insulator between. The copper core carries the RF signal and the surrounding sheath confines the electromagnetic field to a space filled with dielectric insulator. The sheath is also kept grounded to work as a shield for external fields. Before the coaxial cables can be soldered to RF connectors, the dielectric insulators near the two ends of the coaxial cables have to be removed, as excessive dielectric insulator can be pushed out of the coaxial cables after a few thermal cycles and can cause damage to the soldered connectors. The removal of this excess dielectric insulator was performed by first carrying out a few thermal cycles by heating with a heat gun and cooling with a small bucket of liquid nitrogen. The dielectric insulator that was

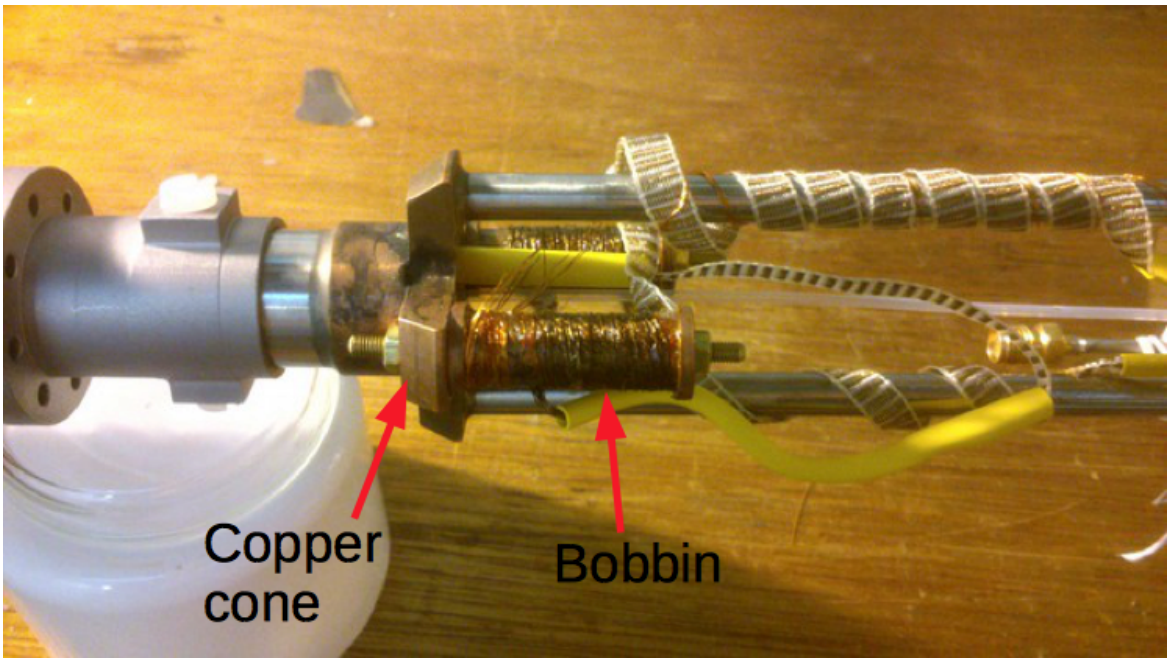

Fig. 3.24 Thermal anchoring of electrical wiring. The constantan wires from the looms and the copper wires were tightly anchored to the copper bobbins in order to dissipate heat from the room temperature bulkhead. The bottom of the probe is to the left.

forced to stick out can then be removed with a cutter knife. This removal needs to be carried out carefully, as damaging the copper inner core can affect the transmission of RF signals. After the thermal-cycle pre-treatment, the coaxial cables were soldered to either SMA or SMP RF connectors. The soldering at the joint between a sheath and an RF connector should be made as smooth as possible to allow better RF transmission. After the RF connectors were attached, the coaxial cables were anchored to the bulkhead and fixed parallel to the probe insert by wrapping with PTFE tape.

Since the coaxial cables can also conduct heat from the room-temperature bulkhead, they have to be thermally anchored to the probe insert before the heat sink to reduce the heat flow that would warm up the cryostat and the device. As can be seen in Figure 3.25, thermal anchoring was performed by tightly wrapping copper wire to both coaxial cables and the stainless-steel rods on the probe. The stainless-steel rods are in direct contact with the copper cone so the heat from the coaxial cable sheath can be transferred to the heat sink via the stainless-steel rods. The bottom ends of the coaxial cables were terminated by SMP or SMA RF connectors to allow an easier RF connection to the sample holder.

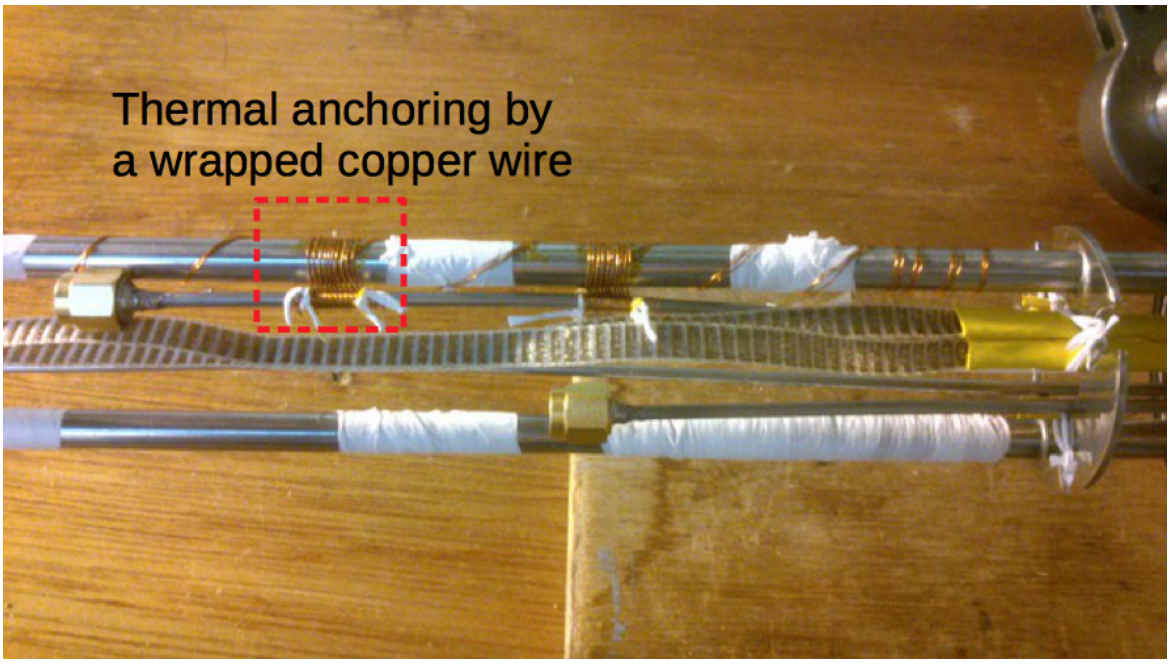

Fig. 3.25 Thermal anchoring of coaxial cables. Coaxial cables were tightly anchored to stainless-steel rods on the probe insert using wrapped copper wires. Heat in the coaxial cables can be transferred to the probe insert and finally dissipated into the heat sink.

Single-mode Fibre

Because the space for placing extra optical components in the black helium-3 cryostat is very limited, photon emission from the SAW-driven n-i-p junction device has to be coupled out of the cryostat so that the photons can be further manipulated or detected using an external optical setup. Hence, an optical fibre extending from the top to the bottom serves as the bridge between the photons in the cryostat and the external optical setup. The optical fibre can also be used to feed a light signal from an external light source such as a pig-tail laser to the device for imaging or photoluminescence (PL) measurement. The optical fibre in the probe is a single-mode fibre with an operating wavelength from 780 nm to 970 nm, which covers the emission wavelength of the 15 nm GaAs/AlGaAs quantum well. Photons collected by the miniaturised lens assembly, which is mentioned in the next paragraph, propagate in the fundamental transverse mode in the 5.5 μm fibre core and reach the top end of the fibre. These photons can then be coupled to the external optical setup via an FC/PC fibre connector. The FC/PC fibre connector and the vacuum seal for the fibre through the bulk head were made by Dr Jorge Pedrós and Dr Yousun Chung [89]. The fibre is very fragile and can be easily broken due to slight stress. Since inevitable scratching can happen on the outer surface of the probe insert during probe lowering, the single-mode fibre was fed through the hollow

inner tube of the probe insert in order to eliminate the possibility of damaging the fibre by scratching. The feeding of the fibre has to be carried out with extreme care because stress during the feeding can break the fibre as well. During feeding, one person should push the fibre into the top end of the hollow tube while the other person should pull the fibre out of the bottom end in a synchronous manner. Even after the fibre is fed through successfully, extra care still needs be taken every time a sample holder is connected or disconnected.

Lens Assembly

As mentioned above, the space for optical components is very limited in the cryostat, so a miniaturised lens assembly designed by Dr Jorge Pedrós was created at the bottom of the probe insert in order to collect photon emissions from the device. This can also be used to send a light signal from an external light source to image the device. A sketch of the lens assembly is provided in Figure 3.26. The lens assembly consists of a titanium lens holder, the single-mode fibre terminated by a glass ferrule, and two aspheric glass lenses. The titanium lens holder is used to fix the glass ferrule and the two aspheric lenses. The two lenses are glued to the titanium lens holder using superglue. The bottom end of the single-mode fibre was first inserted into a glass ferrule, then polished, and finally fixed using epoxy. This was done by Dr Yousun Chung [89]. Regarding the two aspheric lenses, the one near the fibre (the top lens) has a 5.0 mm focal length and a 0.15 numerical aperture (NA) while the lens closer to the device (the bottom lens) has a 1.45 mm focal length and a 0.55 NA. Since the NA of the single-mode fibre is 0.13, the fibre and the top lens have similar NAs so that most of the photons coming from the top lens can be coupled into the 5.5 μm fibre core.

To achieve optimised optical coupling, the glass ferrule was inserted into the titanium lens holder and aligned with the lens system. This alignment was carried out as follows. A light signal from a 785 nm pig-tail laser was sent into the top end of the fibre. The light signal coming out of the ferrule at the bottom end was then focused using the two lenses, and reflected by a gold mirror placed at the focal point of the bottom lens. The reflected light signal was detected using an optical power meter at the top. In this setup, the reflected light signal changed as the glass ferrule slid inside the titanium holder, and the maximum reflected signal was observed when the glass ferrule was placed at the focal point of the top lens. Therefore, the alignment was optimised when the reflected signal was maximised. The glass ferrule was then fixed in place by a screw, which had a Teflon tip to avoid damaging the ferrule.

Regarding the optical properties, because the magnification of this lens assembly is $1.45/5$, the 5.5 μm fibre core corresponds to a collectable area $\sim 1.5\mu$m in diameter when it is focused. The resolution of the lens assembly can be estimated by the minimum Gaussian

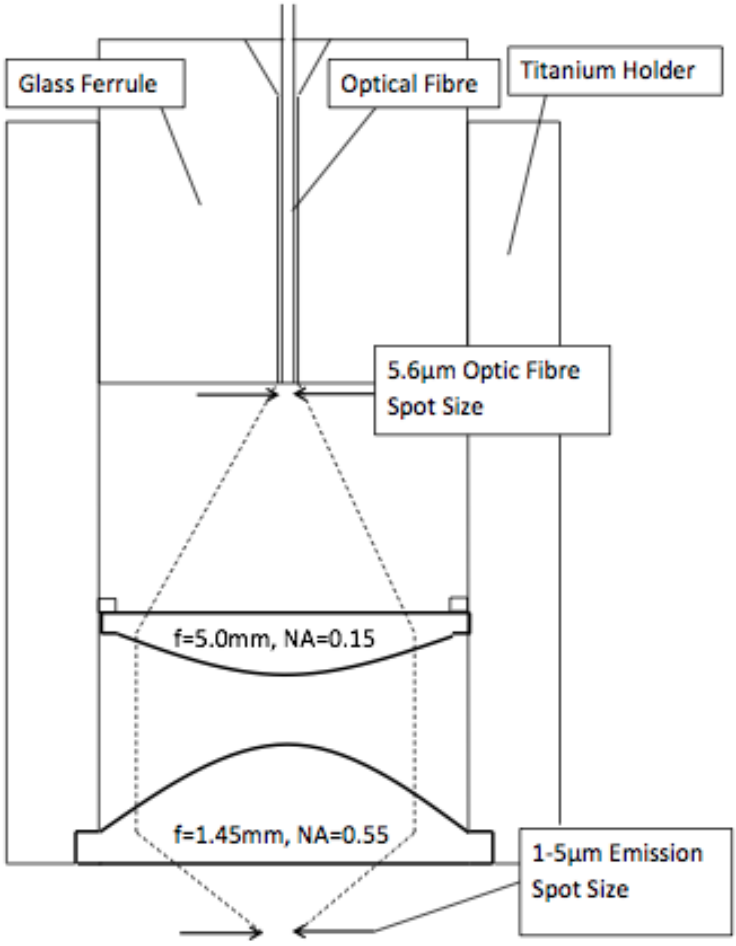

Fig. 3.26 Schematic diagram of the lens assembly. The fibre fixed by a glass ferrule is placed at the focal length of the top aspheric lens inside the titanium lens holder. When the lens assembly is focused on the surface of a device, photons emitted from a 2 μm^2 area are coupled into the 5.5 μm fibre core. Diagram from [97].

beam diameter of the bottom lens, which can be described by the formula

$$w_0 = \frac{2 \cdot \lambda}{\pi \cdot NA}, \tag{3.1}$$

where w_0 is the minimum Gaussian beam diameter, λ is the wavelength of the photons, and NA is the numerical aperture of the bottom lens. With the bottom lens NA = 0.55, and the wavelength is around 800 nm; the minimum beam diameter is about 1.5 μm. Therefore, the resolution is also about 1.5 μm when the lens assembly is focused on the surface of the device.

Piezoelectric Positioner

Because the lens assembly can only collect photon emission in a $2\,\mu m^2$ area when it is focused, it is impossible to mount the device so precisely that the micrometre-scale n-i-p junction is located at the focal point. Therefore, the relative position of the lens assembly to the junction must be remotely adjustable so that the lens assembly can be brought into focus after the device is fixed in place and lowered inside the cryostat. A three-axis piezoelectric positioner is thus utilised for this purpose. In a piezoelectric positioner, the movement along each axis is controlled by one corresponding piezoelectric unit. A piezoelectric unit has three components including a piezoelectric actuator (PA), a driving object and a slider. By applying an AC voltage the PA can extend and retract at the applied frequency. The slider can be moved forward in a "stick-slip" cycle depicted in Figure 3.27 and described as follows: (1) Start period: no voltage is applied on the PA; all components are held still. (2) Stick period: a slowly increasing voltage is applied to the PA; the PA slowly extends to push the driving object. In this period, the external force on the slider is equal to the static friction, so the slider moves with the driving object. (3) Slip period: the voltage rapidly drops to zero. The PA then pulls back the driving object quickly. Now the external force on the slider is larger than the maximum static friction. Therefore, the slider slips on the driving object so that the relative position of the slider to the driving object moves in the direction of the PA extension. (4) Stop period: the voltage is now zero; everything is held still again. The slider has now been moved one step forward after the cycle. Similarly, the slider can be moved in the opposite direction by increasing the voltage rapidly then decreasing it slowly.

The piezoelectric positioner used in the black-helium-3 system, shown in Figure 3.28, is composed of three units for X, Y, and Z movement respectively. The lens assembly is connected to a titanium holder pillar which is fixed to the piezoelectric stepper. The Z unit can thus move the lens assembly up and down to focus on the device surface. The X and Y units can perform a 2D scan to search for photon emission on the device. The AC voltage for driving each stepper is provided by a controller that can output a 1 KHz signal at up to 60 V. Since the amplitude of the AC voltage is very high, the crosstalk can affect the electrical measurement. The piezoelectric positioner and the titanium holder pillar are therefore grounded to reduce crosstalk and charging. However, the effect can still be observed in the electrical transport measurement, though it has been improved by grounding.

It has to be noted that the movement of the piezoelectric positioner is asymmetric, which means the distance of one forward step (one "stick-slip" cycle) is different from the distance of one backward step. This is because piezoelectric materials exhibit mechanical hysteresis, which means the voltage dependence of the piezoelectric strain does not follow the same curve as the applied voltage increases and decreases. In this case, if the lens assembly is

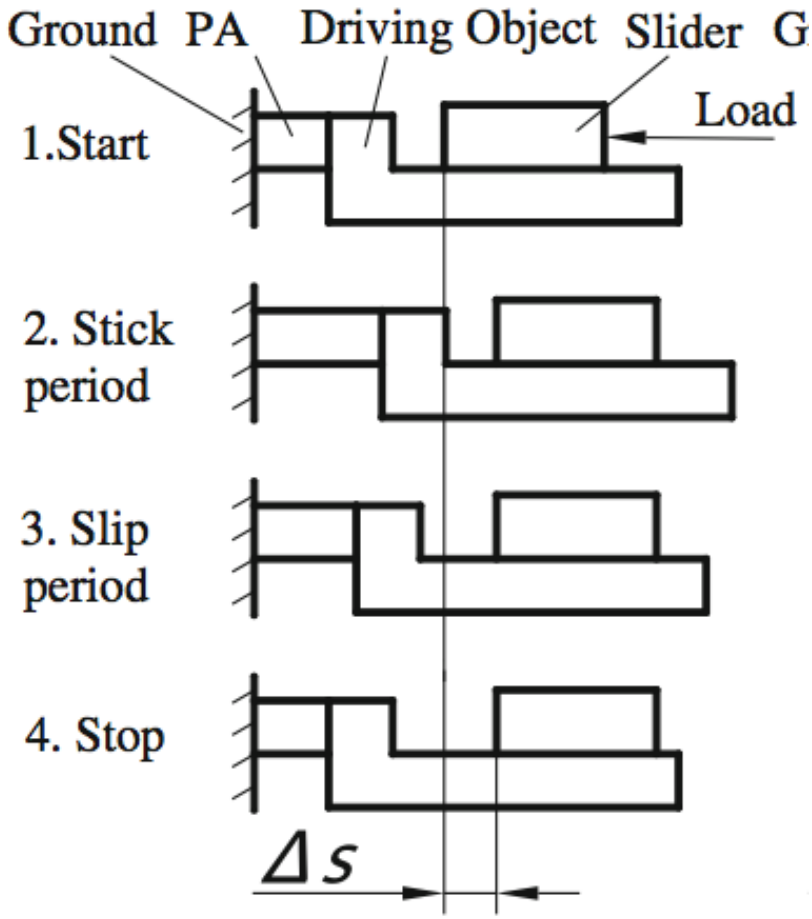

Fig. 3.27 Schematic of a 'stick-slip' cycle of a piezoelectric positioner. Schematic from [98].

moved 10 steps forward and then 10 steps backward along a certain axis, the final position will drift away from the original position due to asymmetric movement. This has to be taken into account in a 2D scan in the XY plane, otherwise the scanned image will be distorted. Details of the asymmetry calibration are given in Chapter 4.

Titanium Cage Assembly

If the sample holder is loosely anchored to the probe, the device will drift or vibrate with the sample holder, which can make the search for photon emission more difficult. Hence, the titanium cage assembly is designed to fix the sample holder firmly so as to minimise variation in the relative position of the sample holder and the probe. Also, the rigid titanium cage provides physical protection for the sample holder, the piezoelectric positioner, and the lens assembly from being damaged by scratching. The titanium cage assembly, shown in Figure 3.28, consists of four titanium plates and one titanium base. The four plates serve

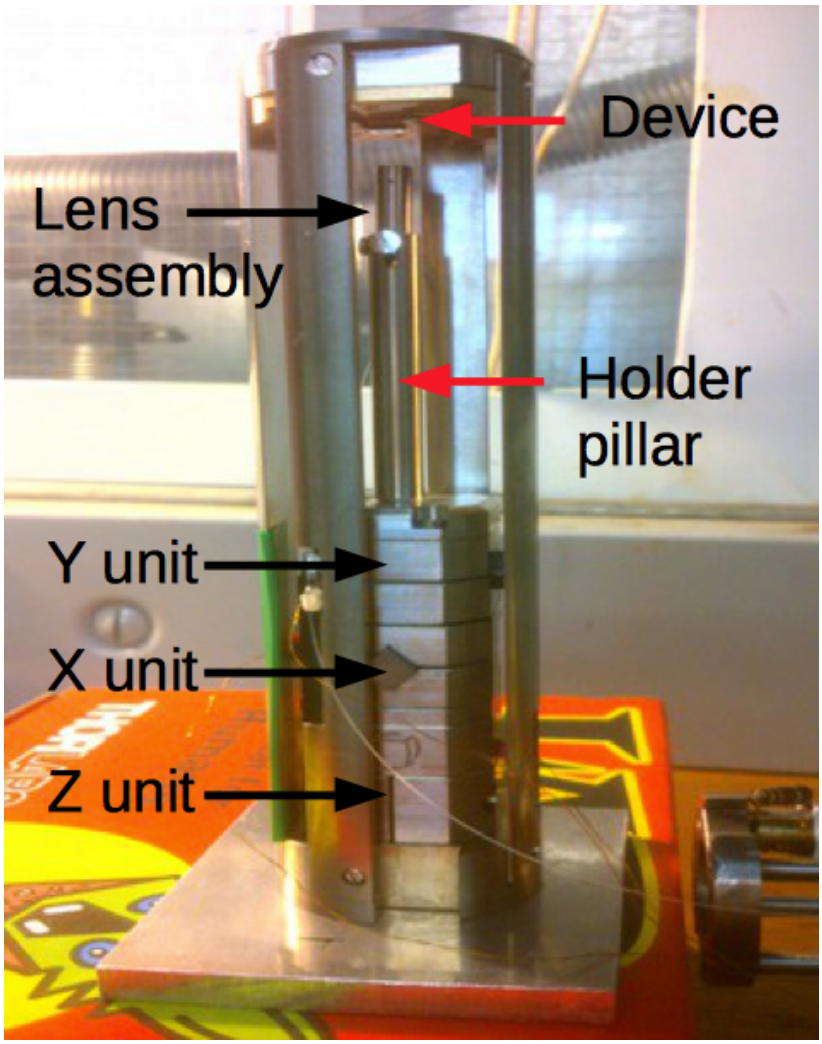

Fig. 3.28 Photograph of the piezoelectric positioner. By driving the X, Y, and Z units, the piezoelectric positioner can move the lens assembly attached to the titanium holder pillar to locate photon emission from a device. The whole setup is held together by the titanium cage consisting of four titanium plates and a base.

as the walls of the cage assembly and give firm support to the titanium base, on which the sample holder is fixed. When the cage assembly is properly tightened by titanium screws, the rigid structure ensures the sample holder will not be easily moved from its anchored position.

When the sample holder is anchored to the titanium base and connected to the wiring on the probe, the position of the wiring must be arranged so that it does not block the movement of the piezoelectric positioner. The free movement of the positioner can be confirmed by performing a 2D XY scan of the device using an external light source such as a 785 nm pig-tail laser. This should be done at room temperature before the probe is lowered into the

cryostat, since lowering and raising the probe takes at least a few hours and the movement of the piezoelectric positioner is slower at low temperature.

Demonstration of Optical Capability

Details of how to image a device and search for photon emission are given in Chapter 4. A short paragraph is presented here to demonstrate the capability of the black-helium-3 system in terms of optical measurement. To image a device, an optical setup shown in Figure 3.29 is employed to send light signals from a fibre-coupled laser to the device surface, and then detect the reflected signal using a detector. A 90:10 fibre beamsplitter is used in this optical setup so that only 10% of the laser power is coupled to the device and 90% of the reflected signal goes to the detector. When the lens assembly is moved up and down in the vertical (Z) direction, the reflected signal changes and reaches its maximum at the focal point. After the lens assembly is parked at the focal point, the piezoelectric positioner then moves the lens assembly horizontally to perform a 2D scan of the device. A scanned image, as shown in Figure 3.29(a), can thus be obtained because of the different reflection intensities on the GaAs and the metal gates.

Once the location of the lens assembly is known from the scanned image, the lens assembly can be moved to the lateral n-i-p junction in the centre of the device. The pig-tail laser is then switched off, and the optical setup is now able to detect the EL signal from the junction. The lens assembly can be moved over a small area to establish the spatial distribution of the EL signal. As shown in Figure 3.29(b), a micrometre-size EL spot is observed from the SAW-driven lateral n-i-p junction. Figure 3.29 demonstrates that the combination of the piezoelectric positioner and the lens assembly is capable of locating photon emission from the device.

3.3.3 μPL Continuous-flow Cryostat

The μPL cryostat system is the other low-temperature system that can perform SAW-driven EL measurement and electrical transport measurement at the same time. Compared with the black helium-3 cryostat, the major advantage of the μPL cryostat is easier optical access. This is because the whole device loaded in the μPL cryostat is optically accessible through a glass window. Light signals from a millimetre-scale area can be collected and imaged in a few seconds in the μPL cryostat while the lens assembly in the black-helium-3 allows only a $2\mu m^2$ area to be seen and it takes half an hour or so to acquire a 0.01 mm^2 scanned image. In the early stages of device development, photon emission occurred in some unexpected places due to insufficient confinement of charge carriers. The location of photon emission could be

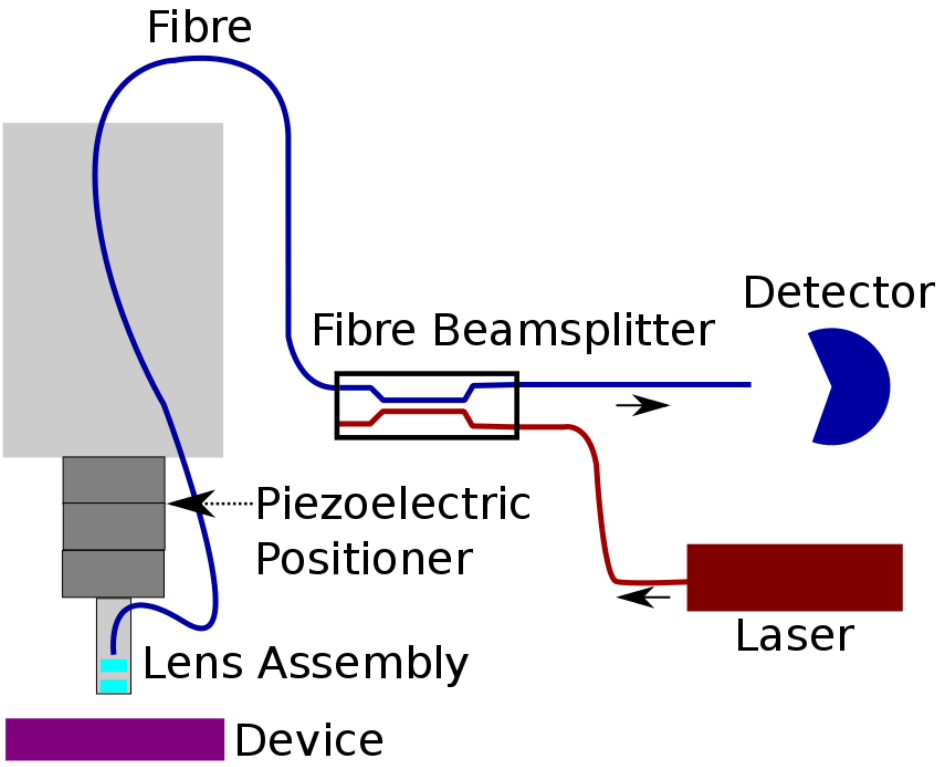

Fig. 3.29 Schematic diagram of the optical setup for black helium-3 cryostat. A light signal for a laser can be coupled into the single-mode fibre in the cryostat by the fibre beamsplitter. The light signal is focused on the device by the lens assembly, and the reflected signal is coupled back into the fibre and then detected by a detector. The piezoelectric positioner can move the lens assembly to perform a scan across the device.

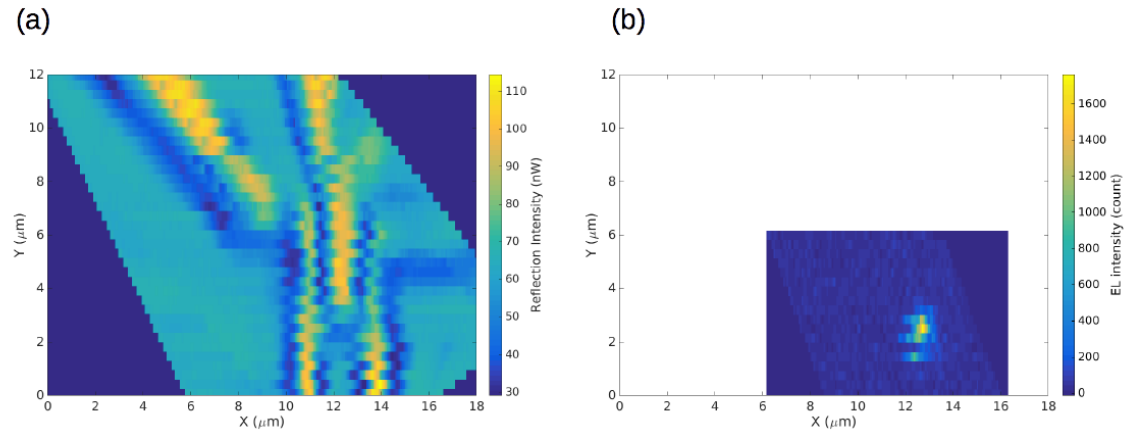

Fig. 3.30 Scanned images of (a) an n-i-p junction using an external light source, and (b) an EL spot from a SAW-driven n-i-p junction.

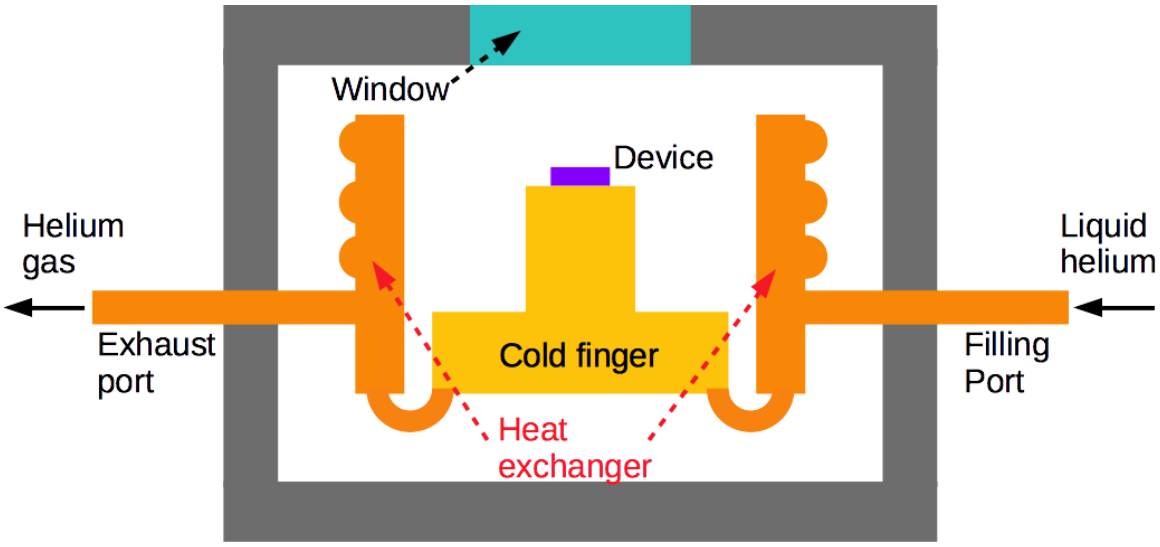

Fig. 3.31 Schematic diagram showing the structure of the μPL continuous flow helium cryostat. Liquid helium flows into the heat exchanger from the filling port to cool the heat exchanger and the cold finger to 4-10 K, and helium gas then leaves the system from the exhaust port. A device mounted on the cold finger can be optically accessed through a glass window at the top of the cryostat.

a few hundred micrometres away from the n-i-p junction. The detection of the off-junction photon emission is very difficult using the black-helium-3 system. The wide field of view of the μPL cryostat makes this system the better option for characterising devices in the early development stages.

The μPL cryostat is a continuous-flow helium cryostat. Figure 3.31 shows its structure. The cryostat chamber is evacuated to reduce the heat load. Liquid helium from a pressurised dewar then flows through the heat exchanger and the cold finger on which the sample holder is anchored. In this way, the temperature of the cryostat can be lowered to a minimum temperature of 4 K when the helium flow rate is high. However, the gold-finger temperature is usually lowered to only about 10 K in order to reduce helium consumption. A thermometer and a heater were anchored to the cold finger to read the temperature and to warm up the cryostat more quickly. In order to perform SAW-driven electrical transport measurements, DC wiring was upgraded to have 32 electrical connections and two coaxial cables.

Due to its simple design and the fact that it is cooled by flowing liquid helium continuously, the μPL cryostat does not use the cooling power of helium efficiently. A 60 L helium dewar can only be used to cool the μPL cryostat to 10 K for under 48 hours, while the same amount of helium can support the black helium-3 cryostat at 1.5 K for 6 days (144 hours). Besides, because the helium dewar needs to be pressurised for cooling, extra care has to be taken during the operation of the μPL cryostat as the pressure in the dewar can build up slowly

and needs to be released regularly. Therefore, the person performing the experiment must stay near the helium dewar to check the pressure. As a result, the μPL cannot be operated remotely and cannot run a continuous experiment for a long time. In addition, stray light can easily be coupled to the device through the window and this seems to cause a bridging-gate charging issue (described in Chapter 4), which further shortens the device's functional time. Due to the difficulties mentioned above, although the μPL cryostat is good for observing EL signals and optimising the recombination location, it is not suitable for experiments performed over a long time, such as auto-correlation measurements for observing photon antibunching.

Improvement of Electrical Wiring

Originally the μPL cryostat had only eight DC wires and two coaxial cables. Moreover, there was basically no thermal anchoring for the old wiring. In order to provide sufficient electrical connections for the SAW-driven n-i-p junction device, a new loom with 24 connections was added to make a total of 32 electrical connections. Since more electrical connections can also contribute more heat conduction, the thermal anchoring of all the DC and RF wiring was improved to avoid warming of the cryostat from the added wiring. The DC wires are made of constantan alloy to ensure low thermal conductance, while electrical conductance is still sufficient. To improve thermal anchoring, the DC wires were first wrapped around the exhaust of the heat exchanger and then fixed using GE varnish, as shown in Figure 3.32(c). The heat in the DC wires from the room temperature end can thus be transferred to the cold exhaust and be carried away by helium gas. After being anchored to the exhaust of the heat exchanger, the DC wires were anchored again to the heat exchanger near the cold finger (Figure 3.32(b)), in order to dissipate more heat before they could reach the sample holder.

The coaxial cables were miniaturised flexible cables with an FEP outer sheath, so they could not be thermally anchored effectively. Therefore, each coaxial cable was cut in half and re-jointed using a 1 dB RF attenuator, which was anchored to the heat exchanger, as shown in Figure 3.32(d). Hence, heat from the coaxial cables can be transferred to the heat sink (the heat exchanger) rather than the sample holder. After the thermal anchoring for both DC and RF wiring was carried out, the DC wires were terminated by two Conan connectors and the coaxial cables were soldered to SMA connectors to ensure easier connections to the customised sample holder.

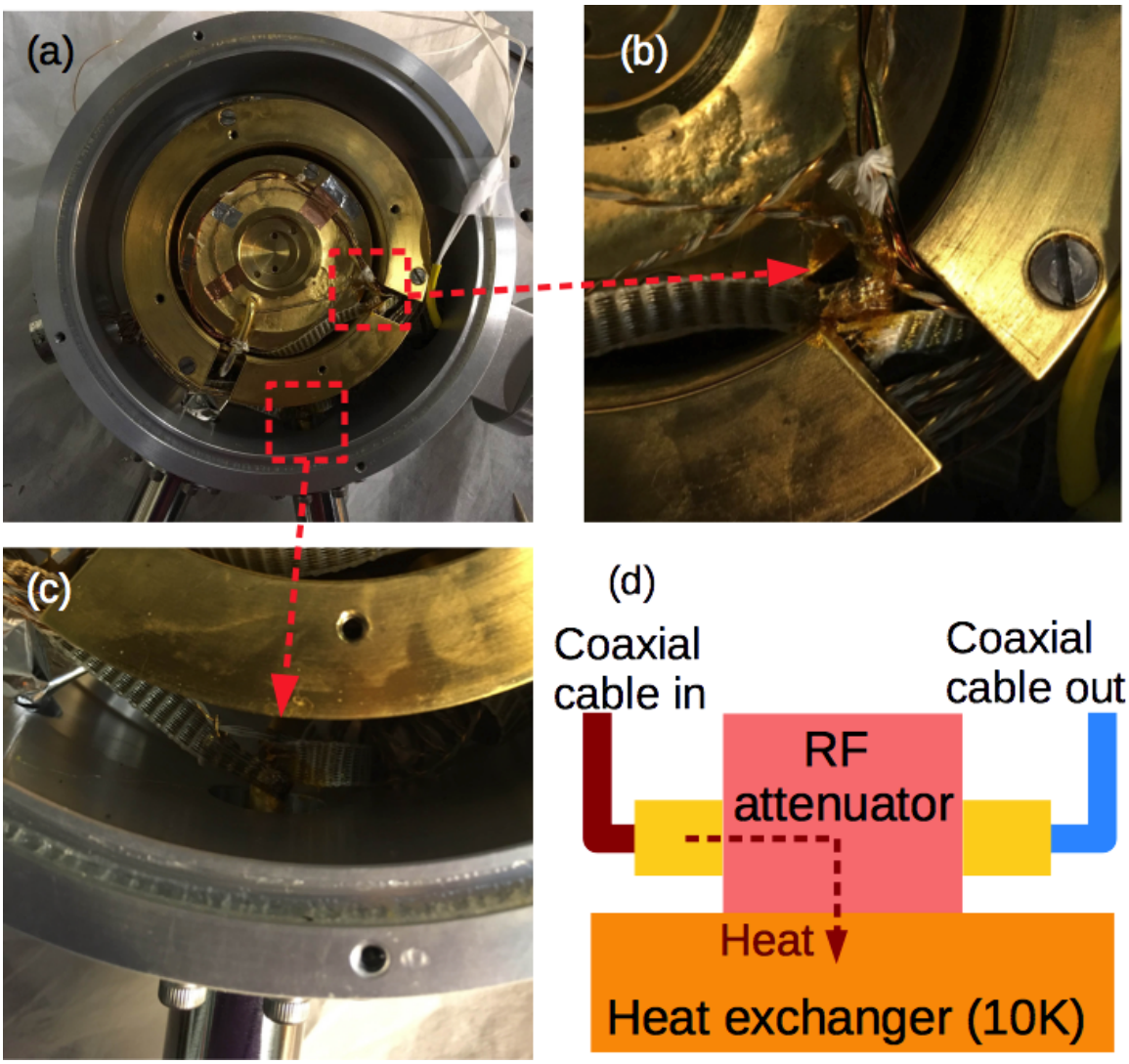

Fig. 3.32 Thermal anchoring of electrical wiring. (a) Bottom view of the μPL cryostat showing two locations of thermal anchoring for DC connections. (b) A magnified photograph showing the thermal anchoring near the cold finger. (c) A magnified photograph showing the thermal anchoring at the helium exhaust port. (d) Schematic diagram depicting thermal anchoring for a coaxial cable, where heat from the coaxial cable can be dissipated to the heat exchanger via an RF attenuator.

Optical Setup for the μPL Cryostat

Because the μPL cryostat has a glass window through which a mounted device is optically accessible using common free-space optical components, it is easy to acquire an image of the device by placing the cryostat under a microscope-like setup, which is shown in Figure 3.33. In this setup, an external light source is used to illuminate the device. The reflected signal is coupled to a CCD camera using a beamsplitter. The CCD camera can then capture an

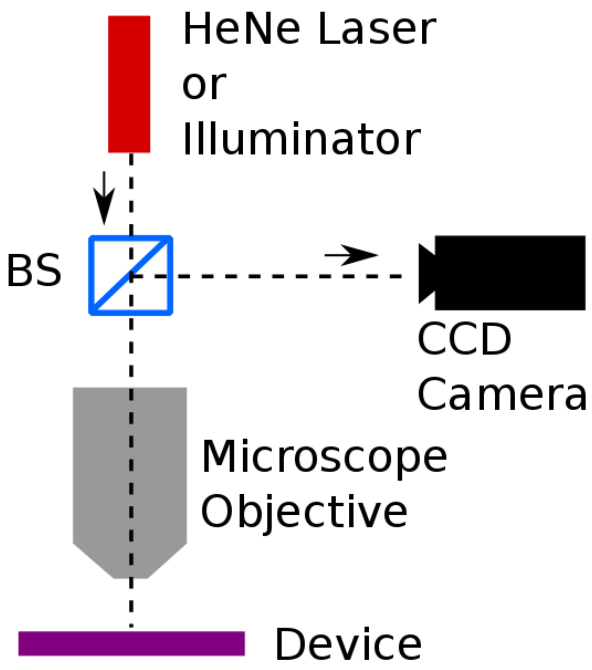

Fig. 3.33 Schematic of the optical setup for the uPL cryostat. The beamsplitter (BS) is used to couple the light signal from the device to a CCD camera. The CCD camera can capture the image of a device illuminated by an external light source (an illuminator). It can also take the EL image from the device when the external illumination is switched off.

image of the device. Similarly, the EL signal from a SAW-driven n-i-p junction on the device can be detected using the same setup when the external light source is switched off. As an example, Figure 3.34(a) shows the image of a SAW-driven n-i-p junction under the optical setup. Figure 3.34(b) shows the EL signal from the same junction.

3.4 Basic Electrical Measurement Techniques

3.4.1 Transducer Test

Since the generation of a SAW is one of the key elements of a functional SAW-driven n-i-p junction device, it is very important to confirm that the IDTs are able to launch SAWs. Therefore, after a SAW-driven n-i-p junction device is bonded to a sample holder, the input return loss and the insertion loss are measured using a network analyser. The network

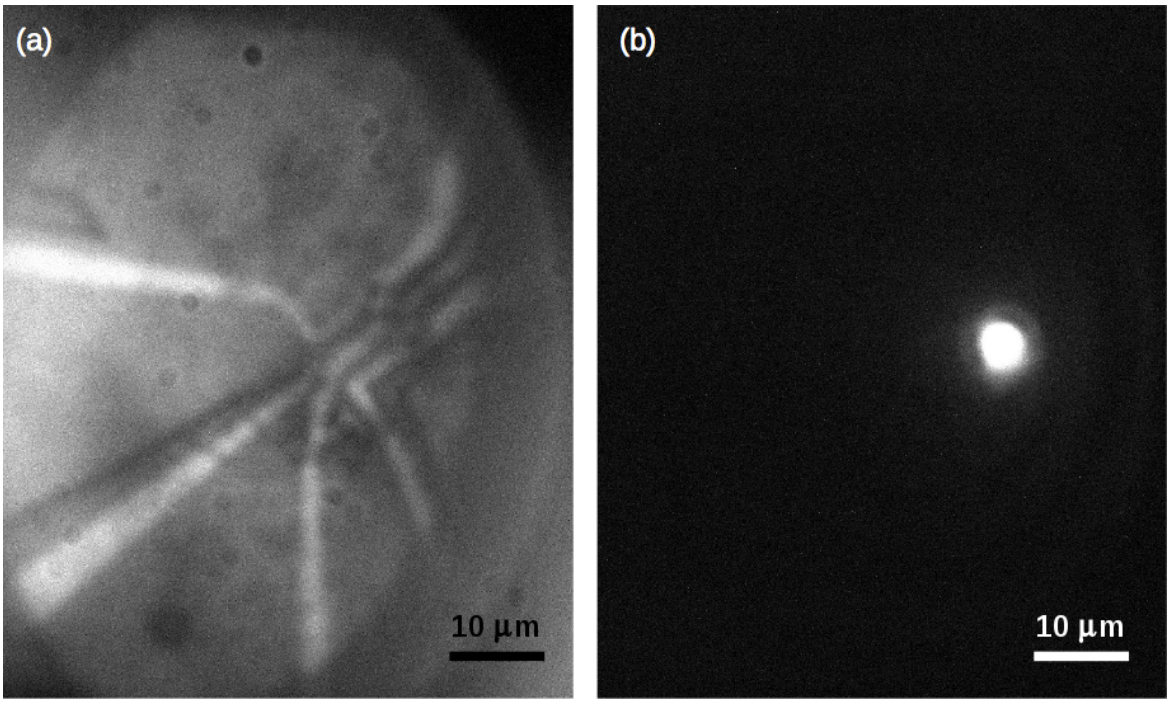

Fig. 3.34 CCD camera images from a device. (a) Image of an n-i-p junction using external light source. (b) EL signal from an n-i-p junction

analyser can characterise the scattering matrix of an electrical system by applying an RF signal to the input port, then measuring the return signal from the same input port and the transmitted signal from the output port. When the applied frequency is equal to the resonance frequency of an IDT, more power is transferred into the IDT to generate a SAW. The generated SAW propagates across the device and eventually reaches the other IDT. The other IDT can absorb part of the SAW power and convert it back to an electrical signal if the two IDTs have the same resonance frequency. If the IDTs on a device are working properly, the frequency dependence of the scattering parameter S_{11} should exhibit a dip at the resonance frequency while the frequency dependence of S_{21} should show a peak at the resonance frequency. Sometimes, it is difficult to observe the peak in the frequency dependence of S_{21} due to the significant damping of the SAW during propagation. However, if a dip in S_{11} can be observed clearly, the generation of a SAW can still be confirmed by a SAW-suppressed photoluminescence (PL), which is explained in Chapter 4.

3.4.2 Electrical Measurement Setup

Once the functioning of the IDTs on the device is confirmed, the sample holder, along with the device, is loaded into a cryostat. The electrical measurement of the device is carried out

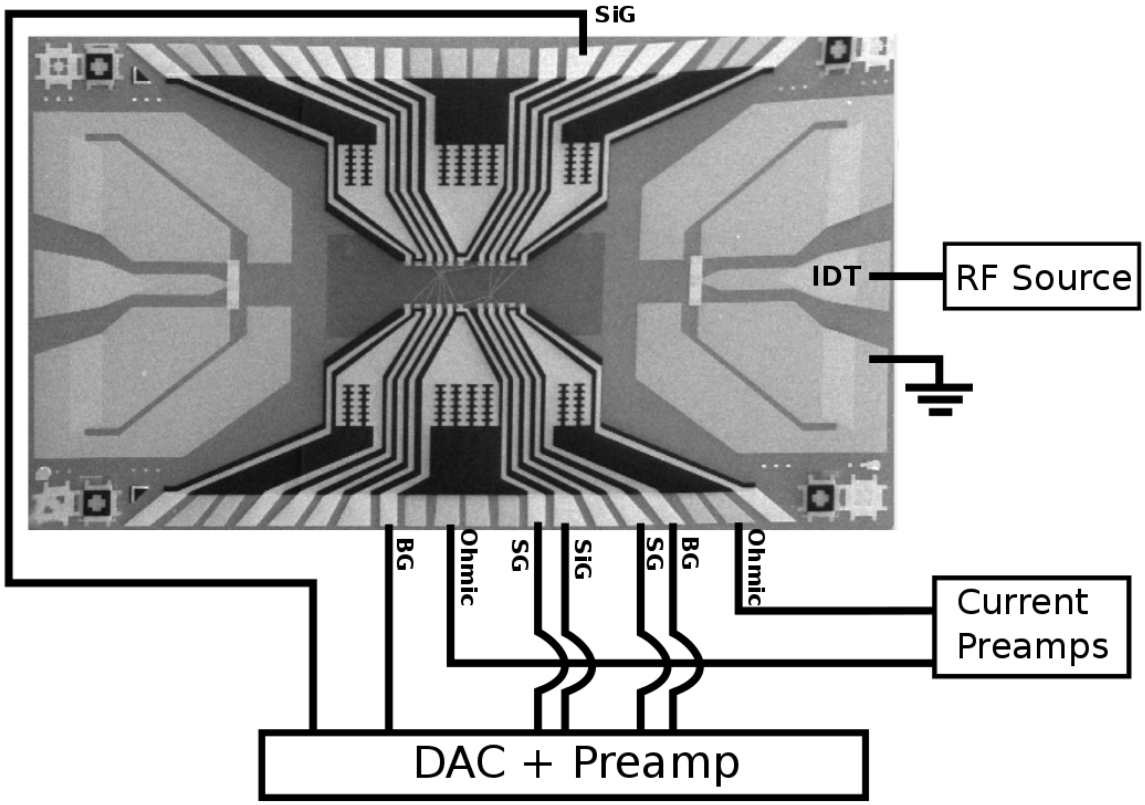

Fig. 3.35 Diagram of the SAW-driven electrical transport measurement. An RF source sends an RF signal to launch a SAW. Two low-noise current pre-amplifiers are used to apply source-drain bias to ohmic contacts and measure the SAW-driven current flow across an n-i-p junction. A six-channel current pre-amplifier combined with a multi-channel DAC provides gate voltages to all the gates that define the n-i-p junction, and also monitors all the leakage currents from these gates. IDT: Inter-digitated transducer. Ohmic: Ohmic contact. BG: Bridging gate. SG: Surface gate. SiG: Side gate. Device image from [89].

when the device is cooled close to the base temperature of the cryostat. In Figure 3.35, the electrical measurement setup is shown for a SAW-driven n-i-p junction device. In this setup, the ohmic contacts for the source and drain of the n-i-p junction are connected to Stanford SR570 low-noise current pre-amplifiers. These two SR570s can apply bias voltages to the ohmic contacts and measure the current flowing through the device. A multi-channel DAC combined with a multi-channel current pre-amplifier designed by Dr Ateeq Nasir provides bias voltages to all required bridging gates, surface gates, and side gates while monitoring leakage currents from all these gates. An RF source connected to one of the IDTs is used to send an RF signal to launch a SAW.

3.5 Conclusion

In this chapter, the fabrication of a SAW-driven n-i-p junction device and the measurement methods have been discussed. The considerations in the design and the fabrication were explained along with the difficulties encountered and their corresponding solutions. Compared with the design of previous generations of devices, the n-type ohmic contacts, the ohmic contact insulator, and the e-beam-defined wet etching have been modified in order to provide more reliable and more reproducible devices. Regarding measurement methods, three low-temperature systems, the RF dip station, the black helium-3 cryostat, and the μPL continuous-flow helium cryostat were discussed. Much effort has been made to modify and improve the wiring in the black helium-3 cryostat and the μPL cryostat significantly for the measurement of SAW-driven n-i-p junction devices. The optical setups in the black helium-3 cryostat and the μPL cryostat were briefly presented. Both of these will be explained in detail in Chapter 4. Finally, the basic electrical measurement techniques that apply to all measurements in the following chapters were discussed. More specific measurement techniques, which are unique to different measurements, will be introduced in later chapters.

Chapter 4

SAW-driven Lateral n-i-p Junction: Characterisation and Optimisation

This chapter discusses characterisation and optimisation of SAW-driven n-i-p junction devices. Following the brief introduction in Chapter 3, the optical setups in the black helium-3 and μPL cryostats are further explained in the first section along with their photon collection efficiencies and the operating procedure for the piezoelectric positioner. In Sections 4.2 to 4.5, measurement results and discussion of devices from four consecutive batches are presented in chronological order, and the development process that led to the optimised SAW-driven n-i-p junction is also shown.

4.1 Optical Setup

4.1.1 μPL cryostat optics

Photon emission from a SAW-driven n-i-p junction device in the μPL cryostat are coupled to a free-space optical setup, as illustrated in Figure 4.1. A 5X or a 50X microscope objective can be used to collect the photons, depending on the required field of view and resolution. A 50:50 beamsplitter allows images and spectra to be captured using a CCD camera and a spectrometer at the same time. When a photoluminescence (PL) measurement is carried out using a 633 nm HeNe laser, a longpass filter is placed before the spectrometer to filter out the laser signal so that only the 809 nm PL signal from the GaAs quantum well (QW) is detected by the spectrometer.

Photon collection efficiency can be estimated from the numerical aperture (*NA*) of a microscope objective and the refractive index n of GaAs. If the 50X microscope objective is used, the angle θ_α (angular aperture) of emitted light that can be collected by the microscope

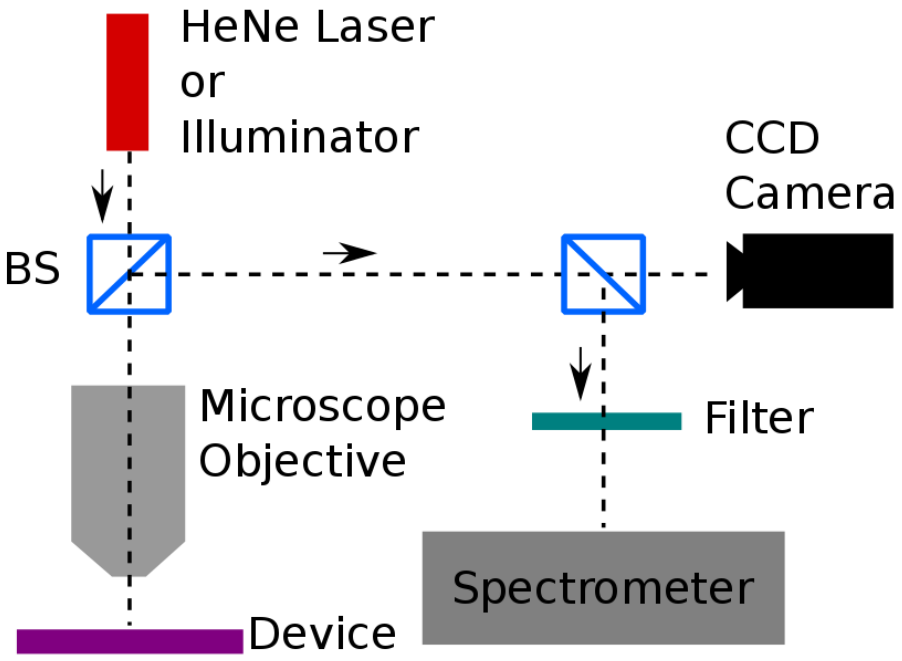

Fig. 4.1 Schematic of the optical setup for photoluminescence (PL) and electroluminescence (EL) in the μPL cryostat. This setup is based on the one shown in Figure 3.33. An extra 50:50 beamsplitter (BS) is employed to send half of the light signal to a spectrometer. A longpass filter is placed before the spectrometer in PL measurements to remove the HeNe-laser signal.

objective is determined by

$$NA = n \cdot \sin\theta_\alpha \,. \tag{4.1}$$

θ_α is thus 0.16 (9°) given $NA = 0.55$ for the 50X objective and $n = 3.5$ at 800 nm [99]. Assuming photon emission from an n-i-p junction is isotropic, the ratio of collectable photons to emitted photons is equal to the solid angle of the angular aperture divided by 4π. This gives rise to a collection ratio of 0.64%. Considering the reflection at the GaAs-air interface in the case of a small incident angle

$$R = \left|\frac{n-1}{n+1}\right|^2 = 1 - T \,, \tag{4.2}$$

where R is the reflection coefficient and T is the transmission coefficient. T is equal to 0.7 given $n = 3.5$. The estimated photon collection efficiency is then $0.7 \cdot 0.64\% = 0.45\%$ for a lateral GaAs n-i-p junction in this optical setup.

4.1.2 Black Helium-3 optics

As mentioned in the previous chapter, in the black helium-3 cryostat, photon emissions are collected using the miniaturised lens assembly. The collected photons are sent to a detector or a spectrometer via the single-mode fibre. Since *NA* of the bottom lens is 0.55, the highest possible photon collection efficiency is also 0.45%, which is the same as for the μPL cryostat with the 50X microscope objective. However, due to imperfect alignment of the lens assembly, its coupling ratio (fibre input to lens-assembly output or lens-assembly input to fibre output) was measured as 86%. Hence, the real photon collection efficiency is reduced to 0.39%.

Operating Procedure for the Piezoelectric Positioner

In the black helium-3 cryostat, photon emission from a lateral n-i-p junction is located using the piezoelectric positioner to move the lens assembly. The piezoelectric positioner is an open-loop-controlled system, meaning the information about the positioner's absolute position is unavailable. The position relative to the device can only be obtained by focusing the attached lens assembly on the device surface and detecting light signals, either photon emission or laser reflection, from known features such as the n-i-p junction or patterned metal gates. Therefore, the procedure for finding the device is important as losing a sense of direction in the sealed cryostat, which cannot be observed from outside, might lead to accidents that damage the lens assembly and the device.

The focusing is carried out by moving the lens assembly vertically (along the Z axis) and maximising the reflection of an external light signal. Before the top-loading probe is mounted on the black helium-3 cryostat, the lens assembly should be moved to about 3 mm from the device along the Z axis and should be roughly aligned with the centre of the device along the horizontal plane (the X and Y axes) to ensure the lens assembly will not touch the device and can focus on the device surface. Since the focal length of the bottom lens is 1.45 mm, this 3 mm initial distance also ensures the focal point can be found by moving the lens assembly towards the device, so uncertainty about movement along the Z axis is reduced. Figure 4.2 shows the reflection intensity of a fibre-coupled 785 nm laser when the lens assembly is around the focal point. The focal point is found when the reflection intensity reaches its maximum. The peak at the focal point is not symmetric due to the asymmetric depth of field [100].

Once the focal point is found, the positioner can then move the lens assembly along the X and Y axes to find features on the device utilising the difference in reflection on the GaAs surface and patterned metal gates. Figure 4.3 shows the reflection intensity changing as the

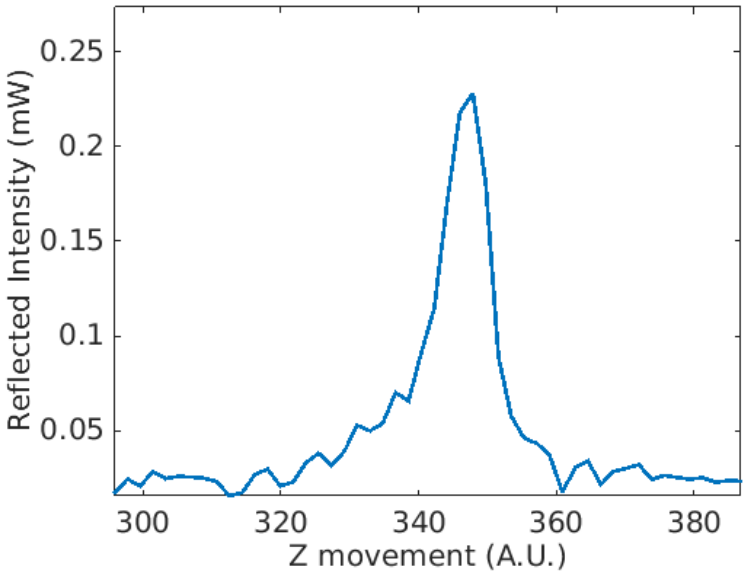

Fig. 4.2 Reflection intensity of a fibre-coupled 785 nm laser as a function of positioner movement along the Z axis, with a driving voltage of 60 V at 4 K. The reflection intensity reaches its maximum when the lens assembly is focused on the device surface.

positioner scans across a metal gate. The reflection intensity is approximately doubled when the laser signal is focused on the metal gate compared with the GaAs surface. Because of the asymmetric movement of the piezoelectric positioner, the intensity curve in a forward movement does not match the curve in a backward movement (see Figure 4.3(a)), which will give rise to a distorted image in a 2D scan using the piezoelectric positioner. The ratio of asymmetry (the movement per forward step to the movement per backward step) can be obtained by measuring the numbers of steps across the same feature for a forward and a backward scan. This ratio is then used to calibrate the numbers of required steps for a forward and a backward scan to move the same distance. Reproducible back-and-forth curves can thus be obtained after asymmetry calibration (see Figure 4.3(b)).

After the focusing and the asymmetry calibration, the positioner can move the lens assembly horizontally to perform a 2D mapping in order to ascertain the relative position to the device. As an example, figure 4.4(a) shows a 2D scanned image of a SAW-driven split-gate device, which was studied in a different project [93]. Most features on the device can be resolved and match the design (see figure 4.4(b)). Provided a relative position to a device is known, the lens assembly can be gradually moved to a desired position, like an n-i-p junction, and collect photon emission when the device is turned on.

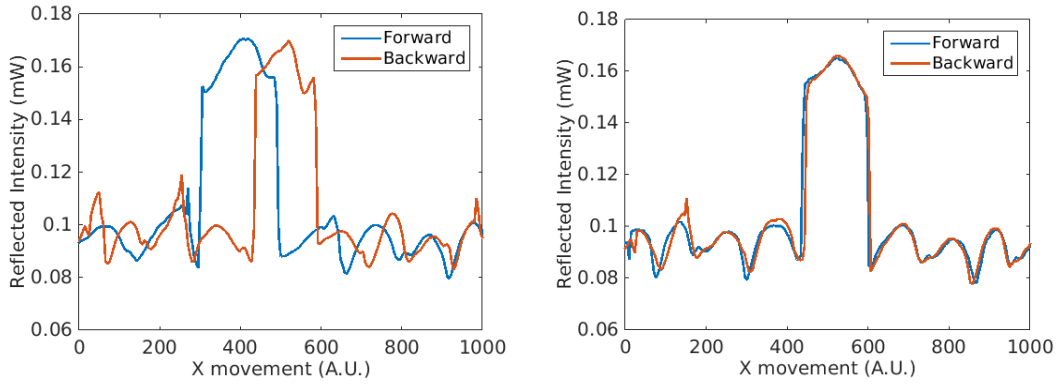

(a) (b)

Fig. 4.3 Reflection intensities of as a function of positioner movement along the X axis (a) without asymmetry calibration, and (b) with asymmetry calibration. (a) The forward and backward curves do not match due to the asymmetric movement of the positioner. (b) Matched curves can be obtained when the asymmetric movement calibrated.

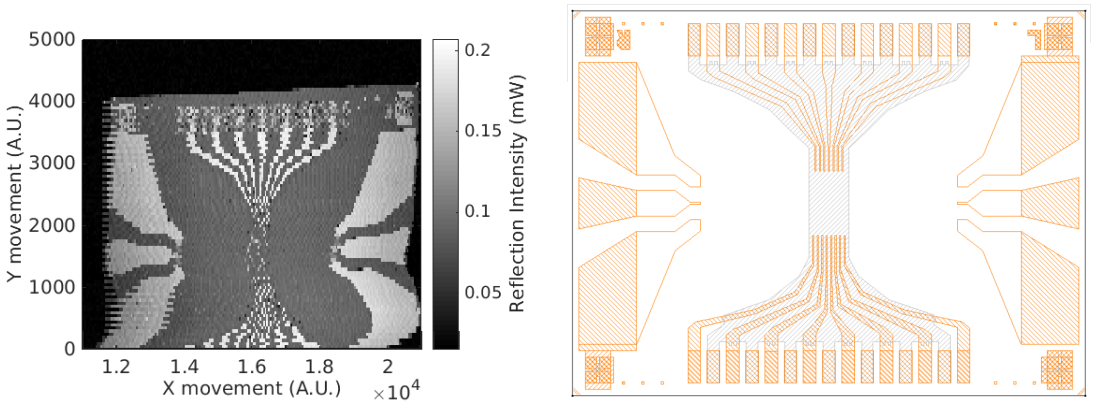

(a) (b)

Fig. 4.4 (a) Scanned image of a SAW-driven split-gate device. The image is slightly distorted due to imperfect asymmetry calibration. (b) Design of the SAW-driven split-gate device for comparison. Orange regions are patterned Ti/Au. This device was designed by Dr Matthew Benesh and studied in his PhD thesis [93].

4.2 Early-generation SAW-driven n-i-p Junction

The first device discussed in this chapter is an early-generation SAW-driven n-i-p junction, which was designed and fabricated by Dr Yousun Chung [89]. This device had been measured by Dr Chung, and was subsequently characterised by the author. For a detail description of this device, please refer to her PhD thesis [89]. Here only essential results are presented to show the basic measurement procedure for a SAW-driven n-i-p junction and to point out required improvements in the next batch. From this point on, this device will be referred to as YC02 since it is from the second batch of devices made by Dr Chung.

4.2.1 YC02 Device Design

The fabrication of YC02 is similar to the process described in Chapter 3. For the details please refer to Dr. Yousun Chung's PhD thesis [89]. One major difference is in the e-beam-defined etch pattern. Figure 4.5(a) shows the ohmic contacts and the etch pattern in YC02. Compared with Figure 3.6, in YC02 each ohmic group (highlighted by a dashed-line rectangle) is not isolated from other ohmic groups. This can lead to electron-hole recombination in unexpected regions, which will be shown later. The lateral n-i-p junction that will be discussed in the following paragraphs is shown in Figure 4.5(b) and (c). The junction is formed by inducing electrons from the top-right (TR) ohmic group and inducing holes from the bottom-middle (BM) ohmic group. A SAW is launched by an IDT on the right-hand side to pump the electrons across an etched channel (with a narrowest width of 0.9 μm) to the region of holes. Note that the length of the channel was chosen to be about one wavelength of the SAW, which is 1 μm in this device, to ensure that a SAW-modulated current was contributed by the SAW dragging charges across a potential barrier, rather than the SAW simply lowering the potential.

4.2.2 Testing of Bridging Gates

YC02 was first measured in the black helium-3 cryostat. It was bonded to the black-helium-3 sample holder, which is mentioned in Chapter 3. Once the device was cooled in the cryostat, the bridging gates had to be tested to confirm that electrons and holes could be induced by applying a bridging-gate voltage V_{BG}. The bridging gates were tested by performing two-terminal measurements between two ohmic contacts in the same ohmic group. An example of this test is shown in Figure 4.6, which was carried out on a device from the same batch as YC02. Figure 4.6(a) and (b) show that currents appear when bridging-gate voltages V_{BG} are higher than the threshold voltages $V_{th(\mathrm{BG})}$, at which electrons and holes

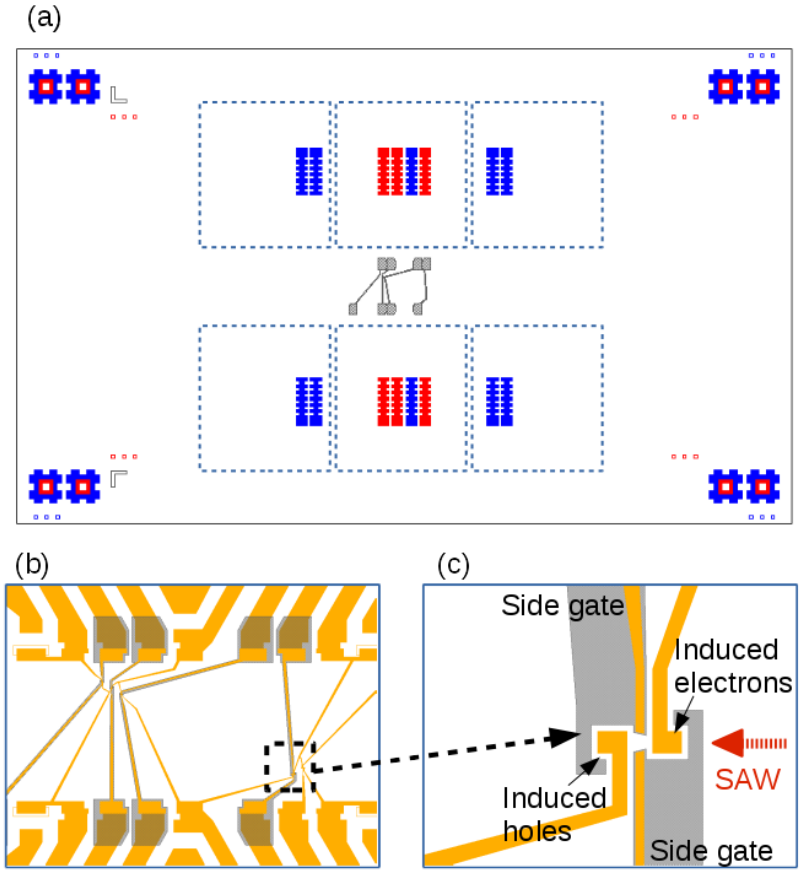

Fig. 4.5 Design of YC02. (a) Diagram showing p-type ohmic contacts (red regions), n-type ohmic contacts (blue regions), and e-beam-defined wet etching (grey regions). The six ohmic groups are highlighted by dashed-line rectangles. (b) Design showing e-beam-defined surface gates (yellow regions) with the wet pattern. (c) Magnified design of the n-i-p junction characterised in this thesis. Electrons and holes are respectively induced by two surface gates to form the n-i-p junction. The narrowest width of the etched channel is 0.9 μm. A SAW can be launched by an IDT to drag electrons to reach the region of holes. The side gates are used to adjust the potential in the intrinsic region.

are induced in the GaAs quantum well (21 V and -5 V respectively). These two voltage thresholds are quite high due to the relatively thick polyimide (800 nm, dielectric constant $\varepsilon = 3$) used as the ohmic insulator in YC02. Note that there is an extra bump of induced current at $-2.8 < V_{\mathrm{BG}} < -1.5$ V in Figure 4.6(b), presumably formed due to the screening effect by charge induced near the GaAs surface [89].

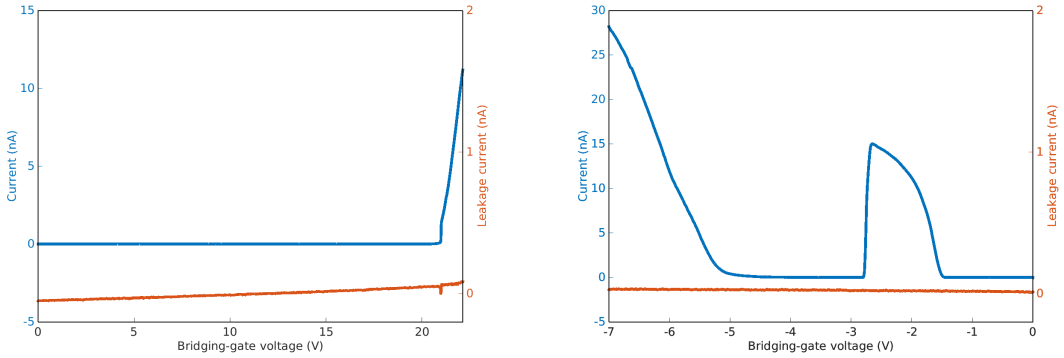

(a) (b)

Fig. 4.6 (a) Current between two n-type ohmic contacts as a function of bridging-gate voltage. The current appears when electrons are induced by applying a bridging-gate voltage $V_{\mathrm{BG}} > 21$ V. (b) Current between two p-type ohmic contacts as a function of bridging-gate voltage. The current appears when holes are induced by applying $V_{\mathrm{BG}} < -5$ V. A bump of inducing current is shown at $-2.8 < V_{\mathrm{BG}} < -1.5$ V, presumably due to screening by charge near the GaAs surface [89].

4.2.3 Forming the n-i-p Junction and SAW-modulated Current

After the functioning of the required bridging gates has been confirmed, the n-i-p junction can then be characterised using the electrical measurement setup shown in Figure 3.35. V_{BG} higher than the inducing thresholds $V_{th(\mathrm{BG})}$ are applied to the bridging gates to induce electrons and holes. Surface-gate voltages V_{SG} are then applied to the surface gates to extend these electrons and holes to the n-i-p junction. The surface-gate thresholds $V_{th(\mathrm{SG})}$ for extending charges to the junction are 0.9 V and -0.7 V for electrons and holes respectively. This asymmetry in $V_{th(\mathrm{SG})}$ is because the low-density p-type background doping makes the Fermi level closer to the valence band [89], and this asymmetry was observed in all the devices fabricated using wafer W1002.

Once these electrons and holes reach the two sides of the n-i-p junction, a source-drain (S-D) bias can be applied to the ohmic contacts to check the functioning of the n-i-p junction. Note that V_{BG} and V_{SG} for inducing one type of charge (electron or hole) need to be increased or decreased together with the bias applied to the corresponding ohmic contact. For example, if $V_{\mathrm{BG}} = 22$ V and $V_{\mathrm{SG}} = 1$ V are applied to induce electrons when the source (electron) bias $V_{\mathrm{Source}} = 0$ V, then V_{BG} and V_{SG} have to be changed to 21.2 V and 0.2 V when $V_{\mathrm{Source}} = -0.8$ V. In this case, the relative potentials of the bridging gates and the surface gates to the induced charges are kept constant so that the charge densities below these gates will be constant no matter how V_{SD} changes [88]. Also, it is best to apply V_{Source} and V_{Drain} in a near-symmetrical way, e.g. $V_{\mathrm{Source}} = -0.8$ V and $V_{\mathrm{Drain}} = 0.7$ V, to avoid injection of

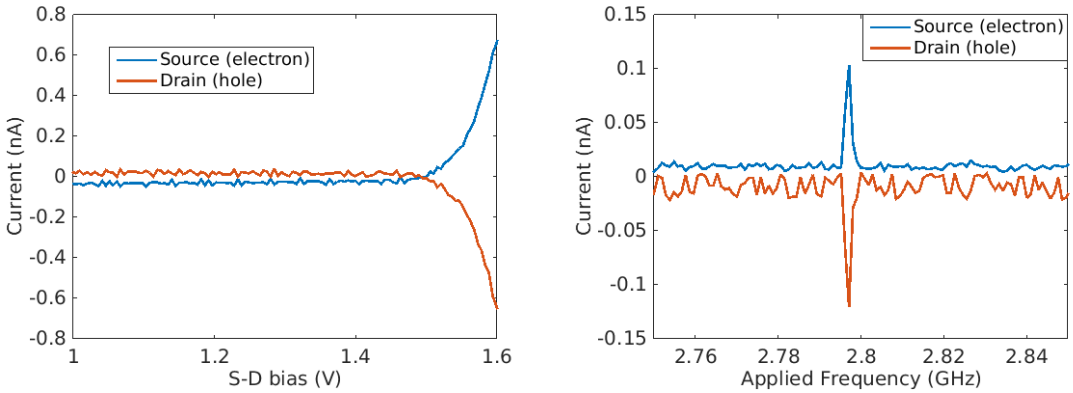

(a) (b)

Fig. 4.7 (a) Source-drain (S-D) current as a function of applied S-D bias across the n-i-p junction. S-D Current appears when the applied bias $V_{SD} > 1.5$ V. The current from the source (electron) ohmic contacts exhibits a similar amplitude to the current into the drain (hole) ohmic contacts. (b) S-D current as a function of frequency f_{RF} applied to the IDT when the source-drain bias is 1.45 V, which is below its DC threshold 1.5 V. RF power is 14 dBm. A peak in the S-D current appears at the resonant frequency of the IDT.

charge into neighbouring intrinsic area [89]. Figure 4.7(a) shows that the S-D current I_{SD} appears when V_{SD} is greater than 1.5 V, which corresponds to the GaAs bandgap of 1.52 eV at 1.5 K. The currents from the source (electron) ohmic contacts and the current into the drain (hole) ohmic contacts have similar amplitudes but opposite signs, which means the current flowing in is equal to the current flowing out. Therefore, the leakage current in YC02 is not significant under forward bias.

After the S-D bias threshold $V_{th(SD)}$ has been found, V_{SD} is set to at least 50 mV below $V_{th(SD)}$ so that noise or crosstalk cannot contribute significantly to S-D current. SAW-driven charge transport can then be tested by applying an RF signal to an IDT at its resonant frequency to launch a SAW. As shown in Figure 4.5(c), the SAW is launched from the right IDT to drag electrons to the region of holes. For a fixed V_{SD}, the potential in the etched intrinsic channel can be adjusted by applying a side-gate voltage V_{SiG} to the side gates to optimise SAW-driven transport. In Figure 4.7(b), where $V_{Source} = -0.8$ V, $V_{Drain} = 0.6$ V, $V_{SiG} = 0$ V and RF power $P_{RF} = 14$ dBm, the S-D current I_{SD} as a function of frequency f_{RF} applied to the IDT shows an enhancement of charge transport at $f_{RF} = 2.8$ GHz. Given the IDT on YC02 has a spatial periodicity of 1 μm and the SAW velocity on GaAs is $\simeq 2800$ m/s, the resonant frequency should be about 2.8 GHz at which a SAW is generated [94]. This indicates that the SAW is helping charge flow between ohmic contacts across the n-i-p junction.

4.2.4 Lack of Electroluminescence at the n-i-p Junction

The lens assembly was moved and focused at the n-i-p junction when the junction was characterised so it could collect the photon emission due to electron-hole recombination at the junction. Although S-D current could be observed at $V_{SD} > V_{th(SD)}$ or by launching a SAW when $V_{SD} < V_{th(SD)}$, electroluminescence (EL) could not be detected within a $10\,\mu m \times 10\,\mu m$ area around the n-i-p junction. The spectrometer with a sensitivity of about 0.16 fW could not get any signal even when the S-D current was more than $1\,\mu A$, which would generate a photon emission of 6 pW even assuming a low internal quantum efficiency of 0.1%. Due to the lack of EL near the junction, it was speculated that the S-D current flowed via some unexpected path between the two ohmic-contact groups (TR and BM) rather than through the intended n-i-p junction. As seen in Figure 4.5(a), there is no well-defined constriction of current flow between any two ohmic-contact groups. If electrons and holes leak to the wide intrinsic area without guidance by the surface gates, they can recombine anywhere in this wide area, especially in regions with a higher density of impurities, which act as recombination centres [101–104].

4.2.5 Electroluminescence from an Unexpected Region

The black helium-3 cryostat is not an ideal system to search for unknown light signals over a large area. The piezoelectric-positioner-controlled lens assembly can only collect photons in a $2\,\mu m^2$ area at one time. Long-time scanning is required to find signals from a larger area. For example, to map a $1\,mm \times 1\,mm$ area with an exposure time of 1 second at each $2\,\mu m^2$ pixel would take five days. As a result, further characterisation of YC02 was carried out in the μPL cryostat because light signals in a millimetre-scale area can be captured by the CCD camera in a few seconds.

In the μPL cryostat, SAW-driven EL could still not be observed. However, EL was detected from an unexpected region when a high S-D bias was applied to the TR and BM ohmic groups. Figure 4.8(a) shows an image of the EL when $V_{SD} = 1.7$ V and $I_{SD} = 1.5\,\mu A$. Figure 4.8(b) is the image overlaid with device design of YC02, and the n-i-p junction that was supposed to emit photons is highlighted by the red rectangle. It is clear that the EL was from a hundred-micrometre-size region far from the intended n-i-p junction. Hence, it is evident that the S-D current flowed via this region rather than the junction. Furthermore, the EL spectrum in Figure 4.8(c) exhibits a peak at 1.492 eV (833 nm), which corresponds to the transition of the conduction band to the carbon acceptor [104–106], rather than the bandgap of the GaAs quantum well [89]. Therefore, this band of EL may occur because of a relatively higher concentration of carbon background doping in this region. This result

explains why no photon emission was observed in the black helium-3 cryostat with a small field of view, and it indicated that a better constriction of current-flow path was needed to ensure electron-hole recombination at an intended n-i-p junction.

4.2.6 Bridging-gate Charging Issue

In the μPL cryostat, a bridging-gate charging issue was observed during measurements. Bridging-gate-induced charges disappeared a few seconds after they had been induced. As seen in Figure 4.9(a), in two-terminal measurement to test the bridging gate, induced holes gave rise to a current at $V_{\mathrm{BG}} < -7\,\mathrm{V}$ when the bridging gate was swept from 0 V to $-9\,\mathrm{V}$ (forward sweep). However, when a backward sweep ($-9\,\mathrm{V}$ to 0 V) was performed a few seconds after the forward sweep, the current had dropped from 40 nA to 5 nA at $V_{\mathrm{BG}} = -9\,\mathrm{V}$ and did not follow the forward-sweep curve. Also, the inducing threshold $V_{th(\mathrm{BG})}$ kept shifting. As shown in Figure 4.9(b), the first forward sweep showed an induced current at $-5\,\mathrm{V}$. After the first forward sweep had been stopped at $-7\,\mathrm{V}$ and V_{BG} had been swept backward, the inducing threshold in the second forward sweep became $-7\,\mathrm{V}$. The third forward sweep also showed a shift in the threshold at the point where the 2nd sweep had been stopped.

This behaviour can be explained by charges being trapped near the surface underneath the bridging gate. The charges quickly accumulate near the surface in a few seconds and screen the electric field from the bridging gate to the quantum well. As a result, holes are no longer induced in the quantum well until a more negative V_{BG} is applied so that the screening effect can be temporarily overcome. This process then repeats many times until V_{BG} cannot be increased any further for fear of leakage. This bridging-gate charging issue was observed in all SAW-driven n-i-p junction devices measured in the μPL cryostat, while such issues were not observed in the black helium-3 cryostat. The reason may be that the μPL cryostat has a glass window that allow stray light to excite charges near the surface and cause charge accumulation under bridging gates. However, these trapped charges can be expelled by setting $V_{\mathrm{BG}} = 0$ and illuminating the device with a white light source (intensity $= 40000\,\mathrm{fc}$) for 20 minutes. Understanding of this bridging-gate charging issue requires further investigation. When later batches of devices were measured in the μPL cryostat, V_{BG} was increased continuously at a rate that could maintain enough electrons and holes in the quantum well.

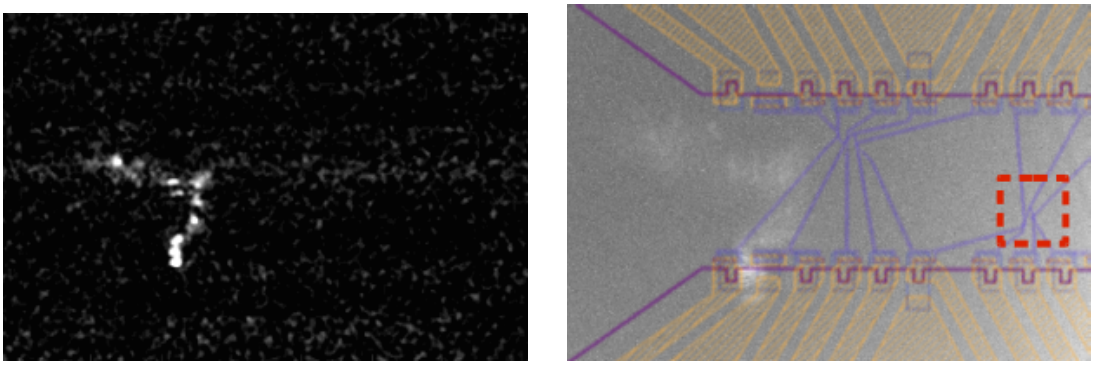

(a) (b)

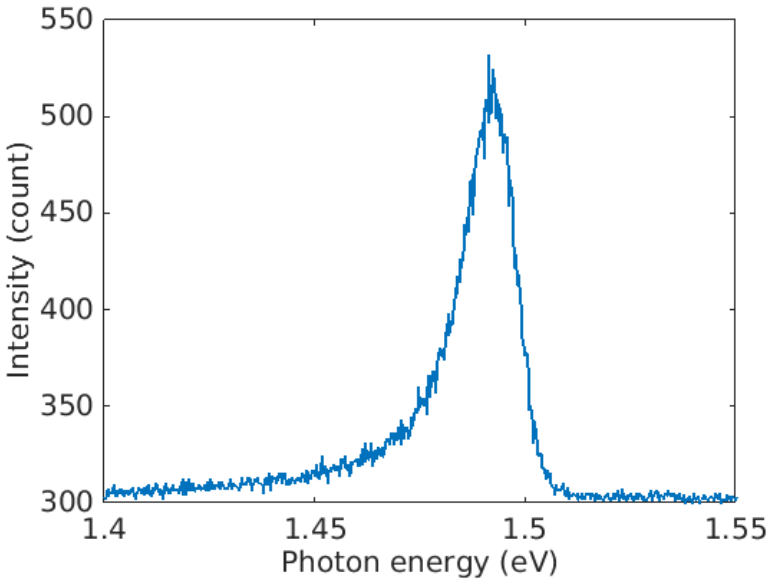

(c)

Fig. 4.8 (a) Image of the EL when $V_{SD} = 1.7$ V was applied. (b) Image of the EL overlaid by the device design. The n-i-p junction under forward bias is highlighted by the red rectangle. (c) Spectrum of the EL. The peak is at 1.492 eV (833 nm).

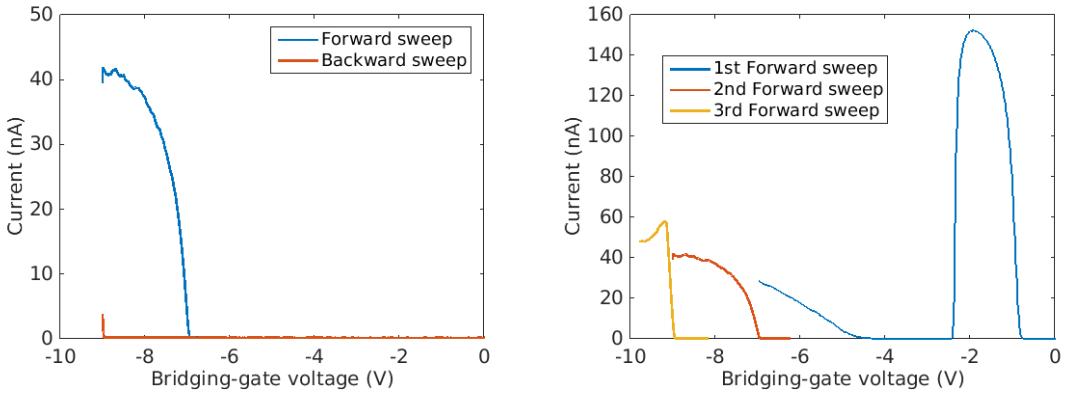

(a) (b)

Fig. 4.9 Induced current as a function of bridging-gate voltage showing the bridging-gate charging issue. (a) V_{BG} is swept from 0 to -9 V in the forward sweep, and a few seconds later from -9 to 0 V in the backward sweep. The current in the backward sweep decays significantly at -9 V and does not follow the curve in the forward sweep. (b) Inducing currents in three consecutive sweeps. The first sweep induces holes at -5 V and stops at -7 V. The second sweep induces holes at -7 V and stops at -9 V. The third sweep induces holes at -9 V.

4.2.7 Bridging-gate Leakage Issue

Another issue with YC02 was that the bridging gate for inducing electrons could leak to the electron ohmic contacts, especially after the device was illuminated by light sources such as a laser or white light. This leakage occured because the high bridging-gate threshold of $V_{th(\mathrm{BG})} = 21$ V required for inducing electrons was able to overcome the Schottky barrier at the bridging-gate bond pad, and cause a leakage current to the ohmic contacts via the quantum well. The high electric field from $V_{\mathrm{BG}} > 21$ V can accelerate electrons near the bond pad. These high-speed electrons (hot electrons) can excite electrons in the valence band to the conduction band and lead to hot-electron electroluminescence [107–110]. Figure 4.10(a) shows the EL when a leakage current greater than 600 uA appeared between the bridging gate ($V_{\mathrm{BG}} = 25$ V) and the electron ohmic contact ($V_{\mathrm{Source}} = -0.9$ V). As seen in Figure 4.10(b), the light signal was actually from the bridging gate bond pad. The leakage in the bond pad may be caused by electrical weak spots that had been created during wire bonding. This bridging-gate leakage issue indicated that induced ohmic contacts requiring high V_{BG} could be problematic, and a new design was needed to eliminate this potential leakage path.

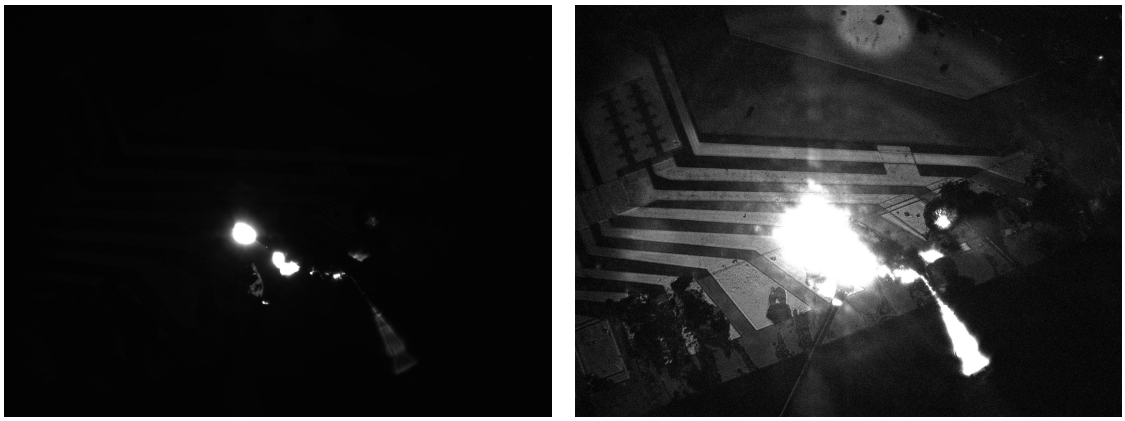

(a) (b)

Fig. 4.10 Images of EL when the bridging gate was leaking. (a) Emission spots were seen when a leakage current $> 600\,\mu$A occurred between the bridging gate and an ohmic contact. (b) Image with a longer exposure time shows that the emission comes from the bridging-gate bond pad.

4.2.8 SAW-suppressed Photoluminescence

A useful technique to test the generation of a SAW by the IDT is SAW-suppressed photoluminescence. In a photoluminescence (PL) measurement in the μPL cryostat, electron-hole pairs are created in the quantum well by optical excitation by a 633 nm HeNe laser. Figure 4.11(a) shows the PL spectrum of the 15 nm GaAs quantum well in wafer W1002 at 4 K. The main 1.536 eV (809 nm) peak is due to the transition of electrons from the conduction band to the first heavy-hole subband, and a secondary peak at 1.543 eV (805 nm) results from the transition of the conduction band to the second heavy-hole subband, based on the fact that the energy difference of the first and second heavy-hole subbnads is about 10 meV (Equation 2.1). If the position of laser excitation is on the path of a SAW beam, photo-excited electrons and holes will be separated and fall into the SAW potential minima and maxima respectively [79, 111, 112]. These separated electrons and holes will then be carried away by the SAW until the SAW potential becomes weaker or screened [79, 112]. As a consequence, the PL intensity at the position of excitation is suppressed due to the electron-hole separation by the SAW [79, 113]. In Figure 4.11(b), when the laser excitation is on the path of the SAW propagation, PL intensity as a function of frequency f_{RF} applied to the IDT at 12 dBm exhibits a clear dip at the IDT resonant frequency of 2.81 GHz, while the PL intensity is not modulated by the applied frequency when laser excitation is not on the path of SAW propagation. This result demonstrates that the presence and frequency of a SAW can be tested *in situ* by the SAW-suppressed PL in the μPL cryostat, which is useful for checking whether an enhanced S-D current in a frequency sweep matches the SAW frequency.

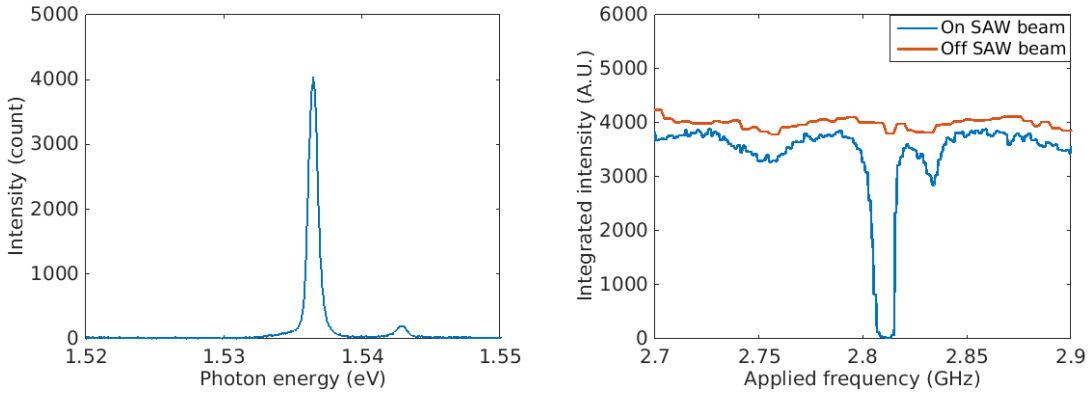

(a) (b)

Fig. 4.11 (a) Photoluminescence (PL) spectrum of the 15 nm GaAs quantum well in wafer W1002 at 4 K. The main peak is at 1.536 eV (809 nm), and the secondary peak is at 1.543 eV (805 nm). (b) Integrated PL intensity as a function of frequency f_{RF} applied to the IDT. When laser excitation is on the path of the SAW beam, PL intensity is suppressed at the IDT resonant frequency. When laser excitation is not in the path of the SAW beam, PL intensity shows no frequency modulation.

4.3 Improved Charge Constriction

After characterisation of the early-generation SAW-driven n-i-p junction YC02, the next batch of devices needed to overcome issues found in YC02. The two main issues were that (1) electrons and holes were not well confined so it was possible for recombination to happen in unexpected regions, and (2) the high bridging-gate thresholds $V_{th(\mathrm{BG})}$ required for inducing charges would possibly cause a large leakage current to the quantum well. Therefore, devices with a few design modifications were fabricated. From now on this batch will be referred to as TKH01, as it was the first batch made by the author.

4.3.1 TKH01 Device Design

In order to eliminate any unexpected current path between two ohmic groups, an ohmic-isolation etch pattern was designed to remove the quantum well in this pattern so that the only connection was through an etched 1D channel. Figure 4.12 shows the ohmic-isolation etch pattern along with the six ohmic groups. Each ohmic group is enclosed by the etch pattern, so a current between two ohmic groups, e.g. TR and BM, is only possible via a 0.8 μm wide 1D channel magnified in the green rectangle.

At the same time, to solve the issue of high $V_{th(\mathrm{BG})}$, the material for the ohmic-insulator was changed from polyimide (thickness $d_{\mathrm{insulator}} = 800\,\mathrm{nm}$, $\varepsilon = 3$) to Al_2O_3 ($d_{\mathrm{insulator}} =$

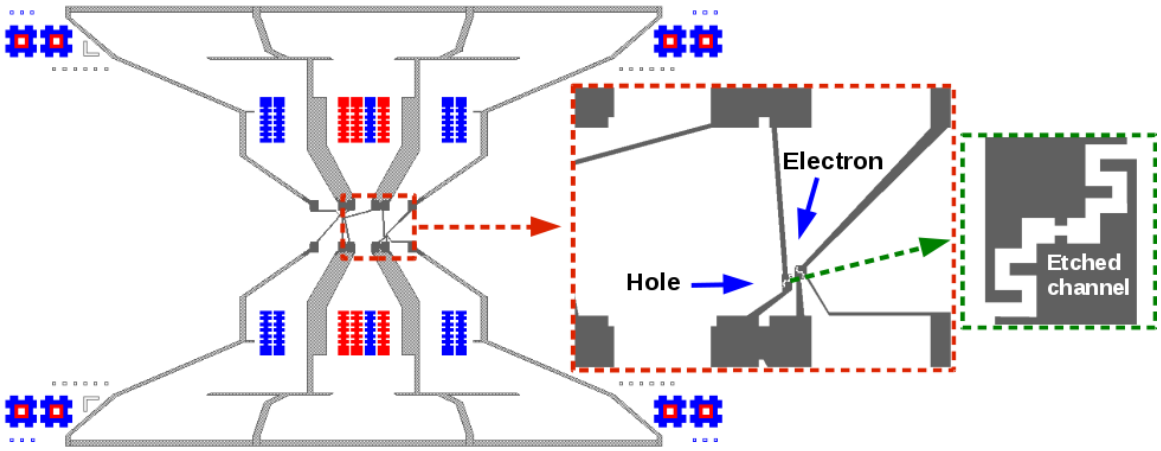

Fig. 4.12 Design of TKH01 showing p-type ohmic contacts (red regions), n-type ohmic contacts, and e-beam-defined etch pattern (grey region). The six ohmic groups are isolated from each other by etching away the quantum well in the etch pattern. The only path between two ohmic groups through which current could flow is along a narrow etched 1D channel with width $= 0.8\,\mu$m, where an n-i-p junction is formed. The current path between the top-right (TR) and the bottom-middle (BM) ohmic groups is highlighted by the red rectangle. Magnified designs of this path and the etched 1D channel are shown in the red rectangle and the green rectangle respectively.

100 nm, $\varepsilon = 10$) by ALD. The relatively smaller thickness and higher dielectric constant of Al_2O_3 lowered the required bridging-gate voltage. As a result, $V_{th(\mathrm{BG})} = 14$–21 V for electrons and -7 V for holes using the 800 nm polyimide were reduced to 1.2 V for electrons and -1.2 V for holes when the 100 nm Al_2O_3 was used. The well-controlled deposition of ALD also made the result more reproducible.

4.3.2 Electroluminescence from the n-i-p Junction

The characterisation of one device from batch TKH01 is presented here. The device was tested in the μPL cryostat in order to check if the ohmic-isolation etch could give rise to photon emission from the n-i-p junction. As with YC02, the bridging-gate charging issue still existed after charges had been induced. As shown in figure 4.13(a), when V_{BG} was fixed at -3 V, induced current in the BM ohmic group exponentially decayed with a time constant $\tau = 2$ s. The capacitance C of this bridging gate to the quantum well is estimated (from the dimension of the gate) to be 6.7×10^{-11} F. Since $\tau = RC$, the resistance R between the two is about 30 GΩ. Due to this charging issue, V_{BG} for inducing electrons and holes had to be continuously increased during measurements to maintain charge densities. After electrons and holes had been induced to form an n-i-p junction across an etched 1D channel, V_{SD}

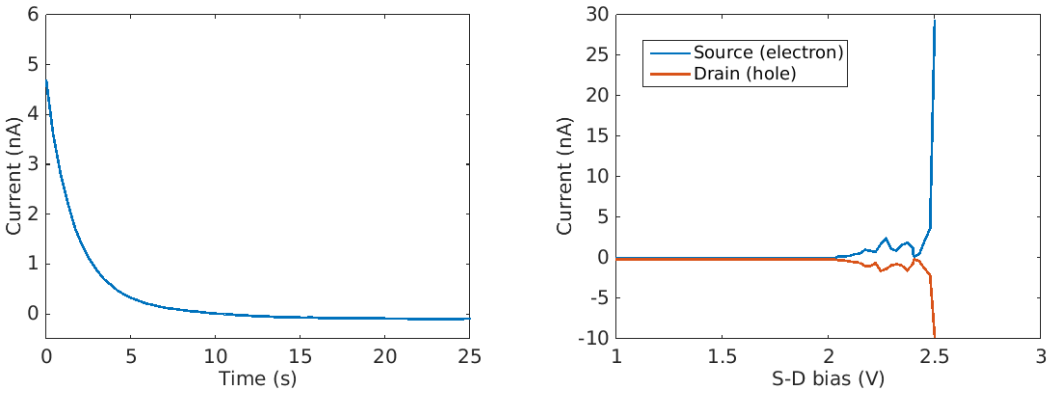

(a) (b)

Fig. 4.13 (a) Induced hole current as a function of time. The current decays with a time constant 2s after being induced. (b) S-D current I_{SD} as a function of S-D bias V_{SD}. The current appears at $V_{SD} > 2$ V.

was applied to the corresponding ohmic contacts to find the S-D bias threshold $V_{th(SD)}$. As seen in figure 4.13(b), S-D current I_{SD} only appeared at $V_{SD} > 2$ V, which is 0.5 V higher than the GaAs bandgap. This may be because the 0.8 μm 1D etched channel was so narrow that a high potential barrier was formed in the intrinsic region. Hence, a much greater V_{SD} than 1.5 V was required for a current to flow across the 1D channel. Besides, this S-D bias threshold would shift during a measurement and could become even as high as 6 V, possibly due to a charging effect. As a result, TKH01 could not be used to test SAW-driven charge transport.

When the potential barrier was overcome at high V_{SD}, EL could be observed from the n-i-p junction under forward bias. Figure 4.14(a) shows an image of the EL when $V_{SD} = 2.5$ V and $I_{SD} = 10$ nA. A bright spot was seen along with an L-shaped stripe of emission. The spectrum of this EL signal in figure 4.14(c) indicates that electrons and holes recombined in the quantum well. Compared with an image of the device at the same position (Figure 4.14(b)), it can be seen that the bright spot originated from the n-i-p junction that was under forward bias, meaning the ohmic-isolation etch did confine the current flow path. As for the L-shaped signal, this was due to electron-hole recombination along the surface gate for inducing holes. This means that electrons with extra energies could enter the other side of the n-i-p junction without recombining with holes near the junction. They could move further in the wide intrinsic region, and finally recombine with holes under the surface gate. Hence, it might be necessary to confine electrons to a micrometre-size area when they arrive at the region of holes, so that most photon emission can be collected in this small area. This

is important especially in the black helium-3 system since the lens assembly can only collect photon emission from a $2\,\mu\mathrm{m}^2$ area.

4.4 Enhanced SAW-driven Charge Transport and Electroluminescence

The third batch of SAW-driven n-i-p junction devices was fabricated to deal with the issues found in YC02 and TKH01. In addition, a more sophisticated gate design was introduced in the hope of providing more flexibility in the device characterisation. A ZnO thin film was also deposited to enhance the strength of the SAW. This third batch is referred to as TKH02 in this thesis. In addition, time-resolved measurements were performed on a device from this batch, which will be discussed in Chapter 5.

4.4.1 TKH02 Device Design

The design of TKH02 is shown in Figure 4.15. As with TKH01, an ohmic-isolation etch ,shown in Figure 4.15(a), was used to ensure a current could only flow through the n-i-p junction. In addition, due to the bridging-gate leakage issue found in YC02, extra etched features, as shown in Figure 4.15(b), were created around bond pads for bridging gates, surface gates, and side gates to eliminate any path for leakage from these bond pads to the ohmic contacts. Figure 4.15(c) shows a magnified design of a SAW-driven n-i-p junction. The width of the 1D channel was increased to $1.2\,\mu$m to improve the electrical conductance. Two pairs of side gates were patterned in the etched region next to the 1D channel so that the potential in the intrinsic region (the 1D channel) could be adjusted with greater flexibility. Extra barrier gates were introduced in the hope of confining electrons to the region of holes once they had arrived. The idea is to apply a barrier-gate voltage V_{Bar} that is more negative than the surface-gate voltage V_{SG} in the region of holes, and a potential barrier surrounding the region of holes is thus formed to stop the electrons leaving the junction once they arrive in the region of holes. Hence, these confined electrons should then recombine with holes in the junction so that photon emission will be concentrated in a small area, which is important for a system with a small field of view like the black helium-3 system. Micrometre-size hollows enclosed by a surface gate and a barrier gate were also created for the same reason. Figure 4.15(d) shows another junction design in TKH02. This n-i-p junction has the same gate structure as that in Figure 4.15(c), but with an extra maze channel along the surface gate and the barrier gate in the region of holes. This elaborately-shaped channel, created by wet

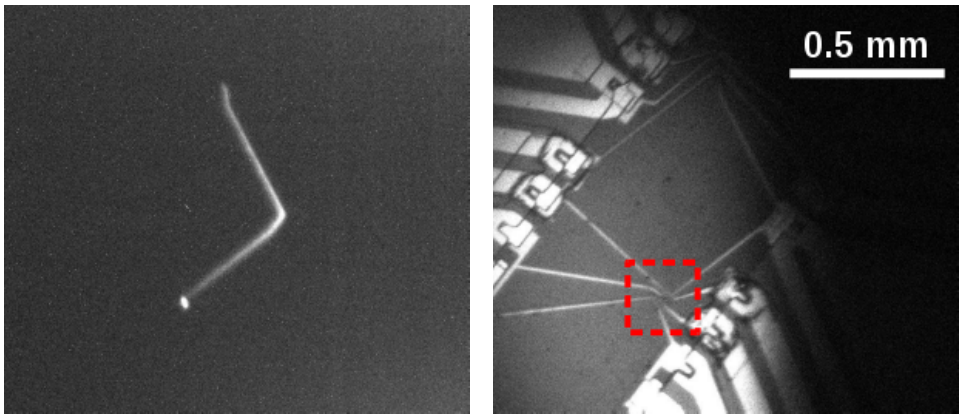

(a) (b)

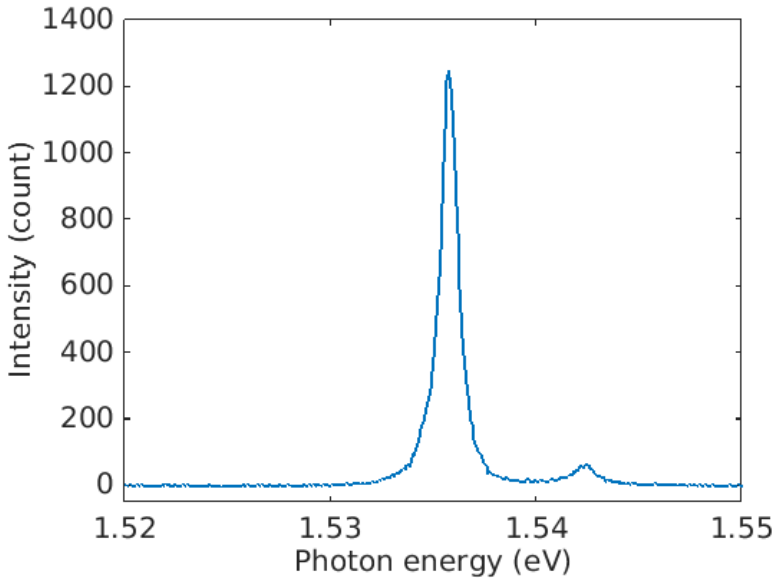

(c)

Fig. 4.14 EL from the n-i-p junction. (a) Image of the EL when $V_{SD} = 2.5$ V, $I_{SD} = 10$ nA. A bright spot and an L-shaped stripe can be seen. (b) Image of the device at the same position as (a). The n-i-p junction under forward bias is highlighted by the red rectangle. The bright spot and the L-shape band in (a) correspond to the n-i-p junction and the surface gate for holes respectively. (c) Spectrum of the EL showning an 1.536 eV (809 nm) main peak and an 1.543 eV (805.5 nm) secondary peak, corresponding to the emission peaks of the quantum well.

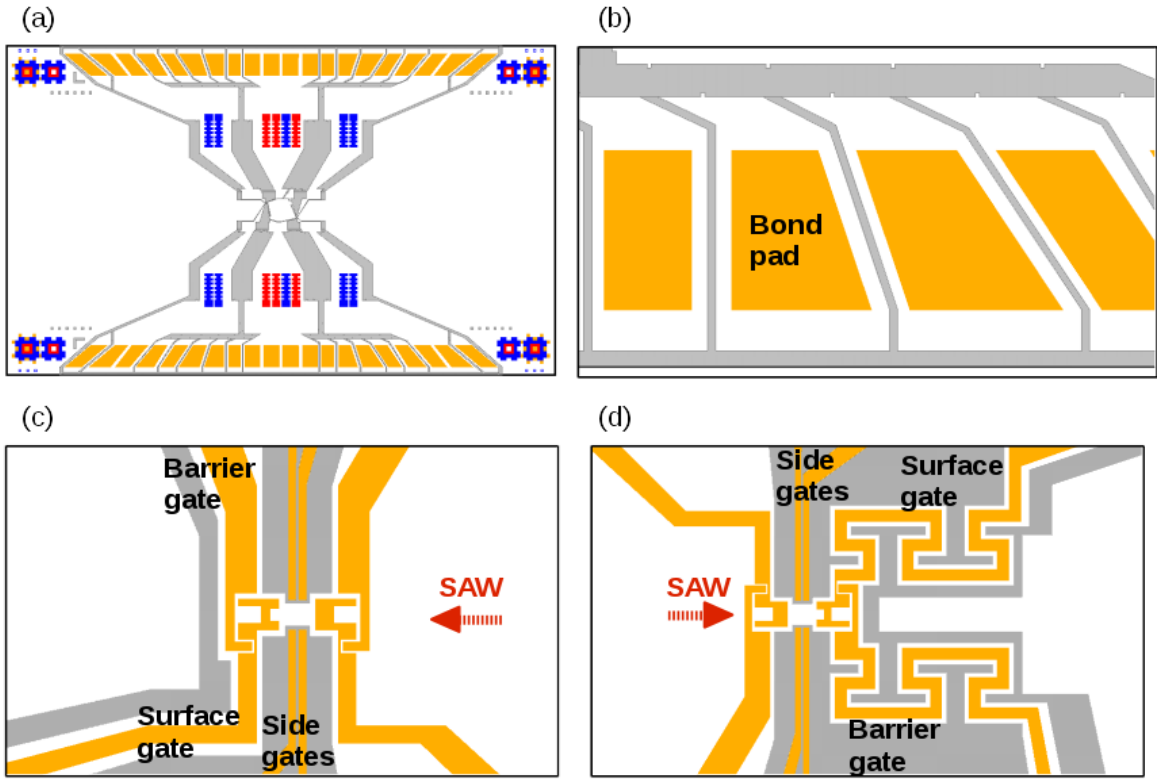

Fig. 4.15 Device design of TKH02. (a) Overview of TKH02 showing ohmic contacts (red and blue regions), bond pads (yellow regions), and e-beam-defined etch pattern (grey regions). (b) Magnified design near bond pads. Etched features are created around bond pads for all the gates to eliminate paths for leakage. (c) Magnified design of a SAW-driven n-i-p junction. The narrowest channel width is 1.2 μm. Two pairs of side gates are patterned to adjust the potential in the 1D channel. Barrier gates are introduced in the hope of confining electrons in the region of holes. (d) Design of the other junction on TKH02. A maze channel for a surface gate and a barrier gate is created by wet etching to reflect ballistic electrons once they arrive in the region of holes.

etching, was designed to cause multiple reflections of ballistic electrons in order to confine them near the n-i-p junction.

In TKH02, a ZnO thin film of 800 nm was deposited on the device discussed in the following paragraphs, in order to enhance the SAW-driven charge transport [94, 95]. The deposition of ZnO was performed using the HiTuS machine by Miss Kham M. Niang. A 20 nm Al_2O_3 thin film was deposited using ALD by Mr Benjamin Ramsay before the ZnO to protect the 2DEG and 2DHG [93].

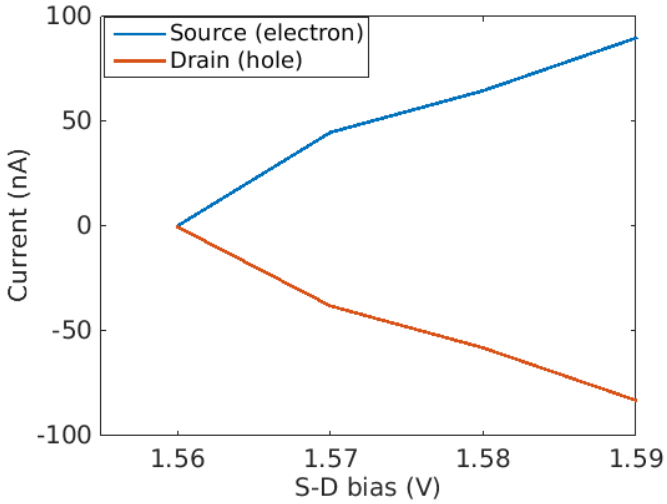

Fig. 4.16 S-D current as a function of S-D bias. The current appears at $V_{\mathrm{SD}} > 1.56$ V.

4.4.2 Electroluminescence under DC Forward Bias

TKH02 was measured in the μPL cryostat. The bridging-gate charging issue was also observed. Hence, V_{BG} needed to be constantly increased to maintain sufficient charge densities near the n-i-p junction. In addition, leakage currents from each surface to the corresponding ohmic contact were observed on both sides of the junction, presumably due to metal-semiconductor inter-diffusion. Therefore, the true S-D current across the n-i-p junction had to be measured by monitoring the surface-gate leakage currents using a multi-channel current pre-amplifier. To collect more photons from the junction, a 50X microscope objective with $NA = 0.55$ was used in the optical system. Figure 4.16 shows I_{SD} as a function of V_{SD}. The threshold $V_{th(\mathrm{SD})}$ at which I_{SD} appears is 1.56 V, which is close to the GaAs bandgap of 1.52 V at 4 K. Also, $V_{th(\mathrm{SD})}$ of 1.56 V was reproducible in the measurements. This indicates that the wider channel width of 1.2 μm makes the n-i-p junction more conductive compared with that of TKH01.

When an S-D bias $V_{\mathrm{SD}} > V_{th(\mathrm{SD})}$ was applied to the n-i-p junction, EL was observed at the junction. Figure 4.17(a) shows a CCD camera image of the EL when $V_{\mathrm{SD}} = 1.6$ V, and Figure 4.17(b) shows a camera image of the junction at the same position using external sub-bandgap illumination to avoid the creation of extra surface charges. When these two images are compared, the EL bright spot corresponds to the n-i-p junction, and the spot size is about 1 μm in diameter. Therefore, electron-hole recombination occurred exclusively at the n-i-p junction when $V_{\mathrm{SD}} = 1.6$ V. However, the spectrum of this EL signal shown in figure 4.17(c) has a peak at 1.531 eV (811.5 nm), rather than the usual quantum-well emission of 1.536 eV (809 nm). One possible explanation for this EL shift is that surface charges

induced by incompletely-oxidised Zn in the ZnO led to band bending, which caused a red shift in the spectrum [114]. Another possible reason for this EL shift is that the surface-gate leakage currents gave rise to electron-hole recombination in the GaAs cap layer or the surface. The true origin of this EL shift will require further study.

4.4.3 SAW-driven Charge Transport and Electroluminescence

After characterisation under a DC forward bias, V_{SD} was set to 1.45 V ($V_{\mathrm{source}} = -0.8$ V and $V_{\mathrm{drain}} = 0.65$ V), which is 100 meV below $V_{th(\mathrm{SD})}$. SAW-driven charge transport and EL were then tested by applying a RF signal to an IDT. Figure 4.18(a) and (b) shows S-D current I_{SD} and EL as a function of frequency applied to the n-i-p junction when $P_{\mathrm{RF}} = 11$ dBm and $V_{\mathrm{SiG}} = -1.6$ V. Enhanced S-D current I_{SD} and EL both appeared at around the frequency $f_{\mathrm{RF}} = 2.64$ GHz, which was the resonant frequency of the IDT. This resonant frequency of 2.64 GHz in the ZnO-deposited TKH02 is different from the resonant frequency of 2.8 GHz in YC02 because of the reduced effective speed of sound in the GaAs-ZnO layer structure [94]. The enhanced I_{SD} and EL when a SAW was generated indicate that electrons were pumped by the SAW across the n-i-p junction and recombined with holes. Interestingly, this SAW-driven EL exhibited a different spectrum from the EL under high forward bias. This spectrum of the SAW-driven EL in figure 4.18(c) shows a stronger peak at 1.536 eV (809 nm), the quantum-well emission, and a secondary peak at 1.530 eV (812 nm), which is close to the peak in the spectrum under forward bias. This result suggests that applying a SAW can suppress the 1.530 eV (812 nm) peak, which is possibly related to surface charges, and restore the quantum-well emission of 1.536 eV (809 nm). Since the amplitude of the SAW is higher at the surface, this may be explained by the SAW clearing some of the surface charges and therefore recovering normal quantum-well emissions.

This ZnO-enhanced SAW amplitude also resulted in an interesting feature when high RF power was applied to the IDT. Figure 4.19(a)–(c) show the dependence of SAW-driven I_{SD} and EL on RF power P_{RF} applied to the IDT. In Figure 4.19(a) and (c), SAW-driven source (electron) current and EL were suppressed at the resonant frequency of 2.64 GHz and thus split into two peaks at $P_{\mathrm{RF}} > 12$ dBm. This unexpected splitting may have occurred because the strong SAW amplitude modulated the density of holes. When a SAW carrying electrons in its potential minima arrives at the region of holes, these potential minima also lower the valance band in this region so that the density of holes will be reduced. As a result, when a strong SAW is generated by applying a high-power RF signal, electrons and holes will be separated in space, and electron-hole recombination is thus suppressed. However, the suppression of I_{SD} was not observed in the drain (holes) current shown in Figure 4.19(b), which should match the source current in Figure 4.19(a). This indicates that there was

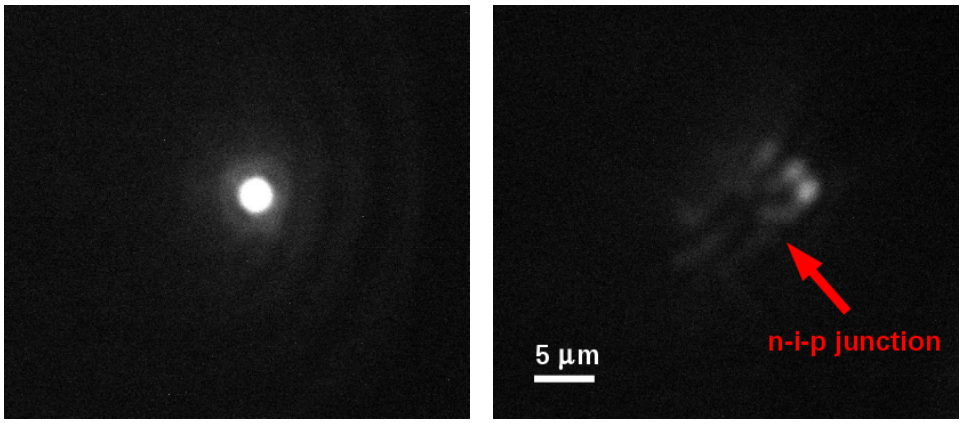

(a) (b)

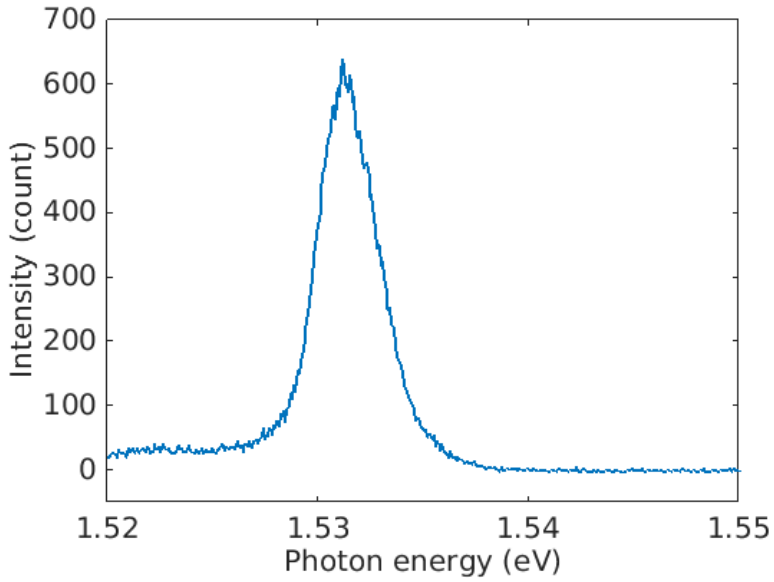

(c)

Fig. 4.17 (a) Image of EL when $V_{SD} = 1.6$ V is applied to an n-i-p junction. (b) Image of the n-i-p junction using external sub-bandgap illumination. The junction pointed by the arrow is determined by comparing this image with images using brighter illumination. (c) Spectrum of the EL signal showing a peak at 1.531 eV (811.5 nm). A small bump at 1.522 eV (816 nm) is possibly related to bulk GaAs.

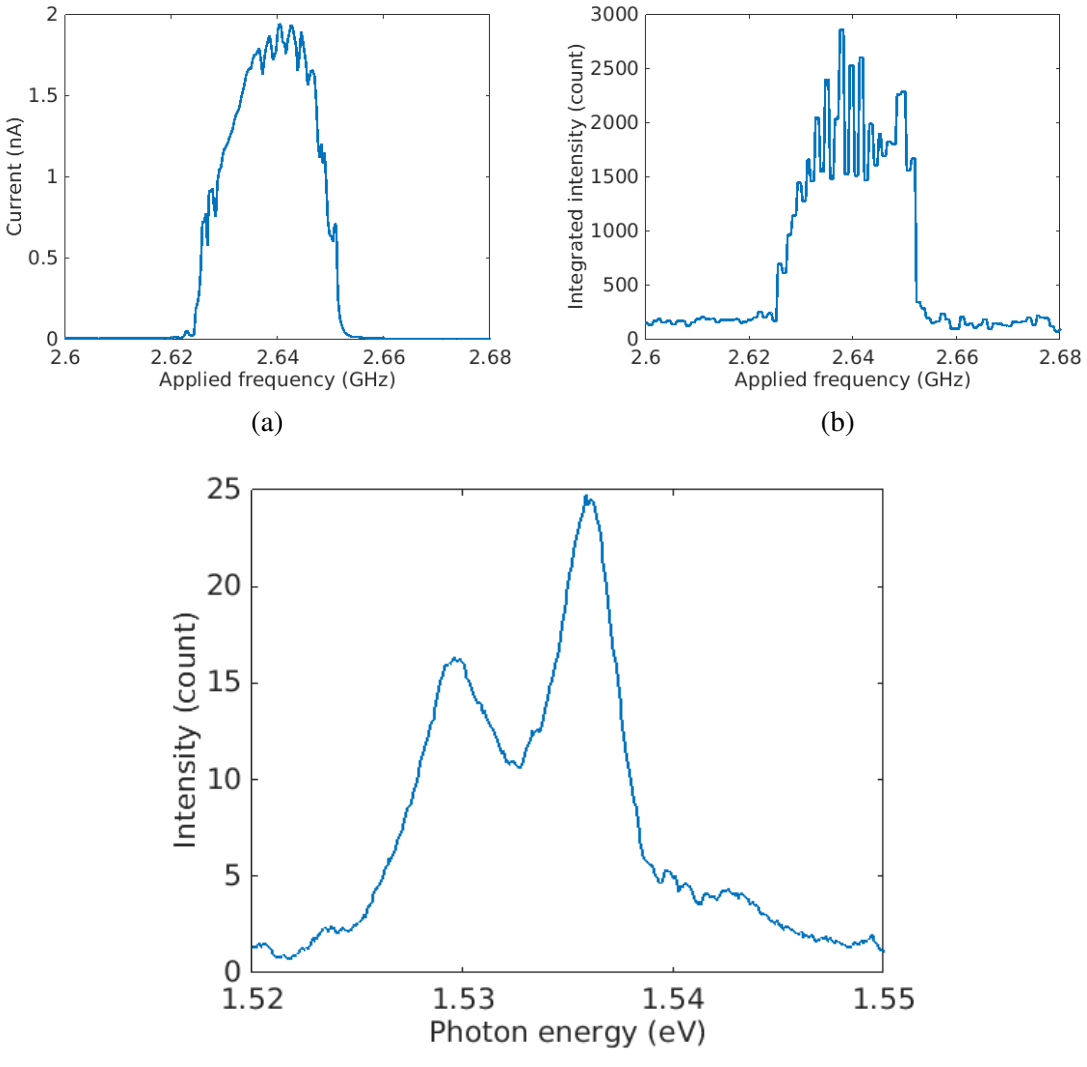

(a) (b)

(c)

Fig. 4.18 (a) I_{SD} as a function of frequency applied to the IDT. (b) EL as a function of frequency applied to the IDT. (c) Spectrum of the SAW-driven EL showing a main peak at 1.536 eV (809 nm) and a secondary peak at 1.530 eV (812 nm).

leakage at the n-i-p junction, although it was not detected as leakage current to any of the gates. This undetectable leakage might be related to a leakage path to the IDT, which will be discussed later.

4.4.4 Photon Emission Efficiency of SAW-driven Electroluminescence

The SAW-driven charge transport and EL can also be modulated by varying side-gate voltages V_{SiG}. In Figure 4.20(a), where $V_{\mathrm{SD}} = 1.45$ V, $P_{\mathrm{RF}} = 11$ dBm and frequency $f_{\mathrm{RF}} = 2.63$ GHz, the I_{SD} maximum at around $V_{\mathrm{SiG}} = -1$ V suggests that the potential slope in the 1D channel is minimised at this side-gate voltage. However, the EL signal exhibits a different dependence on V_{SiG}. The EL intensity increases when V_{SiG} is more negative until the side gates leak to the quantum well at $V_{\mathrm{SiG}} = -1.7$ V. By comparing I_{SD} and EL in Figure 4.20(a), it can be seen that the photon emission efficiency is modulated by V_{SiG}.

The photon emission efficiency η_{emit} (or internal quantum efficiency) can be described as the ratio of N_{ph}, the number of photons that can be collected, to N_{rcb}, the number of recombined electron-hole pairs. In an experiment, η_{emit} can be determined from

$$N_{\mathrm{detect}} = N_{\mathrm{rcb}} \times \eta_{\mathrm{collect}} \times \eta_{\mathrm{emit}}\,, \tag{4.3}$$

where N_{detect} is the number of detected photons, and η_{collect} is the photon collection efficiency of the optical setup. N_{detect} can be obtained by $N_{\mathrm{detect}} = N_{\mathrm{count}} \times D_{\mathrm{sens}}$, where N_{count} is the total number of counts and D_{sens} is the sensitivity of the detector. Also, N_{rcb} from a current I_{SD} in a time period t can be calculated using $N_{\mathrm{rcb}} = t \times I_{\mathrm{SD}}/e$, where e is the unit charge. In the μPL cryostat, the overall photon collection efficiency η_{collect} with the 50X microscope objective and two beamsplitters is $0.5 \times 0.5 \times 0.45\% = 0.11\%$, and the sensitivity of the detector in the spectrometer is 15%. Given that the EL intensity in Figure4.20(a) was detected with an exposure time of 1 s, the photon emission efficiency η_{emit} at each V_{SiG} was calculated and plotted in Figure 4.20(b). η_{emit} exponentially increases as V_{SiG} becomes more negative, and the highest η_{emit} is 0.3% at $V_{\mathrm{SiG}} = -1.7$ V. A possible explanation is as follows: when a V_{SG} is applied to induced holes, most holes are induced underneath the surface gate, which consists of by 15 nm Ti/Au. If electrons recombine with these holes, most photons will be reflected by the surface gate and will not be seen by the optical setup. Nonetheless, when a negative V_{SiG} is applied, holes can further extend outside the surface gate. Photons generated by electrons recombining with these holes are visible without reflection by the surface gate. As a consequence, η_{emit} is higher at a more negative V_{SiG}.

Although η_{emit} can be modulated by V_{SiG}, the maximum η_{emit} of 0.3% is still very low. This may be attributed to non-radiative recombination mechanisms in the n-i-p junction. For

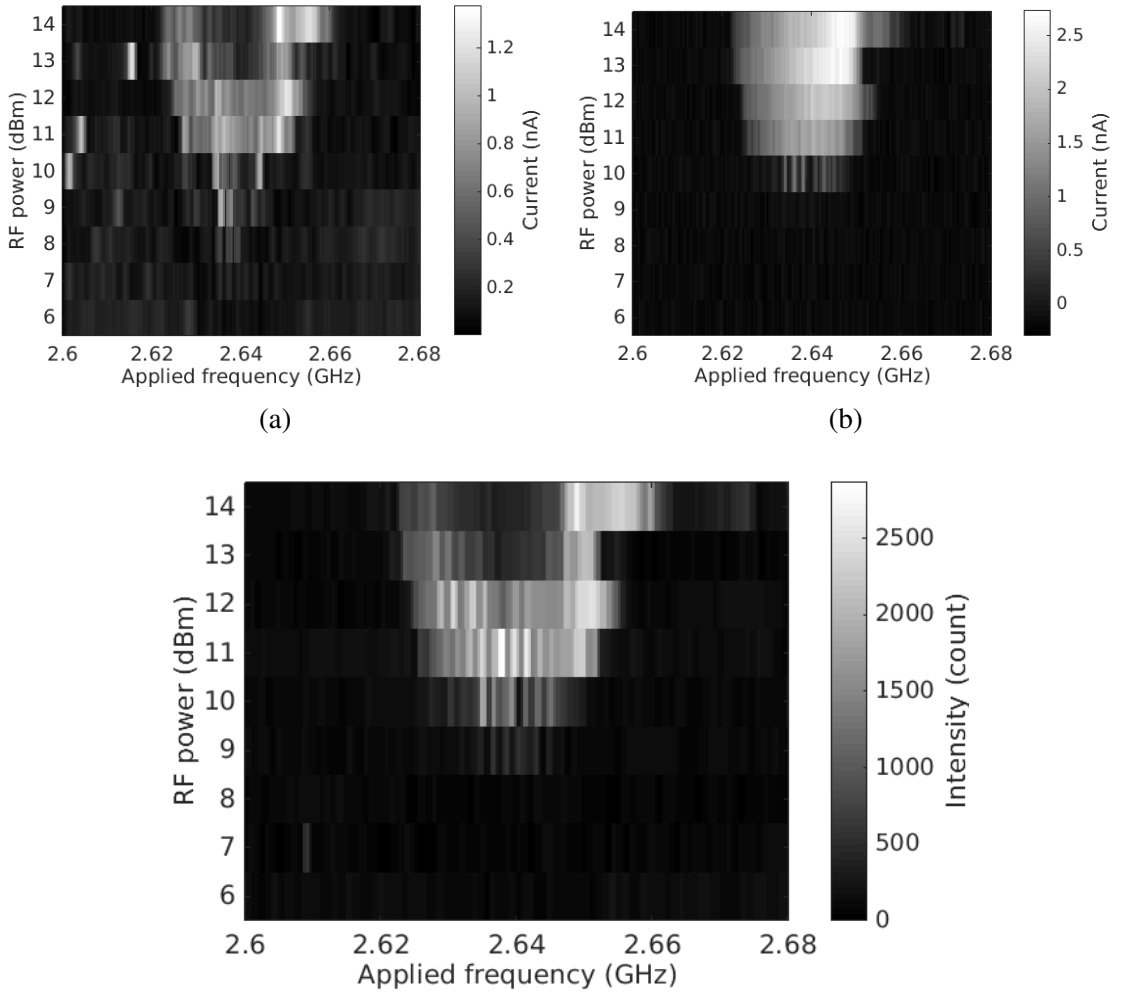

Fig. 4.19 Dependence of SAW-driven I_{SD} (a) from the region of electrons (source) and (b) into the region of holes (drain) on RF power P_{RF} applied to the IDT. (c) Dependence of SAW-driven EL on P_{RF}. Suppression of I_{SD} and EL at the resonant frequency for $P_{RF} > 12$ dBm is observed in (a) and (c), but not in (b).

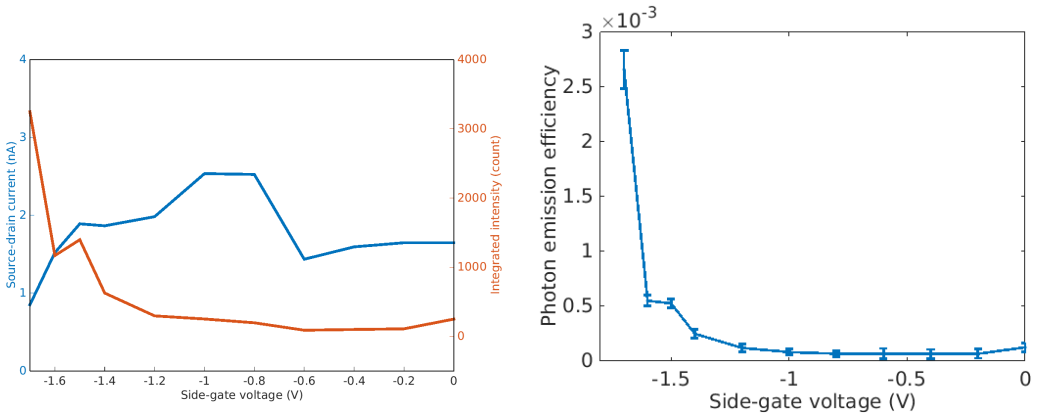

(a) (b)

Fig. 4.20 (a) SAW-driven I_{SD} and EL as a function of side-gate voltage V_{SiG}. (b) Photon emission efficiency η_{emit} calculated from (a) as a function of V_{SiG}.

example, the air-exposed GaAs quantum well on the etched edges can lead to a high density of surface states due to Fermi-level pinning [115, 116]. These surface states are able to cause non-radiative surface recombination and suppress radiative recombination by more than one order of magnitude [116–119]. The true origin of the low photon emission efficiency and methods for its improvement require more investigation.

Barrier gates were designed to provide better confinement of electrons once they arrive at the region of holes. η_{emit} as a function of barrier-gate voltage V_{Bar} is shown in Figure 4.21, where $V_{SG} = -0.8\,V$ (relative to V_{drain}). There is no obvious trend in η_{emit} when V_{Bar} is changed from $-0.8\,V$ to $-1.4\,V$, which is $-0.6\,V$ relative to V_{SG}. However, it was found that the surface gate and the barrier gate were shorted together with a resistance of $1\,M\Omega$. As a result, a potential difference between these two gates could not be established, which could explain why no modulation of V_{Bar} was observed.

4.4.5 Leakage Current Between Ohmic Contacts and IDT

In TKH02, a leakage current between the bottom-right (BR) n-type ohmic group and the right-hand-side IDT was found, especially after the device had been illuminated. Ideally, this should not happen as there was a millimetre-wide intrinsic region between them. Nevertheless, since there was no etched feature between the BR ohmic group and the right IDT, the quantum well was continuous between these two. As a result, a conductive path could be formed if impurities or defects in the AlGaAs were ionised by the illumination and caused charges trapped in the quantum well [120–122], or photo-excited charges flooded the original intrinsic region. Interestingly, the leakage current could be largely reduced by launching a SAW for

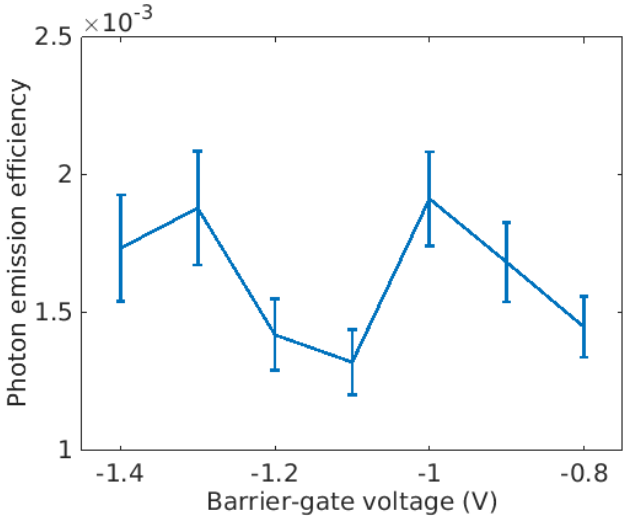

Fig. 4.21 Photon emission efficiency η_{emit} as a function of barrier-gate voltage V_{Bar}.

ten minutes. This may be understood as the SAW clearing some of these trapped charges. Although the current could be reduced, the residual conductance could still contribute to a direct coupling of an RF signal to the n-i-p junction, which will be shown in Chapter 5. Therefore, a physical disconnection between the BR ohmic contacts and the right IDT is necessary.

4.5 Optimised SAW-driven n-i-p Junction

After the characterisation of the previous three batches, the final batch TKH03 was fabricated by the author to optimise the design of the SAW-driven n-i-p junction and solve critical issues found in the previous batches. Time-resolved measurements and autocorrelation measurements were carried out on a device from TKH03, which will be presented in Chapters 5 and 6.

4.5.1 TKH03 Device Design

Figure 4.22(a) and (b) show the design of a SAW-driven n-i-p junction in TKH03. The structure of the gates (see Figure 4.22(b)) is the same as that in TKH02. Compared with TKH02 (see Figure 4.15(c)), an etched trench was added to the right-hand side of the junction to eliminate the leakage path to the IDT found in TKH02. This modification gave rise to a purely SAW-driven EL in time-resolved measurements, which will be presented in Chapter 5. In addition, to carry out time-resolved measurements and autocorrelation measurements where the timing resolution is a limiting factor, IDTs with a lower resonant frequency of

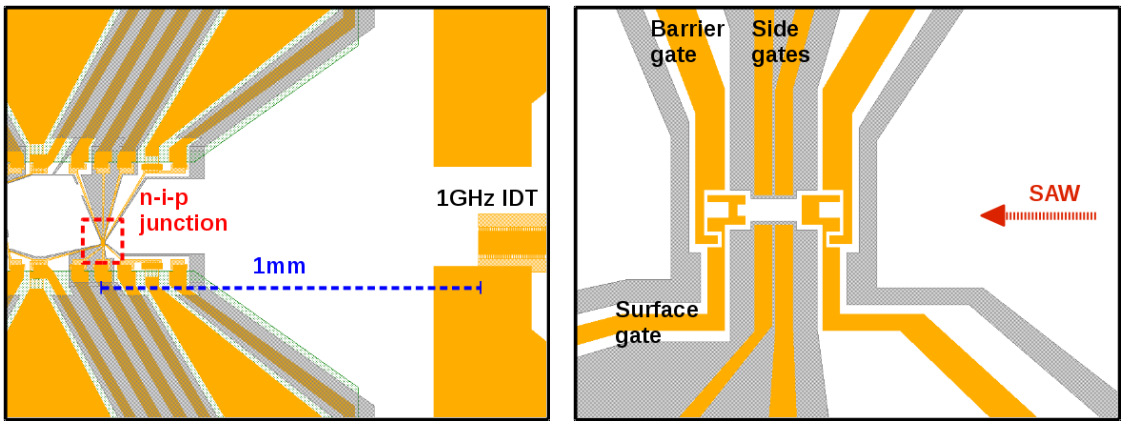

(a) (b)

Fig. 4.22 (a) Design showing a SAW-driven n-i-p junction (highlighted by the red rectangle) and the 1 GHz IDT for launching SAWs. The distance between the n-i-p junction and the IDT is about 1 mm. (b) Magnified design of the n-i-p junction. An etched trench on the right-hand side is added to eliminate the IDT-leakage issue.

1 GHz, rather than the 3 GHz of previous batches, were made on some devices in TKH03. The length of the 1D channel was thus increased to 2.5 μm if the corresponding n-i-p junction was driven by a 1 GHz IDT. ZnO deposition was not carried out in TKH03 due to the possible charging effect found in TKH02.

4.5.2 Characterisation under DC Forward Bias

Because the EL had been observed exclusively in a micrometre-size area near the n-i-p junction in TKH02, it should be possible for the lens assembly in the black helium-3 cryostat with a field of view of 2 μm^2 to collect most of the photon emission. Therefore, a device from TKH03 was measured in the black helium-3 cryostat as this cryostat uses helium more efficiently and is more suitable for measurements over longer period of time. One major advantage to the black helium-3 cryostat is the vanishing of the bridging-gate charging issue. Since the sample space in the black helium-3 cryostat is a totally dark environment, there is no stray light that can potentially lead to surface charging. Presumably as a result of this, the bridging-gate charging issue was not observed in TKH03. Figure 4.23(a) shows the induced current as a function of bridging-gate voltage V_{BG}. I_{SD} appears at $V_{\mathrm{BG}} < -1.5$ V, where holes are induced, and the forward and backward sweeps exhibit no significant hysteresis. Figure 4.23(b) shows induced current as a function of time when $V_{\mathrm{BG}} = -2$ V. The current remained fairly constant over 5 minutes. Figure 4.23(a) and (b) both indicate that there was no bridging-gate charging issue when this device was measured in the black helium-3

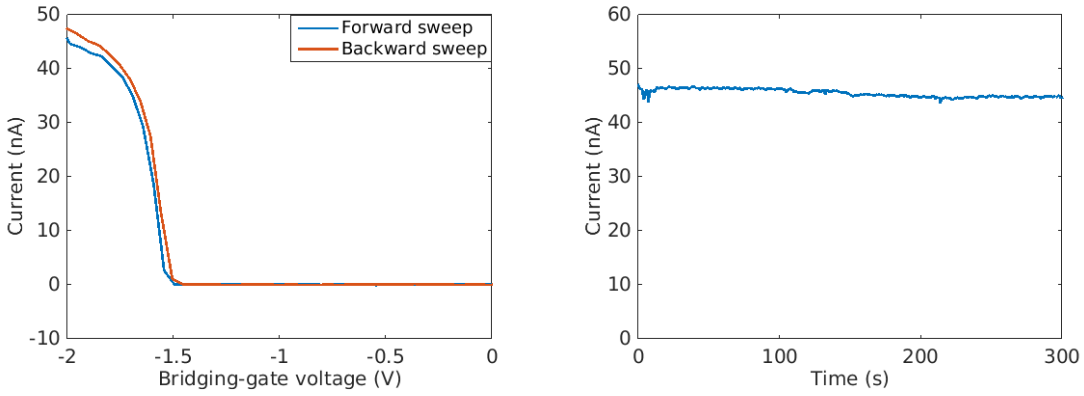

(a) (b)

Fig. 4.23 (a) Induced current as a function of V_{BG}. The current in the forward sweep matches that in the backward sweep. (b) Induced current as a function of time. The current stays at 45 nA over a period of 300 seconds.

cryostat. This meant that V_{BG} did not need to be constantly increased so the device can be characterised over a long period of time.

After electrons and holes had been induced by the surface gates, V_{SD} was applied to the n-i-p junction to find the threshold $V_{th(\mathrm{SD})}$. In Figure 4.24, I_{SD} appears at $V_{\mathrm{SD}} > 1.54$ V, which is very close to the GaAs bandgap 1.52 V at 4 K. The lens assembly was moved by the piezoelectric positioner to find the n-i-p junction and collect the photon emission. Figure 4.25(a) shows a scanned image of the n-i-p junction using the 785 nm pig-tail laser. Although the image is distorted because of an imperfect asymmetry calibration for the piezoelectric positioner, all the gates and etched features can be resolved in the image. After the n-i-p junction had been located, a 2D mapping was performed to search for the EL signal. Figure 4.25(b) shows the 2D mapping of EL when the lens assembly was in focus and $V_{\mathrm{SD}} = 1.6$ V. A bright spot with diameter 0.8 μm was seen in a 10 μm$\times$10 μm area. This indicates that the emissions were only from the n-i-p junction. In Figure 4.25(c) and (d), the lens assembly was moved from the device along the Z axis by roughly 1 μm and 2 μm respectively. The bright spot became broader as the lens assembly was de-focused. These images demonstrate that the combination of the lens assembly and the piezoelectric positioner is able to search for an EL signal if it is concentrated in a small area.

The spectrum of the EL is shown in Figure 4.26, where $I_{\mathrm{SD}} = 1$ μA. A main peak can be seen at 1.534 eV (810 nm). Since the left shoulder of the main peak is higher than the right shoulder, there should be a secondary peak at 1.541 eV (806.5 nm). Note that these two emission peaks are different from the quantum-well spectra measured in the μPL cryostat (see Figure 4.14). However, in Figure 4.26 the difference between the main peak and the

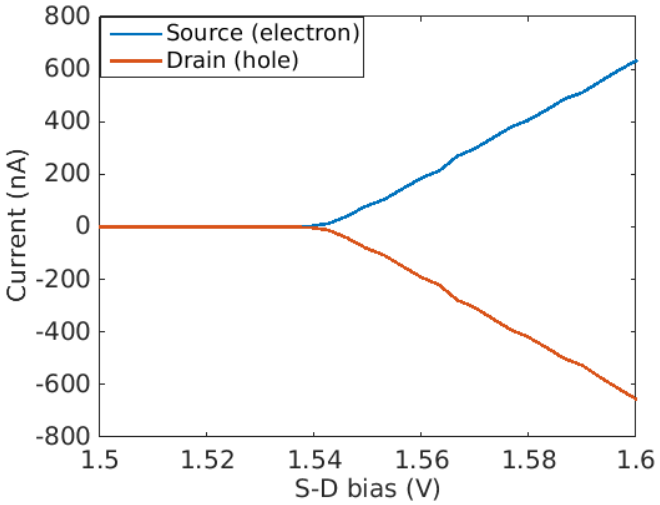

Fig. 4.24 S-D current as a function of V_{SD}.

secondary peak is 3.5 nm, which is the same as the difference in Figure 4.14 (with the main peak at 809 nm and the secondary peak at 805.5 nm). This suggests that the spectrum in Figure 4.26 has shifted by 1 nm in wavelength compared with Figure 4.14. One explanation for this shift is the misalignment of the single-mode fibre to the spectrometer. When the spectrum in Figure 4.26 was taken, the setup of the spectrometer had a linear dispersion of 2 nm/mm. This linear dispersion means that if the incident light was misaligned by 1 mm at the slit of the spectrometer, the resulting spectrum will shift by 2 nm. The slit was set to 0.5 mm when Figure 4.26 was taken. As a result, the maximum possible shift in wavelength was 1 nm, which may explain the shift in Figure 4.26. The large FWHM of 2.5 nm, corresponding to an uncertainty of 5 meV in photon energy, is possibly due to a heating effect from the high current $I_{SD} = 1\,\mu$A at $V_{SD} = 1.6$ V.

4.5.3 SAW-driven Charge Transport and Electroluminescence

To test SAW-driven charge transport and EL, the lens assembly was moved to the n-i-p junction to collect photon emission from electron-hole recombination. V_{SD} was set to 1.45 V, which was 100 mV below $V_{th(SD)}$, so there should be no current or photon emission unless electrons were driven by a SAW to reach the region of holes across the n-i-p junction. Regarding the resonant frequency of the IDT, given that the periodicity of the IDT is 2.5 μm and the SAW velocity is about 2800 m/s, the resonant frequency should be about 1.1 GHz. Figure 4.27(a) shows I_{SD} as a function of frequency f_{RF} applied to the IDT when $P_{RF} = 9$ dBm and $V_{SiG} = -0.75$ V. At the resonant frequency of 1.163 GHz, a SAW is launched from the IDT and carries electrons to the region of holes, an enhanced I_{SD} is thus seen in Figure 4.27(a).

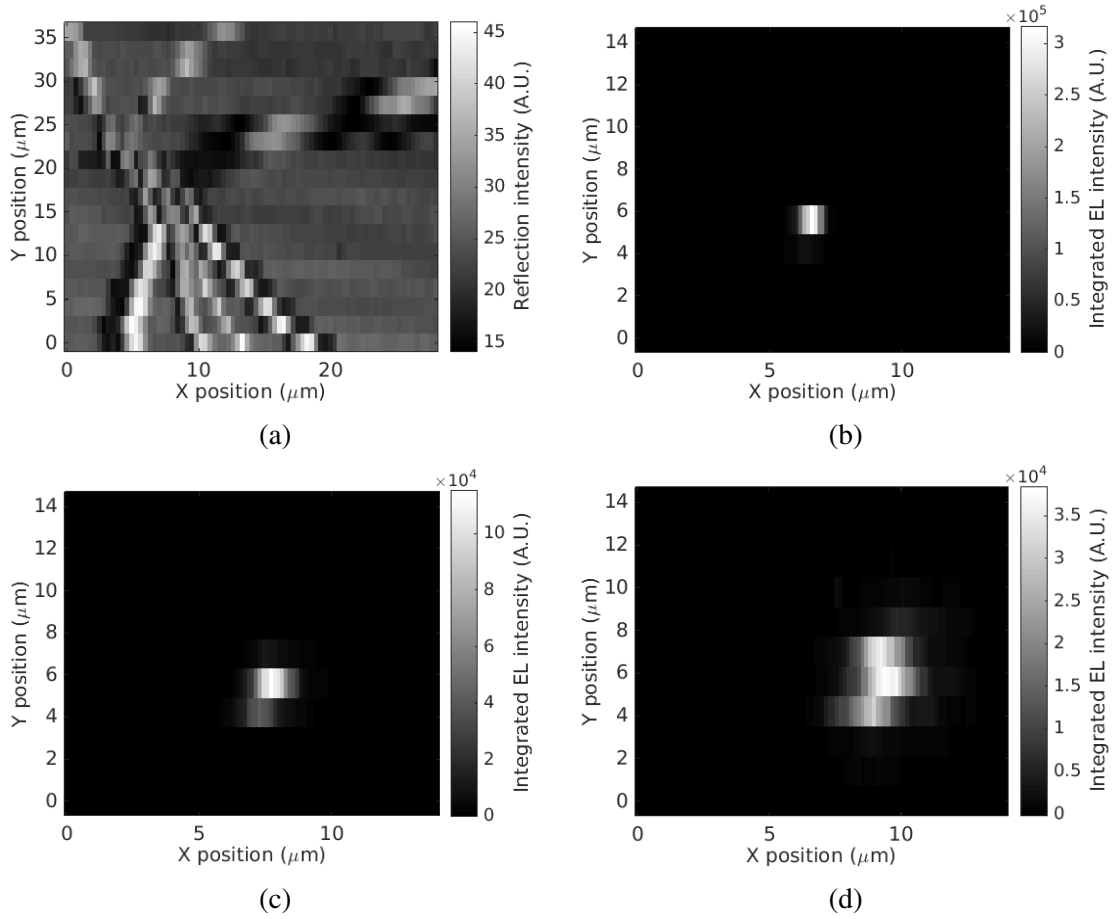

Fig. 4.25 (a) Scanned image of an n-i-p junction using an external 785 nm laser. (b) 2D mapping of EL signal near the n-i-p junction when the lens assembly is focused and $V_{SD} = 1.6$ V. Diameter of the bright spot is $\simeq 0.8\,\mu$m. (c) 2D mapping of EL signal when the lens assembly is raised by $\simeq 1\,\mu$m from the focal point and $V_{SD} = 1.6$ V. Diameter of the bright spot is $\simeq 1.5\,\mu$m. (d) 2D mapping of EL signal when the lens assembly is raised by $\simeq 2\,\mu$m from the focal point and $V_{SD} = 1.6$ V. Diameter of the bright spot is $\simeq 2\,\mu$m.

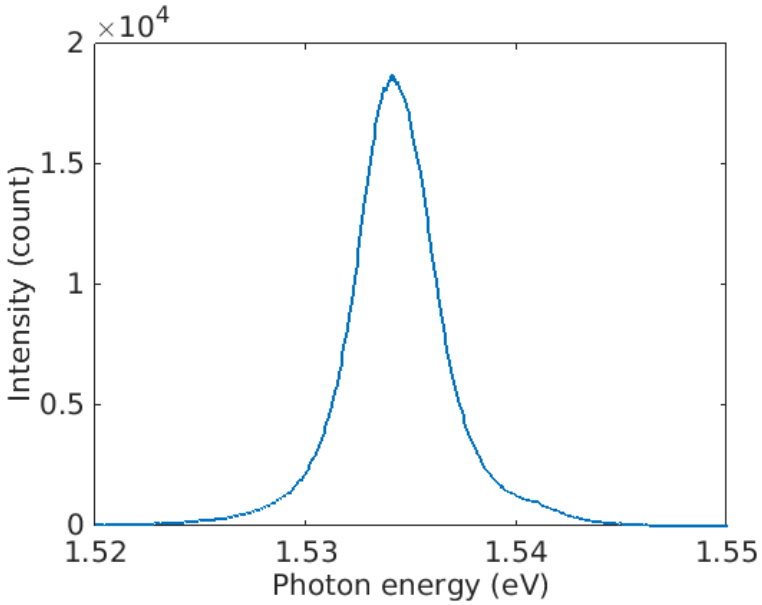

Fig. 4.26 Spectrum of EL when $V_{SD} = 1.6$ V. The main peak is at 1.534 eV (810 nm). A possible secondary peak is at $\simeq$ 1.541 eV (806.5 nm).

In addition, these electrons will then recombine with holes and generate photons with an energy corresponding to the bandgap of the quantum well. In Figure 4.27(b), the EL intensity shows a peak at the same frequency as the I_{SD} enhancement in Figure 4.27(a), meaning the SAW-driven I_{SD} leads to electron-hole recombination at the n-i-p junction. The spectrum of this SAW-driven EL is shown in Figure 4.29(a). The main peak is at the same photon energy of 1.534 eV as in Figure 4.26. The fact that these two spectra have the same main peak suggests this 1.534 eV emission is the quantum-well emission rather than a surface-charge-related emission, which would be suppressed when a SAW is launched. The FWHM of the SAW-driven EL is about 1 meV.

A SAW with a larger amplitude of electrical potential can be generated by applying an RF signal with a higher power. A deeper potential minimum can therefore carry more electrons to the region of holes. Figure 4.28(a) shows the dependence of SAW-driven I_{SD} on applied power P_{RF}. I_{SD} at the resonant frequency of 1.163 GHz appears at $P_{RF} > 9$ dBm, and increases with P_{RF}, and I_{SD} also appears in a larger frequency range as P_{RF} increases. It is clear that SAW-driven charge transport is enhanced by applying a higher-power RF signal. The corresponding EL intensity in Figure 4.28(b) also exhibits the same feature, meaning that enhanced SAW-driven charge transport gives rise to enhanced electron-hole recombination at the n-i-p junction. It should be noted that alternating fringes are shown in both Figure 4.28(a) and (b). These fringes with a periodicity of 2.5 MHz are due to interference of the SAW and crosstalk, which is the EM wave produced by the same RF signal that generates the SAW.

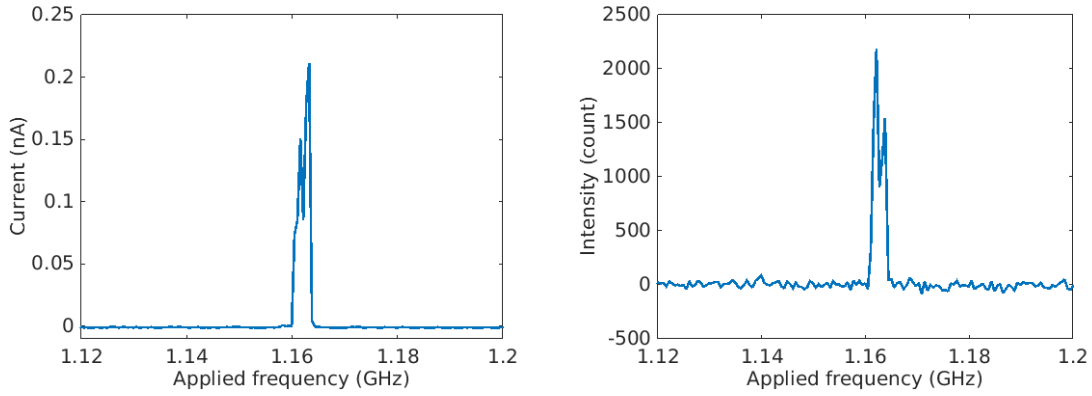

(a) (b)

Fig. 4.27 (a) I_{SD} as a function of frequency f_{RF} applied to the 1 GHz IDT. An enhancement of I_{SD} appears at 1.16 GHz. (b) EL intensity as a function of f_{RF}. An enhancement is shown at the same frequency as in I_{SD}.

When the SAW and the crosstalk are in phase at a certain distance d from the IDT, the phase difference between the SAW and the crosstalk is

$$K_{SAW} \cdot d - K_{crosstalk} \cdot d = 2\pi d\left(\frac{1}{\lambda_{SAW}} - \frac{1}{\lambda_{crosstalk}}\right) = n \cdot 2\pi\,, \tag{4.4}$$

where K_{SAW} is the wave vector of the SAW, $K_{crosstalk}$ is the wave vector of the crosstalk, λ_{SAW} is the wavelength of the SAW, $\lambda_{crosstalk}$ is the wavelength of the crosstalk, and n is an integer. Because $\lambda_{crosstalk}$ in air (about 30 cm) is much larger than λ_{SAW} (about 2.5 μm), equation 4.4 can be re-written as

$$\frac{1}{\lambda_{SAW}} = \frac{f_{RF}}{V_{SAW}} = \frac{n}{d}\,, \tag{4.5}$$

where f_{RF} is the frequency of the RF signal and V_{SAW} is the SAW velocity. Therefore, the periodicity of the interference fringes is expressed as

$$\Delta f_{RF} = \frac{V_{SAW}}{d}\,. \tag{4.6}$$

Considering $V_{SAW} \simeq 2800$ m/s and $d \simeq 1$ mm in TKH03, the periodicity of the interference fringes is expected to be about 2.8 MHz, which is close to the observed periodicity of ~ 2.5 MHz.

A stronger SAW can also affect the spectrum of SAW-driven EL. First, higher power will cause heating and increase the uncertainty in photon energy. Second, SAW-induced strain will lead to the modulation of the GaAs bandgap, which will result in the splitting of photon

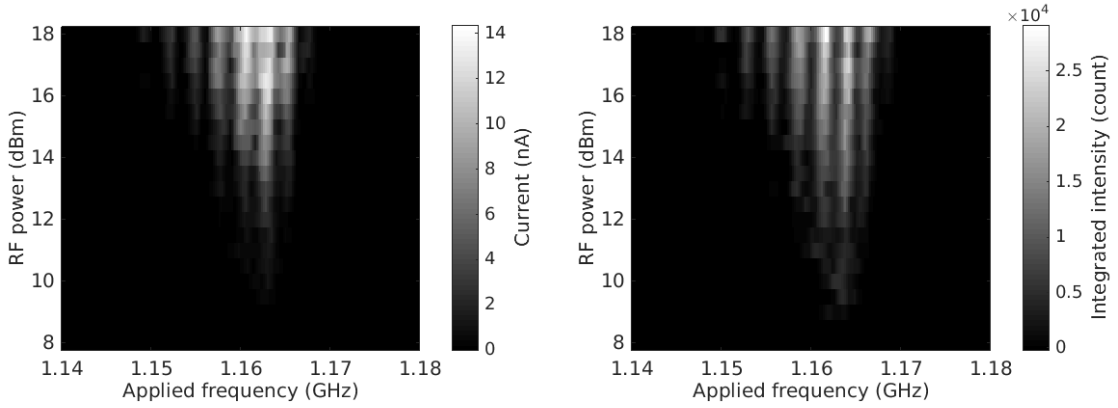

(a) (b)

Fig. 4.28 (a) Dependence of SAW-driven I_{SD} on RF power P_{RF}. I_{SD} at 1.163 GHz disappears at $P_{RF} < 9$ dBm. An oscillation in I_{SD} with a periodicity of 2.5 MHz can be seen. (b) Dependence of SAW-driven EL on P_{RF}. EL at 1.163 GHz disappears at $P_{RF} < 9$ dBm. The 2.5 MHz oscillation is also be observed in EL.

energies [123, 124]. Figure 4.29(a) to (d) show spectra of SAW-driven EL at 9, 11, 13, and 18 dBm respectively. It can be seen that the peak at 1.534 eV becomes wider when a higher P_{RF} is applied to the IDT, which can be understood as a heating effect. However, it seems that two side peaks at 1.533 eV and 1.535 eV appear at $P_{RF} > 11$ dBm. At 18 dBm, these two side peaks are higher than the original main peak. This splitting of photon energy is possibly related to the modulation of the GaAs bandgap [123, 125]. However, since electrons are always confined in the minima of the SAW potential and the potential minima correspond to a smaller bandgap, recombination in the potential minima should only shift the peak to a higher wavelength (smaller photon energy), rather than producing the observed splitting. Further investigation is required to understand this energy splitting of SAW-driven EL fully.

4.5.4 Side-gate Dependence

As with TKH02, side-gate voltages V_{SiG} also have the ability to affect photon emission efficiency η_{emit} in TKH03. Figure 4.30(a) shows SAW-driven I_{SD} and EL intensity as a function of V_{SiG} when $V_{SD} = 1.48$ V, $P_{RF} = 18$ dBm, and $f_{RF} = 1.163$ GHz. As V_{SiG} becomes more negative, the potential barrier in the 1D channel is raised and this leads to a variation of potential slope across the n-i-p junction [126, 87]. SAW-driven charge transport is optimised when the slope of the potential is minimised at $V_{SiG} = -0.5$ V, and I_{SD} decreases when the slope becomes steeper at $V_{SiG} <= -0.5$ V. The EL intensity in Figure 4.30(a) exhibits a maximum at V_{SiG} = -0.75, which is different from the maximum in the I_{SD}. This suggests the photon emission efficiency η_{emit} is modulated by V_{SiG} for the same reason as in the case of

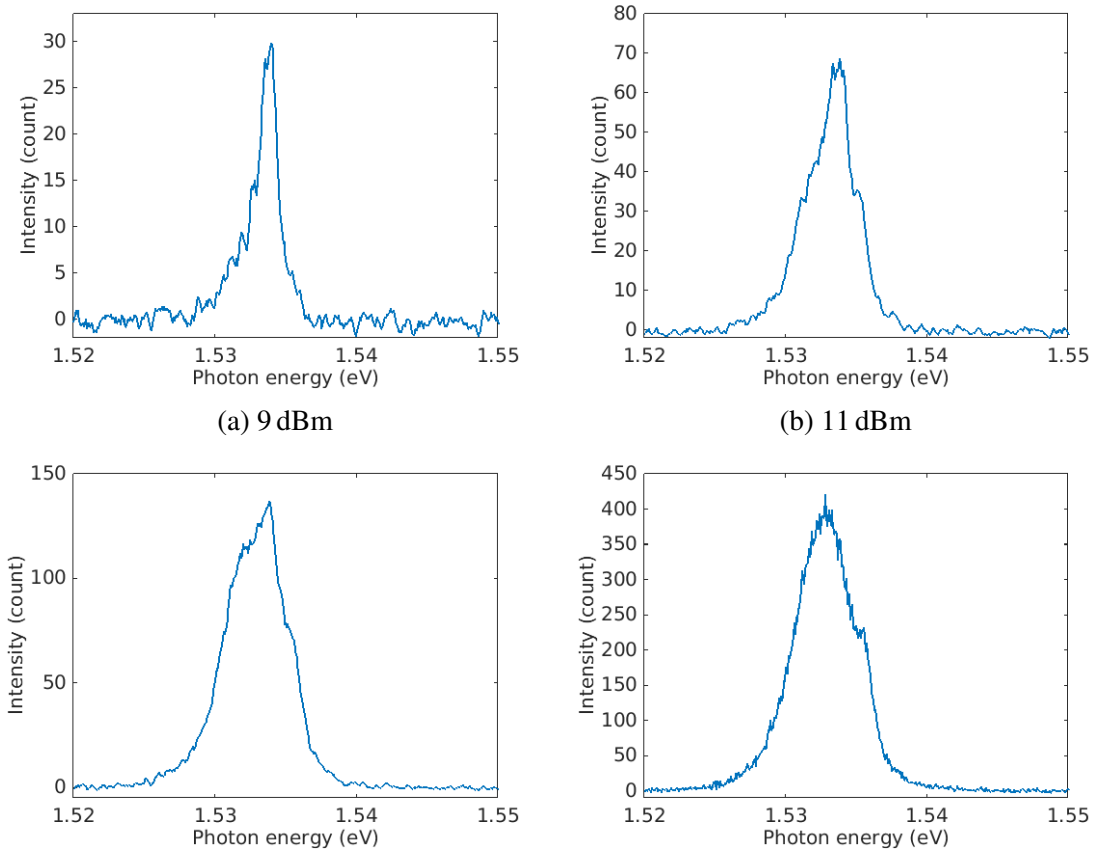

(a) 9 dBm (b) 11 dBm

(c) 13 dBm (d) 18 dBm

Fig. 4.29 (a) Spectrum of SAW-driven EL at $P_{\mathrm{RF}} = 9\,\mathrm{dBm}$ showing a peak at 1.534 eV (810 nm) with FWHM $\simeq 1$ meV. (b) Spectrum of SAW-driven EL at $P_{\mathrm{RF}} = 11\,\mathrm{dBm}$. FWHM $\simeq 4$ meV. (c) Spectrum of SAW-driven EL at $P_{\mathrm{RF}} = 13\,\mathrm{dBm}$. FWHM $\simeq 6$ meV. Two side peaks can be seen at 1.533 eV (811 nm) and 1.535 eV (809 nm). (d) Spectrum of SAW-driven EL at $P_{\mathrm{RF}} = 18\,\mathrm{dBm}$. FWHM $\simeq 3$ nm. The 1.534 eV main peak is hidden away by the two side peaks.

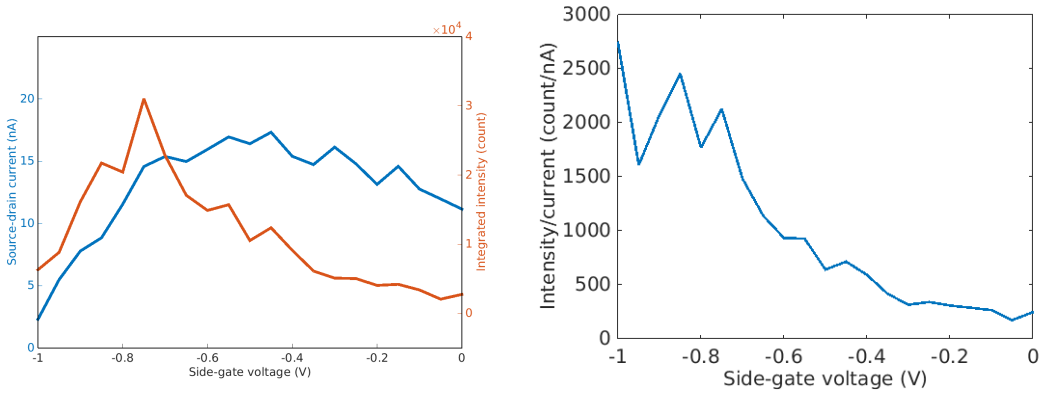

(a) (b)

Fig. 4.30 (a) I_{SD} and EL intensity as a function of V_{SiG}. (b) Ratio of the EL to the I_{SD} in (a), which increases as V_{SiG} is more negative.

TKH02. The ratio of the EL intensity to the I_{SD}, which is proportional to η_{emit}, is shown in Figure 4.30(b). The ratio increases as V_{SiG} becomes more negative, indicating that η_{emit} is enhanced when more holes are extracted from the surface gate and more collectable photons are produced.

Ideally, quantised SAW-driven current $I = n \cdot f_{RF} \cdot e$, where n is the number of electrons in each SAW minimum, f_{RF} is the frequency of a SAW and e is the unit charge, should be observed if $\Delta u_{(\mathrm{SAW\,dot})}(n) = u_{(\mathrm{SAW\,dot})}(n) - u_{(\mathrm{SAW\,dot})}(n-1)$ is comparable to or larger than $\hbar\omega_{(\mathrm{SAW\,bar})}$, where $u_{(\mathrm{SAW\,dot})}(n)$ is the electrochemical potential of SAW-created dynamic quantum dots and $\omega_{(\mathrm{SAW\,bar})}$ is the curvature of the quantum-dot barrier expressed in angular frequency [127, 128]. A high-quality SAW-driven single-photon source must have a well-defined single-electron state in each SAW minimum so that single-photon emissions can be guaranteed. With $f_{RF} = 1.16\,\mathrm{GHz}$ in TKH03, the quantised SAW-driven current with $n = 1$ is then $\simeq 0.18\,\mathrm{nA}$. Normally, quantised SAW-driven currents can be observed as plateaus in I_{SD} when the 1D channel is depleted by applying a negative V_{SiG} [61, 89]. Figure 4.31 shows SAW-driven I_{SD} as a function of V_{SiG} at different P_{RF} when $V_{SD} = 1.45\,\mathrm{V}$ and $f_{RF} = 1.163\,\mathrm{GHz}$. As can be seen in Figure 4.31, SAW-driven I_{SD} is pinched-off when a steep potential slope is created by applying V_{SiG}. Furthermore, the pinch-off curve is shifted negatively in terms of V_{SiG} when a higher P_{RF} is applied, which means a stronger SAW can carry electrons across a region with a steeper potential slope. However, a quantised current at $I_{SD} = 0.18\,\mathrm{nA}$ cannot be observed in Figure 4.31, indicating that $\Delta u_{(\mathrm{SAW\,dot})}$ is too small compared with $\hbar\omega_{(\mathrm{SAW\,bar})}$. More studies will be needed to increase $\Delta u_{(\mathrm{SAW\,dot})}$ in ways that improve confinement of SAW-created dynamic quantum dots and increase electron-electron interaction in these dynamic quantum dots [71].

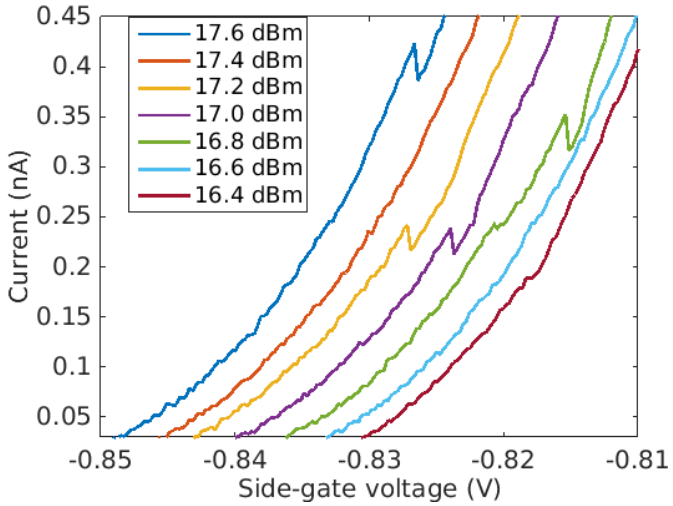

Fig. 4.31 I_{SD} as a function of V_{SiG} at different P_{RF}. I_{SD} is pinched-off at around -0.83 V when $P_{RF} = 16.4$ dBm and the pinch-off curve for I_{SD} shifts towards negative V_{SiG} when a higher P_{RF} is applied.

4.6 Conclusion

In conclusion, the characterisation and optimisation of SAW-driven n-i-p junctions have been presented here. A more detailed description of optical setups in the black helium-3 and μPL systems has also been provided, along with the operating procedure for the piezoelectric positioner. Measurement results from four consecutive batches have also been shown and discussed. The μPL cryostat was employed to study the properties of EL in the first three batches. In batches YC02 and TKH01, it was found that etched features for confining current flow were necessary to observe recombination at a lateral n-i-p junction in an undoped quantum-well structure. With properly designed etch features in the next batch, TKH02, a functioning n-i-p junction was confirmed under DC forward bias, and EL was also detected in a micrometre-size area at the n-i-p junction. Moreover, SAW-driven charge transport and SAW-driven EL were observed using 3 GHz SAWs enhanced by the ZnO thin film. However, the ZnO thin film seemed to cause surface charges that affected the photon emissions. Also, a leakage path possibly caused by trapped charges in a wide intrinsic region was observed between ohmic contacts and an IDT. This leakage path could contribute to additional crosstalk in SAW-related measurements, and it was therefore eliminated by the introduction of an extra etched feature in the final batch TKH03. One device from TKH03 was characterised in the black helium-3 cryostat, since the optimised EL could be collected over a micrometre-size area. SAW-driven charge transport and EL were also observed using 1 GHz SAWs, which are beneficial for the time-resolved and autocorrelation measurements in Chapters 5 and

6. Nonetheless, quantised SAW-driven current could not be observed in TKH03. Further investigation will be required to realise quantised SAW-driven current for a high-quality SAW-driven single-photon source.

Chapter 5

Time-resolved SAW-driven Electroluminescence

Time-resolved optical measurements are useful in order to understand the dynamics of photon-generating charge carriers in a system. In the case of a SAW-driven n-i-p junction, time-resolved measurements of SAW-driven electroluminescence (EL) can reveal the carrier lifetime of SAW-driven electrons in the region of holes. This carrier lifetime of the SAW-driven electrons is crucial for making a SAW-driven single-photon source since the carrier lifetime must be shorter than the period of the SAW. If the carrier lifetime is too long, a photon produced by the recombination of a SAW-driven single electron may overlap with another photon produced by a previous electron. As a consequence, the SAW-driven n-i-p junction may generate two photons at the same time, which will cause the single-photon emission to deteriorate. Moreover, a time-resolved measurement combined with a pulsed RF signal can separate the effect of a SAW from the effect of the corresponding crosstalk in order to confirm how much EL is actually driven by the SAW. This information was helpful for the optimisation of SAW-driven n-i-p junctions.

This chapter presents results from time-resolved measurements of SAW-driven n-i-p junctions. In the first part, the principle of how to measure the SAW-driven EL with sub-nanosecond timing resolution is introduced along with the two time-resolved measurement setups employed in this thesis. Next, results from the ZnO-coated device TKH02 are shown and discussed. In the last part, time-resolved characterisation of the optimised device TKH03 is presented.

5.1 Time-resolved Measurement Setup

In order to characterise photon emission with sub-nanosecond timing resolution, a time-resolved measurement setup is necessary. A common setup consists of a single-photon avalanche photodiode (SPAD), a pulse generator that produces timing pulses, a time-to-digital converter (counter), and excitation input that is synchronised to the timing pulses. The SPAD can be triggered by the detection of a single photon and will then output a signal pulse with low temporal uncertainty (jitter) [129]. The pulse generator should also produce timing pulses with low jitter. The signal pulses and the timing pulses are connected to the counter, and the counter can measure the time difference between a timing pulse and a signal pulse. Finally and most importantly, the excitation input, which triggers the photon emission, must be synchronised to the timing pulses so that the time difference between the photon emission and the excitation inputs can be measured using the counter.

In the case of SAW-driven EL, the excitation input is a SAW. Hence, the RF signal that generates the SAW has to be synchronised to a series of timing pulses. A simplified example is shown in Figure 5.1(a). A SAW that is synchronised to timing pulses carries electrons in the SAW potential minima. Each electron recombines with a hole and generates a photon within the carrier lifetime of the electron. If the carrier lifetime is short enough, the SAW-driven photons will be detected by a SPAD at well-defined moments relative to a timing pulse (see Figure 5.1(a)). Note that not every emitted photon can be detected by the SPAD due to the SPAD's finite sensitivity and the imperfect photon collection efficiency η_{collect} of an optical setup. In a start-stop counter, when a timing pulse (start) has been received, the counter begins time-counting until a signal pulse (stop) is received, and then the counter records that a coincidence has occurred with the time delay between the timing pulse and the signal pulse. Due to the synchronised SAW-driven photons in Figure 5.1(a), a timing-signal-pulse pair is most likely to have a time difference $t = 0.5, 1.5$. Therefore, a histogram, recording the number of coincidences as a function of the time delay t, will exhibit peaks at $t = 0.5, 1.5$ as seen in Figure 5.1(b). As a result, a temporal profile of the SAW-driven EL can be obtained if the overall jitter of a timing pulse, the SPAD, and the counter is significantly shorter than one SAW period.

In the measurements that will be discussed later in this chapter, a Tektronix AWG70002A dual-channel arbitrary waveform generator (AWG) with jitter = 10 ps was used to provide a series of precise timing pulses. This AWG could also provide synchronised RF signals with a limited resolution, which will be discussed in Section 5.1.1. In the other modified setup presented in Section 5.1.2, an Agilent N5171B RF source was employed to output a better sinusoidal function than the AWG, but the synchronisation of the RF source and the timing pulses needed more consideration. An IDQ-ID100 SPAD, with jitter = 40 ps and

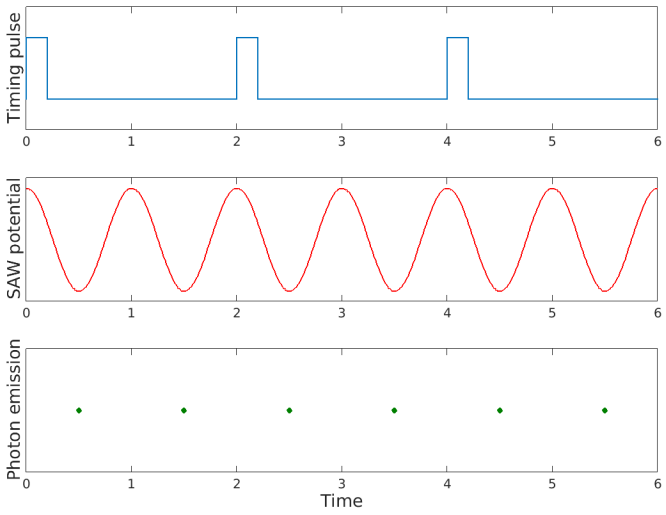

(a)

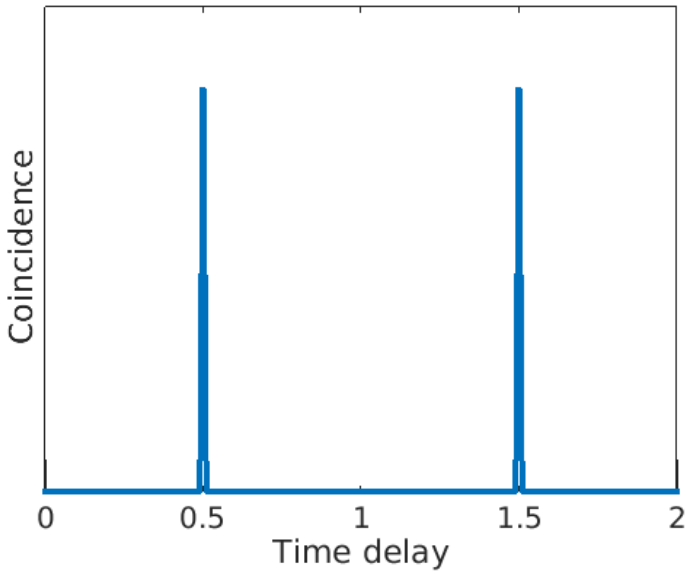

(b)

Fig. 5.1 Simplified example of a time-resolved measurement of SAW-driven EL. (a) Timing pulses (top panel), SAW (middle panel), and photon emission (bottom panel) as a function of time. The timing pulses and the SAW are synchronised so that a timing pulse always occurs at a potential maximum of the SAW. Since electrons are carried in the potential minima, the photons, which trigger a SPAD, are emitted at the potential minima of the SAW. (b) Histogram of a start-stop measurement using a counter, where the start is a timing pulse and the stop is a signal pulse (from the SPAD triggered by a photon). The time differences between the timing pulses and the photons lead to the peaks at $t = 0.5, 1.5$ in the histogram.

sensitivity = 7%, was used to detect photons from SAW-driven n-i-p junctions. To obtain histograms of SAW-driven EL, a QuTAU counter, which has an average time-bin width of 81 ps, was first used. It has to be noted that the time-bin widths in the QuTAU are not uniform and require calibration, which will be discussed in Section 5.1.3. In order to observe the SAW-driven EL with a better timing resolution, a Picoharp 300 counter, which has a much smaller time-bin width of 4 ps, was later employed in the time-resolved measurement setups. The 4 ps time-bin width made the Picoharp 300 a more suitable counter for measurements that require a high timing resolution. The QuTAU was thus replaced by the Picoharp 300 later in this chapter and in Chapter 6.

5.1.1 Setup Using a Arbitrary Waveform Generator

As mentioned previously, in order to obtain a time-correlated histogram of SAW-driven EL, the RF signal that generates the SAW has to be synchronised to the timing pulses from the AWG. Since the AWG70002 is capable of dual-channel output, channel 1 can provide the timing pulses while channel 2 produces an RF signal at the resonant frequency of the IDT. These two channels are based on the same internal oscillator (the clock) in the AWG, so it is guaranteed that the timing pulses and the RF signal will be synchronised. As can be seen in Figure 5.2, a timing pulse from AWG channel 1 is sent to a counter (either QuTAU or Picoharp 300) as a trigger (start), and a synchronised RF signal from channel 2 is sent to the IDT to generate a SAW. A SAW-driven photon from an n-i-p junction is then received by the IDQ-ID100 SPAD and gives rise to a signal pulse (stop) to the counter. A histogram of the SAW-driven EL can therefore be obtained when many such events have been accumulated.

Although the dual-channel AWG can easily generate a synchronised RF signal, the RF signal is not a perfect sinusoidal function due to the AWG's minimum waveform resolution of 125 ps. For instance, to output a 2.65 GHz RF signal, with period = 377 ps, the waveform can only have less than three points per period. As a result, the RF signal for generating a SAW resembles a step function rather than a sinusoidal function. The step function can potentially generate higher harmonic modes of the SAW, although this can be avoided by filtering the RF input. In addition, the maximum output power of the AWG is only -2 dBm, so an extra RF amplifier is required to generate a SAW that is strong enough for the SAW-driven charge transport.

5.1.2 Setup using RF Source Synchronised to Timing Pulses

The other time-resolved measurement setup used in this thesis utilises a pulse generator and a pulse-synchronised RF source. As shown in Figure 5.3, the pulse generator produces timing

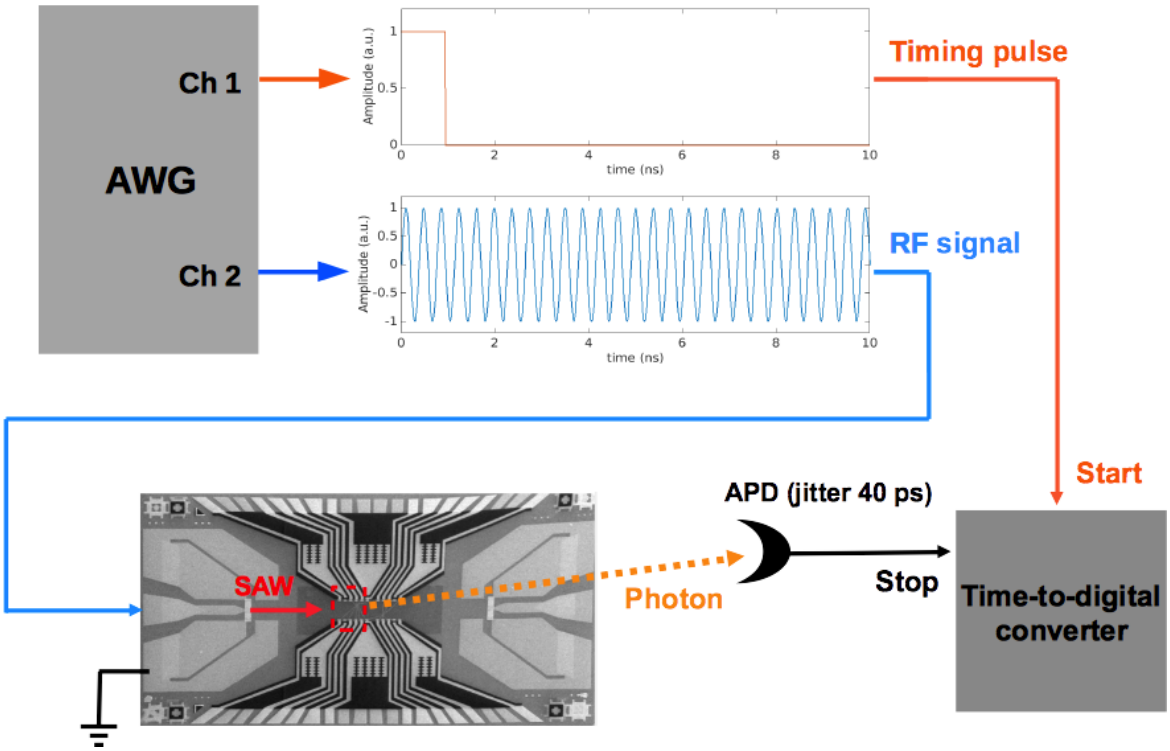

Fig. 5.2 Schematic of the time-resolved measurement setup using an AWG. The timing pulse and the RF signal are both produced by the AWG. The RF signal generates a SAW that gives rise to the SAW-driven photon emission. The photons trigger the avalanche photodiode (APD or SPAD) and lead to the signal pulses. The timing pulses (start) and the signal pulses (stop) are sent to the counter to create a time-resolved histogram of the SAW-driven EL.

pulses, and the RF source generates an RF signal at the resonant frequency of the IDT. Unlike the RF signals from the AWG, which resemble step functions, the RF signal from the RF source is a good sinusoidal function. Hence, this setup will not cause higher harmonics of the SAW. In addition, even without an RF amplifier, the output power can be as high as 18 dBm, which is enough for SAW-driven charge transport.

For a series of timing pulses with a given period t_{pulse}, the condition at which the timing pulses are generated at the same phase of the sinusoidal function of an RF signal is

$$t_{\mathrm{pulse}}/t_{\mathrm{RF}} = n\,, \tag{5.1}$$

where t_{RF} is the period of the RF signal and n is an integer. The equation can be re-written as

$$f_{\mathrm{RF}} = n/t_{\mathrm{pulse}}\,, \tag{5.2}$$

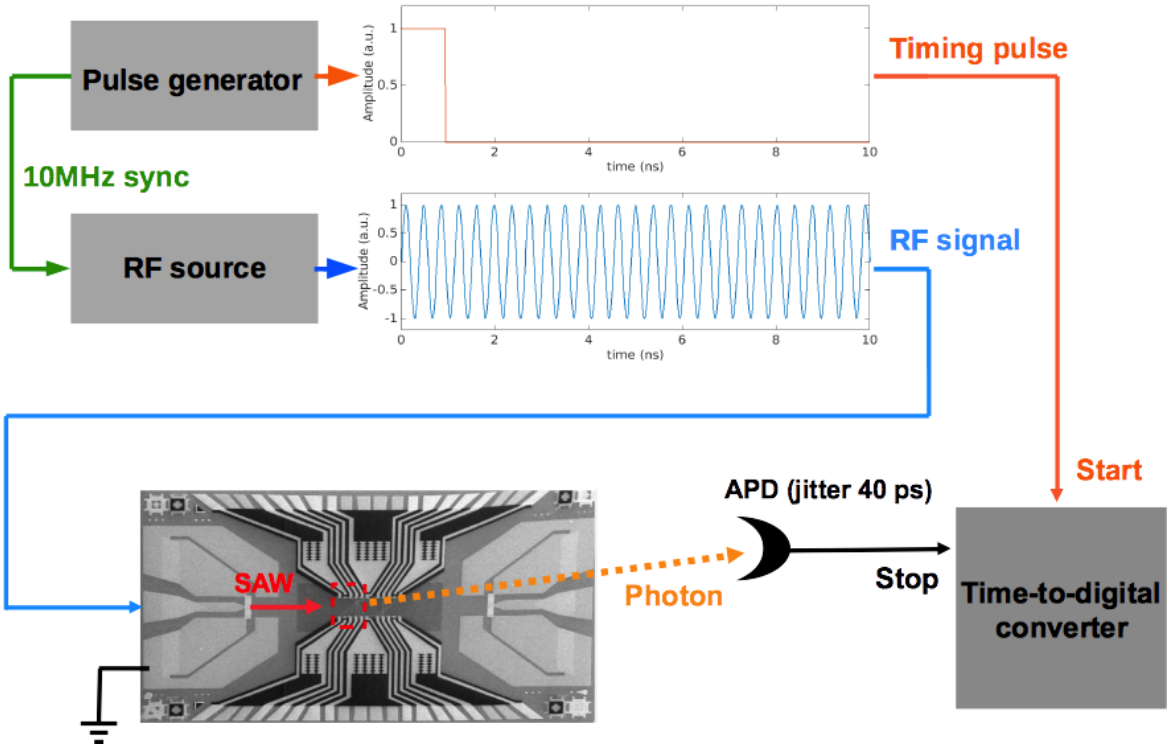

Fig. 5.3 Schematic of the time-resolved measurement setup using a pulse generator and a synchronised RF source. A 10 MHz sync signal is used to achieve synchronisation of the pulse generator and the RF source.

where f_{RF} is the frequency of the RF signal. Therefore, if the pulse period is 1 μs, an f_{RF} that can be synchronised must be a multiple of 1 MHz such as 3.000, 3.001, and 3.002 GHz. Nonetheless, the synchronisation can still fail even if equation 5.2 above is satisfied. This is because internal oscillators in two separate instruments are unlikely to be identical, and this usually leads to a slight difference in their base frequencies (clocks). As a consequence, if the RF source and the pulse generator use their own internal oscillators, the real f_{RF} and t_{pulse} will not satisfy equation 5.2 due to the difference in their clocks. The solution to this problem is for the pulse generator and the RF source to share one clock so that they will produce signals based on the same clock. This can be done by connecting a 10 MHz sync signal from the pulse generator to the RF source, as shown in Figure 5.3. In Figure 5.4(a), a 2.65 GHz RF signal is measured using a Agilent 86100A high-frequency oscilloscope . This 2.65 GHz RF signal is synchronised to timing pulses with $t_{\mathrm{pulse}} = 1\ \mu$s and jitter < 10 ps by connecting the 10 MHz sync signal. The timing pulses are used as trigger signals for the oscilloscope. A clear sinusoidal function is seen in Figure 5.4(a), indicating that the RF signal is synchronised to the timing pulses.

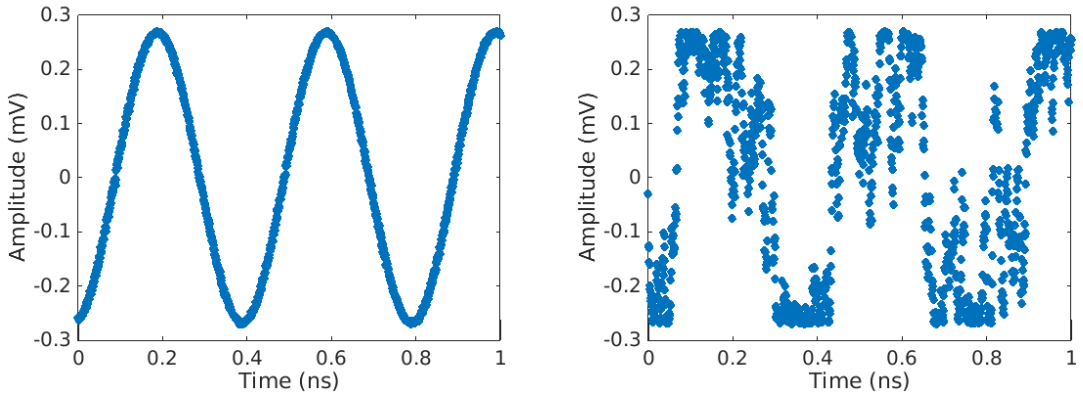

Fig. 5.4 Comparison of RF signals synchronised to timing pulses with different jitter. (a) RF signal synchronised to timing pulses from AWG70002 (jitter < 10 ps) measured by a oscilloscope. A clear sinusoidal function can be seen. (b) RF signal synchronised to timing pulses from Agilent 81101A (jitter $= 40$ ps). The sinusoidal function is less clear.

The jitter of the timing pulses is crucial to the quality of the synchronisation. In Figure 5.4(a), the timing pulses produced by the AWG70002 have jitter < 10 ps. This low jitter gives rise to a clear 2.65 GHz sine curve. On the other hand, in Figure 5.4(b), the timing pulses from an Agilent 81101A pulse generator have jitter $= 40$ ps. This larger jitter causes a higher uncertainty in the phase difference between the timing pulses and the RF signal. As a result, the same 2.65 GHz signal is more blurred in the oscilloscope compared with that in Figure 5.4(a), meaning the synchronisation is not as good as in Figure 5.4(a). So, it is important to use timing pulses with lower jitter, especially for an RF signal with a higher frequency. The AWG70002 was thus used as a high-quality pulse generator in this setup.

5.1.3 Calibration of Alternating Time-bin Widths

The time-resolved measurements that will be discussed in Section 5.2 were recorded using a QuTAU counter. Although the QuTAU has an average time-bin width of 81 ps, the actual time-bin widths alternate, with the even time bins wider than the odd ones. As a consequence, a photon from a constant light source will have a higher probability of being registered in an even time bin, so a constant light source will lead to a tooth-like feature in the time-correlated histogram. Calibration for the alternating time-bin widths is thus necessary to obtain the real histogram. Figure 5.5(a) shows a histogram of EL from an n-i-p junction under a constant forward bias. The tooth-like feature in Figure 5.5(a) is due to the alternating time-bin widths. Figure 5.5(b) is the Fourier transform of Figure 5.5(a). The peak at 6.17 GHz corresponds to 162 ps, which is the period of the tooth-like feature ($81 \cdot 2 = 162$ ps). This artificial

feature can be reduced by scaling the data in the even time bins by a factor r_{scale}. It was found that using $r_{\text{scale}} = 0.497$ could minimise the tooth-like feature. Figure 5.5(c) is the calibrated histogram with $r_{\text{scale}} = 0.497$. Compared with Figure 5.5(a), the tooth-like feature in Figure 5.5(c) is greatly improved. In Figure 5.5(d), the Fourier transform of the calibrated histogram also exhibits a much lower peak at 6.17 GHz. Figure 5.5(c) and (d) both show that the calibration with $r_{\text{scale}} = 0.497$ can reduce the artificial feature and restore the real histogram of a continuous light source.

5.2 ZnO-deposited n-i-p junction with 3GHz SAWs

Time-resolved measurements were first carried out on a SAW-driven n-i-p junction device from TKH02. Basic properties of this device have been discussed in Section 4.4 in Chapter 4. The IDT on this device can generate SAWs at its resonant frequency of 2.65 GHz. An 800 nm ZnO film was deposited on the device in order to enhance the SAW signal.

5.2.1 Electroluminescence Driven by a Continuous SAW

The time-resolved measurement setup using the AWG, presented in Section 5.1.1, was employed on this device. This setup was built with Dr Gabriel Éthier-Majcher and Dr Megan Stanley's help. Because the centre frequency of the SAW on this device is 2.65 GHz, AWG waveforms for the RF signal can only have fewer than three points per SAW period. Figure 5.6 shows two continuous-wave (CW) AWG waveforms that were designed for the time-resolved measurements. AWG waveform 1 in Figure 5.6(a), which is essentially a 2.65 GHz square wave, consists of two points per SAW period. On the other hand, AWG waveform 2 in Figure 5.6(b) has a more sophisticated design, which consists of five points in two SAW periods. The main component of AWG waveform 2 in the frequency domain is at 2.65 GHz. However, AWG waveform 2 also has a 1.325 GHz half-SAW-frequency component due to its waveform design. Ideally, the half-SAW-frequency component is not an issue if the charge transport and the EL are entirely driven by the 2.65 GHz SAW, because the IDT serves as a filter and it can only generate a SAW at its resonant frequency $f_{\text{SAW}} = 2.65$ GHz and at higher harmonics such as $3f_{\text{SAW}}$, $5f_{\text{SAW}}$, $7f_{\text{SAW}}$ etc,. Nevertheless, if the charge transport and the EL can be modulated by crosstalk, this half-SAW-frequency component in AWG waveform 2 will contribute to the measured signal.

First, a time-resolved measurement was carried out using AWG waveform 2. Time-correlated histograms of EL driven by AWG waveform 2 are shown in Figure 5.7(a), where $V_{\text{SD}} = 1.45$ V, $P_{\text{RF}} = 10$ dBm, and the low-resolution counter, QuTAU, was used. A tooth-like

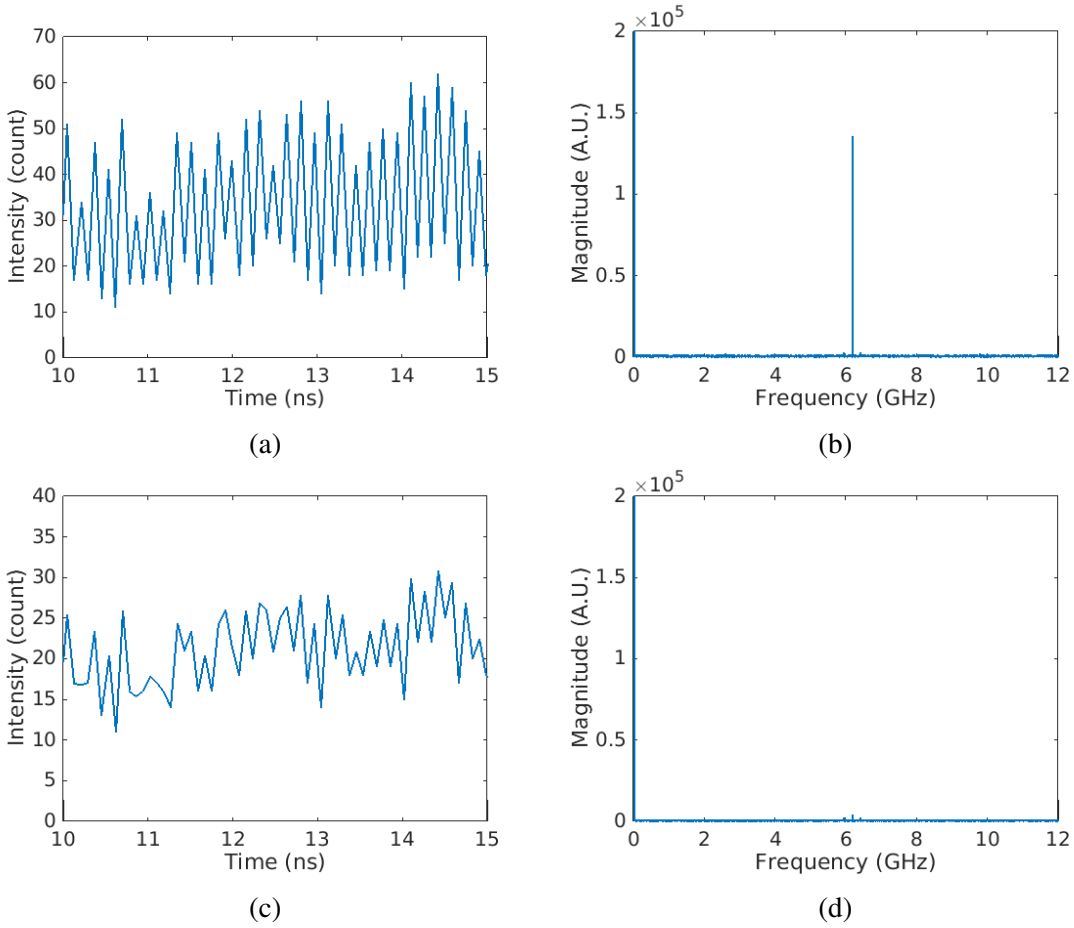

Fig. 5.5 Calibration of the alternating time-bin widths in QuTAU. (a) Time-correlated histogram of EL when a constant V_{SD} is applied. A tooth-like feature is seen due to the alternating time-bin widths. (b) Fourier transform of (a). A high component at 6.17 GHz is shown because of the alternating time-bin widths. (c) Time-correlated histogram calibrated with $r_{scale} = 0.497$. The tooth-like feature is less obvious after the calibration. (d) Fourier transform of (c). The component at 6.17 GHz is greatly reduced after the calibration.

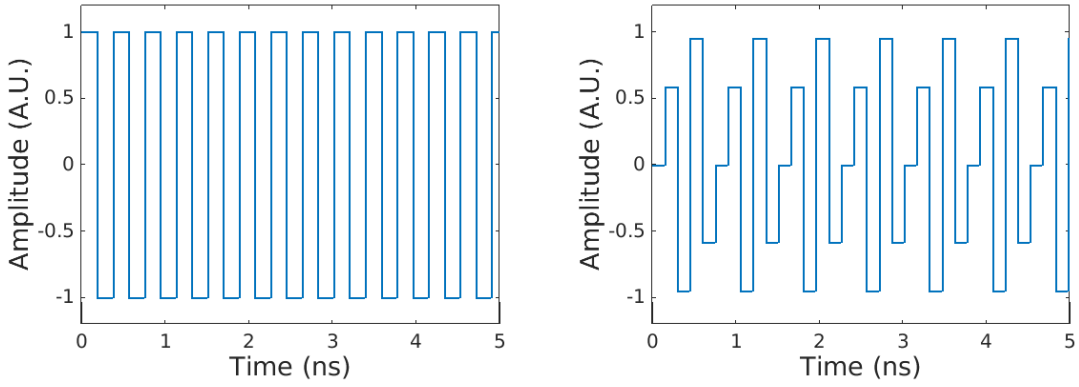

(a) (b)

Fig. 5.6 (a) Waveform 1 from the AWG. This waveform has only 2 points per cycle. (b) Waveform 2 from the AWG. This waveform has 2.5 points per cycle on average.

artificial feature can be seen in the histogram without the time-bin calibration (top panel). When the calibration is performed with $r_{\text{scale}} = 0.497$, the tooth-like feature is eliminated in the calibrated histogram (bottom panel). The effect of the time-bin calibration can also be seen in the Fourier transforms of these histograms (see Figure 5.7(b)). The artificial component at 6.17 GHz is significantly reduced in the Fourier transform of the calibrated histogram, indicating the time-bin calibration is working well. After calibration, a periodic pattern can be observed in the histogram (see Figure 5.7(a) bottom panel), suggesting that the EL is modulated by AWG waveform 2. However, the period of the pattern is about 800 ns, which is twice as long as the SAW period of 377 ns. Moreover, the Fourier transformation in Figure 5.7(b) bottom panel exhibits a dominant component at 1.325 GHz ($0.5 f_{\text{SAW}}$) and a secondary component at 2.65 GHz (f_{SAW}). As previously explained, the SAW-driven EL should not have this half-SAW-frequency component. Hence, it is evident that crosstalk has a significant effect on both the charge transport and the EL in TKH02.

The simpler AWG waveform 1 can also cause EL. A time-correlated histogram of EL driven by AWG waveform 1 and the Fourier transform of this histogram are shown in Figure 5.8(a) and (b) respectively. Although the histogram in Figure 5.8(a) is calibrated, it is difficult to conclude whether any periodic pattern exists or not. Interestingly, the Fourier transform in Figure 5.8(b) shows a dominant peak at 2.65 GHz, indicating that the EL is modulated by AWG waveform 1. Because of the simpler design of AWG waveform 1, the SAW-driven EL and the crosstalk-driven EL will both exhibit a main component at 2.65 GHz and have no signal at 1.325 GHz in Figure 5.8(b). Hence, the absence of the crosstalk-driven EL cannot be confirmed by the lack of the half-SAW-frequency component if AWG waveform 1, a CW 2.65 GHz square wave, is used. In fact, the lack of a clear

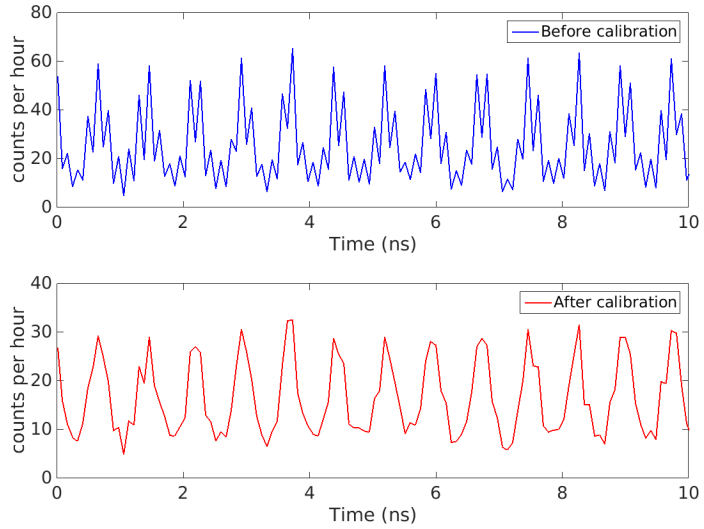

(a)

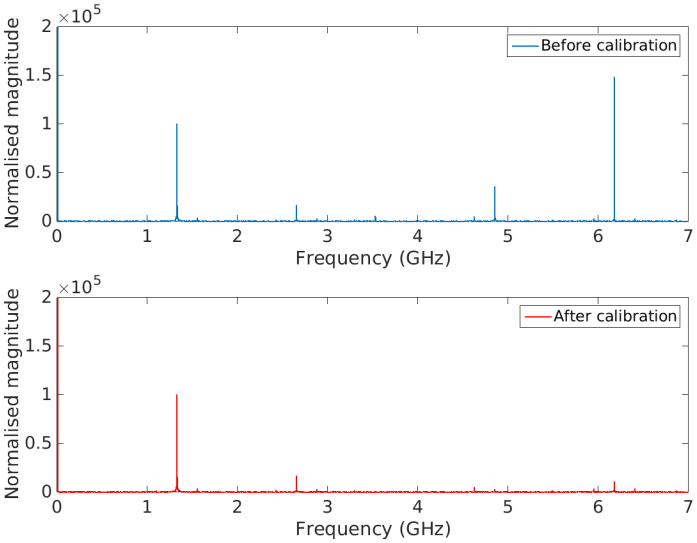

(b)

Fig. 5.7 (a) Time-correlated histograms of the EL driven by AWG waveform 2. The top panel shows the raw data, and the bottom panel gives the calibrated histogram with $r_{\text{scale}} = 0.497$. The tooth-like feature is reduced after the calibration. (b) Fourier transforms of the raw histogram (top panel) and the calibrated histogram (bottom). The 6.17 GHz peak is significantly reduced after the calibration.

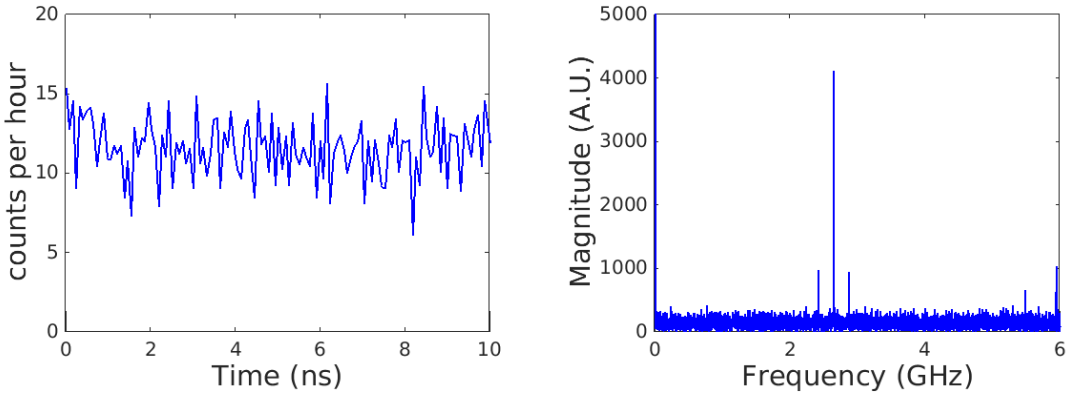

(a) (b)

Fig. 5.8 (a) Time-correlated histogram of the EL driven by AWG waveform 1. The periodic pattern is not easily seen. (b) Fourier transform of (a). A high peak can be seen at 2.65 GHz, corresponding to the SAW period of 377 ps.

periodic pattern in Figure 5.8(a) implies that the SAW-driven EL and the crosstalk-driven EL make a similar contribution, and they are out of phase so that the periodic pattern is blurred. In order to confirm the existence of the crosstalk-driven EL, a method is required to separate the crosstalk-driven EL from the SAW-driven EL in the time domain, which will be discussed in the next paragraph.

5.2.2 Electroluminescence Driven by a Pulsed SAW

Utilising the fact that the SAW travels more slowly than the crosstalk, the crosstalk-driven EL and the SAW-driven EL can be separated in the time domain. In TKH02, the distance between the IDT and the n-i-p junction is about 1.2 mm. Given that the SAW velocity with the 800 nm ZnO is about 2650 m/s, it takes roughly 450 ns for the SAW to propagate from the IDT to the n-i-p junction. On the other hand, the crosstalk travels at the speed of light, so the crosstalk can modulate the n-i-p junction almost instantly. Therefore, if a pulsed RF signal with a pulse length shorter than 450 ns is applied to the IDT, the crosstalk-driven EL will appear immediately when the pulsed RF starts and will disappear when the pulsed RF stops, while the SAW-driven EL will appear roughly 450 ns after the beginning of the pulsed RF. As a result, the SAW-driven EL will be delayed by roughly 450 ns, so the crosstalk-driven EL and the SAW-driven EL can be observed separately.

In Figure 5.9(a) (top panel), a pulsed RF signal with a pulse length of 415 ns is used to separate the SAW-driven and crosstalk-driven EL. The RF signal has the same waveform as AWG waveform 1 (see Figure 5.6(a)) when the pulse is on. When this pulsed 2.65 GHz RF

signal is applied to the IDT, a pulsed SAW is launched from the IDT. Due to the time delay discussed earlier, the crosstalk-driven EL (from 10 ns to 420 ns) and the SAW-driven EL (from 470 ns to 890 ns) can be individually observed in the time-correlated histogram (see Figure 5.9(a), bottom panel). This histogram indicates that the crosstalk and the SAW can both give rise to photon emission in TKH02. Interestingly, the SAW-driven EL exhibits a peak at 490 ns and decays exponentially after this peak. This may be related to a charging effect before the SAW arrives, so there are more electrons that can be pumped at the beginning and later the EL decays as these electrons are cleared by the SAW. Figure 5.9(b)shows the Fourier transforms of the crosstalk-driven EL and the SAW-driven EL. Both of these exhibit a clear peak at 2.65 GHz, meaning they are modulated by the pulsed 2.65 GHz crosstalk and the SAW respectively. In addition, more detailed histograms, shown in Figure 5.10(a) and (b), exhibit periodic patterns with period $\simeq 380$ ns, which corresponds to the RF frequency of 2.65 GHz. Compared with Figure 5.8(a), which is modulated by a CW AWG waveform 1, the periodic patterns in Figure 5.10(a) and (b) can be seen by eye. This is because the crosstalk-driven EL and the SAW-driven EL do not overlap in Figure 5.10(a) and (b) thanks to the pulsed RF signal.

If a pulsed RF signal with the more sophisticated AWG waveform 2 (see Figure 5.6(b)) and a pulse length of 415 ns is used, a difference between the crosstalk-driven EL and the SAW-driven EL can be seen in their Fourier transforms. Figure 5.11(a) shows the time-correlated histogram when the pulsed RF signal with AWG waveform 2 is applied to the IDT. Although the histogram is less clear due to a reduction in RF power when AWG waveform 2 is used, the crosstalk-driven EL and the peak of the SAW-driven EL can be seen at the correct position. In Figure 5.11(b), a clear difference in their Fourier transforms can be seen. The crosstalk-driven EL exhibits a main peak at 1.325 GHz and a secondary peak at 2.65 GHz while the SAW-driven EL only shows a peak at 2.65 GHz. This is because the IDT cannot generate a 1.325 GHz SAW even though there is such a component in the RF signal, while the crosstalk can follow the shape of AWG waveform 2 and cause the 1.325 GHz component in the crosstalk-driven EL. This result confirms again that the EL appearing roughly 450 ns after the RF signal is indeed driven by the SAW.

Since the pulsed RF can separate the crosstalk-driven and SAW-driven EL, these two signals can be measured as a function of the RF frequency, which is shown in Figure 5.12. Here the pulsed RF with AWG waveform 1 and a 415 ns pulse length is used. The integrated SAW-driven EL and the integrated crosstalk-driven EL both reach a maximum at around 2.65 GHz, the resonant frequency of the IDT. Indeed, the SAW-driven EL is expected to show a maximum at the resonant frequency as the SAW is stronger near the resonant frequency. However, it is not clear why the crosstalk-driven EL exhibits a similar dependence on the RF

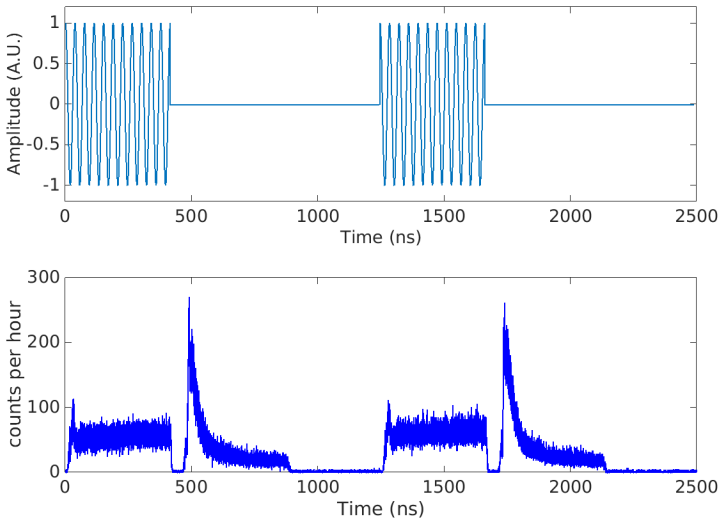

(a)

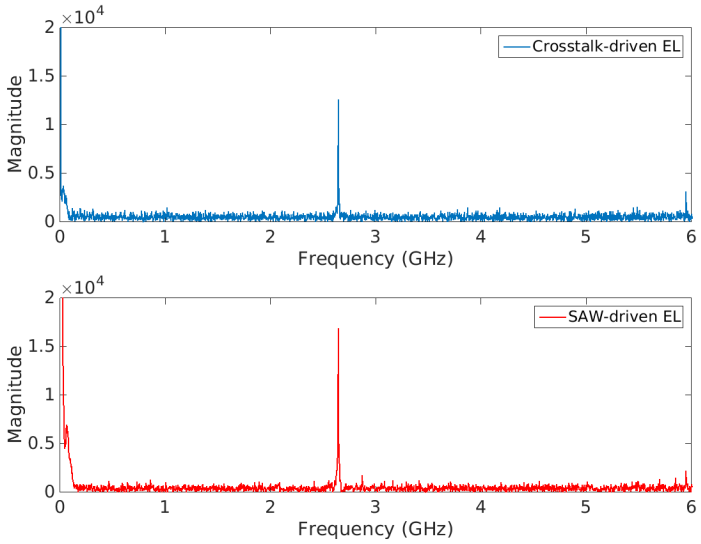

(b)

Fig. 5.9 (a) Time-correlated histogram (bottom panel) of the EL driven by a pulsed RF signal (top panel) with pulse length = 415 ns and AWG waveform 1. The period of the pulsed RF signal is shown greatly increased for clarity. The crosstalk-driven EL (from 10 ns to 420 ns) and the SAW-driven EL (from 470 ns to 890 ns) can be observed separately. (b) Fourier transforms of the crosstalk-driven EL (top panel) and the SAW-driven EL (bottom panel). Both show a single peak at 2.65 GHz.

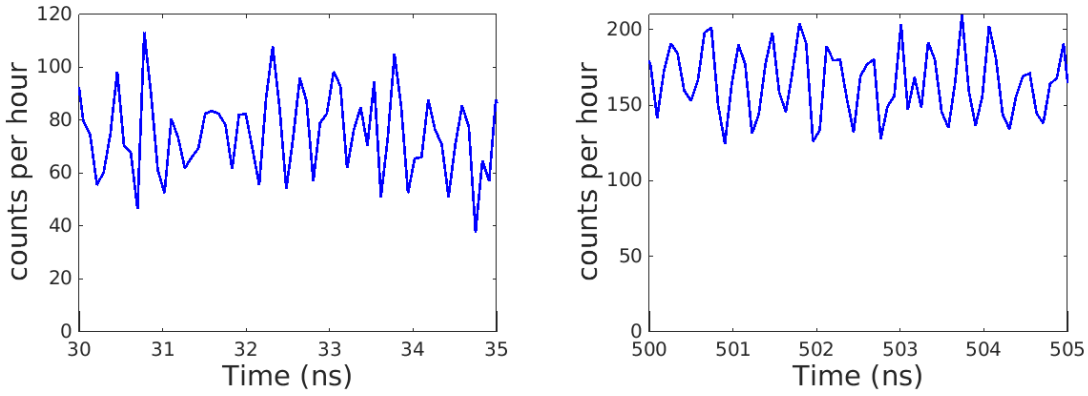

(a) (b)

Fig. 5.10 Magnified histograms of (a) the crosstalk-driven EL and (b) the SAW-driven EL in Figure 5.9(a) bottom panel. Periodic patterns can be visually observed in (a) and (b).

frequency. It might be related to the conductive path between the induced electrons and the IDT, which was discussed in Section 4.4.5. It seems that the direct coupling of the voltage on the IDT to the n-i-p junction is enhanced at the resonant frequency of the IDT, which causes the enhancement of the crosstalk-driven EL, but the reason for this enhancement will require further investigation.

As mentioned in Section 4.4.5, there might be some charges trapped in the wide region between the IDT and the n-i-p junction. Also, it was found that applying a SAW for ten minutes seemed to clear these trapped charges. Interestingly, a similar effect can be observed in the time-correlated histogram. Figure 5.13 shows the integrated EL per minute in a measurement period of 40 minutes, using the same pulsed RF signal as in Figure 5.9. The integrated crosstalk-driven EL remains fairly constant over the 40-minute duration. On the other hand, the integrated SAW-driven EL is weaker at the beginning; it increases in the first 15 minutes and then stays at the same level as the crosstalk-driven EL. This can be understood as the trapped charges screening the SAW at the beginning so that the SAW-driven charge transport is less effective. As the SAW runs for a longer period of time, the trapped charges are gradually cleared away. As a consequence, the screening effect is reduced and a stronger SAW can lead to more electron-hole recombination, which explains why the SAW-driven EL increases during the first 15 minutes. After the first 15 minutes, the charging effect and the charge clearing may reach equilibrium so that the SAW-driven EL remains constant.

Although the SAW-driven EL can be observed in TKH02 using a pulsed RF signal, the crosstalk-driven EL always makes a significant contribution in this device. This is not ideal for making a SAW-driven single-photon source because the crosstalk will produce extra photons when a continuous RF signal is applied. Since a leakage current was found between

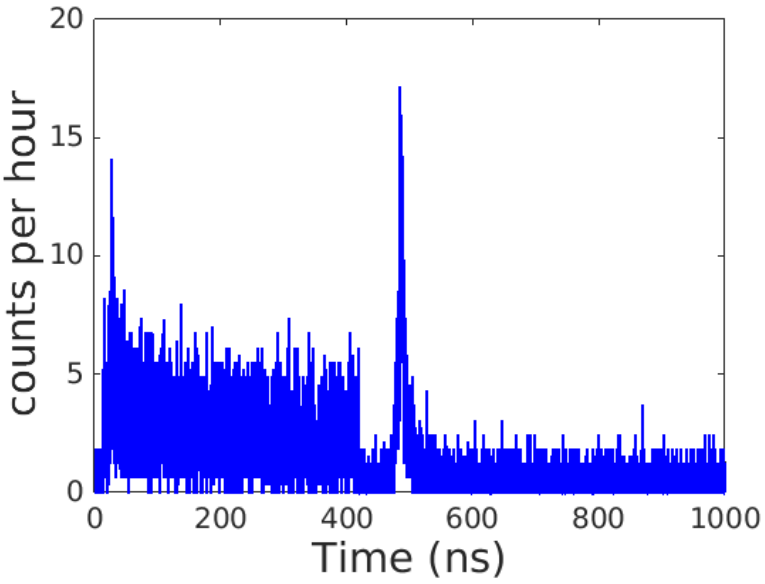

(a)

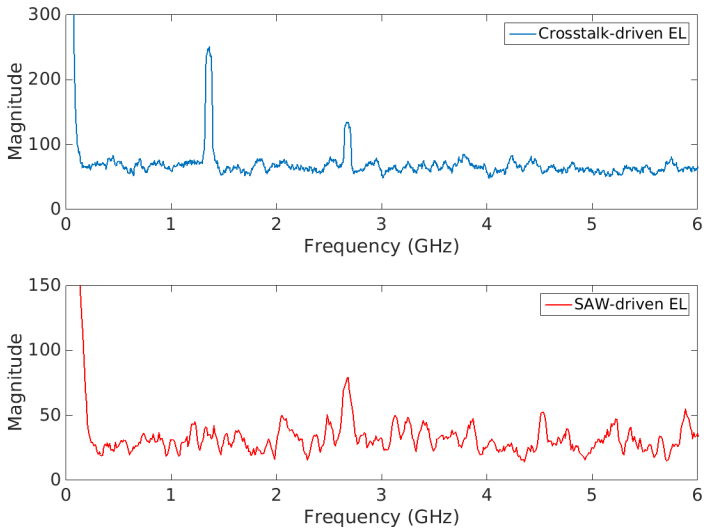

(b)

Fig. 5.11 (a) Time-correlated histogram of the EL driven by a pulsed RF signal with pulse length = 415 ns and AWG waveform 2. The crosstalk-driven EL and the SAW-driven EL can both be seen. (b) Fourier transforms of the crosstalk-driven EL (top panel) and the SAW-driven EL (bottom panel). The crosstalk-driven EL exhibits a main peak at 1.325 GHz and a secondary peak at 2.65 GHz. On the other hand, the SAW-driven EL shows a single peak at 2.65 GHz.

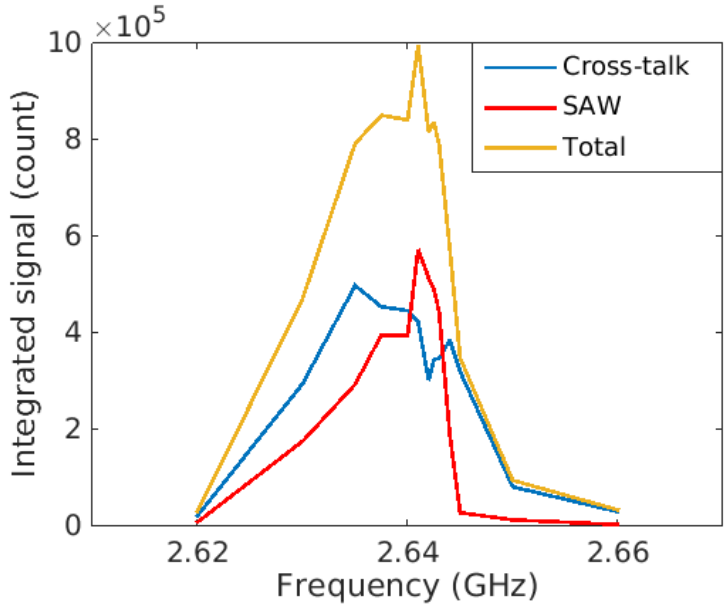

Fig. 5.12 Dependence of the SAW-driven EL, the crosstalk-driven EL, and the overall signal, on the frequency applied to the IDT.

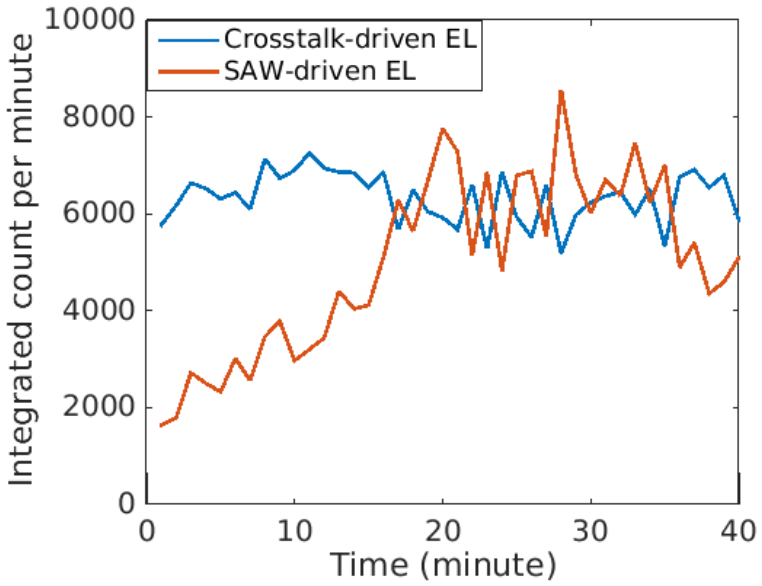

Fig. 5.13 SAW-driven EL and crosstalk-driven EL as a function of the measurement time.

the induced electrons and the IDT, it was suspected that the crosstalk-driven EL was mainly due to a direct coupling of the voltage on the IDT to the n-i-p junction via this leakage path. Therefore, in the next batch TKH03, an etched trench was added to eliminate this potential leakage path, which is discussed in Section 4.5. In addition, the limited timing resolution of QuTAU made it very difficult to resolve the 2.65 GHz periodic pattern clearly in the histograms. Hence, a better counter with higher timing resolution was necessary, and a SAW with a lower frequency would be beneficial for a clearer time-correlated histogram, which is useful for the estimation of the carrier lifetime.

5.3 Optimised n-i-p junction with 1GHz SAWs

Improved time-resolved measurements were carried out on the optimised n-i-p junction from TKH03. Basic properties of this device have been discussed in Section 4.5. The IDT on this device can generate a SAW with $f_{\mathrm{SAW}} = 1.163\,\mathrm{GHz}$. Compared with the 2.65 GHz SAW on TKH02, this 1GHz SAW on TKH03 has a longer SAW period, so the photons emitted from each SAW minimum are more separated in the time domain. Hence, the time-resolved profile of the EL can be observed more easily. In addition, the Picoharp 300 counter with a minimum time-bin width of 4 ps was used in these measurements. The 1.163 GHz SAW and Picoharp 300 both made time-correlated histograms clearer so that more detailed features in the SAW-driven EL could be resolved.

5.3.1 Optimised SAW-driven Electroluminescence

Pulsed RF signals from the AWG (AWG waveform 1 as in Figure 5.6(a), with pulse length = 322 ns) were first used for time-resolved measurements on TKH03. Figure 5.14(a) shows a time-correlated histogram of the SAW-driven EL, where $V_{\mathrm{SD}} = 1.45\,\mathrm{V}$, $V_{\mathrm{SiG}} = -0.6\,\mathrm{V}$, $f_{\mathrm{RF}} = 1.163\,\mathrm{GHz}$, $P_{\mathrm{RF}} = 11.5\,\mathrm{dBm}$, and the surface-gate voltage for inducing holes $V_{\mathrm{SG(hole)}} = -1\,\mathrm{V}$ (relative to V_{drain}, as explained in Section 4.2.3 in Chapter 4). An EL signal only appears at time delay $t = 545$–$805\,\mathrm{ns}$, which corresponds to the effect of the pulsed SAW. This can be confirmed when a higher P_{RF} is applied. In Figure 5.14(c) and (e), where $P_{\mathrm{RF}} = 14\,\mathrm{dBm}$ and 16 dBm respectively, an extra EL signal appears at $t = 120$–$440\,\mathrm{ns}$, which is roughly 400 ns before the main EL signal. Given the propagation time of the SAW is about 400 ns, the main EL signal at $t = 545$–$805\,\mathrm{ns}$ is actually the SAW-driven EL while the weaker EL at $t = 120$–$440\,\mathrm{ns}$ is the crosstalk-driven EL. The crosstalk-driven EL lasts almost as long as the pulse length of 322 ns while the SAW-driven EL lasts for less than 322 ns. It is because the IDT has a Q factor of 50–100 so that the SAW needs 43–86 ns to build up and to relax. At

the beginning and end of the pulse, the SAW is not strong enough to pump electrons across the n-i-p junction, so the SAW-driven EL has a shorter length than the RF pulse. However, it is not clear why the increase of the SAW-driven EL at the beginning is slower than the decrease at the end. In principle, the increase and the decrease should happen at the same rate. Furthermore, in Figure 5.14(c) and (e), a peak can be seen at the beginning of the crosstalk-driven EL. This may be related to a charging effect, as mentioned in Section 5.2.2.

Interestingly, in Figure 5.14(a) there is no sign of the crosstalk-driven EL, meaning the effect of the crosstalk is almost negligible at $P_{\mathrm{RF}} = 11.5\,\mathrm{dBm}$. The integrated EL driven by the SAW and the crosstalk as a function of P_{RF} is shown in Figure 5.15(a). The SAW-driven EL is always much higher than the crosstalk-driven EL. As shown in Figure 5.15(b), the ratio of the crosstalk-driven EL to the SAW-driven EL is less than 0.02 when $P_{\mathrm{RF}} < 14\,\mathrm{dBm}$. Therefore, the effect of the crosstalk is negligible when a lower P_{RF} is used. As mentioned in Section 5.2, this crosstalk-free SAW-driven EL is ideal for making a SAW-driven single-photon source. Compared with TKH02, which has significant crosstalk-driven EL, TKH03 exhibits improved performance in terms of the SAW-driven EL. This can be attributed to the etched trench between the IDT and the n-i-p junction on TKH03. This etched trench eliminates the potential conductive path between the IDT and the junction so that the voltage on the IDT cannot directly affect the junction via the quantum well. As a consequence, the effect of the crosstalk is reduced and is observable only when P_{RF} is high.

Figure 5.14(b) shows the detailed features of the SAW-driven EL at $P_{\mathrm{RF}} = 11.5\,\mathrm{dBm}$, where periodic peaks can be clearly seen. Each peak exhibits a sharp rise and then an exponential decay with a time constant of 100–200 ps, which corresponds to the carrier lifetime. Also, the period of these peaks is about 860 ps, corresponding to a SAW frequency of 1.163 GHz. The shape of an individual peak can be understood as the injection of electrons by the SAW. When an electron is pumped across the n-i-p junction by the SAW, the probability of an electron being in the region of holes will instantly increase to one as the electron arrives. The probability of the electron being in the conduction band will then decay exponentially as the electron has a chance of recombining with a hole. Since the EL is proportional to the product of the numbers of electrons and holes in the case of weak injection [130], if the number of holes is not significantly affected by the SAW, a sharp rise and then an exponential decay in the EL can therefore be observed. Hence, Figure 5.14(b) indicates that this EL is due to the SAW-driven charge transport, which is the key mechanism of a SAW-driven single-photon source. Note that each peak in Figure 5.14(b) only decays to 20% of its peak value when the next peak appears. For a perfect single-photon source, the photon emission from an excitation should decay to 0% before a next excitation occurs so that single photons from two different excitations will not overlap. One reason for this non-zero low level in

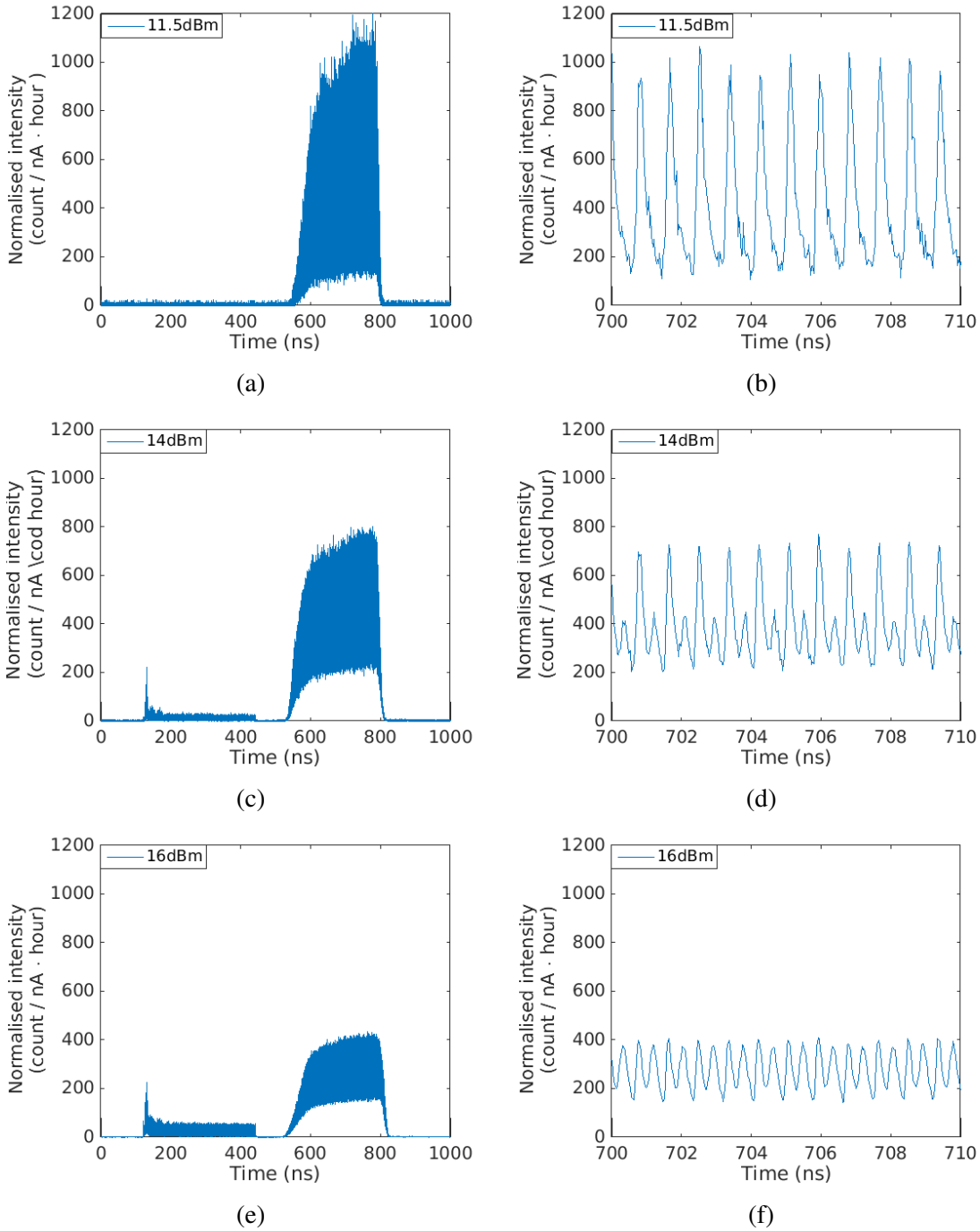

Fig. 5.14 Time-correlated histograms of the EL on TKH03 when pulsed RF signals at (a) 11.5 dBm, (c) 14 dBm, and (e) 16 dBm are applied to the IDT. The crosstalk-driven EL is only observable in (c) and (e). Magnified histograms of the SAW-driven EL in (a), (c), and (e) are shown in (b), (d), and (f) respectively. Clear periodic peaks due to the 1.163 GHz SAW can be seen in (b) while unexpected secondary peaks appear in (d) and (f).

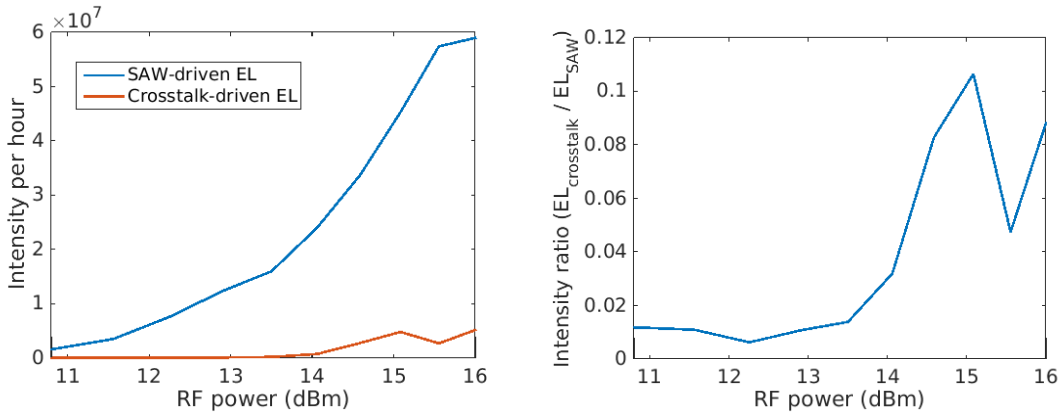

(a) (b)

Fig. 5.15 (a) Integrated SAW-driven EL and crosstalk-driven EL as a function of P_{RF}. (b) Ratio of the crosstalk-driven EL to the SAW-driven EL as a function of P_{RF}.

the EL is that the carrier lifetime of the SAW-driven electrons is not short enough. Another reason may be that there is a non-zero background in the SAW-driven EL, which could be related to the background of the detector or a constant density of electrons trapped in the region of holes. A more detailed estimation of the carrier lifetime and the background will be presented in the next section.

On the other hand, if the SAW can affect the density of holes, more complicated features will appear. Figures 5.14(d) and (f) show the detailed features of the SAW-driven EL at $P_{\mathrm{RF}} = 14$ dBm and 16 dBm. Unexpected secondary peaks appear about 430 ps after the main peaks, which is half of the SAW period. Since this time corresponds to the maximum of the SAW potential arriving at the region of holes, these secondary peaks are not caused by the regular SAW-driven charge transport. They could be related to the higher harmonics of the SAW. For example: a second harmonic SAW with a frequency of $2f_{\mathrm{SAW}}$ can transport electrons twice in one original SAW period and lead to these secondary peaks. However, even harmonics of the SAW should not exist in this kind of IDT, and AWG waveform 1 used in this measurement should have no $2f_{\mathrm{SAW}}$ component. A plausible explanation for these secondary peaks is that the stronger SAW actually modulates the density of holes. At 430 ps after the SAW-driven charge transport, the SAW potential reaches its maximum in the region of holes. If the SAW amplitude is large, the maximum of the SAW potential can raise the valence band and attract more holes. As a result, the density of holes is maximised at this moment, and a peak in the EL thus appears 430 ps after the main peak.

Although these extra secondary peaks had appeared when the AWG-waveform with $P_{\mathrm{RF}} > 14$ dBm were used in the earlier time-resolved measurements, it has to be noted that these secondary peaks did not occur, as seen in Figure 5.16(a), when a synchronised RF

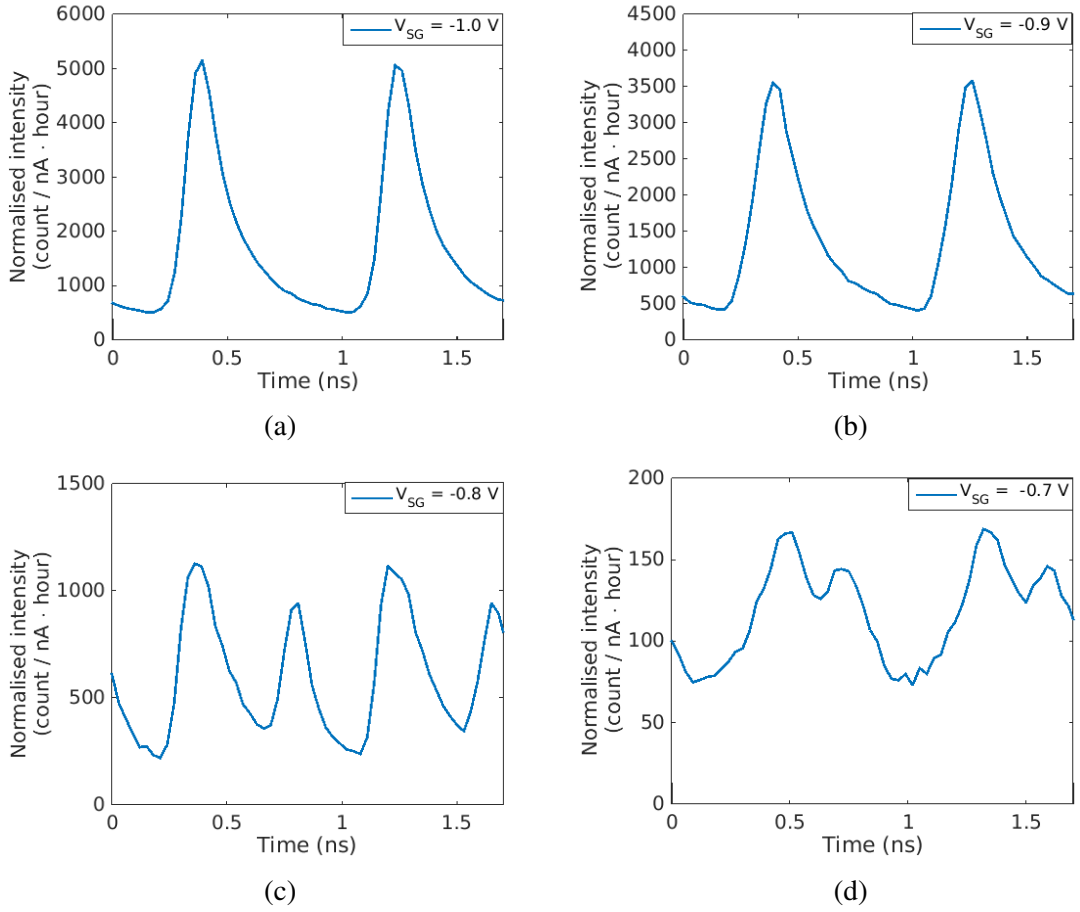

Fig. 5.16 Time-correlated histograms at different $V_{\mathrm{SG(hole)}}$, where $V_{\mathrm{SG(hole)}}$ = (a) -1 V, (b) -0.9 V, (c) -0.8 V, and (d) -0.7 V. Secondary peaks appear in (c) and (d).

source with an even higher P_{RF} was later used at a similar gate-voltage condition, where $V_{\mathrm{SD}} = 1.45$ V, $V_{\mathrm{SiG}} = -0.35$ V, $f_{\mathrm{RF}} = 1.163$ GHz, $P_{\mathrm{RF}} = 18$ dBm, and $V_{\mathrm{SG(hole)}} = -1$ V. Since the measurements using the synchronised RF source were carried out after the measurements using the AWG-waveform RF, it might be that the properties of the SAW-driven n-i-p junction TKH03 had drifted over time so that a much higher P_{RF} was actually required to cause these secondary peaks. Another explanation is that these secondary peaks are related to other frequency components in AWG waveform 1. Further investigation is needed to understand more about these secondary peaks.

An effect possibly related to the modulation of the density of holes was also observed when hole-surface-gate voltage $V_{\mathrm{SG(hole)}}$ was closed to its threshold (about -0.8–-0.7 V). Figure 5.16(a), (b), (c) and (d) show the averaged EL at $V_{\mathrm{SG(hole)}} = -1, -0.9, -0.8$, and -0.7 V respectively. The EL was normalised by the source-drain current I_{SD} (0.27, 0.12, 0.10 and 0.69 nA respectively) and the measurement time. Periodic peaks in the SAW

period can be seen at $V_{\mathrm{SG(hole)}} = -1\,\mathrm{V}$ and $-0.9\,\mathrm{V}$ while extra secondary peaks appear when $V_{\mathrm{SG(hole)}} = -0.8\,\mathrm{V}$ and $-0.7\,\mathrm{V}$. This may be explained as the SAW potential causing a more significant modulation of the density of holes when $V_{\mathrm{SG(hole)}}$ is closer to the threshold. If $V_{\mathrm{SG(hole)}}$ is almost at the threshold, a small variation in the valence band can give rise to a big change in the density of holes. This might result in the secondary peaks in Figure 5.16(c), where $V_{\mathrm{SG(hole)}} = -0.8\,\mathrm{V}$. On the other hand, when $V_{\mathrm{SG(hole)}}$ is well above the threshold, the density of holes that is already high will not be affected too much by the small variation in the valence band. The temporal profile of the EL in Figure 5.16(a) and (b) ($V_{\mathrm{SG(hole)}} = -1\,\mathrm{V}$ and $-0.9\,\mathrm{V}$) is therefore dominated by the density of electrons pumped by the SAW. However, it is not clear why the main peaks and the secondary peaks at $V_{\mathrm{SG(hole)}} = -0.7\,\mathrm{V}$ (see Figure 5.16(d)) seem to shift from their usual positions, as seen in Figure 5.16(c). The distance between a main peak and a neighbouring secondary peak is about 250 ps, which is less than half of the SAW period, so the argument about the modulation of the density of holes cannot apply in Figure 5.16(c). It may speculated that, when $V_{\mathrm{SG(hole)}} = -0.7\,\mathrm{V}$, the EL might occur in two different spots since this lower $V_{\mathrm{SG(hole)}}$ is not sufficient to confine the SAW-driven electrons to the n-i-p junction, which can be checked by the low photon emission efficiency η_{emit} in Figure 5.16(d). The time difference between the main and the secondary peaks in Figure 5.16(d) might correspond to the SAW-propagation time between these two spots. Nonetheless, this speculation will need to be confirmed by using the μPL system to take a wider image of the EL when $V_{\mathrm{SG(hole)}} = -0.7\,\mathrm{V}$.

Figure 5.17 shows the dependence of the SAW-driven EL and the crosstalk-driven EL on applied frequency, where $V_{\mathrm{SD}} = 1.45\,\mathrm{V}$, $V_{\mathrm{SiG}} = -0.6\,\mathrm{V}$, $V_{\mathrm{SG(hole)}} = -1\,\mathrm{V}$, $P_{\mathrm{RF}} = 13\,\mathrm{dBm}$, and AWG waveform 1 is used. Compared with TKH02 in Figure 5.12, the SAW-driven EL and the crosstalk-driven EL in TKH03 exhibit different behaviours. The SAW-driven EL shows a peak at 1.163 GHz, indicating that the SAW-driven charge transport only occurs at the resonant frequency of the IDT. On the other hand, the crosstalk-driven EL seems to be suppressed at the resonant frequency. This might be understood as more energy being converted into the SAW at the resonant frequency so that less energy is radiated as crosstalk. A suppression of the crosstalk will then appear at the resonant frequency of the IDT. However, it might also be that the black-helium-3 sample space happened to have such a cavity resonance. Further investigation will be needed in order to reach a conclusion.

5.3.2 Fitting for SAW-driven Electroluminescence

As shown in the previous section, using the 1.163 GHz SAW and the Picoharp 300 counter, individual peaks in the SAW-driven EL can be clearly observed. In order to extract more precise information about the carrier lifetime of the SAW-driven electrons and the possible

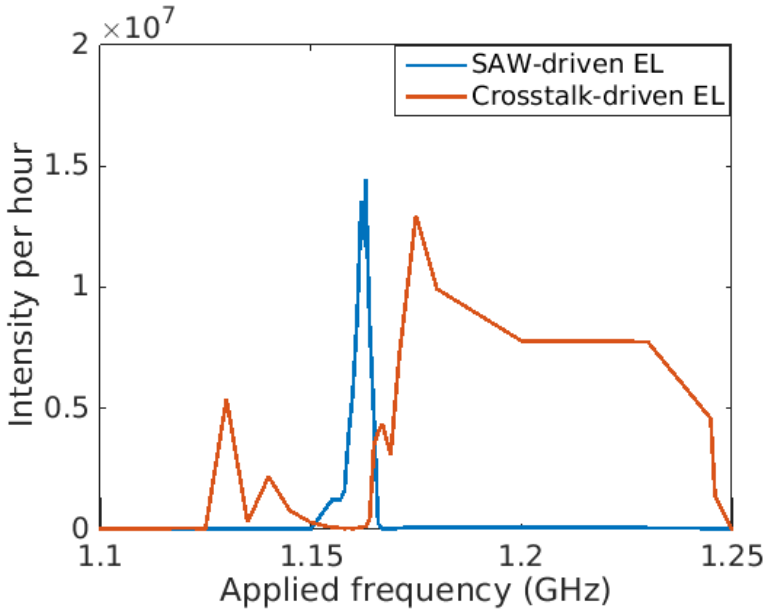

Fig. 5.17 Dependence of the SAW-driven EL and the crosstalk-driven EL on applied frequency. The SAW-driven EL exhibits a peak at 1.163 GHz while the crosstalk-driven EL shows no signal at 1.163 GHz.

non-zero background in the EL, a theoretical function describing the SAW-driven EL has to be established to fit the measurement results. Because the SAW-driven charge transport gives rise to a sudden increase in the density of electrons in the region of holes, and the density of electrons then decays due to the electron-hole recombination, the basic function for each peak in a time-correlated histogram will be

$$\begin{aligned} f(t,t_0,A_{\mathrm{EL}},\tau) &= 0 && \text{when} \quad t < t_0\,; \\ &= A_{\mathrm{EL}} \cdot \exp((t-t_0)/\tau) && \text{when} \quad t \geq t_0\,, \end{aligned} \tag{5.3}$$

where t is time, t_0 is the arrival time of the SAW potential minimum leading to the peak, A_{EL} is the amplitude (peak value), and τ is the carrier lifetime of SAW-driven electrons. Since the EL is driven by a series of SAW potential minima, the overall function can be written as

$$F(t,t_0,A_{\mathrm{EL}},\tau,t_{\mathrm{SAW}}) = \sum_{i=0,1,2,3\ldots} f(t,t_0+i\cdot t_{\mathrm{SAW}},A_{\mathrm{EL}},\tau)\,, \tag{5.4}$$

where t_{SAW} is the period of the SAW. Figure 5.18(a) shows an example of F with $t_0 = 1$, $A_{\mathrm{EL}} = 1$, and $\tau = 0.5$. Note that each peak in Figure 5.18(a) does not decay to 0 when the next peak is shown, which is due to the finite carrier lifetime. Compared with a real time-correlated histogram such as that in Figure 5.16(a), the basic function F in Figure 5.18(a)

exhibits unrealistic sharp peaks because the effect of jitter (uncertainty in time) is not included in F. A source for the jitter is the response of the IDQ-ID100 SPAD, which has a timing resolution of 40 ps. Ideally, the response of a perfect SPAD should be a delta function. However, the response curve of an IDQ-ID100 SPAD exhibits a sharp peak with an FWHM of 40 ps and a 1 ns long decaying tail, as shown in Figure 5.19 [131]. This response curve works as a point spread function $PSF(t)$ so that the measured histogram will be blurred. In addition, the temporal uncertainty of SAW-driven electrons, originating from uncertainty about the position of electrons in each SAW potential minimum, can also be another source of jitter. This jitter in the SAW-driven charge transport can be expressed as a Gaussian function

$$g(t,w) = \frac{1}{w\sqrt{2\pi}} \exp\left(-\frac{1}{2}\left(\frac{t}{w}\right)^2\right), \tag{5.5}$$

where w is the parameter related to the FWHM according to FWHM $\sim 2.3w$. Considering these sources of jitter, the time-resolved histogram $H(t)$ of the SAW-driven EL can be described as the convolution of the basic function F, the Gaussian function g, and the response curve PSF

$$H(t) = ((F * g) * PSF)(t) + BG_{\mathrm{EL}}, \tag{5.6}$$

where BG_{EL} is a constant for a constant background in the SAW-driven EL, which may result from a constant density of electrons trapped in the region of holes or a background signal from the SPAD. $H(t)$ is therefore determined by those previously mentioned parameters t_0, t_{SAW}, τ, w, A and BG_{EL}. Figure 5.18(b) shows an example of $H(t)$ with $t_0 = 1$, $A_{\mathrm{EL}} = 1$, $\tau = 0.5$, $BG = 0$, and $w = 0.05$. It can be seen that the peaks become more blurred when the effect of jitter is added.

If an experimental time-resolved histogram is produced with a known SAW period t_{SAW}, information about the carrier lifetime τ, the jitter in the SAW-driven charge transport w, and the background level BG_{EL} can be obtained by fitting the histogram to H. Figure 5.20(a) shows an averaged time-correlated histogram of the SAW-driven EL where $V_{\mathrm{SD}} = 1.45$ V, $I_{\mathrm{SD}} = 0.6$ nA, $V_{\mathrm{SiG}} = -0.6$ V, $f_{\mathrm{RF}} = 1.163$ GHz, and $P_{\mathrm{RF}} = 18$ dBm. Figure 5.20(b) shows the best-fit curve for the data, using a nonlinear least-squares method, which gives $\tau = 102 \pm 7$ ps, $w = 37 \pm 2$ ps, and $BG_{\mathrm{EL}} = 182 \pm 20$. The carrier lifetime τ of 102 ps is much shorter than the SAW period of 860 ps so that single photons from consecutive SAW potential minima do not overlap significantly, which is beneficial for making a SAW-driven single-photon source. This short carrier lifetime may be related to a pronounced non-radiative recombination rate due to surface traps, which causes the low photon emission efficiency η_{emit}. The width parameter w of 37 ps corresponds to an FWHM of 85 ps in the jitter of the SAW-driven charge transport. This 85 ps temporal uncertainty is equivalent to a spatial uncertainty of

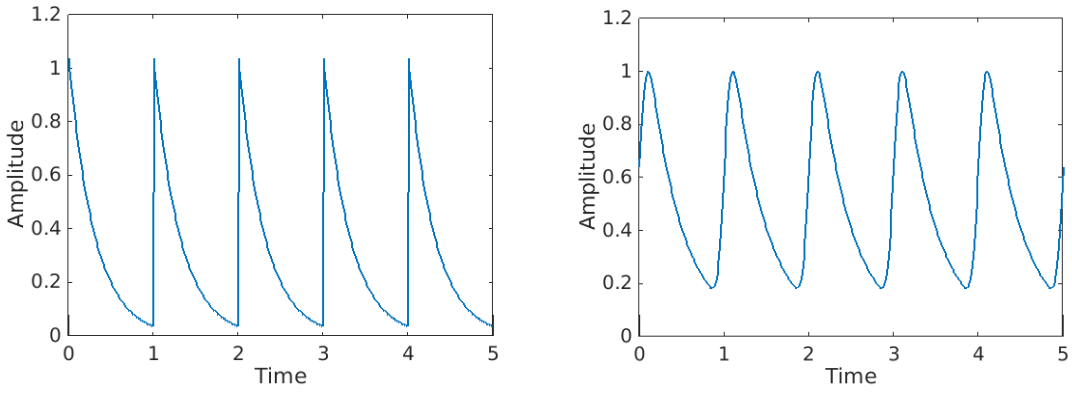

(a) (b)

Fig. 5.18 (a) Example of function F with $t_0 = 1$, $A_{\mathrm{EL}} = 1$, and $\tau = 0.5$. (b) Example of function H with $t_0 = 1$, $A_{\mathrm{EL}} = 1$, $\tau = 0.5$, $BG_{\mathrm{EL}} = 0$, and $w = 0.05$.

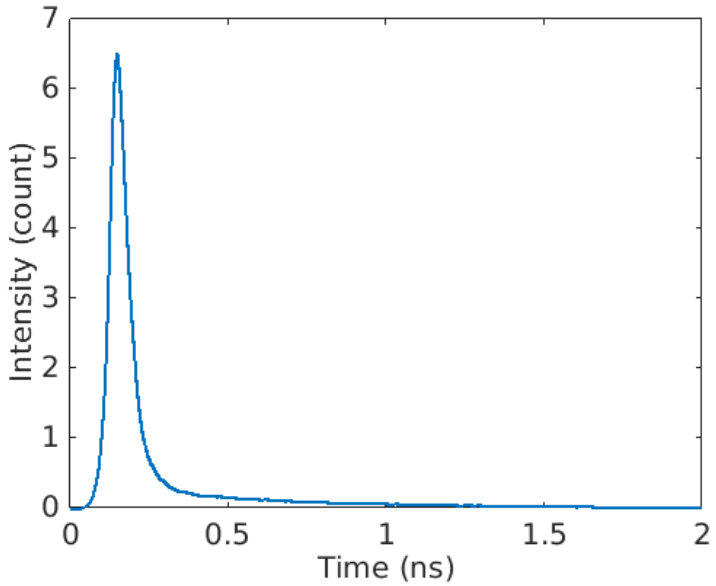

Fig. 5.19 Response curve of IDQ-ID100 SPAD. Diagram from [131]. FWHM of the peak is about 40 ps, and a 1 ns decaying tail can be observed.

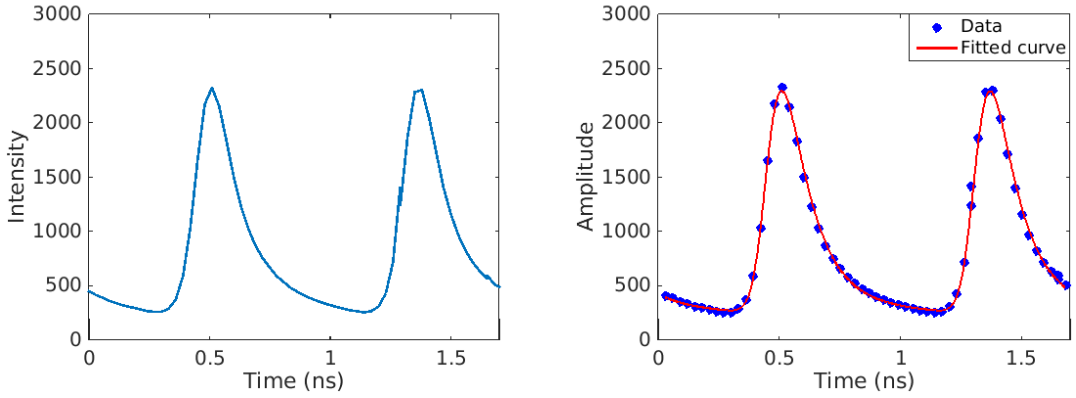

(a) (b)

Fig. 5.20 (a) Averaged time-correlated histogram of the SAW-driven EL where $V_{SD} = 1.45$ V, $I_{SD} = 0.6$ nA, $V_{SiG} = -0.6$ V, $f_{RF} = 1.163$ GHz, and $P_{RF} = 18$ dBm. (b) Best-fit curve for the histogram in (a), using function H. The best fitted curve gives $\tau = 102 \pm 7$ ps, $w = 37 \pm 2$ ps, and $BG_{EL} = 182 \pm 20$.

$V_{SAW} \cdot FWHM = 2850 \times 85 \times 10^{-12}$ m $= 242$ nm, meaning a SAW-driven electron might oscillate within a range of 242 nm around a SAW potential minimum ($\lambda_{SAW} = 2.5\,\mu$m). This uncertainty should be reduced if a better confinement of the SAW-driven electrons is achieved. Finally, a constant background BG_{EL} of 182 is roughly 8% of the peak value of 2300. The true origin of this background needs further study. Nonetheless, this constant background will have to be considered in the analysis of photon antibunching in the SAW-driven EL, which will be presented in the next chapter.

5.4 Conclusion

In summary, the time-resolved setups and the time-resolved measurement results of the SAW-driven EL have been presented in this chapter. First, the principle of time-resolved measurements and the methods for producing SAWs that are synchronised to timing pulses are introduced. Next, the time-correlated histograms from the ZnO-deposited TKH02 are presented. Using continuous RF input, the histograms and their Fourier transforms indicate that the SAW and the crosstalk both contribute to the EL on TKH02. When a pulsed RF signal is used, the effects of the SAW and the crosstalk can be separately observed in the time-correlated histograms. This separation allows the behaviours of these two signals to be studied individually as functions of applied frequency and measurement time. In the last part of this chapter, the time-resolved measurements on the optimised SAW-driven n-i-p junction TKH03 are shown. The optimised design largely suppresses the effect of the crosstalk.

Also, using the high-performance Picoharp 300 counter and the 1.163 GHz SAW, features showing the dynamics of the SAW-driven charge transport can be clearly observed in the time-correlated histogram. On the other hand, the unexpected secondary peaks at certain conditions suggest that the SAW may modulate the density of holes when it is strong or $V_{\mathrm{SG(hole)}}$ is close to its inducing threshold. Finally, a function describing the SAW-driven EL is introduced for fitting the measurement results. The carrier lifetime of 102 ps, which is short compared with the SAW period of 860 ps, indicates that TKH03 is a promising design for the observation of photon antibunching in SAW-driven EL.

Chapter 6

Photon Antibunching in SAW-driven Electroluminescence

In Chapter 4, the optimised SAW-driven n-i-p junction TKH03 showed clear SAW-driven charge transport and SAW-driven electroluminescence (EL) when an RF signal is applied to an IDT at its resonant frequency of 1.163 GHz. Subsequently in Chapter 5, time-resolved measurements confirmed that the EL is due to periodic injection of SAW-driven electrons into the region of holes. Fitting of the EL shows that the carrier lifetime of these SAW-driven electrons is about 100 ps, which is much shorter than the SAW period of 860 ps. Hence, it is promising to observe photon antibunching or even single-photon emission in the SAW-driven EL from TKH03.

This chapter focuses on the second-order correlation function ($g^{(2)}(\Delta t)$) of the SAW-driven EL, which can reveal non-classical photon statistics in a quantum photon source. First, a setup for measuring $g^{(2)}(\Delta t)$ and the principle of the setup are introduced. Then, the autocorrelation histograms of the SAW-driven EL are presented along with data analysis that shows evident photon antibunching driven by the SAW. Finally, theoretical calculation, simulation, and modelling related to SAW-driven single-photon sources are demonstrated to learn more from the measurement results and to gain ideas for future improvements.

6.1 Hanbury Brown-Twiss Experiment Setups

Photon antibunching and single-photon emission can be tested by measuring the second-order correlation function $g^{(2)}(\Delta t)$ of the photons. This can be done using a Hanbury Brown-Twiss (HBT) experiment setup, which was originally designed to measure the angular diameter

of stars [16]. Nowadays, the HBT experiment setup is commonly employed in the field of quantum optics.

6.1.1 Autocorrelation Histogram and Second-order Correlation Function

A schematic of the HBT setup used in this thesis is shown in Figure 6.1, where a beam of photons from a light source is split into two beams by a 50:50 fibre beamsplitter. Each beam is sent to a single-photon avalanche photodiode (SPAD). These two SPADs will produce signal pulses when they are triggered by the incoming photons. In a start-stop autocorrelation method, a signal pulse from SPAD 1 (start) will cause the time-to-digital converter (counter) to begin timing until the counter receives a signal pulse from SPAD 2 (stop). The counter then records one coincidence at the time delay between these two signal pulses. A simplified example is shown in Figure 6.2. The two beams of photons (Figure 6.2, left) will give rise to the autocorrelation histogram (Figure 6.2, right), which is the number of coincidences as a function of time delay Δt. Experimentally, if SPADs are used in an HBT setup and the probability of detecting one photon in one time interval is much smaller than 1, the normalised autocorrelation histogram can be approximated as the second-order correlation function $g^{(2)}(\Delta t)$, which can be expressed as

$$g^{(2)}(\Delta t) = \frac{\langle \psi | \hat{a}^\dagger(t)\hat{a}^\dagger(t+\Delta t)\hat{a}(t+\Delta t)\hat{a}(t) | \psi \rangle}{\langle \psi | \hat{a}^\dagger(t)\hat{a}(t) | \psi \rangle^2} \tag{6.1}$$

in quantum mechanics, where $\hat{a}$ and $\hat{a}^\dagger$ represent the annihilation and creation operators for the photon number states in an electromagnetic field ψ.

If a stream of perfect single photons is measured by the HBT setup, since a single photon cannot be detected by both SPADs, the two SPADs will never produce signal pulses at the same time (as shown in Figure 6.3, left). As a result, there will be no coincidence occurring at time delay $\Delta t = 0$. Hence, a perfect single-photon source should exhibit $g^{(2)}(0) = 0$. On the other hand, if a practical single-photon source, produced by periodic excitations, can emit single photons most of the time, but also has a small probability of emitting multiple photons, then $g^{(2)}(0)$ will be greater than, but close to, 0. So the number of coincidences will be greatly suppressed at $\Delta t = 0$, as can be seen in Figure 6.3, bottom right, where the autocorrelation histogram exhibits periodic peaks corresponding to the excitation period and a specially suppressed peak at $\Delta t = 0$ (Figure from [13]). Generally, a quantum light source, which can produce photon number states, will manifest $g^{(2)}(0) < 1$, indicating that photon

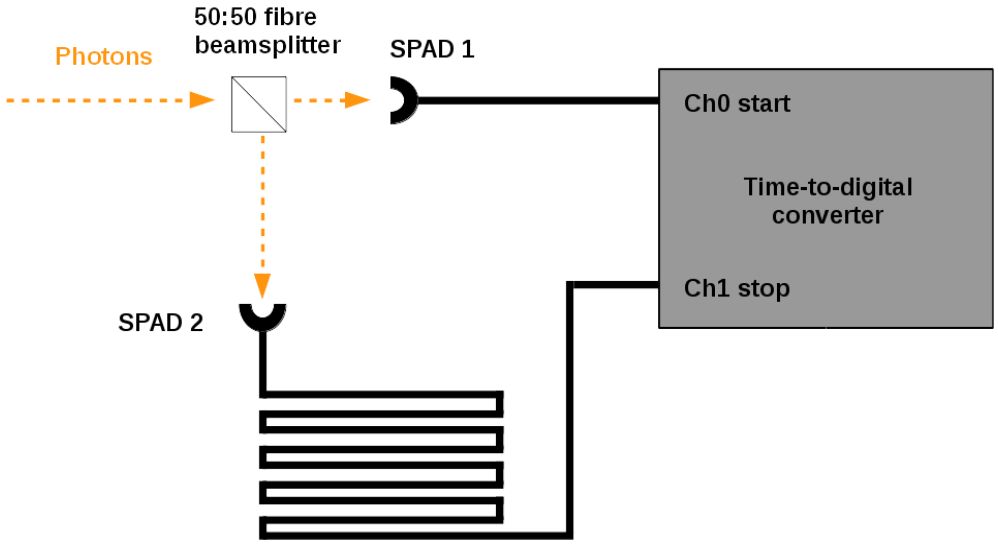

Fig. 6.1 Schematic of the Hanbury Brown-Twiss experimental setup used in this thesis. A stream of photons coming via an optical fibre is split into two beams by a 50:50 fibre beamsplitter. Each of the two beams is sent to one of the single-photon avalanche photodiodes (SPAD 1 and 2). Signal pulses triggered by detection events are connected to two input channels of a counter via BNC cables. An autocorrelation is recorded as the counter records the correlation coincidences of the two input channels.

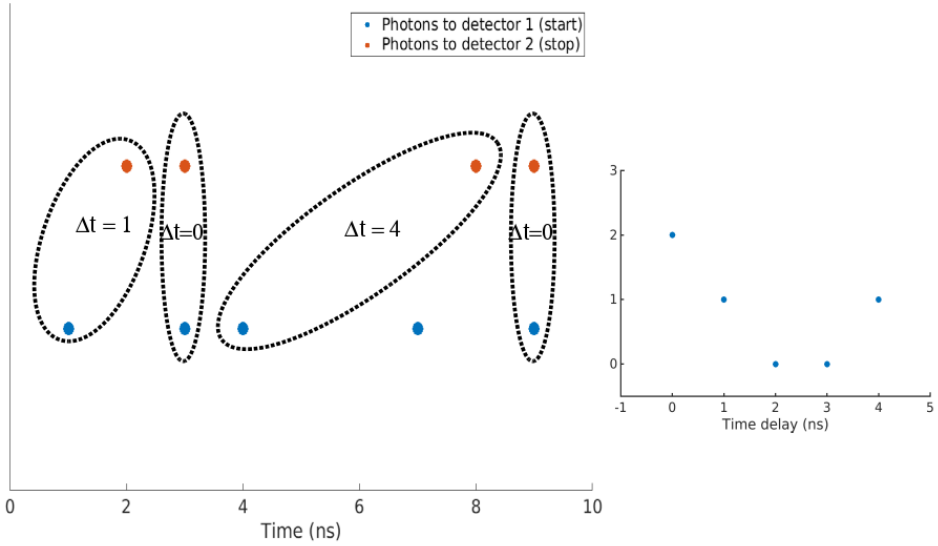

Fig. 6.2 Simplified example showing how a counter records an autocorrelation histogram using the start-stop method. Left: Detection events in the two photon detectors as a function of time. The counter records coincidences as a function of time delay Δt using the start-stop method. For instance, the first pair (a start event (blue) and a stop event (orange)) will lead to one coincidence at $\Delta t = 1$. Right: The autocorrelation histogram caused by the detection events shown to the left.

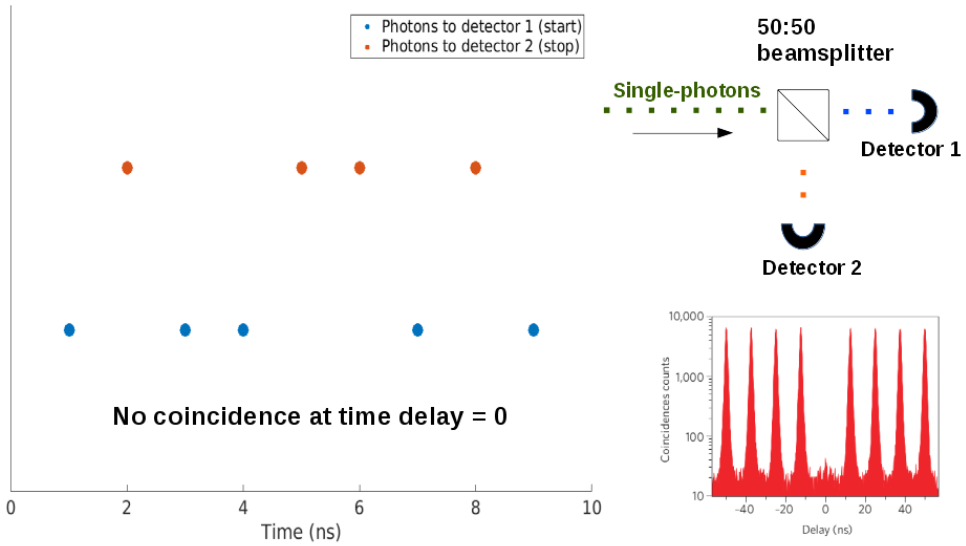

Fig. 6.3 Example showing the HBT experiment with a single-photon source. Left: Detection events in the two photon detectors as a function of time. Events in the two detectors never occur at the same time since a single photon can only be detected by one detector. Top right: The HBT setup with incoming single photons. Bottom right: Autocorrelation histogram of a single-photon source. The signal at $\Delta t = 0$ is suppressed due to photon antibunching.

antibunching is occurring. A common criterion for a quantum light source to be considered as a single-photon source is $g^{(2)}(0) < 0.5$ [55, 132, 133].

6.1.2 Estimation of built-in time delay of HBT Setups

A Picoharp 300 counter with a minimum timing resolution of 4 ps was used in the HBT setup. An IDQ-ID100 fibre-coupled SPAD (jitter = 40 ps) and a PDM free-space SPAD (jitter = 50 ps), with a fibre-coupling adapter made by Professor Richard Phillips, were employed as two detectors in an earlier setup. Two identical IDQ-ID100 SPADs have subsequently been used in a more recent setup. Experimentally, due to the difference between the optical paths to the two detectors, and the electrical cables to the two channels of the counter, an autocorrelation histogram will exhibit a second-order correlation function shifted by a built-in time delay Δt_0. This delta Δt_0 corresponds to the overall time difference because of the optical paths, the cables, and the internal time difference of the two channels.

$$\Delta t_0 = \Delta t_{(\mathrm{BS-SPAD2})} - \Delta t_{(\mathrm{BS-SPAD1})} + \Delta t_{(\mathrm{SPAD2-stop})} - \Delta t_{(\mathrm{SPAD1-start})} + \Delta t_{(\mathrm{start-stop})}\,, \quad (6.2)$$

where $\Delta t_{(\mathrm{BS-SPAD1})}$ ($\Delta t_{(\mathrm{BS-SPAD2})}$) is the travelling time of a photon from a beamsplitter to SPAD 1 (SPAD2), $\Delta t_{(\mathrm{SPAD1-start})}$ is the propagation time of a signal pulse from SPAD 1 to

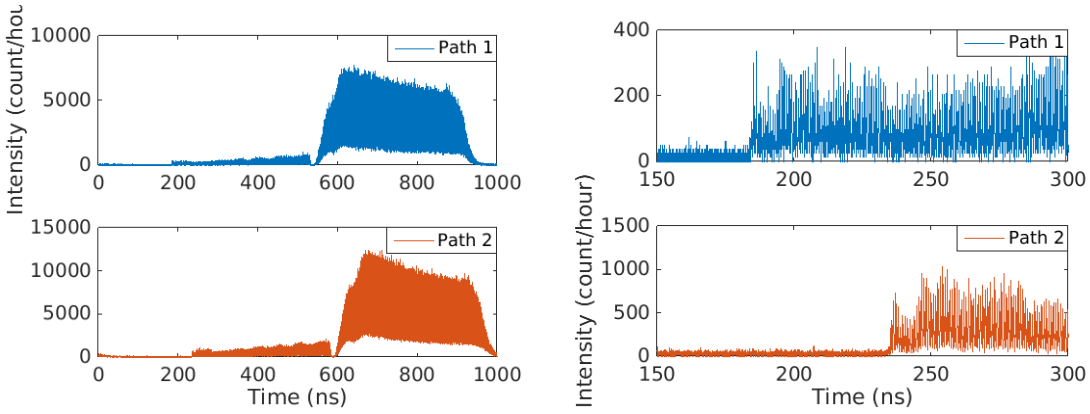

(a) (b)

Fig. 6.4 (a) Time-correlated histograms of SAW-driven EL measured using path 1 (BS–SPAD 1–counter, top panel) and path 2 (BS–SPAD 2–counter, bottom panel). (b) Magnified histograms showing a shift of ~ 51 ns between the two.

channel 0 (start), $\Delta t_{(\mathrm{SPAD2-stop})}$ is the propagation time of a signal pulse from SPAD 2 to channel 1 (stop), and $\Delta t_{(\mathrm{start-stop})}$ is the internal time difference between the two channels. In a start-stop autocorrelation method, the effect of photon antibunching can only be observed if $\Delta t_0 \geq 0$. Hence, a 10 m long BNC cable was added to SPAD 2 in order to cause a $\Delta t_{(\mathrm{SPAD2-stop})} \sim 50$ ns, so Δt_0 would be around 50 ns if other terms in Equation 6.2 are relatively small.

In fact, Δt_0 can be determined more accurately by using the two paths (BS-SPAD 1-counter and BS-SPAD 2-counter) to perform time-resolved measurements of one EL signal. By comparing the time-correlated histograms using the two paths, the first four terms $\Delta t_{(\mathrm{BS-SPAD2})} - \Delta t_{(\mathrm{BS-SPAD1})} + \Delta t_{(\mathrm{SPAD2-stop})} - \Delta t_{(\mathrm{SPAD1-start})}$ can be obtained. Figure 6.4(a) shows the time-correlated histograms of EL driven by a pulsed RF signal, measured using path 1 (BS-SPAD 1-counter) and path 2 (BS-SPAD 2-counter) in the more recent HBT setup. The crosstalk-driven EL and the SAW-driven EL both can be seen in the histograms. The profiles of the two histograms are almost identical, except for a shift in the X axis, which is more obvious in the magnified plots in Figure 6.4(b). By comparing the shift between the two histograms, it was found that the time difference due to the optical paths and electrical cables was about 51 ns.

In addition, there might be an internal time difference $\Delta t_{(\mathrm{start-stop})}$ between the two channels of the counter. This can be simply checked by sending two pulses with a known time difference Δt_{test} to the two channels, and measuring the autocorrelation histogram. If $\Delta t_{(\mathrm{start-stop})}$ is significant, the position of the coincidence peak will deviate from Δt_{test}. Figure 6.5 shows the correlation histogram of two pulses with $\Delta t_{\mathrm{test}} = 85.6$ ns. A peak is

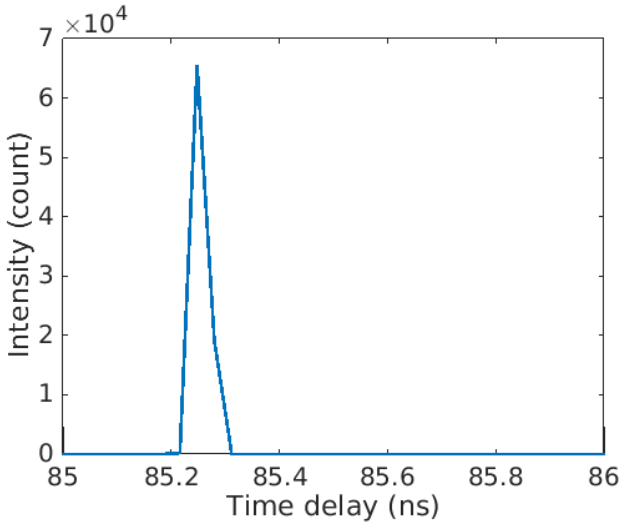

Fig. 6.5 Correlation histogram of two pulses with a known time difference $\Delta t_{\text{test}} = 85.6\,\text{ns}$. A peak in the histogram appears at $\Delta t = 85.25\,\text{ns}$.

shown at 85.25 ns, indicating $\Delta t_{(\text{start}-\text{stop})} = -0.35\,\text{ns}$. Therefore, in this more recent HBT setup, the overall time delay $\Delta t_0 = 51 - 0.35 = 50.65\,\text{ns}$.

6.2 Autocorrelation Histograms of SAW-driven Electroluminescence

Autocorrelation histograms of SAW-driven EL were taken by sending the EL signal via an optical fibre, without any spectral filtering, to the HBT setup discussed earlier. Histograms presented below are all taken from the optimised SAW-driven n-i-p junction TKH03 in the black-helium-3 cryostat. Because this cryostat uses liquid helium more efficiently and devices are more stable in it, compared with the μPL cryostat, the black-helium-3 cryostat is more suitable for taking autocorrelation histograms of SAW-driven EL, which usually take a few days to accumulate enough coincidences due to the low emission efficiency η_{emit}.

6.2.1 Stabilising SAW-driven Source-drain Current

Ideally, autocorrelation histograms should be taken at the quantised SAW-driven current $I_{\text{SD}} = 1ef_{\text{RF}} = 0.186\,\text{nA}$. However, quantisation of the SAW-driven current cannot be observed in TKH03, possibly because the confinement of the SAW potential is not good enough. Hence, I_{SD} was adjusted to 0.8-0.9ef_{RF} so that the probability of having one electron in each SAW minimum was high and the effect of the vacuum state was minimised [133]. Nonetheless,

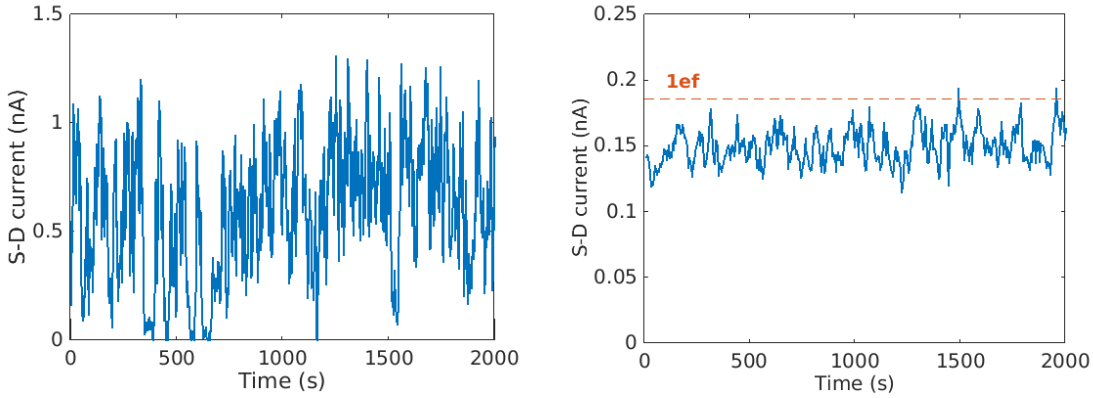

(a) (b)

Fig. 6.6 (a) SAW-driven current as a function of time. The current drifts between 0 and 1 nA when source-drain bias and SAW power are fixed. (b) SAW-driven current adjusted using a PID control loop. The average current $\sim 0.8 f_{\mathrm{RF}} = 0.15$ nA varies within a range of ± 0.02 nA.

the SAW-driven current I_{SD} could not be kept stable by just keeping the gate voltages, the S-D bias, and the SAW power fixed. For example: Figure 6.6(a) shows I_{SD} as a function of time when $V_{\mathrm{SD}} = 1.45$ V, $V_{\mathrm{SiG}} = -0.75$ V, and $P_{\mathrm{RF}} = 10$ dBm. I_{SD} drifts from 0 to 1 nA over a 2000 s period of measurement. The instability of I_{SD} made it difficult to record an autocorrelation histogram when $I_{\mathrm{SD}} = 0.8$-$0.9 e f_{\mathrm{RF}}$. This instability may be related to a charging effect near the n-i-p junction so that the potential drifts and affects the SAW-driven charge transport. In order to deal with this instability, a PID control loop was used so that constant adjustment could be made to V_{SD} to keep I_{SD} around 0.8-$0.9 e f_{\mathrm{RF}}$. Figure 6.6(b) shows I_{SD}, stabilised by a PID control loop, as a function of time when $V_{\mathrm{SiG}} = -0.6$ V and $P_{\mathrm{RF}} = 18$ dBm. As can be seen, I_{SD} was kept fairly stable around 0.15 nA so that an autocorrelation histogram could be taken at the proper condition. Note that I_{SD} still occasionally drifted above $1 e f_{\mathrm{RF}}$, so the coincidences that occurred at these moments should be removed from the final histogram in order to show the real $g^{(2)}(\Delta t)$ when the SAW-driven charge transport is in the single-electron regime.

6.2.2 Observation of Photon Antibunching

When I_{SD} is much higher than $1 e f_{\mathrm{RF}}$, the effect of photon antibunching is expected to be less obvious. Figure 6.7(a) shows the autocorrelation histogram of the SAW-driven EL at the condition described in Figure 6.6(a), where I_{SD} drifted from 0 to 1 nA and $I_{\mathrm{SD}} \sim 0.6$ nA $\sim 3 e f_{\mathrm{RF}}$ on average. Periodic peaks with a period of 860 ns, resulting from the SAW frequency $f_{\mathrm{RF}} = 1.163$ GHz, can be resolved in the histogram. These peaks indicate that the

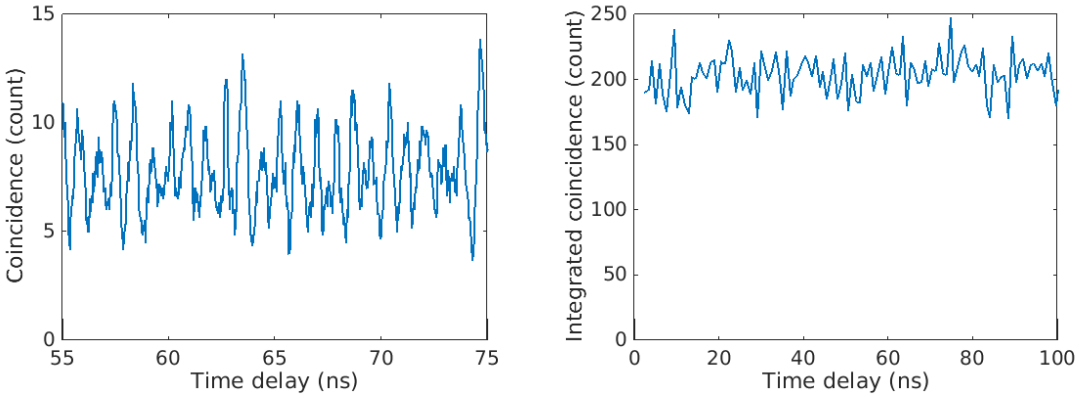

(a) (b)

Fig. 6.7 (a) Autocorrelation histogram of the SAW-driven EL when $I_{SD} \sim 3ef_{RF}$. Clear periodic features corresponding to the 860 ps SAW period can be seen. (b) Signal from each peak (integrated over one SAW period) as a function of time delay. No obvious suppression due to photon antibunching can be observed around 64 ns.

histogram is caused by the autocorrelation of the SAW-driven EL. Δt_0 of the HBT setup used for Figure 6.7 was estimated to be about 64 ns, which means a suppressed peak due to photon antibunching will appear at $\Delta t = 64$ ns in the histogram. However, the peak at $\Delta t = 64$ ns does not seem to be significantly lower than other peaks. Evidence of photon antibunching can be further checked by integrating coincidences within each peak and plotting the integrated coincidences as a function of Δt, as shown in Figure 6.7(b). The integrated coincidences do not show any sign of suppression at 64 ns either. The lack of photon antibunching in Figure 6.7 is not surprising since I_{SD} was not stable and was significantly higher than $1ef_{RF}$. Hence, the SAW-driven charge transport was not in the single-electron regime most of the time.

On the other hand, if I_{SD} is about $1ef_{RF}$, the autocorrelation histogram of the SAW-driven EL should exhibit a suppressed peak, indicating $g^{(2)}(0) < 1$. Figure 6.8(a) shows the autocorrelation histogram of the SAW-driven EL at the condition described in Figure 6.6(b), where I_{SD} was stabilised by a PID control loop and average $I_{SD} = 0.9ef_{RF}$. In addition, the HBT setup used in Figure 6.8 is the setup discussed in Section 6.1.2, in which $\Delta t_0 \sim 50.65$ ns. Interestingly, the peak at 51 ns appears to be lower than other peaks nearby. Also, the integrated coincidences shown in Figure 6.8(b) clearly indicate that the coincidences at 51 ns are suppressed. The integrated signal at 51 ns is suppressed to 78% of the average high level. This suppression appearing at $\Delta t = \Delta t_0$ is evidently a sign of photon antibunching. Hence, this result indicates that the SAW-driven n-i-p junction TKH03 can operate as a quantum light source.

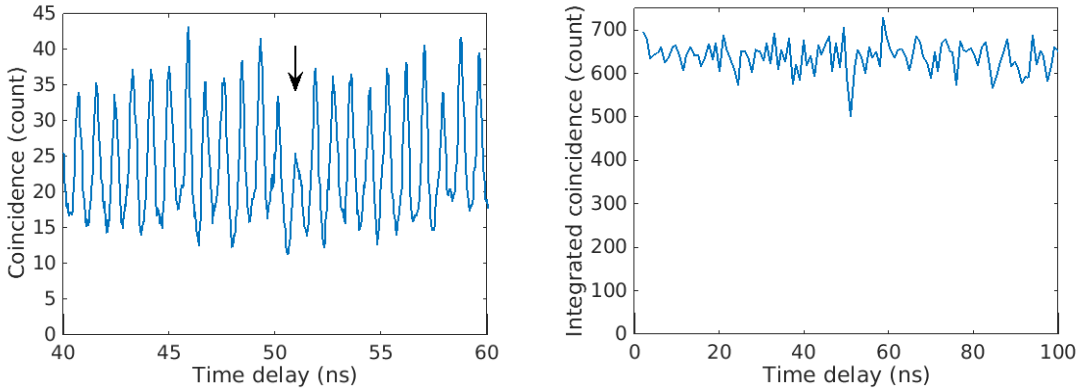

(a) (b)

Fig. 6.8 (a) Autocorrelation histogram of the SAW-driven EL when $I_{SD} = 0.9ef_{RF}$. The peak at 51 ns seems to be lower than other peaks. (b) Signal from each peak (integrated over one SAW period) as a function of time delay. The suppression of signal at $\Delta t = 51$ ns is very obvious.

The evidence of photon antibunching can be observed more obviously by filtering out coincidences that occurred when I_{SD} was too high or too low. To be able to perform the filtering, histograms were recorded every 10 s with time stamps, and I_{SD} was recorded as a function of time. The filtering can thus be performed by checking whether I_{SD} recorded during a certain histogram was outside a desired limit or not, and then removing the coincidences from this histogram if I_{SD} was outside that limit. Figure 6.9(a) shows an autocorrelation histogram filtered from that in Figure 6.8(a) using an upper limit of 0.19 nA ($1ef_{RF}$) and a lower limit of 0.15 nA ($0.8ef_{RF}$), resulting in a filtered $I_{SD} = 0.89 \pm 0.05ef_{RF}$. The peak at 51 ns appears to be relatively lower after filtering. Also, the integrated count at 51 ns in Figure 6.9(b) is further suppressed to 65% of the average high level. This means the evidence of photon antibunching is more pronounced when the signal from the vacuum state or multiple-electron regime is filtered out.

Although Figure 6.9(b) exhibits a suppressed signal of 65%, this does not necessarily mean $g^{(2)}(0)$ is 0.65. This is because there may be a background signal in the SAW-driven EL, as shown in Section 5.3.2. This background signal BG_{EL} in the time-correlated histogram will also lead to a background BG_{g2} in the corresponding autocorrelation histogram. Also, if an individual peak is wider than the 860 ns period, the integrated signal at 51 ns will have contributions from the two neighbouring peaks. Therefore, the background BG_{g2} and the actual shape of individual peaks both have to be considered in order to extract the real $g^{(2)}(0)$ of the SAW-driven EL. These analyses will be presented in the next section.

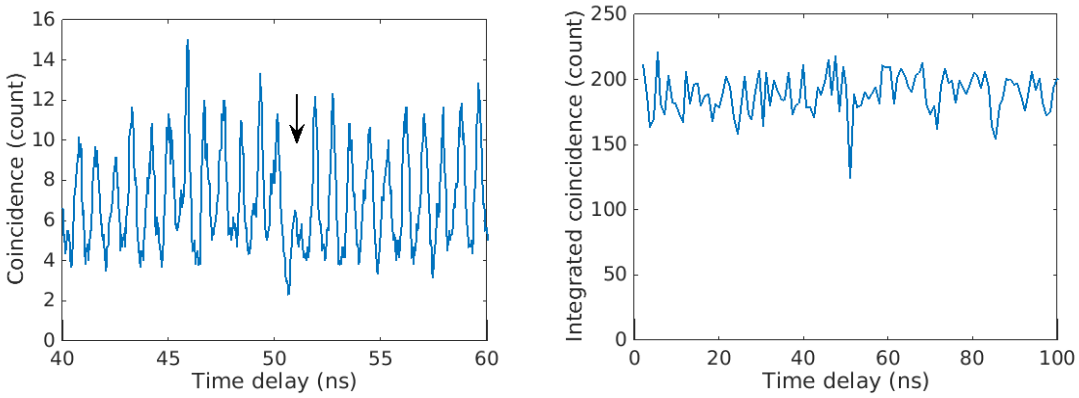

(a) (b)

Fig. 6.9 (a) Filtered autocorrelation histogram of the SAW-driven EL where coincidences when $I_{SD} > 1ef_{RF}$ or $I_{SD} < 0.8ef_{RF}$ are removed. The peak at 51 ns is clearly lower than others. (b) Signal from each peak (integrated over one SAW period) as a function of time delay. The signal at $\Delta t = 51$ ns is suppressed to 65% of the average high level.

6.3 Extracting $g^{(2)}(t)$ from the Autocorrelation Histogram

6.3.1 Time-resolved Electroluminescence in the SAW-driven Single-electron Regime

An autocorrelation histogram results from the autocorrelation of two beams split from photons in SAW-driven EL, so properties of the autocorrelation histogram can be derived if the properties of the SAW-driven EL are known. To allow further analysis of the filtered autocorrelation histogram, which shows a clear photon antibunching effect, characterisation of the SAW-driven EL, which corresponds to a single-electron regime, is essential. Figure 6.10 shows an averaged time-correlated histogram of SAW-driven EL when the number of SAW-driven electrons in each SAW minimum ~ 1, along with the best-fit curve using the function $H(t)$ (Equation 5.6) discussed in Section 5.3.2. The best fit gives the carrier lifetime $\tau = 100 \pm 7$ ps, the jitter in the SAW-driven charge transport $w = 29 \pm 2$ ps, the peak amplitude $A_{EL} = 729 \pm 9$ and the background $BG_{EL} = 43 \pm 5$ (6% of A_{EL}). The carrier lifetime, the jitter, and the ratio of BG_{EL} and A_{EL} are very similar to the values obtained in Section 5.3.2, in which the number of SAW-driven electrons in each SAW minimum ~ 3 on average. Therefore, the dynamics of SAW-driven electrons and the background in EL remain fairly constant over the SAW-driven few-electron regime. An autocorrelation histogram taken in such a condition should thus result from the autocorrelation of a SAW-driven EL with $\tau \sim 100$ ps, $w \sim 30$ ps and $BG_{EL} \sim 6\%$ of A_{EL}.

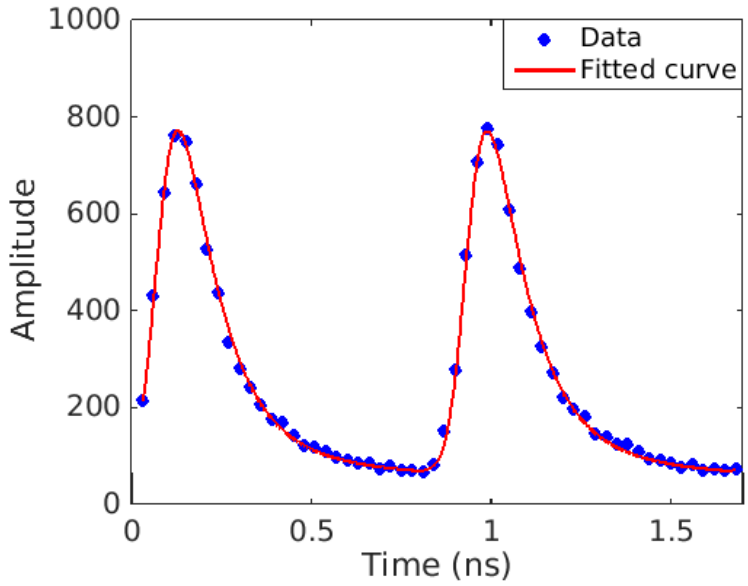

Fig. 6.10 Averaged time-correlated histogram of SAW-driven EL when the number of SAW-driven electrons in each SAW minimum ~ 1 and the best-fit curve using Equation 5.6 with $\tau = 100 \pm 7$ ps, $w = 29 \pm 2$ ps, $A_{\mathrm{EL}} = 729 \pm 9$ and $BG_{\mathrm{EL}} = 43 \pm 5$.

6.3.2 Theoretical Functions for Autocorrelation Histograms

In order to check if the autocorrelation histogram in Figure 6.9(a) is due to the autocorrelation of a SAW-driven EL like the one in Figure 6.10, a theoretical function describing the autocorrelation histogram of the SAW-driven EL has to be established. First, the autocorrelation $G_{\mathrm{auto}}(\Delta t)$ of a real signal $S(t)$ can be expressed as

$$G_{\mathrm{auto}}(\Delta t) = \int S(u)S(u-\Delta t)du\,. \tag{6.3}$$

This can be re-written as

$$\begin{aligned} G_{\mathrm{auto}}(\Delta t) &= \int S(u)S(-(\Delta t-u))du = \int S(u)S_{\mathrm{mirror}}(\Delta t-u)du \\ &= (S * S_{\mathrm{mirror}})(\Delta t)\,, \end{aligned} \tag{6.4}$$

where $S_{\mathrm{mirror}}(t)$ is the mirror image of $S(t)$ so that $S_{\mathrm{mirror}}(t) = S(-t)$. So, the autocorrelation $G_{\mathrm{auto}}(\Delta t)$ can also be understood as the convolution of $S(t)$ and its mirror image $S_{\mathrm{mirror}}(t)$.

In the case of an autocorrelation histogram of the SAW-driven EL, the function $G_{\mathrm{auto}}(\Delta t)$ becomes

$$G_{\mathrm{auto}}(\Delta t) = (H * H_{\mathrm{mirror}})(\Delta t)\,. \tag{6.5}$$

where $H = ((F * g) * PSF) + BG_{\mathrm{EL}}$ (Equation 5.6). This means the autocorrelation histogram can be obtained by the convolution of the SAW-driven EL $H(t)$ and its mirror image $H_{\mathrm{mirror}}(t)$. One such example using numerical calculation is shown in Figure 6.11, where Figure 6.11(a) is $H(t)$ with $\tau = 0.2$, $w = 0.05$, $BG_{\mathrm{EL}} = 0$ and $t_{\mathrm{SAW}} = 1$, Figure 6.11(b) is $H_{\mathrm{mirror}}(t)$, and Figure 6.11(c) is the normalised convolution of $H(t)$ and $H_{\mathrm{mirror}}(t)$, corresponding to the autocorrelation histogram $G_{\mathrm{auto}}(\Delta t)$ of the SAW-driven EL signal $H(t)$. Equation 6.5 and Figure 6.11 demonstrate that the overall appearance of the peaks in an autocorrelation histogram is determined by the parameters of the SAW-driven EL. Note that $G_{\mathrm{auto}}(\Delta t)$ does not take account the quantum nature of single photons. Hence, the suppressed signal at $\Delta t = 0$ due to photon antibunching will not appear in $G_{\mathrm{auto}}(\Delta t)$.

In Figure 6.11(c), the minima between the peaks are quite high, almost 50% of the peak value. This is because individual peaks are wider than t_{SAW} so these peaks merge together. To calculate the contribution of one specific peak to the autocorrelation histogram, a theoretical function describing the shape of each peak also has to be established. Since F is the summation of a series of equally-spaced function f (see Equation 5.4), it can be shown that

$$\begin{aligned} G_{\mathrm{auto}}(\Delta t) &= \sum_{i=-n}^{n} (h * h_{\mathrm{mirror}})(\Delta t + i \cdot t_{\mathrm{SAW}}) \\ &= \sum_{i=-n}^{n} g_{\mathrm{auto}}(\Delta t + i \cdot t_{\mathrm{SAW}}), \end{aligned} \tag{6.6}$$

where $n \to \infty$ is the number of EL peaks, and

$$h(t) = ((f * g) * PSF) + BG_{\mathrm{EL}}/n. \tag{6.7}$$

$h(t)$ can be understood as the EL signal from a SAW minimum. So, the autocorrelation histogram can be seen as the summation of a series of equally-spaced functions, with $g_{\mathrm{auto}} = (h * h_{\mathrm{mirror}})$. Figure 6.12(a) shows an example of $h(t)$ with $\tau = 0.2$, $w = 0.05$, and $BG_{\mathrm{EL}} = 0$ while Figure 6.12(b) shows the mirror image $h_{\mathrm{mirror}}(t)$. Their convolution $g_{\mathrm{auto}}(\Delta t)$ is plotted in Figure 6.12(c). This single peak can be understood as the actual shape of individual peaks in Figure 6.11(c), which means that the contribution from a specific peak can be individually evaluated even though there is significant overlap between these peaks. So, if the theoretical function $g_{\mathrm{auto}}(\Delta t)$ for SAW-driven EL is known, the real signal from a suppressed peak, such as that in Figure 6.9(a), can be estimated more accurately.

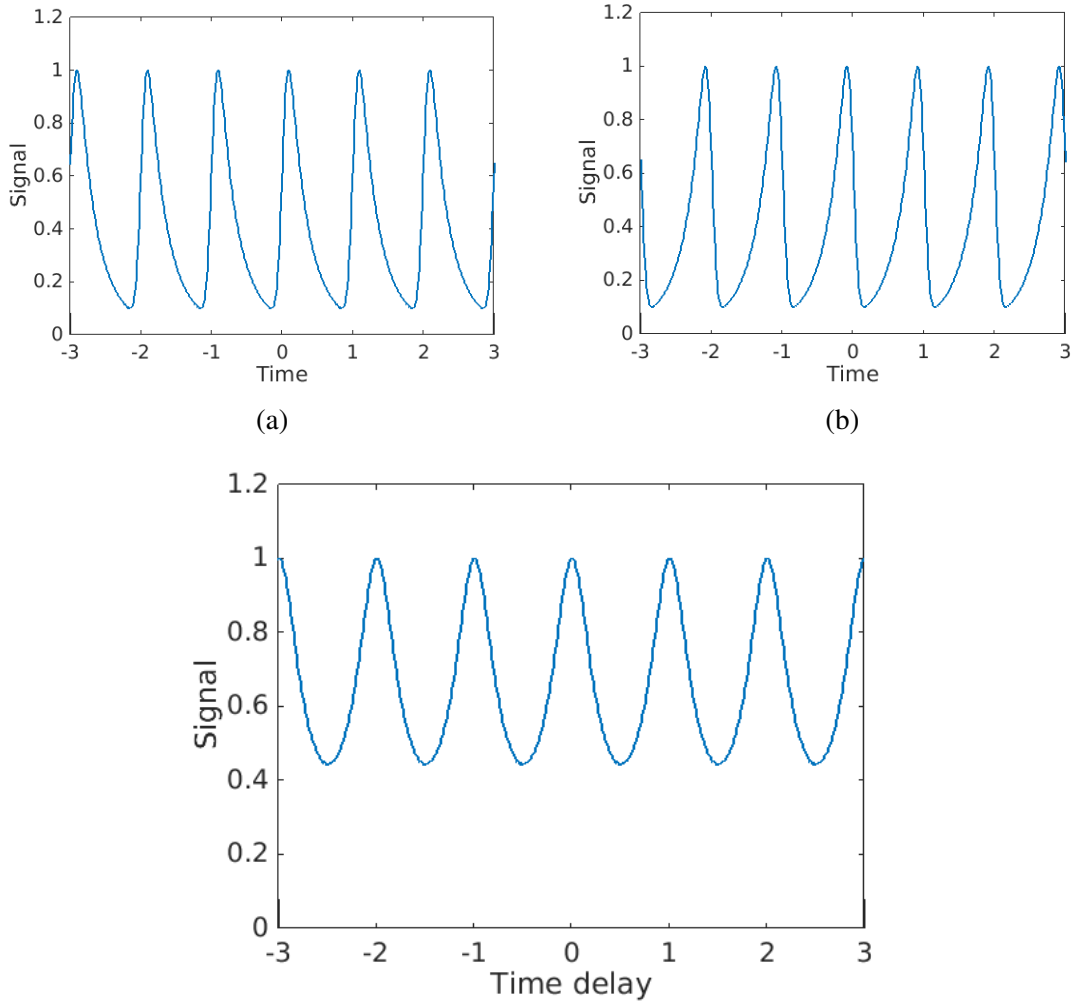

Fig. 6.11 (a) Example of $H(t)$ with $\tau = 0.2$, $w = 0.05$, $BG_{\mathrm{EL}} = 0$ and $t_{\mathrm{SAW}} = 1$. (b) Mirror image $H_{\mathrm{mirror}}(t)$ of $H(t)$. (c) $G_{\mathrm{auto}}(\Delta t)$, which is the convolution of $H(t)$ and $H_{\mathrm{mirror}}(t)$.

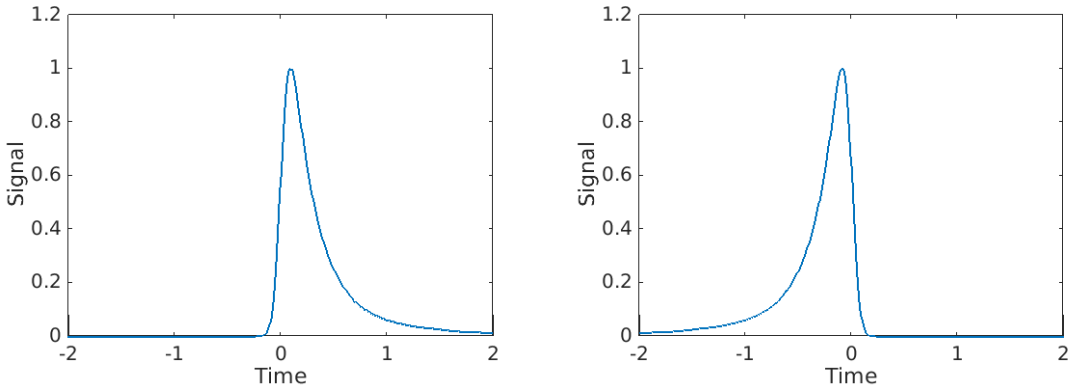

(a)

(b)

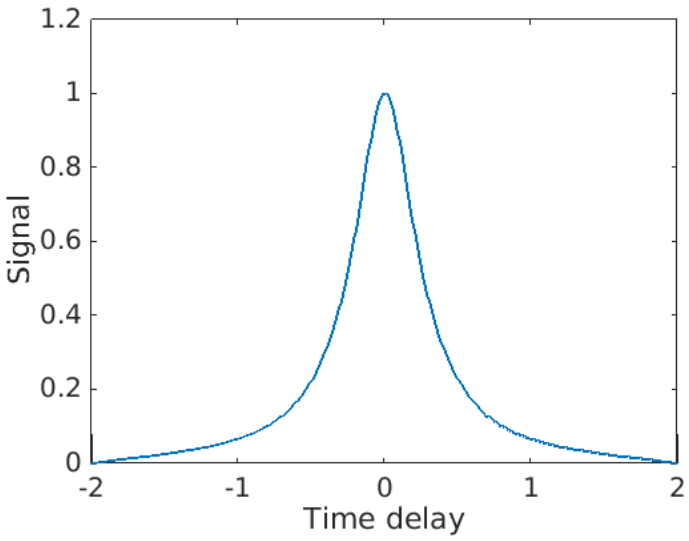

(c)

Fig. 6.12 (a) Example of $h(t)$ with $\tau = 0.2$, $w = 0.05$, and $BG_{\mathrm{EL}} = 0$. (b) Mirror image $h_{\mathrm{mirror}}(t)$ of $h(t)$. (c) $g_{\mathrm{auto}}(\Delta t)$, which is the convolution of $h(t)$ and $h_{\mathrm{mirror}}(t)$.

6.3.3 Effect of Background in Electroluminescence on an Autocorrelation Histogram

The best-fit curves for the SAW-driven EL in Figure 5.18 and Figure 6.10 both indicate there is a constant background $BG_{\mathrm{EL}} = 6\%$-8% of the amplitude A_{EL}. This may be because of some SAW-driven electrons trapped in the region of holes, which lead to a constant probability of finding an electron in that region. It could also come from ambient light since there was no spectral filtering employed in the HBT setup. It may also be attributed to a background signal from the SPAD. This background BG_{EL} in the SAW-driven EL will have an effect on the autocorrelation histogram. This effect will need to be considered in the analysis of $g^{(2)}(\Delta t)$. Therefore, it is important to understand how much a given BG_{EL} in SAW-driven EL affects the resulting autocorrelation. This can be tested by comparing the autocorrelation histograms $G_{\mathrm{auto}}(\Delta t)$ of a SAW-driven EL $H(t)$ with and without the background BG_{EL}, using the numerical method employed in Figure 6.11. In order to make the test more representative of the real experiment, a function describing the real SAW-driven EL $H(t)$ is created with a carrier lifetime $\tau = 100\,\mathrm{ps}$ and a jitter $w = 30\,\mathrm{ps}$, which were obtained from the fitting in Section 6.3.1. The corresponding autocorrelation histograms $G_{\mathrm{auto}}(\Delta t)$ are then numerically calculated as the convolution of $H(t)$ and $H_{\mathrm{mirror}}(t)$, with two different background conditions ($BG_{\mathrm{EL}} = 0$ and $BG_{\mathrm{EL}} = 6\% \cdot A_{\mathrm{EL}}$). The autocorrelation histograms with $BG_{\mathrm{EL}} = 0$ and $BG_{\mathrm{EL}} = 6\% \cdot A_{\mathrm{EL}}$ are shown in Figure 6.13. As can be seen, compared with the autocorrelation with $BG_{\mathrm{EL}} = 0$, the autocorrelation with $BG_{\mathrm{EL}} = 6\% \cdot A_{\mathrm{EL}}$ is raised by a constant background BG_{g2}. Therefore, $BG_{\mathrm{EL}} = 6\% \cdot A_{\mathrm{EL}}$ in the SAW-driven EL will give rise to a background BG_{g2}, which is 18.1% of the peak value, in the resulting autocorrelation histogram. On the other hand, $BG_{\mathrm{EL}} = 8\% \cdot A_{\mathrm{EL}}$ will lead to $BG_{\mathrm{g2}} = 23.2\%$ of the peak value. These tests indicate that, with $BG_{\mathrm{EL}} = 6\%$-8% of A_{EL} in the SAW-driven EL, the autocorrelation histogram in Figure 6.9(a) should have a constant background $BG_{\mathrm{EL}} \sim 20\%$ of the average peak value, which is roughly $11 \cdot 20\% = 2.2$.

Because BG_{EL} only causes a constant background BG_{g2} in the autocorrelation, Equation 6.5 can be re-written as

$$G_{\mathrm{auto}}(\Delta t) = (H' * H'_{\mathrm{mirror}})(\Delta t) + BG_{\mathrm{g2}}\,, \tag{6.8}$$

where $H'(t) = ((F * g) * PSF)(t)$ is the function for the SAW-driven EL without BG_{EL}, and $H'_{\mathrm{mirror}}(t)$ is its mirror image. This form of $G_{\mathrm{auto}}(\Delta t)$ will be used for fitting the averaged autocorrelation histogram from Figure 6.9(a), which will be presented in the next paragraph.

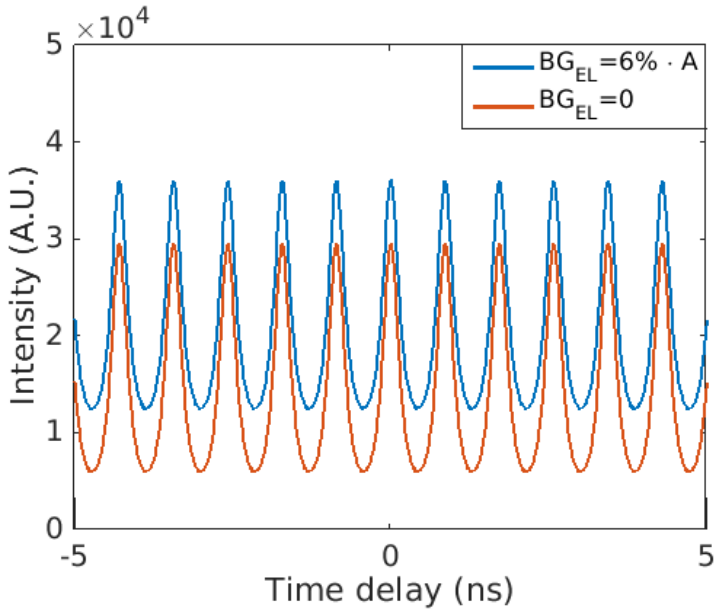

Fig. 6.13 Numerical calculation of $G_{\text{auto}}(\Delta t)$ with $\tau = 100\,\text{ps}$, $w = 30\,\text{ps}$, and with different background $BG_{\text{EL}} = 0$ and $BG_{\text{EL}} = 6\%$ of A_{EL}. $G_{\text{auto}}(\Delta t)$ with $BG_{\text{EL}} = 6\%$ manifests a constant background $BG_{\text{g2}} = 18.1\%$ of the peak value

6.3.4 Fitting for the Averaged Autocorrelation Histogram

In the previous part of Section 6.3, the parameters for the dynamics in the SAW-driven single-electron regime, the function $G_{\text{auto}}(\Delta t)$ for describing an autocorrelation histogram, and the effect of a background BG_{EL} in the SAW-driven EL on the background BG_{g2} in the autocorrelation histogram, have all been investigated. At this point, it is possible to evaluate the real second-order correlation function $g^{(2)}(\Delta t)$ in the filtered histogram in Figure 6.9(a), by assuming that the parameters (τ, w, BG_{EL}) for the dynamics in Figure 6.9(a) are the same as those fitted in Figure 6.10 and creating a modified autocorrelation function based on these parameters to fit the data in Figure 6.9(a). Nonetheless, since the time-correlated histogram was not measured at the same time as the autocorrelation histogram was recorded, the dynamics in these two might vary due to some charging effect, although the variation should be minor. Hence, it is best first to fit the autocorrelation histogram, averaged from Figure 6.9(a), using Equation 6.8 with unconstrained parameters τ, w, BG_{EL}. If the parameters from the best fit of $G_{\text{auto}}(\Delta t)$ agree with those obtained from the best fit of $H(t)$, it will be a good indication that the results from two different types of experiment (the time-resolved measurement and HBT experiment) are consistent, and the models for $H(t)$ and $G_{\text{auto}}(\Delta t)$ are correct to a large extent. Also, if there is a slight difference between

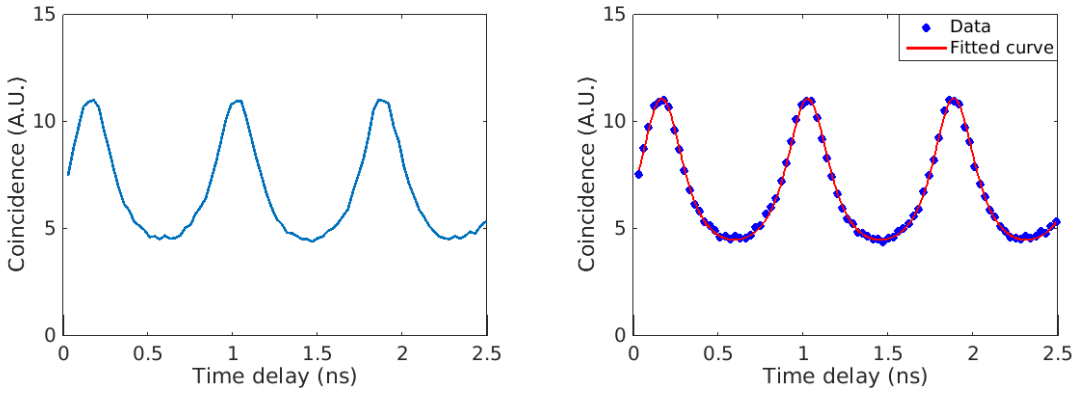

(a) (b)

Fig. 6.14 (a) Averaged autocorrelation histogram from Figure 6.9(a). (b) Best-fit curve to the data using $G_{\text{auto}}(\Delta t)$ with $\tau = 99.6 \pm 0.1$ ps, $w = 33 \pm 2$ ps, and $BG_{\text{g2}} = 2.79 \pm 0.06$.

these two sets of parameters, the parameters from the best fit of $G_{\text{auto}}(\Delta t)$ will be more representative of the dynamics during the time when Figure 6.9(a) was taken.

As can be seen in the filtered autocorrelation histogram in Figure 6.9(a), the peaks do not manifest uniform intensity due to the sample variance in a finite amount of data (coincidences). In order to be able to fit more uniform data, the autocorrelation histogram is averaged over $\Delta t = 0$ ns to 2000 ns (more than 2300 peaks) to obtain an averaged autocorrelation histogram, as shown in Figure 6.14(a). This averaged autocorrelation histogram corresponds to the averaged SAW-driven EL that causes the histogram in Figure 6.9(a). The averaged autocorrelation histogram is then fitted using $G_{\text{auto}}(\Delta t)$ in Equation 6.8, with only one constraint, $t_{\text{SAW}} = 859.8$ ps. Figure 6.14(b) shows the best-fit curve along with the data. It gives $\tau = 99.6 \pm 0.1$ ps, $w = 33 \pm 2$ ps, and the background $BG_{\text{g2}} = 2.79 \pm 0.06$ ($25.1 \pm 0.6\%$ of the average peak value of 11.1). Compared with the parameters obtained from Figure 6.10 ($\tau = 100 \pm 7$ ps, $w = 29 \pm 2$ ps and $BG_{\text{EL}} = 6 \pm 0.6\% \cdot A_{\text{EL}}$, corresponding to $BG_{\text{g2}} = 18.1 \pm 2.1\%$), the two sets of parameters agree with each other quite well, especially τ and w. As explained earlier, this indicates that results from two different experiments are consistent, and suggests that the functions describing the SAW-driven EL and the autocorrelation histogram are faithful to the real dynamics of SAW-driven charge transport. Also, it will be more correct to use the parameters obtained from Figure 6.14(b) when evaluating $g^{(2)}(\Delta t)$ in Figure 6.9(a).

6.3.5 Extraction of the Second-order Correlation Function $g^{(2)}(\Delta t)$

After obtaining the proper parameters for the autocorrelation histogram, the real $g^{(2)}(\Delta t)$ can finally be extracted from the data in Figure 6.9(a). In this autocorrelation histogram, a

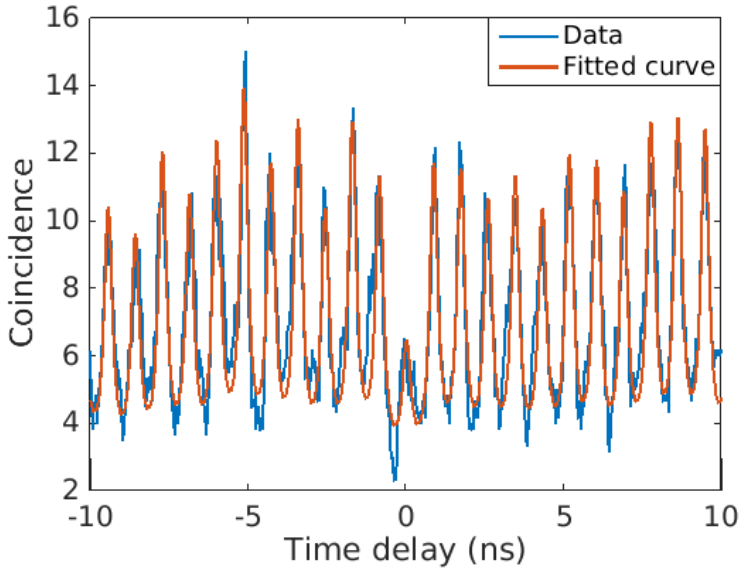

Fig. 6.15 Autocorrelation histogram in Figure 6.9(a) shifted by -51 ns and the best-fit curve using Equation 6.9.

constant background $BG_{\mathrm{g2}} = 2.79$ leads to an offset in the Y axis, and the shape of individual peaks is determined by $\tau = 99.6$ ps and $w = 33$ ps. Due to the statistical sample variance, these peaks at $\Delta t = \Delta t_{(\mathrm{i})}$ have different amplitudes $A_{\mathrm{g2(i)}}$, which are proportional to $g^{(2)}(\Delta t_{(\mathrm{i})})$. A modified autocorrelation function reflecting the variance can be expressed as

$$G'_{\mathrm{auto}}(\Delta t) = \sum_{i=-\infty}^{\infty} A_{\mathrm{g2(i)}} \cdot (h' * h'_{\mathrm{mirror}})(\Delta t + i \cdot t_{\mathrm{SAW}}) + BG_{\mathrm{g2}}\,, \tag{6.9}$$

where $h'(t)$ is the single peak in EL with $BG_{\mathrm{EL}} = 0$ and $h'_{\mathrm{mirror}}(t)$ as its mirror image. In order to evaluate $g^{(2)}(\Delta t)$, $A_{\mathrm{g2(i)}}$ at individual peaks have to be obtained by fitting the autocorrelation histogram to $G'_{\mathrm{auto}}(\Delta t)$ with $\tau = 99.6$ ps, $w = 33$ ps, and $BG_{\mathrm{g2}} = 2.79$. Figure 6.15 shows the data from Figure 6.9(a) shifted by -51 ns (so that the photon-antibunching peak appears at $\Delta t = 0$), along with the best-fit curve for the suppressed peak and the nearest 120 peaks. The fit curve agrees with the data to a great extent, except for some lower points between two peaks. The overestimation at these points might be improved with further investigation into the fitting function, but the fitted amplitude $A_{\mathrm{g2(i)}}$ may not be affected very much.

The fitting process assigns to each peak an amplitude $A_{\mathrm{g2(i)}}$. The second-order correlation function $g^{(2)}(\Delta t)$ is then obtained from the normalised $A_{\mathrm{g2(i)}}$ as a function of time delay, as shown in Figure 6.16. A dip at $\Delta t = 0$ can be clearly observed, indicating photon antibunching in the SAW-driven EL. The value at $\Delta t = 0$ corresponds to $g^{(2)}(0) = 0.39 \pm 0.05$. Hence, the

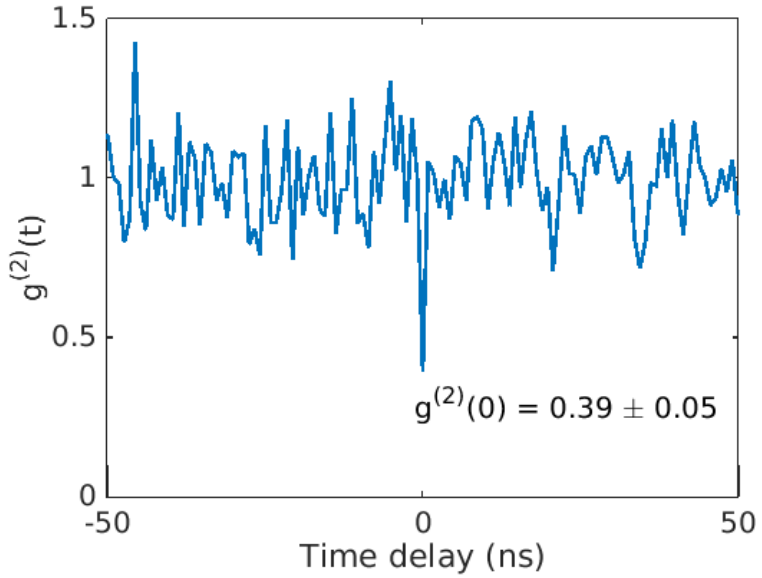

Fig. 6.16 Normalised amplitude A_{g2} as a function of delay time, which is equivalent to $g^{(2)}(\Delta t)$.

SAW-driven n-i-p junction TKH03 demonstrates $g^{(2)}(0) < 0.5$, the common criterion for single-photon sources.

6.4 Theoretical Analyses for Probability Distribution

After obtaining $g^{(2)}(0) = 0.39 \pm 0.05$ when the average number of electrons per SAW minimum $n_{\mathrm{avg}} = 0.89 \pm 0.05$, further theoretical analysis can be carried out in order to estimate the probability of single-photon emission from the SAW-driven n-i-p junction TKH03.

6.4.1 Theoretical Limits to Single-photon and Multi-photon Probabilities

Because the average number of SAW-driven electrons per SAW minimum, n_{avg}, is 0.89, the average number of electron-hole pairs per SAW cycle, $p_{\mathrm{e-h}}$, is also 0.89. In this SAW-driven n-i-p junction, n_{avg}, and so $p_{\mathrm{e-h}}$, can be evaluated simply by measuring the SAW-driven current across the junction. However, in most types of single-photon source, estimation of $p_{\mathrm{e-h}}$ is not as straightforward as for this device. In QD-based single-photon sources, $p_{\mathrm{e-h}}$ (or n_{avg}) can be defined as the occupation factor of an exciton in a quantum dot per excitation. $p_{\mathrm{e-h}}$ is a function of excitation power, and is usually assumed to be unity at

saturation power [13, 17]. In order to evaluate $p_{\mathrm{e-h}}$ of a QD-based single-photon source driven by optical excitation, the overall optical collection efficiency and the internal quantum efficiency both have to be accurately characterised. As for a QD-based single-photon source driven by electrical excitation, where a current is passed to inject electron-hole pairs into embedded quantum dots, the current passes by not only a specific quantum dot, but also other quantum dots nearby and the bulk n-i-p junction surrounding them [54, 134]. As a result, the current does not represent the average number of electron-hole pairs in one quantum dot, so n_{avg} and $p_{\mathrm{e-h}}$, which are useful for estimating the probability distribution of photon numbers, cannot be determined as simply as in the SAW-driven n-i-p junction.

If n electrons carried in a SAW minimum arrive at the region of holes, up to n photons will be produced when they recombine with holes, and these photons will then cause coincidences in an autocorrelation histogram. Hence, n_{avg} and $g^{(2)}(0)$ are not independent variables. In fact, they are both functions of the probability distribution of electron numbers in a SAW minimum (and photon numbers in the SAW-driven EL). In this section, it will be shown that limits for the single-photon probability and the multi-photon probability can be derived from the values of n_{avg} and $g^{(2)}(0)$ utilising their dependence on the probability distribution.

Because the number of electrons carried in a SAW minimum can be 0, 1, 2, 3 and so on, the probability P_n of having n electrons will follow a probability distribution. The wave function $|\psi\rangle$ for the electrons in a SAW minimum can be expressed as a general superposition state

$$|\psi\rangle = \sqrt{P_0}|0\rangle + \sqrt{P_1}|1\rangle + \sqrt{P_2}|2\rangle + \sqrt{P_3}|3\rangle + \cdots \tag{6.10}$$

with

$$\sum_{i\geq 0} P_i = 1 \text{ and } 0 \leq P_i \leq 1\,,$$

where $|i\rangle$ is the i-particle state (i-electron state in a SAW minimum ,or i-photon state in the SAW-driven EL) in the Fock basis, and P_i is the probability of measuring i electrons (i photons). The probability distribution of electron numbers and photon numbers in $|\psi\rangle$ manifests $n_{\mathrm{avg}} = N$ and $g^{(2)}(0) = G$, N and G can be expressed quantum mechanically as

$$N = \langle\psi|\hat{a}^\dagger\hat{a}|\psi\rangle \tag{6.11}$$

and

$$G = \frac{\langle\psi|\hat{a}^\dagger\hat{a}^\dagger\hat{a}\hat{a}|\psi\rangle}{\langle\psi|\hat{a}^\dagger\hat{a}|\psi\rangle^2} = \frac{\langle\psi|\hat{a}^\dagger\hat{a}^\dagger\hat{a}\hat{a}|\psi\rangle}{N^2}\,. \tag{6.12}$$

Now consider a multi-particle quantum state $|\tilde{\psi}\rangle$ with no $|0\rangle$ (vacuum state) or $|1\rangle$ (single-electron or single-photon state) projection in the Fock basis

$$|\tilde{\psi}\rangle = \sqrt{P_2'}|2\rangle + \sqrt{P_3'}|3\rangle + \sqrt{P_4'}|4\rangle + \cdots \tag{6.13}$$

with

$$\sum_{i\geq 2} P'_i = 1 \text{ and } 0 \leq P'_i \leq 1\,.$$

The average number of particles in $|\tilde{\psi}\rangle$ is

$$\begin{aligned}\langle\tilde{\psi}|\hat{a}^\dagger\hat{a}|\tilde{\psi}\rangle &= \sum_{i\geq 2} P'_i \cdot i = \sum_{j\geq 0} P'_{j+2}\cdot(j+2) = 2\sum_{j\geq 0} P'_{j+2} + \sum_{j\geq 0} P'_{j+2}\cdot(j) \\ &= 2 + \sum_{j\geq 0} P'_{j+2}\cdot(j) \geq 2\,.\end{aligned} \tag{6.14}$$

In addition

$$\begin{aligned}\langle\tilde{\psi}|\hat{a}^\dagger\hat{a}^\dagger\hat{a}\hat{a}|\tilde{\psi}\rangle &= \sum_{i\geq 2} P'_i \cdot i\cdot(i-1) = \sum_{i\geq 2} P'_i\cdot i^2 - \sum_{i\geq 2} P'_i\cdot i \\ &= 2 + 3\sum_{j\geq 0} P'_{j+2}\cdot(j) + \sum_{j\geq 0} P'_{j+2}\cdot(j^2) \\ &\geq \langle\tilde{\psi}|\hat{a}^\dagger\hat{a}|\tilde{\psi}\rangle \geq 2\,.\end{aligned} \tag{6.15}$$

Therefore,

$$\frac{\langle\tilde{\psi}|\hat{a}^\dagger\hat{a}|\tilde{\psi}\rangle}{\langle\tilde{\psi}|\hat{a}^\dagger\hat{a}^\dagger\hat{a}\hat{a}|\tilde{\psi}\rangle} \leq 1\,. \tag{6.16}$$

Since $|\tilde{\psi}\rangle$ is a multi-particle state, a general quantum state $|\psi\rangle$ can be expressed with the help of $|\tilde{\psi}\rangle$

$$|\psi\rangle = \sqrt{1-X-Y}|0\rangle + \sqrt{X}|1\rangle + \sqrt{Y}|\tilde{\psi}\rangle\,, \tag{6.17}$$

where X is the single-particle probability P_1, and Y is the multi-particle probability P_{multi}. Now N and G can be re-written as

$$N = X + Y\langle\tilde{\psi}|\hat{a}^\dagger\hat{a}|\tilde{\psi}\rangle \tag{6.18}$$

and

$$G = \frac{Y\langle\tilde{\psi}|\hat{a}^\dagger\hat{a}^\dagger\hat{a}\hat{a}|\tilde{\psi}\rangle}{N^2}\,. \tag{6.19}$$

Hence, the upper limit of the multi-particle probability P_{multi} can be obtained using Equations 6.15 and 6.19 as

$$P_{\text{multi}} = Y = \frac{GN^2}{\langle\tilde{\psi}|\hat{a}^\dagger\hat{a}^\dagger\hat{a}\hat{a}|\tilde{\psi}\rangle} \leq \frac{GN^2}{2} \tag{6.20}$$

and the lower limit of the single-particle probability P_1 can be found by substituting Y from Equation 6.19 into Equation 6.18 and using the inequality in Equation 6.16

$$P_1 = X = N - N^2G\frac{\langle\tilde{\psi}|\hat{a}^\dagger\hat{a}|\tilde{\psi}\rangle}{\langle\tilde{\psi}|\hat{a}^\dagger\hat{a}^\dagger\hat{a}\hat{a}|\tilde{\psi}\rangle} \geq N - N^2G. \tag{6.21}$$

Note that the two inequalities above will become equalities if the multi-particle state $|\tilde{\psi}\rangle$ is the pure two-particle state $|2\rangle$.

Since the SAW-driven n-i-p junction was measured to have $n_{\text{avg}} = 0.89$ and $g^{(2)}(0) = 0.39$, the above relations give the single-photon probability $P_1 \geq 0.58$ and the multi-photon probability $P_{\text{multi}} \leq 0.15$. If the zero-photon case (the vacuum state) is ignored, the ratio of the single-photon probability and the non-zero-photon probability is about $0.58/(0.58+0.15) = 0.79 \simeq 0.8$, which means that, when a detector receives a SAW-driven EL signal from the junction, if the background BG_{EL} can be removed, the signal has a probability of $\sim 80\%$ of being single-photon emission.

6.4.2 Simulation of HBT Experiments

After gaining information about the probability distribution of photon numbers in the device, it will be interesting to test if a possible probability distribution can actually lead to the measured $g^{(2)}(0) = 0.39$ in an HBT experiment. Since it is not trivial to manipulate the probability distribution in a real experiment, such tests can be performed by running a simulation of the HBT experiment in a computer. The simulation is carried out as follows: first, a light source can emit a stream of photons at $t = 0, 1, 2, 3...$ The time interval corresponds to the SAW period. The number of photons in each time interval follows a specified probability distribution. For instance, if $(P_0, P_1, P_2, P_3 \ldots) = (0.6, 0.3, 0.1, 0 \ldots)$, then 60% of time intervals will have 0 photons, 30% of time intervals will have 1 photon, and 10% of the time intervals will have 2 photons. Every photon has a chance P_{collect} of being coupled to the HBT setup, corresponding to the collection efficiency of the optics. Every photon that has been coupled to the HBT setup is then sent to one of two detectors with equal probabilities, corresponding to a beamsplitter. Subsequently, each of the two detectors records the time

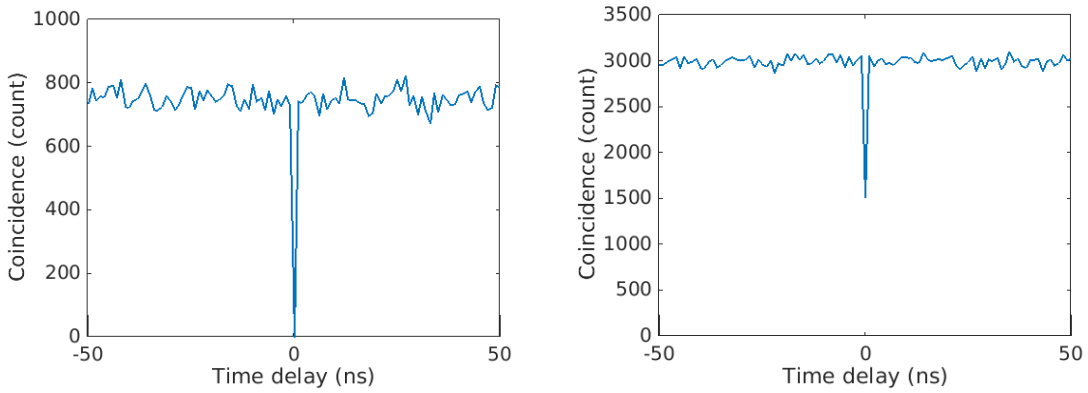

(a) (b)

Fig. 6.17 (a) Simulation for the autocorrelation histogram of a perfect single-photon source. The signal at 0 is suppressed to 0, meaning $g^{(2)}(0) = 0$. (b) Simulation for the autocorrelation histogram of a pure two-photon source. The signal at 0 is suppressed to a half of the average high level, meaning $g^{(2)}(0) \simeq 0.5$.

when at least one photon arrives. Finally, an autocorrelation histogram is formed after a program compares the detection events in the two detectors, as explained in Figure 6.2.

To check if the HBT simulation is working properly, a probability distribution corresponding to a perfect single-photon source $(P_0, P_1, P_2 \ldots) = (0, 1, 0 \ldots)$ is first used for the simulation. The simulation result is shown in Figure 6.17(a). As can be seen, the number of coincidences drops to 0 at $\Delta t = 0$, meaning the simulation shows the correct result $g^{(2)}(0) = 0$ for a perfect single-photon source. Next, $(P_0, P_1, P_2 \ldots) = (0, 0, 1 \ldots)$, a pure two-photon state, is used for the simulation. A calculation with Equation 6.1 gives $g^{(2)}(0) = 0.5$ for the pure two-photon state. The HBT simulation also shows the same result, where the number of coincidences drops to a half at $\Delta t = 0$.

At this point, it has been confirmed that the HBT simulation can produce faithful result. Hence, a possible probability distribution for the real experiment can now be tested. If the multi-photon state is dominated by the two-photon state ($|\tilde{\psi}\rangle = |2\rangle$), then the probability distribution satisfying $n_{\text{avg}} = 0.89$ and $g^{(2)}(0) = 0.39$ becomes $(P_0, P_1, P_2) = (0.27, 0.58, 0.15)$. The simulation result with this probability distribution is shown as the red curve in Figure 6.18. A clear dip is seen at $\Delta t = 50$, which is a time delay added to reflect the real experiment. $g^{(2)}(0) = 0.4$ can be obtained from the simulation result, which is close to the measurement result $g^{(2)}(0) = 0.39 \pm 0.05$. This indicates that this probability distribution $(P_0, P_1, P_2) = (0.27, 0.58, 0.15)$ might be close to the real case in the measurement since it can lead to values of n_{avg} and $g^{(2)}(0)$ that are similar to the measurement result.

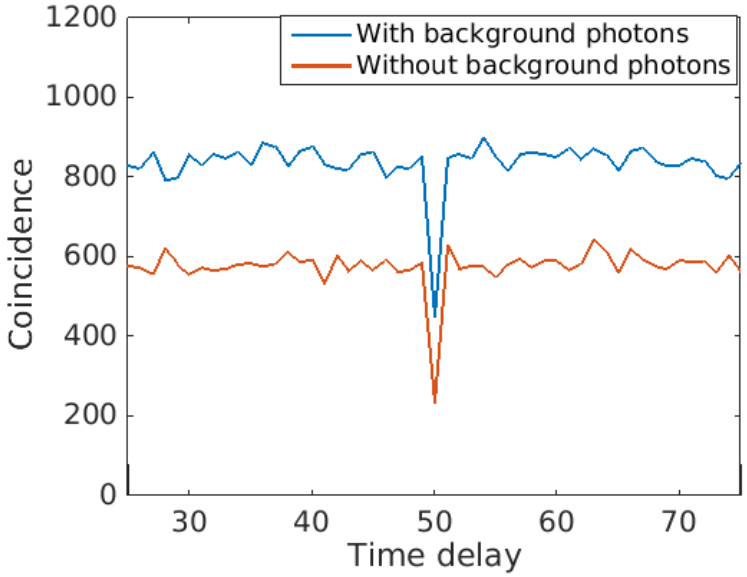

Fig. 6.18 HBT simulation result for a probability distribution $(P_0, P_1, P_2) = (0.27, 0.58, 0.15)$ with un-correlated background photons (blue curve) and without background photons (red curve). The histogram without background photons exhibits $g^{(2)}(0) = 0.4$, which is close to the value extracted from the experiment. Also, the histogram with 17% of overall EL being uncorrelated background photons shows an offset corresponding to 31% of the average high level.

In addition, the HBT simulation can be used to test the effect of uncorrelated background photons on the autocorrelation histogram, which has been studied numerically in Section 6.3.3. The uncorrelated background photons can be simulated as an extra stream of photons that follows a Poisson distribution. Note that, since the EL signal in each time interval (each SAW period) is represented by a single value, the signals in the time-correlated histogram and the autocorrelation histogram have to be integrated over one SAW period in order to compare the measurement result and the HBT simulation. After integration, in the time-correlated histogram (see Figure 6.10), the background with $BG_{\mathrm{EL}} = 6\% \cdot A_{\mathrm{EL}}$ is actually 17% of the total signal, which means 17% of the EL signal within a SAW period is uncorrelated background photons. Also, in the autocorrelation histogram (see Figure 6.14(b)), these uncorrelated photons give rise to 38% of the overall coincidences.

The HBT simulation with the same probability distribution $(P_0, P_1, P_2) = (0.27, 0.58, 0.15)$ plus a stream of uncorrelated photons with average number $= 0.18$ (17% of the total signal) is shown in the blue curve in Figure 6.18. Compared with the autocorrelation histogram without background photons (red curve), the histogram is raised by an offset in the y axis. This offset is $31 \pm 4\%$ of the average maximum level, which is similar to the measurement result of 38%. Therefore, the simulation confirms that the background BG_{EL} observed in the time-resolved measurement does cause an offset in the autocorrelation histogram, which must be considered in the analysis of $g^{(2)}(\Delta t)$.

6.4.3 Modelling of SAW-driven Charge Transport

The last element of the theoretical analysis in this chapter will be to build a simplified quantum-mechanics-based model for the SAW-driven charge transport, and then test if this model can provide a qualitative description of the transport, as well as seeing whether a probability distribution of electron numbers satisfying $n_{\mathrm{avg}} \simeq 0.9$ and $g^{(2)}(0) \simeq 0.39$ can be predicted by the model or not.

To build the model, the first step is to calculate the electrostatic potential of the SAW-driven n-i-p junction with S-D bias and gate voltages close to the experiment. The blue curve in Figure 6.19 shows the conduction band along the SAW-propagation direction (the x axis), where the source (electron) bias $V_{\mathrm{source}} = -0.8$ V, the drain (hole) bias $V_{\mathrm{drain}} = 0.65$ V, and the side-gate voltage $V_{\mathrm{SiG}} = -0.4$ V. This calculation of the electrostatic potential, based on the real device geometry, was carried out by Mr Hangtian Hou using the partial differential equation solver Nextnano [135, 136]. As can be seen, the potential difference between the region of electrons (left) and the region of holes (right) is about 80 meV, so electrons cannot overcome this potential difference and recombine with holes unless a SAW drags these electrons to the region of holes. The red curve in Figure 6.19 shows the calculated conduction

band with superposition of a SAW potential (amplitude $A_{\mathrm{SAW}} = 20\,\mathrm{meV}$). The SAW potential minima work as dynamic quantum dots, trapping the electrons and transporting them to the region of holes. During the transportation of electrons, some of them will tunnel out of the potential minima if the electrochemical potential $u_{(\mathrm{SAWdot})}$ of the dynamic quantum dots is close to or higher than the quantum-dot barrier height V_0 created by the SAW. The probability of tunnelling in one attempt can be described by the transmission probability of noninteracting electrons through a saddle-point potential [127, 128]

$$T = \frac{1}{1+e^{-\pi\varepsilon_n}} \tag{6.22}$$

with

$$\varepsilon_n = 2[u_{(\mathrm{SAWdot})} - \hbar\omega_y(n_y + \frac{1}{2}) - V_0)]/\hbar\omega_{\mathrm{Barrier}}\,, \tag{6.23}$$

where $\omega_{\mathrm{Barrier}}$ is the curvature of the quantum-dot barrier expressed in frequency, ω_y is the curvature of the potential perpendicular to the SAW-propagation direction (the y axis), which is related to the electrostatic potential of the etched 1D channel, and n_y is the quantum number of the wave function on the y axis. The 2D potential of a SAW-created quantum dot can be approximated as an anisotropic 2D harmonic oscillator with two different frequencies along the x and y axes

$$V(x,y) = \frac{1}{2}m{\omega_x}^2x^2 + \frac{1}{2}m{\omega_x}^2y^2 \tag{6.24}$$

with energy states

$$E(n_x,n_y) = (\frac{1}{2}+n_y)\hbar\omega_x + (\frac{1}{2}+n_y)\hbar\omega_y\,, \tag{6.25}$$

where $\omega_x = \omega_{\mathrm{SAW}}$ (the curvature at the bottom of the SAW minimum) and n_x is the quantum number of the wave function on the x axis. Assuming (1) $\omega_x > \omega_y$ (which is true for the simulation result shown later) (2) the charging energy E_{c} for adding one electron is dominated by the patterned gates rather than electron-electron interactions, and (3) spin-spin interactions can be ignored, then the electrochemical potential $u_{(\mathrm{SAWdot})}(N)$ for the first six electrons in the dot can be written as [71]

$$\begin{aligned}
u_{(\mathrm{SAWdot})}(1) &= E_{\mathrm{c}} + E(0,0)\\
u_{(\mathrm{SAWdot})}(2) &= 2E_{\mathrm{c}} + E(0,0)\\
u_{(\mathrm{SAWdot})}(3) &= 3E_{\mathrm{c}} + E(0,1)\\
u_{(\mathrm{SAWdot})}(4) &= 4E_{\mathrm{c}} + E(0,1)\\
u_{(\mathrm{SAWdot})}(5) &= 5E_{\mathrm{c}} + E(1,0)\\
u_{(\mathrm{SAWdot})}(6) &= 6E_{\mathrm{c}} + E(1,0)\,.
\end{aligned} \tag{6.26}$$

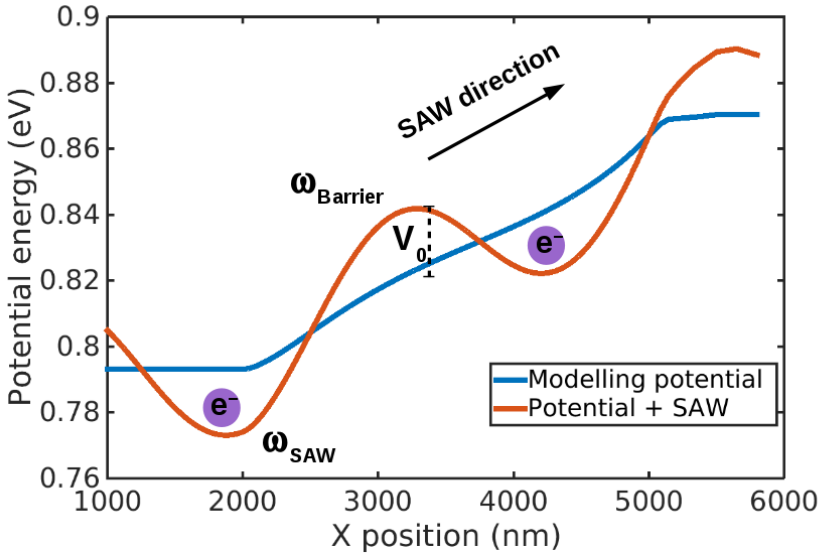

Fig. 6.19 Electrostatic potential of the conduction band (blue curve) of a SAW-driven n-i-p junction, calculated using Nextnano by Hangtian Hou. The red curve shows the electrostatic potential superposed by a SAW potential with SAW amplitude of 20 meV. Electrons are trapped in the SAW minimums and dragged from the region of electrons ($x = 2000$ nm) to the region of holes ($x = 5000$ nm). Each SAW minimum works as a dynamic quantum dot (with potential height V_0, curvature at the top of the barrier ω_{Barrier}, and curvature at the bottom of the quantum dot ω_{SAW}).

Therefore, the tunnelling probabilities of the first N electrons in the SAW-created dot (with a given SAW amplitude and at a given dot position during transport) can be calculated using Equation 6.22 once ω_{Barrier}, ω_{SAW}, ω_{y}, and V_0 are obtained from fitting the conduction band with a SAW superposed at the corresponding phase. Subsequently, a probability distribution of electron numbers in the dot can be calculated by the evolution of electron population, due to tunnelling, from an initial state (e.g. 5 electrons at the beginning) in the region of electrons ($x = 2000$ nm in Figure 6.19) to the final state in the region of holes ($x = 5000$ nm).

The modelling result in Figure 6.20 shows the average number of electrons corresponding to the final probability distribution at $x = 5000$ nm as a function of SAW amplitude A_{SAW} and charging energy E_{c}, where the initial state is 5 electrons at $x = 2000$ nm. The result in Figure 6.20(a) shows some anomalous vertical lines that do not match the overall trend. These are caused by poorly-fitted V_0 and ω_{Barrier} at the corresponding SAW amplitudes. In order to observe the overall trend in the modelling result, these anomalous lines were removed and replaced by interpolated data. The modified result is shown in Figure 6.20(b). As can be seen, at a fixed E_{c}, when A_{SAW} decreases, the number of electrons also decreases from 5 to 0 due to weakening of the confinement of the SAW-created quantum dot. In addition, at

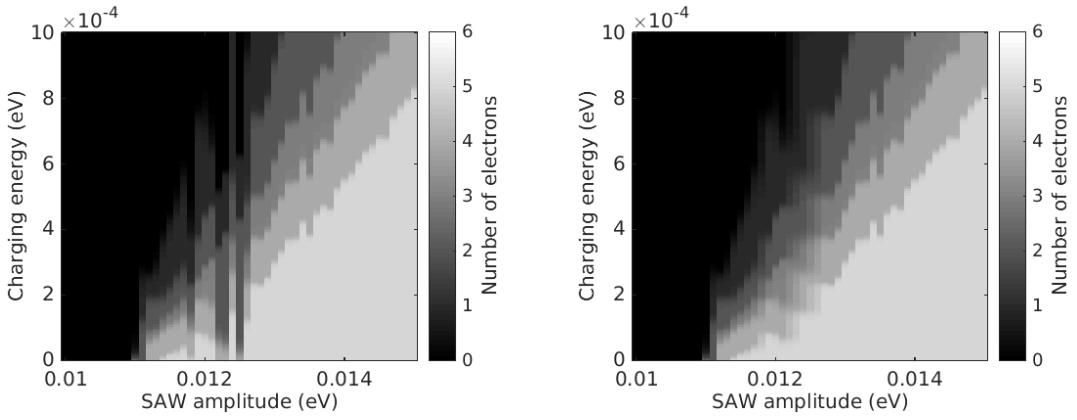

Fig. 6.20 Modelling result of the SAW-driven charge transport. (a) Number of SAW-driven electrons arriving at the region of holes as a function of SAW amplitude and charging energy. Anomalous vertical lines are due to poorly-fitted V_0 and ω_{Barrier} at corresponding SAW amplitude. (b) Modified result after data from anomalous lines are removed and replaced by interpolated data.

a higher E_c, the steps between different electron numbers are wider in terms of A_{SAW} and are more well-defined (with a higher contrast), suggesting a more clearly quantised SAW-driven current $I_{\text{SD}} = nef_{\text{RF}}$. This is because a higher E_c means a bigger energy difference in $u_{(\text{SAWdot})}(N)$ according to Equation 6.26. Since quantised SAW-driven current cannot be observed in the SAW-driven n-i-p junction TKH03, it is likely that the charging energy E_c is too low in this device. Hence, observation of quantised SAW-driven current and a further improved SAW-driven single-photon source might be achieved by increasing E_c in future devices.

Finally, because each configuration of A_{SAW} and E_c leads to a probability distribution, the average electron number and the corresponding second-order correlation function $g^{(2)}(0)$ can be evaluated for each configuration. Interestingly, when $A_{\text{SAW}} = 11$ meV and $E_c = 0.02$ meV, the final probability distribution $(P_0, P_1, P_2, P_3, P_4, P_5) = (0.22, 0.58, 0.19, 0.01, 0, 0)$ gives rise to $n_{\text{avg}} = 0.99$ and $g^{(2)}(0) = 0.44$, which are close to the measurement result $n_{\text{avg}} = 0.89 \pm 0.05$ and $g^{(2)}(0) = 0.39 \pm 0.05$, and the plausible probability distribution $(P_0, P_1, P_2) = (0.27, 0.58, 0.15)$. This indicates that, if this simple model for the SAW-driven charge transport does reflect the real dynamics to some extent, the probability distribution derived from the theoretical limits in Eqautions 6.21 and 6.20 may actually represent the real situation in the experiment. That is, if the background BG_{EL} ($\sim 17\%$ of overall EL signal) can be removed, the SAW-driven EL signal received by a detector has a probability of $\sim 80\%$ of being single-photon emission.

6.5 Conclusion

In summary, the autocorrelation histograms of the SAW-driven EL and analysis of the measurement result are presented in this chapter. First, details of the HBT experimental setup employed in the measurement are explained. Next, the autocorrelation histograms of the SAW-driven EL recorded using the HBT setup are shown. When the SAW-driven n-i-p junction is in the single-electron regime, where $I_{\mathrm{SD}} \simeq 1ef_{\mathrm{RF}}$, the effect of photon antibunching can be clearly observed in the histogram, meaning that the SAW-driven n-i-p junction is indeed a quantum light emitter. In order to extract the second-order correlation function $g^{(2)}(\Delta t)$, the autocorrelation histogram is further analysed by fitting the histogram to a function describing the autocorrelation of a SAW-driven EL. This analysis shows $g^{(2)}(0) = 0.39 \pm 0.05$, which is below the common criterion for a single-photon source $g^{(2)}(0) < 0.5$. Also, to investigate the probability distribution of the SAW-driven electron numbers (and photon numbers) in this SAW-driven n-i-p junction, theoretical calculation, simulation, and modelling have been carried out. These theoretical analyses suggest that, if the un-correlated background photons ($\sim 17\%$ of the overall EL) can be removed, $\sim 80\%$ of the SAW-driven EL received by a detector will be single photons. Finally, the simulation result shows that SAW-driven current quantisation may be achieved by increasing the charging energy E_{c} in future devices.

Chapter 7

Conclusions and Future work

7.1 Development of SAW-driven n-i-p Junctions

In this thesis, a SAW-driven n-i-p junction that can produce single photons has been developed. As well as this device, three earlier batches of devices have been characterised. It has been found that the confinement of charge carriers is critical for the observation of SAW-driven electroluminescence. Hence, a wet-etch pattern is used to eliminate unwanted current-flow paths. In this way, electron-hole recombination is concentrated in the junction, and EL from the n-i-p junction can therefore be observed. In order to enhance the SAW potential, deposition of a ZnO thin film was carried out in the third batch. SAW-driven charge transport and the corresponding EL signal were both observed on these ZnO-coated devices. However, the crosstalk-driven EL signal was significant compared with the SAW-driven EL signal, making these devices unsuitable for producing SAW-driven single photons. The significant crosstalk-driven EL signal may be the result of direct coupling of RF voltage via the quantum well between an IDT and a junction. In the final batch, TKH03, a trench was etched between the two to prevent this direct voltage coupling. As a result, the optimised device shows clear charge transport and an EL signal that is purely driven by a SAW.

In principle, the SAW-driven current should exhibit quantised plateaus at $I_{\mathrm{SD}} = nef_{\mathrm{SAW}}$. However, quantised SAW-driven current was not observed in these devices. The reason may be that the charging energy in the SAW-created dynamic quantum dots is too small, so that the SAW cannot carry a well-defined number of electrons in each minimum. It might be useful first to calculate the capacitance caused by the surface gates and the side gates in TKH03, then it might be possible to increase the charging energy by modifying the gate design based on the calculation. Hopefully, quantised SAW-driven current will be observed in such a device.

One issue with these junctions is the low photon emission efficiency. The highest efficiency measured was $\sim 2\%$, meaning that (1) most SAW-driven electrons escape from the junction area so that photons cannot be collected near the junction, or (2) electron-hole recombination is mainly non-radiative due to trapping in surface states. Hence, the efficiency may be enhanced by improving the confinement for SAW-driven electrons using a different gate design so that more electrons are trapped in the junction area, or by reducing the surface-state density using surface passivation.

7.2 Time-resolved SAW-driven Electroluminescence

To study the dynamics of the SAW-driven electrons in the region of holes, time-resolved measurements were performed by applying a SAW that was phase-locked to a series of timing pulses. This was achieved by employing either a two-channel AWG or an RF source synchronised to a low-jitter pulse generator. Using a proper time-resolved experimental setup, time-correlated histograms of the SAW-driven EL were obtained. The profile of the SAW-driven EL showed a periodic feature at the SAW frequency, indicating that a packet of electrons is transported to the region of hole in each SAW minimum. In addition, by launching a pulsed SAW, the SAW-driven EL and the crosstalk-driven EL could be separated in the time domain, so that they could be individually observed. On the optimised device TKH03, the crosstalk-driven EL was negligible (only 1%) compared with the SAW-driven EL. Moreover, using a high-timing-resolution setup, the time-correlated histograms from TKH03 exhibited fast electron-hole recombination. By fitting the time-resolved data to a model for the SAW-driven EL, it was found that the carrier lifetime of the SAW-driven electrons is about 100 ps, which is much shorter than the SAW period of 860 ps. Therefore, two photons caused by two consecutive SAW-driven single electrons do not have a significant overlap in time, making the optimised device TKH03 a good candidate for a SAW-driven single-photon source.

The carrier lifetime of the SAW-driven electrons might be affected by the density of holes since it is easier for an electron to find a hole to recombine with in a region with a higher density of holes. It will be interesting to carry out a detailed study of the carrier lifetime as a function of the hole-surface-gate voltage. It will also be interesting to measure the difference between SAW-driven electrons and SAW-driven holes in terms of their carrier lifetimes.

7.3 Photon Antibunching in SAW-driven Electroluminescence

In the last experiment, photon antibunching in the SAW-driven EL signal was tested using a Hanbury Brown-Twiss experimental setup. The SAW-driven current was first stabilised around $1ef_{\mathrm{SAW}}$ using a PID control loop. The corresponding SAW-driven EL was sent to the HBT setup so that an autocorrelation histogram could be recorded. Suppression of autocorrelation coincidences at time delay $\Delta t = 0$ showed evidence of photon antibunching. However, the true second-order correlation function $g^{(2)}(0)$ cannot be obtained directly from the histogram since the peaks in the histogram have significant overlap, and uncorrelated background photons lead to a constant background in the autocorrelation histogram. Therefore, a theoretical function describing the autocorrelation histogram of SAW-driven EL was established in order to extract the real $g^{(2)}(0)$ in the data. By fitting the data to this function, it was found that the SAW-driven EL shows $g^{(2)}(0) = 0.39 \pm 0.05$, which is lower than the common single-photon-source criterion $g^{(2)}(0) < 0.5$. This result shows that the SAW-driven n-i-p junction TKH03 can produce single-photon emission. Furthermore, theoretical calculation, simulation, and modelling were carried out in order to estimate the probability distribution of photon numbers in the SAW-driven EL. These theoretical analyses suggest that, if the background signal can be filtered or reduced, $\sim 80\%$ of the SAW-driven EL will be single photons.

Because quantised SAW-driven current could not be observed in this device, the number of electrons in each SAW minimum was not well-defined. This may be why $g^{(2)}(0)$ is not very low compared with self-assembled static quantum dots. If a device showing quantised SAW-driven current can be fabricated, the well-defined single-electron state in each SAW minimum should lead to a lower $g^{(2)}(0)$, making the device a better single-photon source.

7.4 Future Work

Compared with conventional single-photon sources, which rely on the presence of a single emitter such as a trapped atom, a defect in a Diamond, or a self-assembled quantum dot, the SAW-driven single-photon source produces single-photon emission by a different approach. It is done by transporting single electrons to a region of holes using a lithography-defined SAW transducer and an n-i-p junction. Hence, this SAW-driven single-photon source is fabricated in a totally deterministic way, which is more suitable for an integrated quantum photonic network. However, to be useful for a quantum repeater or for quantum computing, a good photon indistinguishability is important. The SAW-driven EL shows a spectrum with FWHM

of 1 meV, which is one or two orders of magnitude larger than the spectral FWHM from a quantum dot. The total FWHM is caused by homogeneous (natural linewidth and phonon scattering) and inhomogeneous (local electric field and potential fluctuation) broadening. It was found that, in a very high-quality 15 nm GaAs quantum well, the homogeneous broadening leads to about 150-200 μeV (FWHM), and the inhomogeneous broadening gives rise to about 100 μeV at 8 K [137]. Therefore, if a device can be made in such a high-quality quantum well, the spectral FWHM from the SAW-driven single-photon source may be reduced to about 200 μeV, which will improve the photon indistinguishability.

In addition, since it has been shown that a SAW can achieve quantised charge transport, it is possible to carry two electrons in each SAW minimum to the region of holes. Because these two electrons with opposite spins occupy the same energy level, they will in principle produce entangled photons. Therefore, this SAW-driven n-i-p junction is a potential entangled-photon source, which can be used in quantum teleportation. Furthermore, the SAW-driven n-i-p junction might even produce more than two entangled photons since quantised ten-electron transport was achieved using a SAW [61]. The ability to produce multiple entangled photons can be utilised in quantum metrology, where entangled quantum states are employed to achieve enhanced measurement accuracy.

References

[1] Nicolas Gisin, Grégoire Ribordy, Wolfgang Tittel, and Hugo Zbinden. Quantum cryptography. *Reviews of Modern Physics*, 74(1):145–195, 2002.

[2] Artur K. Ekert. Quantum cryptography based on Bellâs theorem. *Physical Review Letters*, 67(6):661–663, 1991.

[3] Hoi Kwong Lo and H. F. Chau. Unconditional security of quantum key distribution over arbitrarily long distances. *Science*, 283(5410):2050–2056, 1999.

[4] H J Kimble. The quantum internet. *Nature*, 453:1023–1030, 2008.

[5] S. Pirandola, J. Eisert, C. Weedbrook, A. Furusawa, and S. L. Braunstein. Advances in quantum teleportation. *Nature Photonics*, 9(10):641–652, 2015.

[6] Ryszard Horodecki, Paweł Horodecki, Michał Horodecki, and Karol Horodecki. Quantum entanglement. *Reviews of Modern Physics*, 81(2):865–942, 2009.

[7] Vittorio Giovannetti, Seth Lloyd, and Lorenzo Maccone. Quantum-enhanced measurements: Beating the standard quantum limit. *Science*, 306(5700):1330–1336, 2004.

[8] Vittorio Giovannetti, Seth Lloyd, and Lorenzo MacCone. Advances in quantum metrology. *Nature Photonics*, 5(4):222–229, 2011.

[9] E Knill, R Laflamme, and G J Milburn. A scheme for efficient quantum computation with linear optics. *Nature*, 409(6816):46–52, jan 2001.

[10] Pieter Kok, W J Munro, Kae Nemoto, T C Ralph, Jonathan P Dowling, and G J Milburn. Linear optical quantum computing with photonic qubits. *Reviews of Modern Physics*, 79(1):135–174, 2007.

[11] Göran Lindblad. A General No-Cloning Theorem. *Letters in Mathematical Physics*, 47(2):189–196, 1999.

[12] William K. Wootters and Wojciech H. Zurek. The no-cloning theorem. *Physics Today*, 62(2):76–77, 2009.

[13] Pascale Senellart, Glenn Solomon, and Andrew White. High-performance semiconductor quantum-dot single-photon sources. *Nature Nanotechnology*, 12(11):1026–1039, 2017.

[14] Igor Aharonovich, Dirk Englund, and Milos Toth. Solid-state single-photon emitters. *Nature Photonics*, 10(10):631–641, 2016.

[15] Andrew J. Shields. Semiconductor quantum light sources. *Nature Photonics*, 1(4):215–223, 2007.

[16] R. Hanbury Brown and R. Q. Twiss. Correlations between photons in two different beams of light. *Nature*, 2:1–2, 1956.

[17] N. Somaschi, V. Giesz, L. De Santis, J. C. Loredo, M. P. Almeida, G. Hornecker, S. L. Portalupi, T. Grange, C. Antón, J. Demory, C. Gómez, I. Sagnes, N. D. Lanzillotti-Kimura, A. Lemaítre, A. Auffeves, A. G. White, L. Lanco, and P. Senellart. Near-optimal single-photon sources in the solid state. *Nature Photonics*, 10(5):340–345, 2016.

[18] C. K. Hong, Z. Y. Ou, and L. Mandel. Measurement of subpicosecond time intervals between two photons by interference. *Physical Review Letters*, 59(18):2044–2046, 1987.

[19] Charles Santori, David Fattal, Jelena Vučković, Glenn S. Solomon, and Yoshihisa Yamamoto. Indistinguishable photons from a single-photon device. *Nature*, 419(6907):594–597, 2002.

[20] Yu Ming He, Yu He, Yu Jia Wei, Dian Wu, Mete Atatüre, Christian Schneider, Sven Höfling, Martin Kamp, Chao Yang Lu, and Jian Wei Pan. On-demand semiconductor single-photon source with near-unity indistinguishability. *Nature Nanotechnology*, 8(3):213–217, 2013.

[21] A. J. Bennett, D. C. Unitt, P. See, A. J. Shields, P. Atkinson, K. Cooper, and D. A. Ritchie. Electrical control of the uncertainty in the time of single photon emission events. *Physical Review B - Condensed Matter and Materials Physics*, 72(3):033316, 2005.

[22] F. Hargart, C. A. Kessler, T. Schwarzbäck, E. Koroknay, S. Weidenfeld, M. Jetter, and P. Michler. Electrically driven quantum dot single-photon source at 2 GHz excitation repetition rate with ultra-low emission time jitter. *Applied Physics Letters*, 102(1):011126, 2013.

[23] Michael E. Reimer, Gabriele Bulgarini, Nika Akopian, Moïra Hocevar, Maaike Bouwes Bavinck, Marcel A. Verheijen, Erik P A M Bakkers, Leo P. Kouwenhoven, and Val Zwiller. Bright single-photon sources in bottom-up tailored nanowires. *Nature Communications*, 3, 2012.

[24] Dominic Mayers. Unconditional security in quantum cryptography. *Journal of the ACM*, 48(3):351–406, 2001.

[25] Kazuya Takemoto, Yoshihiro Nambu, Toshiyuki Miyazawa, Yoshiki Sakuma, Tsuyoshi Yamamoto, Shinichi Yorozu, and Yasuhiko Arakawa. Quantum key distribution over 120km using ultrahigh purity single-photon source and superconducting single-photon detectors. *Scientific Reports*, 5, 2015.

[26] Charles H Bennett and Gilles Brassard. Quantum Cryptography: Public Key Distribution, and Coin-Tossing. In *Proc. 1984 IEEE International Conference on Computers, Systems, and Signal Processing*, pages 175–179, 1984.

[27] Nadia Al-Saidi. *Information Security based Nano and Bio-Cryptography.* IGI-Global, 1 edition, may 2014.

[28] Rainer Kaltenbaek, Robert Prevedel, Markus Aspelmeyer, and Anton Zeilinger. High-fidelity entanglement swapping with fully independent sources. *Physical Review A - Atomic, Molecular, and Optical Physics*, 79(4):040302, 2009.

[29] Juan Yin, Yuan Cao, Yu Huai Li, Sheng Kai Liao, Liang Zhang, Ji Gang Ren, Wen Qi Cai, Wei Yue Liu, Bo Li, Hui Dai, Guang Bing Li, Qi Ming Lu, Yun Hong Gong, Yu Xu, Shuang Lin Li, Feng Zhi Li, Ya Yun Yin, Zi Qing Jiang, Ming Li, Jian Jun Jia, Ge Ren, Dong He, Yi Lin Zhou, Xiao Xiang Zhang, Na Wang, Xiang Chang, Zhen Cai Zhu, Nai Le Liu, Yu Ao Chen, Chao Yang Lu, Rong Shu, Cheng Zhi Peng, Jian Yu Wang, and Jian Wei Pan. Satellite-based entanglement distribution over 1200 kilometers. *Science*, 356(6343):1140–1144, jun 2017.

[30] W. P. Grice. Arbitrarily complete Bell-state measurement using only linear optical elements. *Physical Review A*, 84(4):042331, 2011.

[31] Daniel Huber, Marcus Reindl, Yongheng Huo, Huiying Huang, Johannes S. Wildmann, Oliver G. Schmidt, Armando Rastelli, and Rinaldo Trotta. Highly indistinguishable and strongly entangled photons from symmetric GaAs quantum dots. *Nature Communications*, 8, 2017.

[32] Tomohisa Nagata, Ryo Okamoto, Jeremy L. O'Brien, Keiji Sasaki, and Shigeki Takeuchi. Beating the standard quantum limit with four-entangled photons. *Science*, 316(5825):726–729, 2007.

[33] M. Müller, H. Vural, C. Schneider, A. Rastelli, O. G. Schmidt, S. Höfling, and P. Michler. Quantum-Dot Single-Photon Sources for Entanglement Enhanced Interferometry. *Physical Review Letters*, 118(25):257402, 2017.

[34] Bryn Bell, Srikanth Kannan, Alex McMillan, Alex S. Clark, William J. Wadsworth, and John G. Rarity. Multicolor quantum metrology with entangled photons. *Physical Review Letters*, 111(9):093603, 2013.

[35] Nazgul Jenish and Ingmar R. Prucha. Central limit theorems and uniform laws of large numbers for arrays of random fields. *Journal of Econometrics*, 150(1):86–98, 2009.

[36] H. J. Kimble, Yuri Levin, Andrey B. Matsko, Kip S. Thorne, and Sergey P. Vyatchanin. Conversion of conventional gravitational-wave interferometers into quantum nondemolition interferometers by modifying their input and/or output optics. *Physical Review D - Particles, Fields, Gravitation and Cosmology*, 65(2):022002, 2002.

[37] Aasi J. et. Al. Enhanced sensitivity of the LIGO gravitational wave detector by using squeezed states of light. *Nature Photonics*, 7(8):613–619, 2013.

[38] Sergei Slussarenko, Morgan M. Weston, Helen M. Chrzanowski, Lynden K. Shalm, Varun B. Verma, Sae Woo Nam, and Geoff J. Pryde. Unconditional violation of the shot-noise limit in photonic quantum metrology. *Nature Photonics*, 11(11):700–703, 2017.

[39] Xi Lin Wang, Luo Kan Chen, W. Li, H. L. Huang, C. Liu, C. Chen, Y. H. Luo, Z. E. Su, D. Wu, Z. D. Li, H. Lu, Y. Hu, X. Jiang, C. Z. Peng, L. Li, N. L. Liu, Yu Ao Chen, Chao Yang Lu, and Jian Wei Pan. Experimental ten-photon entanglement. *Physical Review Letters*, 117(21):210502, 2016.

[40] H. J. Kimble, M. Dagenais, and L. Mandel. Photon Antibunching in Resonance Fluorescence. *Physical Review Letters*, 39(11):691–695, 1977.

[41] Markus Hijlkema, Bernhard Weber, Holger P. Specht, Simon C. Webster, Axel Kuhn, and Gerhard Rempe. A single-photon server with just one atom. *Nature Physics*, 3(4):253–255, 2007.

[42] D B Higginbottom, L Slodička, G Araneda, L Lachman, R Filip, M Hennrich, and R Blatt. Pure single photons from a trapped atom source. *New Journal of Physics*, 18(9):093038, 2016.

[43] Igor Aharonovich and Elke Neu. Diamond nanophotonics. *Advanced Optical Materials*, 2(10):911–928, 2014.

[44] N. Mizuochi, T. Makino, H. Kato, D. Takeuchi, M. Ogura, H. Okushi, M. Nothaft, P. Neumann, A. Gali, F. Jelezko, J. Wrachtrup, and S. Yamasaki. Electrically driven single-photon source at room temperature in diamond. *Nature Photonics*, 6(5):299–303, 2012.

[45] Ph Tamarat, T. Gaebel, J. R. Rabeau, M. Khan, A. D. Greentree, H. Wilson, L. C.L. Hollenberg, S. Prawer, P. Hemmer, F. Jelezko, and J. Wrachtrup. Stark shift control of single optical centers in diamond. *Physical Review Letters*, 97(8):083002, 2006.

[46] A. Sipahigil, K. D. Jahnke, L. J. Rogers, T. Teraji, J. Isoya, A. S. Zibrov, F. Jelezko, and M. D. Lukin. Indistinguishable photons from separated silicon-vacancy centers in diamond. *Physical Review Letters*, 113(11):113603, 2014.

[47] Xing Ding, Yu He, Z. C. Duan, Niels Gregersen, M. C. Chen, S. Unsleber, S. Maier, Christian Schneider, Martin Kamp, Sven Höfling, Chao Yang Lu, and Jian Wei Pan. On-Demand Single Photons with High Extraction Efficiency and Near-Unity Indistinguishability from a Resonantly Driven Quantum Dot in a Micropillar. *Physical Review Letters*, 116(2):0202401, 2016.

[48] Kerry J. Vahala. Optical microcavities. *Nature*, 424(6950):839–846, 2003.

[49] A. J. Bennett, D. C. Unitt, P. See, A. J. Shields, P. Atkinson, K. Cooper, and D. A. Ritchie. Microcavity single-photon-emitting diode. *Applied Physics Letters*, 86(18):1–3, 2005.

[50] C Schneider, A Huggenberger, T Sünner, T Heindel, M Strauß, S Göpfert, P Weinmann, S Reitzenstein, L Worschech, M Kamp, S Höfling, and A Forchel. Single site-controlled In(Ga)As/GaAs quantum dots: growth, properties and device integration. *Nanotechnology*, 20(43):434012, 2009.

[51] Dan Dalacu, Michael E. Reimer, Simon Frédérick, Danny Kim, Jean Lapointe, Philip J. Poole, Geof C. Aers, Robin L. Williams, W. Ross McKinnon, Marek Korkusiński, and Pawel Hawrylak. Directed self-assembly of single quantum dots for telecommunication wavelength optical devices, 2010.

[52] Edward B. Flagg, Andreas Muller, Sergey V. Polyakov, Alex Ling, Alan Migdall, and Glenn S. Solomon. Interference of single photons from two separate semiconductor quantum dots. *Physical Review Letters*, 104(13):137401, 2010.

[53] Raj B. Patel, Anthony J. Bennett, Ian Farrer, Christine A. Nicoll, David A. Ritchie, and Andrew J. Shields. Two-photon interference of the emission from electrically tunable remote quantum dots. *Nature Photonics*, 4(9):632–635, 2010.

[54] Z. Yuan. Electrically Driven Single-Photon Source. *Science*, 295(5552):102–105, 2002.

[55] Alberto Boretti, Lorenzo Rosa, Andrew Mackie, and Stefania Castelletto. Electrically Driven Quantum Light Sources. *Advanced Optical Materials*, 3(8):1012–1033, 2015.

[56] C. L. Foden, V. I. Talyanskii, G. J. Milburn, M. L. Leadbeater, and M. Pepper. High-frequency acousto-electric single-photon source. *Physical Review A*, 62(1):011803, jun 2000.

[57] Christopher J B Ford. Transporting and manipulating single electrons in surface-acoustic-wave minima. *Physica Status Solidi (B) Basic Research*, 254(3):1600658, 2017.

[58] Sylvain Hermelin, Shintaro Takada, Michihisa Yamamoto, Seigo Tarucha, Andreas D. Wieck, Laurent Saminadayar, Christopher Bäuerle, and Tristan Meunier. Electrons surfing on a sound wave as a platform for quantum optics with flying electrons. *Nature*, 477(7365):435–438, 2011.

[59] R P G McNeil, M Kataoka, C J B Ford, C H W Barnes, D Anderson, G A C Jones, I Farrer, and D A Ritchie. On-demand single-electron transfer between distant quantum dots. *Nature*, 477(7365):439–442, sep 2011.

[60] J. M. Shilton, V. I. Talyanskii, M. Pepper, D. A. Ritchie, J. E.F. Frost, C. J.B. Ford, C. G. Smith, and G. A.C. Jones. High-frequency single-electron transport in a quasi-one-dimensional GaAs channel induced by surface acoustic waves. *Journal of Physics Condensed Matter*, 8(38):L531–L539, 1996.

[61] Michael Robert Astley. *Surface-acoutic-wave-defined dynamic quantum dots*. PhD thesis, University of Cambridge, 2008.

[62] C. L. Salter, R. M. Stevenson, I. Farrer, C. A. Nicoll, D. A. Ritchie, and A. J. Shields. An entangled-light-emitting diode. *Nature*, 465(7298):594–597, 2010.

[63] R. Winik, D. Cogan, Y. Don, I. Schwartz, L. Gantz, E. R. Schmidgall, N. Livneh, R. Rapaport, E. Buks, and D. Gershoni. On-demand source of maximally entangled photon pairs using the biexciton-exciton radiative cascade. *Physical Review B*, 95(23):235435, 2017.

[64] C. H. W. Barnes, J. M. Shilton, and A. M. Robinson. Quantum computation using electrons trapped by surface acoustic waves. *Physical Review B*, 62:8410, 2000.

[65] Thomas Heinzel. *Mesoscopic Electronics in Solid State Nanostructures: Second Edition*. John Wiley & Sons, 2008.

[66] Emil S. Koteles and J. Y. Chi. Experimental exciton binding energies in GaAs/AlxGa1-xAs quantum wells as a function of well width. *Physical Review B*, 37(11):6332–6335, 1988.

[67] R. Landauer. Spatial Variation of Currents and Fields Due to Localized Scatterers in Metallic Conduction. *IBM Journal of Research and Development*, 1:223, 1957.

[68] P. Ramvall, N. Carlsson, I. Maximov, P. Omling, L. Samuelson, W. Seifert, Q. Wang, and S. Lourdudoss. Quantized conductance in a heterostructurally defined Ga0.25In0.75As/InP quantum wire. *Applied Physics Letters*, 71(7):918–920, 1997.

[69] V I Borisov, V G Lapin, A G Temiryazev, A I Toropov, and A I Chmil'. Features of the conductance quantization for etched 1D channels. *Journal of Communications Technology and Electronics*, 54(4):468–472, 2009.

[70] Hiroshi Irie, Yuichi Harada, Hiroki Sugiyama, and Tatsushi Akazaki. In0:75Ga0:25as quantum point contacts utilizing wrap-gate geometry. *Applied Physics Express*, 5(2):024001, 2012.

[71] L. P. Kouwenhoven, D. G. Austing, and S. Tarucha. Few-electron quantum dots. *Reports on Progress in Physics*, 64(6):701–736, 2001.

[72] J S Peng and G Li. *Introduction to Modern Quantum Optics*. World Scientific, 1998.

[73] John Garrison and Raymond Chiao. *Quantum Optics*, volume 9780198508. Oxford University Press, 2008.

[74] Niels Bohr and J. Rud. Nielsen. *The correspondence principle : 1918-1923*. North-Holland, 1976.

[75] Colin Campbell. Surface Acoustic Wave Devices and their Signal Processing Applications. *Surface Acoustic Wave Devices and their Signal Processing Applications*, pages 9–30, 1989.

[76] M Kataoka, M R Astley, A L Thorn, D K L Oi, C H W Barnes, C J B Ford, D Anderson, G A C Jones, I Farrer, D A Ritchie, and M Pepper. Coherent Time Evolution of a Single-Electron Wave Function. *Physical Review Letters*, 102(15):156801, 2009.

[77] S. Hermelin, S. Takada, M. Yamamoto, S. Tarucha, A. D. Wieck, L. Saminadayar, C. Bäuerle, and T. Meunier. Fast and efficient single electron transfer between distant quantum dots. *Journal of Applied Physics*, 113(13):136508, 2013.

[78] B. Bertrand, S. Hermelin, S. Takada, M. Yamamoto, S. Tarucha, A. Ludwig, A. D. Wieck, C. Bäuerle, and T. Meunier. Fast spin information transfer between distant quantum dots using individual electrons. *Nature Nanotechnology*, 11(8):672–676, 2016.

[79] C. Rocke, S. Zimmermann, A. Wixforth, J. P. Kotthaus, G. Böhm, and G. Weimann. Acoustically driven storage of light in a quantum well. *Physical Review Letters*, 78(21):4099–4102, 1997.

[80] F Iikawa, J A H Stotz, U Jahn, R Hey, P V Santos, O D D Couto, and S Lazic. Photon anti-bunching in acoustically pumped quantum dots. *Nature Photonics*, 3:645–648, 2009.

[81] M. Weiß, S. Kapfinger, T. Reichert, J. J. Finley, A. Wixforth, M. Kaniber, and H. J. Krenner. Surface acoustic wave regulated single photon emission from a coupled quantum dot-nanocavity system. *Applied Physics Letters*, 109(3):033105, 2016.

[82] B. Villa, A. J. Bennett, D. J.P. Ellis, J. P. Lee, J. Skiba-Szymanska, T. A. Mitchell, J. P. Griffiths, I. Farrer, D. A. Ritchie, C. J.B. Ford, and A. J. Shields. Surface acoustic wave modulation of a coherently driven quantum dot in a pillar microcavity. *Applied Physics Letters*, 111(1):011103, 2017.

[83] T. Hosey, V. Talyanskii, S. Vijendran, G. A C Jones, M. B. Ward, D. C. Unitt, C. E. Norman, and A. J. Shields. Lateral n-p junction for acoustoelectric nanocircuits. *Applied Physics Letters*, 85(3):491–493, 2004.

[84] S J Smith, G R Nash, C J Bartlett, L Buckle, M T Emeny, and T Ashley. Lateral light emitting n-i-p diodes in InSbAl[sub x]In[sub 1x]Sb quantum wells. *Applied Physics Letters*, 89(11):111118, 2006.

[85] J R Gell, P Atkinson, S P Bremner, F Sfigakis, M Kataoka, D Anderson, G A C Jones, C H W Barnes, D A Ritchie, M B Ward, C E Norman, and A J Shields. Surface-acoustic-wave-driven luminescence from a lateral p-n junction. *Applied Physics Letters*, 89(24):243505, 2006.

[86] J R Gell, M B Ward, A J Shields, P Atkinson, S P Bremner, D Anderson, M Kataoka, C H W Barnes, G A C Jones, and D A Ritchie. Temporal characteristics of surface-acoustic-wave-driven luminescence from a lateral p-n junction. *Applied Physics Letters*, 91(1):013506, 2007.

[87] Giorgio De Simoni, Vincenzo Piazza, Lucia Sorba, Giorgio Biasiol, and Fabio Beltram. Acoustoelectric luminescence from a field-effect n-i-p lateral junction. *Applied Physics Letters*, 94(12):121103, 2009.

[88] Van-Truong Dai, Sheng-Di Lin, Shih-Wei Lin, Yi-Shan Lee, Yin-Jie Zhang, Liang-Chen Li, and Chien-Ping Lee. High-quality planar light emitting diode formed by induced two-dimensional electron and hole gases. *Optics express*, 22(4):3811–7, feb 2014.

[89] Yousun Chung. *A Potential Single-Photon Source Driven by a Surface Acoustic Wave*. PhD thesis, Unversity of Cambridge, 2015.

[90] Seok-Kyun Son. *Electron transport by surface acoustic waves in an undoped system*. PhD thesis, University of Cambridge, 2014.

[91] Antonio Rubino. Development of a SAW driven source of polarised single photons, first year report. Technical report, University of Cambridge, 2016.

[92] Enrico Zanoni, Alessandro Callegari, Claudio Canali, Fausto Fantini, Hans L. Hartnagel, Fabrizio Magistrali, Alessandro Paccagnella, and Massimo Vanzi. Metal–GaAs interaction and contact degradation in microwave MESFETs. *Quality and Reliability Engineering International*, 6(1):29–46, jan 1990.

[93] Matthew Benesh. *Charge Transport Dynamics of Surface Acoustic Waves in a GaAs/AlGaAs 2DEG*. PhD thesis, University of Cambridge, 2013.

[94] J. Pedros, L. Garcia-Gancedo, C. J. B. Ford, C. H. W. Barnes, J. P. Griffiths, G. A. C. Jones, and A. J. Flewitt. Guided propagation of surface acoustic waves and piezoelectric field enhancement in ZnO/GaAs systems. *Journal of Applied Physics*, 110(10):103501, 2011.

[95] HangTian Hou. SAW enhancement in ZnO/GaAs/AlGaAs systems. Technical report, University of Cambridge, 2018.

[96] R. Newbury. *Top Loading Sorption Pumped He-3 Insert Operating Instructions*. Oxford Instruments Limited, 1990.

[97] Alexander Justin. Semiconductor Single-Photon Systems using Surface Acoustic Waves, project report. Technical report, University of Cambridge, 2012.

[98] Z M Zhang, Q An, J W Li, and W J Zhang. Piezoelectric friction–inertia actuator—a critical review and future perspective. *The International Journal of Advanced Manufacturing Technology*, 62(5-8):669–685, 2012.

[99] J. S. Blakemore. Semiconducting and other major properties of gallium arsenide. *Journal of Applied Physics*, 53(10):R123, 1982.

[100] Karl Kraus. *Photogrammetry: geometry from images and laser scans*. Wlater de Gruyter, 2 edition, 2007.

[101] R. K. Ahrenkiel, R. Ellingson, W. Metzger, D. I. Lubyshev, and W. K. Liu. Auger recombination in heavily carbon-doped GaAs. *Applied Physics Letters*, 78(13):1879–1881, 2001.

[102] J Yang, D G Zhao, D S Jiang, P Chen, Z S Liu, J J Zhu, X J Li, X G He, J P Liu, L Q Zhang, H Yang, Y T Zhang, and G T Du. Emission efficiency enhanced by reducing the concentration of residual carbon impurities in InGaN/GaN multiple quantum well light emitting diodes. *Optics Express*, 24(13):13824–13831, 2016.

[103] W. Bludau and E. Wagner. Carrier lifetime controlled by capture into deep and shallow centers in GaAs. *Applied Physics Letters*, 29(3):204–206, 1976.

[104] Lorenzo Pavesi and Mario Guzzi. Photoluminescence of AlxGa1-xAs alloys. *Journal of Applied Physics*, 75(10):4779–4842, 1994.

[105] Masashi Ozeki, Kenya Nakai, Kouichi Dazai, and Osamu Ryuzan. Photoluminescence study of carbon doped gallium arsenide. *Japanese Journal of Applied Physics*, 13(7):1121–1126, 1974.

[106] B. J. Aitchison, N. M. Haegel, C. R. Abernathy, and S. J. Pearton. Enhanced hot-electron photoluminescence from heavily carbon-doped GaAs. *Applied Physics Letters*, 56(12):1154–1156, 1990.

[107] Roberto Menozzi. Hot electron effects and degradation of GaAs and InP HEMTs for microwave and millimetre-wave applications. *Semiconductor Science and Technology*, 13(10):1053–1063, 1998.

[108] M. Montes Bajo, C. Hodges, M. J. Uren, and M. Kuball. On the link between electroluminescence, gate current leakage, and surface defects in AlGaN/GaN high electron mobility transistors upon off-state stress. *Applied Physics Letters*, 101(3):033508, 2012.

[109] H. P. Zappe. Hot-electron electroluminescence in GaAs transistors. *Semiconductor Science and Technology*, 7(3):391–400, 1992.

[110] J. R. Barker. Hot electron phenomena and electroluminescence. *Journal of Luminescence*, 23(1-2):101–126, 1981.

[111] Mauricio M. De Lima and Paulo V. Santos. Modulation of photonic structures by surface acoustic waves. *Reports on Progress in Physics*, 68(7):1639–1701, 2005.

[112] F. Alsina, P. V. Santos, H.-P. Schönherr, W. Seidel, K. H. Ploog, and R. Nötzel. Surface-acoustic-wave-induced carrier transport in quantum wires. *Physical Review B*, 66(16):165330, 2002.

[113] Y. Takagaki, E. Wiebicke, H. J. Zhu, R. Hey, M. Ramsteiner, and K. H. Ploog. Suppression of the photoluminescence quenching due to surface acoustic waves in high magnetic fields. *Semiconductor Science and Technology*, 17(2):161–165, 2002.

[114] R. Songmuang, Le Thuy Thanh Giang, J. Bleuse, M. Den Hertog, Y. M. Niquet, Le Si Dang, and H. Mariette. Determination of the Optimal Shell Thickness for Self-Catalyzed GaAs/AlGaAs Core-Shell Nanowires on Silicon. *Nano Letters*, 16(6):3426–3433, 2016.

[115] Raffaella Calarco, Michel Marso, Thomas Richter, Ali I. Aykanat, Ralph Meijers, André V.D. Hart, Toma Stoica, and Hans Luth. Size-dependent photoconductivity in MBE-grown GaN - Nanowires. *Nano Letters*, 5(5):981–984, 2005.

[116] O. Demichel, M. Heiss, J. Bleuse, H. Mariette, and I. A. Fontcuberta Morral. Impact of surfaces on the optical properties of GaAs nanowires. *Applied Physics Letters*, 97(20):201907, 2010.

[117] Nanako Shiozaki, Sanguan Anantathanasarn, Taketomo Sato, Tamotsu Hashizume, and Hideki Hasegawa. Surface-related reduction of photoluminescence in GaAs quantum wires and its recovery by new passivation. *Applied Surface Science*, 244(1-4):71–74, 2005.

[118] D. Sager, C. Gutsche, W. Prost, F. J. Tegude, and G. Bacher. Recombination dynamics in single GaAs-nanowires with an axial heterojunction: N- versus p-doped areas. *Journal of Applied Physics*, 113(17):174303, 2013.

[119] Tim Burgess, Dhruv Saxena, Sudha Mokkapati, Zhe Li, Christopher R. Hall, Jeffrey A. Davis, Yuda Wang, Leigh M. Smith, Lan Fu, Philippe Caroff, Hark Hoe Tan, and Chennupati Jagadish. Doping-enhanced radiative efficiency enables lasing in unpassivated GaAs nanowires. *Nature Communications*, 7, 2016.

[120] T. N. Theis and S. L. Wright. Origin of]] residual" persistent photoconductivity in selectively doped GaAs/AlxGa1-xAs heterojunctions. *Applied Physics Letters*, 48(20):1374–1376, 1986.

[121] J. Z. Li, J. Y. Lin, H. X. Jiang, M. Asif Khan, and Q. Chen. Persistent photoconductivity in a two-dimensional electron gas system formed by an AlGaN/GaN heterostructure. *Journal of Applied Physics*, 82(3):1227–1230, 1997.

[122] E. P. De Poortere, Y. P. Shkolnikov, and M. Shayegan. Field-effect persistent photoconductivity in AlAs and GaAs quantum wells with Al x Ga 1 x As barriers. *Physical Review B*, 67(15):153303, apr 2003.

[123] P. V. Santos, F. Alsina, J. A. H. Stotz, R. Hey, S. Eshlaghi, and A. D. Wieck. Band mixing and ambipolar transport by surface acoustic waves in GaAs quantum wells. *Physical Review B*, 69(15):155318, 2004.

[124] Tetsuomi Sogawa, Haruki Sanada, Hideki Gotoh, Hiroshi Yamaguchi, and Paulo V. Santos. Spatially modulated photoluminescence properties in dynamically strained GaAs/AlAs quantum wells by surface acoustic wave. *Applied Physics Letters*, 100(16):162109, 2012.

[125] Jennifer Rachel Gell. *Surface-acoustic-wave driven light sources*. PhD thesis, University of Cambridge, 2007.

[126] M. Kataoka, C. H. W. Barnes, H. E. Beere, D. A. Ritchie, and M. Pepper. Experimental investigation of the surface acoustic wave electron capture mechanism. *Physical Review B*, 74(8):085302, aug 2006.

[127] M. Buttiker. Quantized transmission of a saddle-point constriction. *Physical Review B*, 41(11):7906–7909, apr 1990.

[128] M. R. Astley, M. Kataoka, C. J.B. Ford, C. H.W. Barnes, D. Anderson, G. A.C. Jones, I. Farrer, D. A. Ritchie, and M. Pepper. Energy-dependent tunneling from few-electron dynamic quantum dots. *Physical Review Letters*, 99(15):156802, 2007.

[129] S. Cova, M. Ghioni, A. Lacaita, C. Samori, and F. Zappa. Avalanche photodiodes and quenching circuits for single-photon detection. *Applied Optics*, 35(12):1956, 1996.

[130] Jasprit Singh. *Electronic and optoelectronic properties of semiconductor structures*. Cambridge University Press, 1 edition, 2003.

[131] IDQ. ID100 Spec Sheet, 2015.

[132] Sonia Buckley, Kelley Rivoire, and Jelena Vuckovic. Engineered Quantum Dot Single Photon Sources. *Reports On Progress In Physics*, 75(12):52, 2012.

[133] P Grünwald. What gˆ(2)(0)1/2 tells you - and what it does not. *ArXiv e-prints*, 1711.05897, nov 2017.

[134] Xing Lin, Xingliang Dai, Chaodan Pu, Yunzhou Deng, Yuan Niu, Limin Tong, Wei Fang, Yizheng Jin, and Xiaogang Peng. Electrically-driven single-photon sources based on colloidal quantum dots with near-optimal antibunching at room temperature. *Nature Communications*, 8(1), 2017.

[135] Hangtian Hou, Yousun Chung, Girish Rughoobur, Tzu-Kan Hsiao, Ateeq Nasir, Andrew J Flewitt, John Griffiths, Ian Farrer, David A Ritchie, and Chris J Ford. Experimental verication of electrostatic boundary conditions in gate-patterned quantum devices. *Journal of Physics D: Applied Physics*, 51:244004, may 2018.

[136] Nextnano GmbH. Nextnano.

[137] Vivek Srinivas, John Hryniewicz, Yung Jui Chen, and Colin E.C. Wood. Intrinsic linewidths and radiative lifetimes of free excitons in GaAs quantum wells. *Physical Review B*, 46(16):10193–10196, 1992.